Ryerson University
Digital Commons @ Ryerson

Theses and dissertations

1-1-2005

# Rigid body dynamics and simulation of a three-cylinder, four-stroke internal combustion engine coupled with an aircraft propeller

Scott A. Warwick
*Ryerson University*

Follow this and additional works at: http://digitalcommons.ryerson.ca/dissertations

 Part of the Mechanical Engineering Commons

Recommended Citation
Warwick, Scott A., "Rigid body dynamics and simulation of a three-cylinder, four-stroke internal combustion engine coupled with an aircraft propeller" (2005). *Theses and dissertations.* Paper 396.

This Thesis is brought to you for free and open access by Digital Commons @ Ryerson. It has been accepted for inclusion in Theses and dissertations by an authorized administrator of Digital Commons @ Ryerson. For more information, please contact bcameron@ryerson.ca.

MAR 13 2006

B16999265

TJ
756
.W37
2005

# Rigid Body Dynamics and Simulation of a Three-Cylinder, Four-Stroke Internal Combustion Engine Coupled with an Aircraft Propeller

by

Scott A. Warwick

Bachelor of Aerospace Engineering

Ryerson University

A thesis

Presented to Ryerson University

In partial fulfillment of the

Requirements for the degree of

Master of Applied Science

In the Program of

Mechanical Engineering

Toronto, Ontario, Canada

© Scott A. Warwick, 2005

PROPERTY OF
RYERSON UNIVERSITY LIBRARY

UMI Number: EC53773

INFORMATION TO USERS

The quality of this reproduction is dependent upon the quality of the copy submitted. Broken or indistinct print, colored or poor quality illustrations and photographs, print bleed-through, substandard margins, and improper alignment can adversely affect reproduction.

In the unlikely event that the author did not send a complete manuscript and there are missing pages, these will be noted. Also, if unauthorized copyright material had to be removed, a note will indicate the deletion.

UMI®

UMI Microform EC53773
Copyright 2009 by ProQuest LLC
All rights reserved. This microform edition is protected against unauthorized copying under Title 17, United States Code.

ProQuest LLC
789 East Eisenhower Parkway
P.O. Box 1346
Ann Arbor, MI 48106-1346

## *Author's Declaration*

I hereby declare that I am the sole author of this thesis.

I authorize Ryerson University to lend this thesis to other institutions or individuals for the purpose of scholarly research.

Signature

I further authorize Ryerson University to reproduce this thesis by photocopying or by other means, in total or in part, at the request of other institutions or individuals for the purpose of scholarly research.

Signature

RIGID BODY DYNAMICS AND SIMULATION OF A THREE-CYLINDER,
FOUR-STROKE INTERNAL COMBUSTION ENGINE COUPLED WITH AN AIRCRAFT PROPELLER

Master of Applied Science, 2005
Scott A. Warwick
Mechanical Engineering
Ryerson University

## *Abstract*

Dynamical behaviors of a system consisting of a Saito-450 3-cylinder, 4-stroke engine and a variable pitch propeller are studied. The kinemtical equations for the planar 8-bar internal combustion engine are established using a complex number method. The nonlinear dynamical equation for the engine-propeller system is obtained using the Lagrange equation and solved numerically using a computer code written in the Matlab language.

Various simulations were performed to study the transient and steady state dynamical behaviors of the sophisticated multiple rigid body system while taking into account the engine pressure pulsations and aerodynamic load. The steady-state motions of the propeller shaft for different engine powers and speeds were obtained and decomposed using the Fast Fourier Technique (FFT).

Results presented in this thesis provide necessary input for studies of flexible body dynamics where the torsional vibration of the propeller shaft is of practical interest to design engineers in the aerospace industry.

## *Acknowledgements*

I wish to thank my advisor, Professor Shudong Yu, for his patience, entheusiastic guidance and expertise throughout this project, without which, this project would not have been successfully completed.

I also wish to thank Ruben Perez, Alan Machin and Andrew Heim for their theoretical and technical support in a time of need.

## *Dedication*

I dedicate this thesis to my wife Barbara who was, and is, the source of my inspiration and whose support has never waivered throughout the course of this project.

# *Table of Contents*

## *List of Tables*

## *List of Figures*

## *Nomenclature*

| | | |
|---|---|---|
| $a_0$ | Average Value of the Fourier Series as Obtained by FFT | - |
| $a_1$ | Acceleration of Piston #1 | $m/s^2$ |
| $a_7$ | Acceleration of Piston #2 | $m/s^2$ |
| $a_9$ | Acceleration of Piston #3 | $m/s^2$ |
| $a_{cg3}$ | Acceleration of Mass Center of Connecting Rod #1 | $m/s^2$ |
| $a_{cg6}$ | Acceleration of Mass Center of Connecting Rod #2 | $m/s^2$ |
| $a_{cg8}$ | Acceleration of Mass Center of Connecting Rod #3 | $m/s^2$ |
| $a_i$ | Real $i^{th}$ Spectral Coefficient | - |
| $A$ | Cubic Spline Variable Matrix | - |
| $A_k$ | Cubic Spline Coefficients ($k = 0,1,2,3$) | - |
| $A_c$ | Cylinder Cross Sectional Area | $m^3$ |
| $A_p$ | Piston Cross Sectional Area | $m^2$ |
| $b_i$ | Complex $i^{th}$ Spectral Coefficient | - |
| $B$ | Number of Propeller Blades | - |
| $c$ | Airfoil Chord | m |
| $c_d$ | Section Drag Coefficient | - |
| $c_{di}$ | Drag Coefficient at the $i^{th}$ Blade Station | - |
| $c_D$ | Drag Coefficient | - |
| $c_l$ | Section Lift Coefficient | - |
| $c_{lo}$ | Uncorrected Lift Coefficient | - |
| $c_{loc}$ | Local Chord | m |
| $c_{l\alpha}$ | Lift Curve Slope | $rad^{-1}$ |
| $c_L$ | Lift Coefficient | - |
| $c_p$ | Specific Heat of the Working Fluid | kJ/kg·K |
| $C_A$ | Slope of Engine Power Curve | Nm/rad |
| $C_B$ | Slope of Propeller Load Curve | Nm/rad |
| $d$ | Characteristic Length of Blade Section | m |
| $d_p$ | Distance from Mass Center to Fulcrum | m |
| $D$ | Drag | N |
| $D_{ist}$ | Position of Piston | m |
| $D_p$ | Diameter of Propeller | m |
| $g$ | Gravitational Constant | $m/s^2$ |
| $h$ | Angular Increment | rad |
| $h_{exh}$ | Height of Exhaust Tappet | m |
| $h_{int}$ | Height of Intake Tappet | m |
| $h_{valve}$ | Linear Position of the Valves | m |
| $H_1$ | Power Generated | W |
| $H_2$ | Power Consumed | W |
| $H_l$ | Propeller Torque | Nm |
| $H_m$ | Engine Torque | Nm |
| $I$ | Mass Moment of Inertia | $kgm^2$ |
| $I_{CM}$ | Moment of Inertia of Propeller about its Mass Center | $kgm^2$ |
| $J$ | Advance Ratio | - |
| $J_i$ | Moment of Inertia of the $i^{th}$ Component | $kgm^2$ |

| | | |
|---|---|---|
| $k$ | Spring Constant | N/m |
| $k_c$ | Polytropic Exponent of Compression | - |
| $k_e$ | Polytropic Exponent of Expansion | - |
| $L$ | Lift | N |
| $m_p$ | Mass of Propeller | kg |
| $m_i$ | Mass of $i^{th}$ Link | kg |
| $\dot{m}$ | Mass Flow Rate | kg/s |
| $M_\infty$ | Freestream Mach Number | - |
| $n$ | Rotational Speed of Propeller | rad/s |
| $P_3$ | Maximum Cylinder Pressure | Pa |
| $P_c$ | Pressure During the Compression Stroke | Pa |
| $P_e$ | Exhaust Pressure | Pa |
| $P_i$ | Pressure Within the $i^{th}$ Cylinder | Pa |
| $P_{ivc}$ | Cylinder Pressure at Intake Valve Closing | Pa |
| $q$ | Cubic Spline Constraint Matrix | - |
| $Q$ | Total Work Done by Gas Pressure | Nm |
| $Q_i$ | Work Done by Gas Pressure of the $i^{th}$ Cylinder | Nm |
| $Q_p$ | Torque | Nm |
| $r$ | Local Blade Radius Measured from the Hub | m |
| $r_c$ | Compression Ratio | - |
| $r_{ca}$ | Distance from Crank Shaft to the Piston | m |
| $r_k$ | Linear Geometric parameters for an 8-bar engine mechanism ($k$ =1,...,16) | m |
| $r_{max}$ | Maximum Distance of Piston from the Crank Shaft Center | m |
| $r_{RA}$ | Length of the Rocker Arm from the Fulcrum to the Valve Contact Point | m |
| $R$ | Universal Gas Constant | J/kgK |
| $R_k$ | Complex Position Vectors for an 8-bar engine mechanism ($k$ =1,...,9) | m |
| $Re$ | Reynolds Number | - |
| $R_p$ | Radius of Propeller Blade | m |
| $\bar{s}$ | Fourier Representation of Position | m |
| $S$ | Propeller Planform Area | $m^2$ |
| $t$ | Airfoil Thickness | m |
| $t/c$ | Thickness to Chord Ratio | - |
| $T$ | Kinetic Energy | J |
| $\widetilde{T}$ | Kinetic Energy Normalized with respect to $\dot{\theta}_2^2$ | J/rad |
| $\widetilde{T}_i$ | Kinetic Energy Normalized with respect to $\theta_2$ of the $i^{th}$ Component | J/rad |
| $T_{amb}$ | Ambient Temperature | K |
| $T_e$ | Temperature | K |
| $T_h$ | Thrust | N |
| $T_p$ | Period of Physical Pendulum | s |
| $T_{thermocouple}$ | Temperature Read from a Thermocouple | K |
| $U$ | Potential Energy | J |
| $v_1$ | Velocity of Piston #1 | m/s |
| $v_7$ | Velocity of Piston #2 | m/s |
| $v_9$ | Velocity of Piston #3 | m/s |
| $v_{cg3}$ | Velocity of Mass Center of Connecting Rod #1 | m/s |
| $v_{cg6}$ | Velocity of Mass Center of Connecting Rod #2 | m/s |

| | | |
|---|---|---|
| $v_{cg8}$ | Velocity of Mass Center of Connecting Rod #3 | m/s |
| $V$ | Cylinder Volume as a Function of Crankshaft Angular Position | $m^3$ |
| $V_{air}$ | Air Velocity | m/s |
| $V_c$ | Clearance Volume | $m^3$ |
| $V_{ivc}$ | Cylinder Volume at Intake Valve Closing | $m^3$ |
| $V_s$ | Swept Volume | $m^3$ |
| $V_E$ | Resulting Air Speed Impinging on the Propeller Section Taking Into Account the Blade Section Downwash | m/s |
| $V_R$ | Resulting Air Speed Impinging on the Propeller Section Taking Into Account the Forward Speed of the Aircraft | m/s |
| $V_T$ | Propeller Tip Speed | m/s |
| $V_\infty$ | Freestream Velocity | m/s |
| $W_i$ | Work Absorbed by the Propeller | Nm |
| $x$ | Local Blade Radius Normalized with respect to the Total Blade Radius | - |
| $x_{exh}$ | Actual Angular Deflection of the Exhaust Rocker Arm | rad |
| $x_{int}$ | Actual Angular Deflection of the Intake Rocker Arm | rad |
| $x_{sp}$ | Spring Position | m |
| $x_i$ | Linear Spring Displacement as a Function of $\theta_2$ | m |
| $\{y\}$ | Initial Position Array | - |
| $y_1$ | Substitution Variable for Differential Order Reduction | - |
| $\dot{y}_1$ | Derivative of Substitution Variable for Differential Order Reduction | - |
| $y_2$ | Substitution Variable for Differential Order Reduction | - |
| $\dot{y}_2$ | Derivative of Substitution Variable for Differential Order Reduction | - |
| $Y_1$ | Pressure at the End of the Compression Stroke | Pa |
| $Y'_1$ | Slope at the End of the Compression Stroke | Pa/rad |
| $Y_2$ | Pressure at the Beginning of the Exhaust Stroke | Pa |
| $Y'_2$ | Slope of the Pressure at the Beginning of the Expansion Stroke | Pa/rad |
| $y_{exh}$ | Approximate Deflected Height of the Exhaust Tappet | m |
| $y_{int}$ | Approximate Deflected Height of the Intake Tappet | m |
| $y_{RAexh}$ | Approximate Angular Deflection of the Exhaust Rocker Arm | rad |
| $y_{RAint}$ | Approximate Angular Deflection of the Intake Rocker Arm | rad |
| $y_{sp}$ | Pressure Value Resulting from the Cubic Spline | Pa |
| $y_{spr}$ | Approximate Spring Deflection | m |
| | | |
| $\alpha_2$ | Angular Acceleration of Crank Arm | $rad/s^2$ |
| $\alpha_3$ | Angular Acceleration of Connecting Rod #1 | $rad/s^2$ |
| $\alpha_6$ | Angular Acceleration of Connecting Rod #2 | $rad/s^2$ |
| $\alpha_8$ | Angular Acceleration of Connecting Rod #3 | $rad/s^2$ |
| $\alpha_i$ | Induced Angle of Attack | rad |
| $\alpha_r$ | Angular Deflection of the Rocker Arm | rad |
| $\beta$ | Local Blade Pitch | rad |
| $\gamma$ | Specific Heat | $N/m^3$ |
| $\Delta$ | Spring Pre-Load | m |
| $\Delta r_i$ | Width Between Blade Stations | m |
| $\Delta H_1$ | Perturbed Propeller Torque | Nm |

| | | |
|---|---|---|
| $\Delta H_m$ | Perturbed Engine Torque | Nm |
| $\Delta\omega$ | Perturbed Engine Operating Speed | rad/s |
| $\dot{\theta}_2$ | Angular Velocity of the Crankshaft | rad/s |
| $\ddot{\theta}_2$ | Angular Acceleration of the Crankshaft | rad/s$^2$ |
| $\theta_k$ | Angular Geometric parameters for an 8-bar engine mechanism ($k$ =1,...,11) | rad |
| $\theta_s$ | Oscillation Angle of Propeller when Treated as a Pendulum | rad |
| $\lambda$ | Non-Dimensional Ratio of Forward Flight Speed to the Local Speed of the Blade Station | - |
| $\mu$ | Air Viscosity | $\frac{Ns}{m^2}$ |
| $\rho$ | Air Density | Pa |
| $\sigma$ | Local Propeller Solidity | - |
| $\phi$ | Induced Angle of Attack Resulting from the Forward Speed of the Propeller | rad |
| $\omega$ | Rotational Speed of the Propeller | rad/s |
| $\omega_2$ | Angular Velocity of the Crank Arm | rad/s |
| $\omega_3$ | Angular Velocity of Connecting Rod #1 | rad/s |
| $\omega_6$ | Angular Velocity of Connecting Rod #2 | rad/s |
| $\omega_8$ | Angular Velocity of Connecting Rod #3 | rad/s |
| $\omega_n$ | Natural Frequency | rad/s |

# *Chapter 1 INTRODUCTION*

Internal combustion engines or reciprocating engines have been powering aircraft from the first flight of the Wright Flyer to modern day general aviation and commercial aircraft. What all of these aircraft throughout history have in common is that a propeller has been attached to reciprocating engines to provide power for flight.

What has also been known throughout the history of aviation is that the crankshafts of internal combustion engines rotate unevenly throughout a cycle, which causes significant torsional vibration in the system. This vibration is transmitted into the passenger cabin through the engine mounts and aircraft structure, as well as into the propeller, affecting its performance. Efforts have been made to determine the effect of mounting a propeller on the dynamics of an internal combustion engine. However, the methods used to date treat the propeller as an inertial mass, neglecting the aerodynamic loading variation caused by an uneven rotation of the crankshaft.

The non-uniform nature of the torque produced by a reciprocating engine is reflected in the cyclic variation of crankshaft angular speed. The motion of the crankshaft is determined by combinations of gas torque, inertia torque, and instantaneous aerodynamic torque.

## *Section 1.1 Background*

Aviation is a highly regulated activity intended to ensure the safety of all flying passengers and individuals on the ground. The Code of Federal Regulations (CFR) is an evolving set of rules, maturing with the current state of technology, to ensure that catastrophic events are prevented and never repeated.

When a company develops an engine, that engine must pass a series of tests to be certified safe for aircraft use. The same series of regulations also applies to propeller manufacturers, ensuring their propeller is suitable for aircraft use.

Often engine manufacturers attempt to certify their engine with a particular propeller, or a range of propellers, thereby simplifying the process of of matching a propeller to an engine and then certifying the system in accordance with 14CFR33.43, Vibration Test.

The Orenda Recip. Company attempted to certify a 94″ McCauley propeller with the Orenda OE600A 8-cylinder liquid cooled reciprocating engine in 2000. The Orenda findings [Orenda Recip. Inc., 2000] indicated that this particular propeller-engine combination did

conform to 14CFR33.43; however, it was noted that the 1.5 harmonic was the primary cause of crankshaft torsional displacement, with the harmonic damper installed under aerodynamically static conditions at take-off power. The 1.5 harmonic is a frequency that is 1.5 times the operating speed of the Orenda engine.

The McCauley propeller tested by the Orenda Recip. Company was a variable pitch propeller, which was why the maximum torsional displacements were observed under aerodynamically static conditions. What was of particular interest to the engineers at Orenda was the cause of the 1.5 harmonic dominating the crankshaft torsional displacement.

Several efforts dating back to 1932 [Root, 1932], [Den Hartog, 1956], and [Pulkrabek, 2004] have attempted to simulate the dynamical response of internal combustion engines operating on two and four-stroke cycles; however, each of these analytical efforts has either been valid only for one-cylinder engine or has not made adequate provisions for the dynamical behavior of the load, in this case an aerodynamically active propeller.

Lack of results in the area of system dynamical response was seen and a solution was required to explain why the 1.5 harmonic is predominant in the torsional vibration of the crankshaft.

## *Section 1.2 Scope*

The scope of the present research was to develop a methodology and a computer model which can be used with confidence in the aerospace industry to predict the engine dynamical behaviors and torsional vibrations in the crankshaft and the propeller shaft. A computer program – SIMPEL - was developed by the author in the Matlab language, which predicts the transient and steady state responses of a rigid-body multi-cylinder engine coupled with a rigid variable pitch propeller for a given power setting or throttle opening.

The propeller was modeled with the use of blade element theory to obtain the overall torque response, in functional form, for a given blade pitch setting. To model the system response, the Lagrange equation was employed to obtain the nonlinear governing differential equation for analysis of the motion of the engine crankshaft.

Two test cases were simulated; the first test case neglected the kinematics of the cam system, and the second case took the cam system into account. The results of these two simulations were then compared to determine the effect of the cam system on the dynamical response of the propeller-engine combination.

## *Section 1.3 Dynamics of a System of Rigid Bodies*

One of the two major components of the dynamical system was the 4-stroke internal combustion engine. A 7 hp four-stroke internal combustion engine (Saito-450) was purchased and used as the basis for the simulation. The analysis of the engine was performed in two phases; in the first phase the effects of the cam subsystem, which consists of tappet, push rod, rocker arm, valve and spring (called the accessory drive system), were neglected, and in the second phase the cam shaft subsystem was included.

During the first phase of the analysis, the valve timing was required to establish the duration of the various thermodynamic strokes for each of the three cylinders.

The first step in the engine simulation was to perform a kinematic analysis of the reciprocating mechanism. This mechanism has 8 links and one degree of freedom. The position and velocity of each link was first calculated over a period of $2\pi$ and the kinetic energy of each member was then found and normalized with respect to the angular position of the crankshaft.

The cylinder pressure of the Otto cycle was modeled as a function of the crankshaft angular position by assuming the compression and expansion were polytropic processes [Eriksson et al., 2002]. A detailed analysis of combustion processes is beyond the scope of this thesis so the cylinder pressure during the burning phase was approximated with a clamped cubic spline [Kuo, 1996]. The cylinder pressure for each of the three cylinders was generated using the same procedure; however, due to the unique internal mechanism kinematics, the pressure within each cylinder as a function of the crankshaft angular position was unique to that cylinder. The phase shift required for the correct engine firing sequence was obtained from the kinematical analysis.

## *Section 1.4 Propeller and Aerodynamics*

The propellers used on large aircraft have the ability to change the blade pitch while the propeller is in operation. These variable pitch propellers ensure that the propeller-engine system is operating at the most efficient design point possible for each phase of flight.

Orenda Recip. Company found that for the OE600A 8-cylinder liquid cooled engine coupled with a 93″ Hartzell, 94″ or 106″ McCauley propeller, the highest crankshaft stresses were experienced in take-off configuration. This finding is a result of the variable pitch propeller. If a propeller is fixed-pitch, the same conclusion may not be drawn.

To mimic the testing performed at Orenda on a smaller, more economical scale, a variable pitch propeller was procured that was a suitable match for the Saito-450 engine.

To model the propeller, the modified blade element theory was used taking into account the downwash induced by the blade sections. The propeller blade was first divided into 20 sections, which are each treated as 2-D airfoils. The blade element theory was then used to determine the lift and drag forces acting on each blade section. Once the forces acting on each blade section were calculated, the respective forces were summed over the entire blade to determine the total resulting thrust and torque.

Since the propeller is a rotating body, each blade section experienced an ever-increasing free stream velocity as the distance from the axis of rotation increases. The propeller was also geometrically twisted such that both the chord and cross sectional blade profile varied with the radial distance from the axis of rotation.

The propeller blade was aerodynamically twisted at each blade station as the distance from the axis of rotation increases. This means that the 2-D airfoils at different blade stations have different angles of attack for a given blade pitch setting.

To conduct the blade element analysis for the variable pitch propeller employed, the airfoil cross section at each station was approximated using a NACA 4-digit airfoil; the geometric and aerodynamic twist was then derived as a function of the blade pitch setting. All of these quantities were passed in batch mode to the MIT developed X-Foil airfoil code, made accessible via the Internet.

The results obtained from the propeller blade element analysis provide the torque of the propeller as a second order polynomial, which is desirable for inclusion into the equation of motion.

## *Section 1.5 Engine and Dynamics of a System of Rigid Bodies*

This 4.25 cubic inch radial engine weighs 6.5 pounds, including the short manifold exhaust pipes. It turns a 22x10 propeller at 8000 RPM on 15% 2-stroke fuel producing over 40 lbs of static thrust. It delivers this power with very little vibration-about 1/10th the vibration levels of comparable single cylinder 2-stroke engines. The crank drives one crank pin with a master rod, while two slave rods are pinned to the master rod, giving a 1-3-2 firing order. A single rear-mounted two-needle carburetor feeds intake manifolds. Exhaust tubes are included to direct exhaust gasses away from the aircraft.

The propeller-engine system has one degree of freedom, and the Lagrange equation was used to establish the single nonlinear differential equation. This is a second-order differential equation, which can be converted to two first-order differential equations and then solved using a fixed-step Euler method. Of interest to the author was the system response for any given throttle setting.

This thesis will outline the modeling of the variable pitch propeller, the simulation of the Saito-450 internal combustion engine, and present the results obtained from two simulation test cases.

# *Chapter 2 ENGINE*

A multi-cylinder internal combustion was purchased to conduct the simulation and research required to determine the transient and steady state response of the system when coupled with an aerodynamic load. In this section, the thermodynamic and internal pressure characteristics were modeled.

## *Section 2.1 Engine Specifications*

The information shown in Figure 2.1 is taken from the web site of the North American distributor of Saito engines, Horizon Hobby.

450 3-Cylinder Radial Dual Plug: HH
by SAITO ENGINES
Product Number: SAIE450R3D
**Specifications:**

**Type:** 4-stroke
**Displacement:** 4.25 cu in
**Bore:** 1.33 in
**Stroke:** 1.08 in
**Cylinders:** AAC
**Total Weight:** 99 oz
**Crankshaft Threads:** M10 x 1.25
**Prop Range:** 21x10 - 24x10
**RPM Range:** 1,200 - 8,000

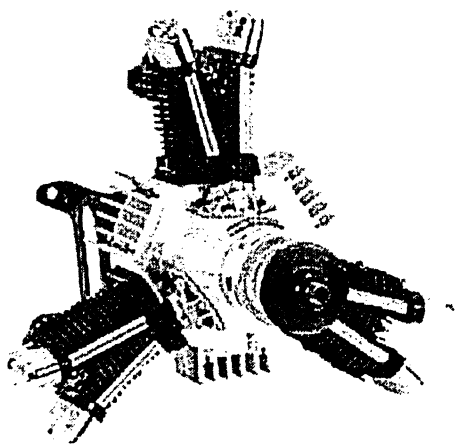

**Figure 2.1: Saito-450 manufacturer specifications.**

Based on the information available in Figure 2.1, it was determined that this would be a suitable engine with which to conduct the required research. The criterion of multi-cylinder engine was met, and the engine was capable of mating with a propeller of such size as to produce significant torque and thrust.

## *Section 2.2 Pressure-Volume Curve*

Consider a radial engine as one in which several cylinders are fixed in the frame and arranged in a vertical circle about the shaft axis at equal angular intervals. In radial engines there is usually one master connecting rod on each crankshaft, the other connecting rods being articulated to it [Root, 1932].

## *Section 2.2.1 Otto Cycle*

The Otto cycle is an ideal air-cooled cycle consisting of four distinct processes taking place over two complete crankshaft rotations. In an ideal engine, the intake stroke begins when the piston is at the Top Dead Centre (TDC) and lasts from the TDC to the Bottom Dead Center (BDC). The isentropic compression stroke occurs immediately after the intake stroke and lasts from the BDC to the TDC. At the end of the compression stroke, heat is added to the system from an external ignition source (constant volume process) and occurs while the piston is at the TDC. The next process is an isentropic expansion, taking place from the TDC to the BDC. This process is followed by the exhaust stroke where heat is rejected from the cylinder and lasts from the BDC to the TDC. The area enclosed under the pressure-volume (P-V) curve can be interpreted as the work done by the cylinder in one cycle (720 degrees of crankshaft rotation).

The Otto cycle is characterized by the P-V curve shown in Figure 2.2.

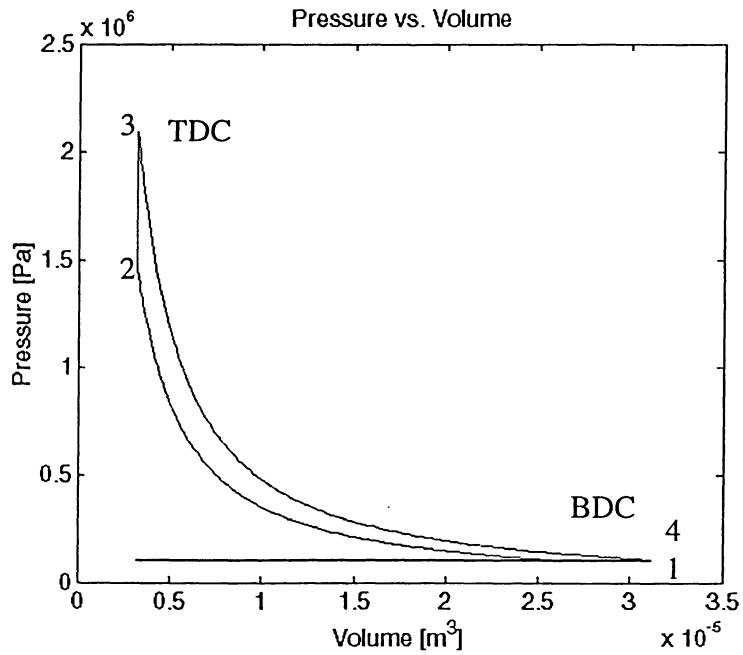


**Figure 2.2: The Otto cycle P-V curve.**

When developing the engine portion of the SIMPEL computer model, there are many parameters that must be measured. These parameters are the piston diameter, cylinder bore, lengths of the connecting rods and the crank throw. The measurements were taken with a pair of digital calipers, and the swept volume of the cylinder was calculated based on the kinematical analysis of the linkage.

## *Section 2.2.2 Clearance Volume*

The clearance volume was measured experimentally and used in the calculation of the work done by the gas pressure, and the compression ratio. The entire assembly was weighed when it was dry to obtain a baseline weight of the assembly. Water was then introduced into the cylinder through one valve as the crankshaft was positioned at the BDC. The entire assembly was weighed again on a triple beam balance and this weight was recorded. The crankshaft was then rotated such that the piston was at the TDC, the extra water being allowed to evacuate the cylinder through one of the valves. Once all of the excess water had been expunged from the cylinder the entire assembly was again weighed and this weight was recorded.

Since the density of water at room temperature is known and the mass of water contained within the cylinder was measured, the clearance volume of the cylinder was calculated. There is a slight discrepancy in the stroke lengths between cylinder #1 and cylinders #2 & #3, which would affect the clearance volume; however, this variation is small and was neglected. The clearance volume was found to be $3.0 \times 10^{-6}$ $m^3$, the cylinder volume at BDC was found to be $2.7 \times 10^{-5}$ $m^3$ and the swept volume was found to be $2.4 \times 10^{-5}$ $m^3$.

## *Section 2.2.3 Compression Ratio*

The compression ratio was calculated based on experimental data to be 9 by Eq. (2.1).

$$r_c = \frac{V_c + V_s}{V_c} = 9 \tag{2.1}$$

where $r_c$ is the compression ratio, $V_c$ is the clearance volume and $V_s$ is the swept volume.

A compression ratio of 9 compares well with accepted compression ratios for standard air-cooled Otto cycle engines in production today [Moran & Shapiro, 1996].

## *Section 2.2.4 Pressure vs. Crank Angle*

Construction of the pressure vs. crankshaft position (P-θ) curve was approached in a modular fashion by considering in sequence cylinders #1, #2, and #3, and finally superimposing all curves with the appropriate phase shift to account for the firing sequence.

To determine the angular intervals of crankshaft rotation over which all of the processes involved with the 4-stroke cycle action, the cam assembly of the Saito-450 engine was inspected.

The cam profiles were modeled, and by using the cam timing combined with the cylinder position information, the pressure vs. crankshaft angular position was modeled.

The tappet axis, passing through the cam shaft axis of rotation for each intake and exhaust tappet, was measured to be +15° and -15° away from the global vertical, respectively. The peak of the intake cam was found to be 40.5° (clockwise) away from the same vertical reference and the peak of the exhaust cam was found to be 36° (counter clockwise) away from the vertical centre line. Figure 2.3 shows the front view of the cam assembly from the Saito-450 engine. The two cams are fixed to the cam gear creating one piece; and the three cam assemblies are identical.

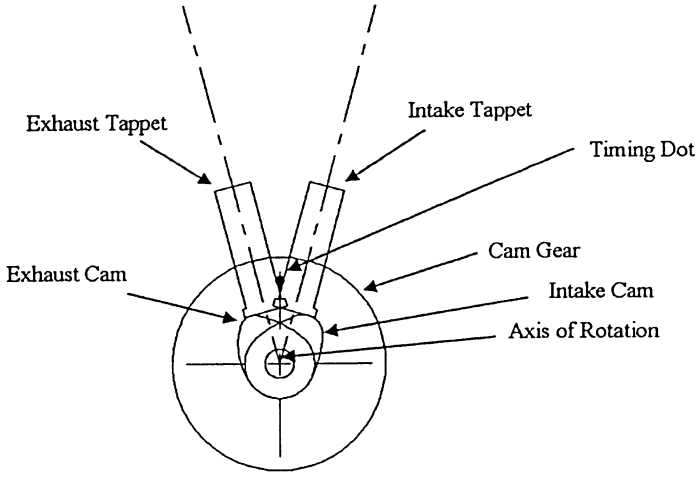


**Figure 2.3: Front view of the Saito-450 cam assembly.**

Each cam assembly was mounted to the crank case such that the timing dot of each cam assembly was placed radially inward toward the crankshaft axis of rotation. The crankshaft was oriented such that the respective piston was at the TDC opposite to the combustion stroke. With each cam assembly assembled using the timing dot as a reference; the 4-stroke cycle intervals were determined over a period of $4\pi$ and found in Table 2.1.

**Table 2.1: Crankshaft degree intervals for each of the 4 stroke processes.**

| | Intake | Compression | Burning | Expansion | Exhaust |
|---|---|---|---|---|---|
| **Piston #1** | 1° – 194° | 195° – 350° | 351° – 399° | 400° – 499° | 500° – 720° |
| **Piston #2** | 485° – 678° | 679° – 114° | 115° – 163° | 164° – 263° | 264° – 484° |
| **Piston #3** | 233° – 426° | 427° – 582° | 583° – 631° | 632° – 11° | 12° – 232° |
| **Interval** | 193° | 155° | 48° | 99° | 220° |

One approximation was made while determining the length of the expansion and exhaust strokes. This approximation was that during the exhaust and intake strokes significant valve

overlap occurred and since analytical methods were unable to thermodynamically take this valve overlap into account, the processes were truncated thereby eliminating the overlap.

Since the exhaust stroke was truncated to accommodate the intake stroke, the length of the expansion stroke also had to be altered for all engine cycles to fit within a $4\pi$ interval. An expansion length of 99° was chosen, and an exhaust stroke of 220° allowed for exhaust valve opening and adequate gas volume elimination [Pulkrabek, 2004].

The intake valve closing determines how much air-fuel mixture is contained within the cylinder and available for the rest of the 4-stroke cycle. The intake stroke was assumed to occur at standard atmospheric conditions, 101.325 kPa and 15 °C, neglecting heat transfer effects and was determined to take place over 193° instead of the theoretical 180° due to the realities of the practical engine. As the piston moved from the TDC to the BDC, a partial vacuum is created within the cylinder dropping the pressure below atmospheric. It is this pressure differential that draws the air-fuel mixture into the cylinder through the intake valve. As the air flows past the intake valve opening there is a constriction and the air speed increases past this constriction.

This additional reduction in pressure aids in drawing more air-fuel mixture into the cylinder. A pressure differential still exists within the cylinder as the piston reaches the BDC; therefore, air will continue to enter the cylinder as the piston begins to move back towards the TDC. At some point after the BDC, the pressure within the cylinder will equalize with ambient and it is at this point of pressure equilibrium when the intake valve would ideally close.

If the intake valve were to close too early, air is prevented from entering the cylinder that would otherwise be drawn in resulting in a reduction in volumetric efficiency. If the intake valve were to close after the point of pressure equilibrium, air is being forced back out through the intake valve that could have been used for combustion again resulting in a reduction in volumetric efficiency.

Once the intake valve closes the polytropic compression process begins based on ideal gas theory. The exponent for the polytropic compression process ($k_c$) was taken to be 1.25 [Eriksson et al., 2002]. For the compression process, the pressure was calculated by using Eq. (2.2).

$$P_c(\theta_2) = P_{ivc}\left(\frac{V_{ivc}}{V(\theta_2)}\right)^{k_c} \tag{2.2}$$

where $V_{ivc}$ is the volume of the cylinder at the point when the intake valve closes, $P_{ivc}$ is the pressure in the cylinder when the intake valve closes, and $P_c(\theta_2)$ is the cylinder pressure during the compression phase as a function of the crank shaft angular position, $\theta_2$. The volume as a function of crank angle $V(\theta)$ was calculated using Eq. (2.3) and through appropriate substitutions generated Eq. (2.4) based on the positions of the pistons as determined through the kinematic analysis.

$$V(\theta_2) = A_c \cdot D_{ist} + V_c \tag{2.3}$$

$$V(\theta_2) = A_c[r_{max} - r_{ca}(\theta_2)] + V_c \tag{2.4}$$

where $A_c$ is the piston area, $D_{ist}$ is the distance through which the piston moved, $V_c$ is the clearance volume, $r_{max}$ is the distance from the crank shaft center of rotation to the piston pin while the piston is at the TDC, and $r_{ca}$ is the distance from the crank shaft center of rotation to the piston pin at any crank shaft angular position, $\theta_2$.

The Saito-450 engine is not a typical 4-stroke engine in that it does not use a spark plug and alternator system to initiate combustion within the cylinders. This engine uses two glow plugs per cylinder to initiate combustion of the air-fuel mixture with a compression ratio found to be 9, indicating an Otto cycle [Moran & Shapiro, 1996].

Ignition of the air fuel mixture is initiated by the two glow plugs located at the top of the cylinder and was assumed to begin 9° before TDC and ending 39° after TDC. This provides a total burn angle of 48° for all cylinders [Eriksson, 2002 & Kuo, 1996]. The combustion process is not completely understood but a general model assumes a spherical flame front initiated at, in this case, each glow plug and the flame front propagates outward into the combustion chamber. Initially, the flame front moves relatively slowly due to its small size and does not generate enough energy to quickly heat the surrounding gasses. As a result, the cylinder pressure does not raise the cylinder temperature very quickly resulting in very little compression heating. Only after the first 5% to 10% of the air-fuel mass is burned does the flame velocity reach higher values with the corresponding fast rise in pressure [Pulkrabek, 2004].

For a given engine, combustion occurs faster at higher engine speed. The real time for the combustion process is therefore less, but the real time for the engine cycle is also less, and the burn angle is only slightly changed [Pulkrabek, 2004].

To simulate the pressure distribution throughout the combustion process, a cubic spline was used to join the end of the compression process with the beginning of the expansion process. The clamped cubic spline was selected for the combustion modeling because there is a requirement for position continuity and slope control at the end of the compression stroke and both slope and positional continuity at the beginning of the expansion processes.

The general form of the cubic spline equation may be written as

$$p_c = \begin{bmatrix} 1 & \theta_2 & \theta_2^2 & \theta_2^3 \end{bmatrix} \begin{bmatrix} A_0 \\ A_1 \\ A_2 \\ A_3 \end{bmatrix} \tag{2.5}$$

where $p_c$ is the pressure during the compression stroke; $A_k$ , $k = 0,1,2,3$, are unknown coefficients, which can be determined by enforcing the boundary conditions at the end of compression and the beginning of expansion. The boundary conditions include values of pressure and its rate of change with respect to the crank angle. The cubic spline coefficients will change with the throttle setting since the throttle setting controls the peak cylinder pressure thereby controlling the engine power output.

Once the spline coefficients have been determined, the cubic spline equation can be generated from the following equation

$$y_{sp}(\theta) = A_0 + A_1\theta_2 + A_2\theta_2^2 + A_3\theta_2^3 \tag{2.6}$$

To change the peak pressure while using the cubic spine approach, a discontinuity in the slope at the end of the compression stroke was introduced through a slope magnification factor. The purpose of this variable is to change the peak pressure and work produced by the compressed gas to achieve various power outputs. See Section 2.2.7 for a more thorough discussion regarding the slope magnification factor.

The expansion pressure as a function of crankshaft angular position was modeled through Eq. (2.7). The variable $P_3$ is the maximum pressure in the cylinder, $V_c$ is assumed to be at the TDC since the position for 50% mass fraction burned is assumed to be at the optimal value [Eriksson et al., 2002].

$$P_e(\theta_2) = P_3\left(\frac{V_c}{V(\theta_2)}\right)^{k_e} \tag{2.7}$$

where $V(\theta_2)$ is the cylinder volume as a function of crankshaft angular position during the expansion interval and $k_e$ is the polytropic exponent for the expansion phase and was taken to be 1.3 [Eriksson et al., 2002].

The polytropic exponent for the expansion process ($k_e$) is not equal to 1.4, which is the ratio of specific heats for air at standard atmospheric conditions for two main reasons. First, air-fuel mixture is not purely air and second, the post-combustion cylinder gas is very hot. The ratio of specific heats of any real gas decreases with increasing temperature and a polytropic index of 1.3 indicates heat loss from the cylinder during expansion [Blair, 1999].

The exhaust stroke begins at 40° before the BDC for cylinder #1 and 23° before the BDC for cylinder #2 and 63° before BDC for cylinder #3. Typically the exhaust stroke is initiated between 20° and 60° before BDC so that the pressure in the cylinder has been fully reduced by the BDC when the exhaust stroke begins.

During blowdown, the exhaust gasses initially escape at sonic velocity under choked flow conditions, which results in a finite time required for the cylinder pressure to decrease to nearly atmospheric conditions [Pulkrabek, 2004].

One disadvantage of having the exhaust valve open before the piston reaches the BDC is that some useful work is lost during the last portion of the expansion stroke. Similar to the case of the intake valve, the timing of the exhaust valve is critical to maximizing the volumetric efficiency. If the exhaust valve opens too early, more than the necessary amount of work is lost during the end of the expansion stroke. If the valve opens late, there is an excess amount of gas pressure in the cylinder and this resists the piston movement from the BDC towards the TDC and increases the negative pumping work of the engine cycle. The ideal time to open the exhaust valve is dependant on engine speed and is optimized for only one operating condition resulting in a loss of volumetric efficiency when operated at off-design conditions [Pulkrabek, 2004].

The burned air-fuel mixture is ejected from the cylinder during the 220° exhaust stroke interval. The pressure during this interval is assumed to decrease linearly from the end of the expansion process to the beginning of the intake process. The temperature and pressure at the end of the expansion stroke vary with the engine operating condition but the temperature and pressure at the beginning of the exhaust stroke are the same as the conditions at the end of the expansion stroke. Generally the exhaust gas temperature and pressure at not the same as the intake air-fuel mixture conditions, so with no valve overlap there will be a discontinuity in the P-

$\theta_2$ curve. In reality there is valve overlap resulting in mixing the intake with exhaust air thereby eliminating any discontinuities in the P-$\theta_2$ curve.

It is very difficult to directly measure the mass flow and the air-fuel ratio so it is assumed that an ideal air-fuel ratio is maintained at all times, that there is optimal mixing between the air and the fuel being introduced into the cylinders, and that the 50% mass fraction burned is at the optimal value at all times.

## *Section 2.2.5 Firing Sequence*

The Saito-450 radial engine has three cylinders and the firing sequence is cylinders 2-1-3 as provided by the manufacturer. If a 0° reference is selected at the beginning of the intake stroke of cylinder #1, then cylinder #2 will fire first at a crank angle of 127°, cylinder #1 will fire at a crank angle of 360° and cylinder #3 will fire at 595°. Figure 2.4 is an illustration taken from the Saito-450 Instruction Manual showing the direction of propeller rotation in addition to the firing sequence.

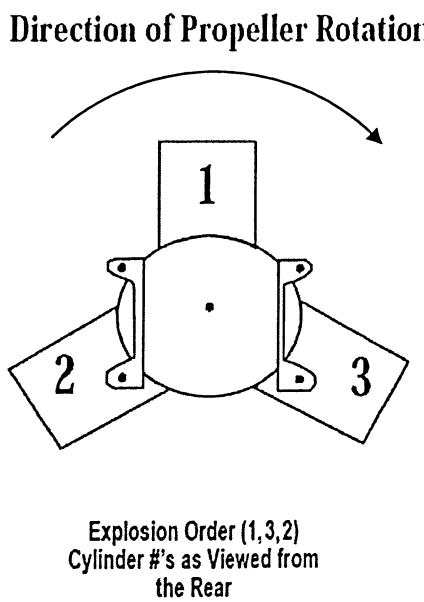


**Figure 2.4: Firing sequence and direction of propeller rotation**

The degree offset between cylinders #2 & #1 is 233° and the degree offset of cylinders #3 & #1 are 235°. The reason the degree offsets are not equidistant at 240° is that the internal mechanism of this engine is an 8-bar link that can be broken down into three sub-mechanisms; one conventional 4-bar crank slider with zero offset and two 5-bar links connecting to the master

connecting rod, both with zero offset. It is the presence of the 5th link connecting pistons #2 & #3 to the connecting rod of piston #1 that accounts for the shifting of the cylinder timing. See Section 3.14 for more details.

The combined pressure versus crank angle diagram taking into account the valve timings can be seen in Figure 2.5. This diagram illustrates the subtle effect of the fifth link on the pressure versus crankshaft angle profile as well as the change in peak pressures. These differences are very small but are taken into account in order to model the test engine more accurately.

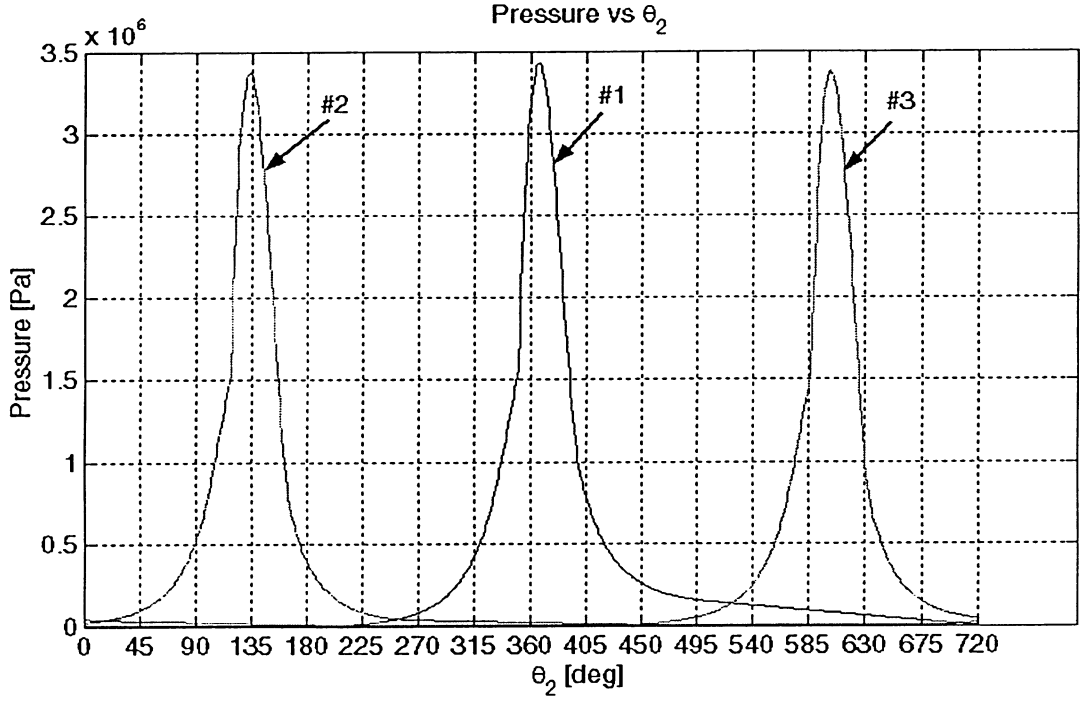


**Figure 2.5: Pressure vs. $\theta_2$ curve for all three cylinders.**

The cylinder pressure has been calculated as a function of crankshaft angular displacement in discrete form. To verify that the peak pressure increases with increasing throttle setting, an experiment was devised that measured the exhaust gas temperature at various operating speeds; the results of which can be seen in Section 2.2.6.

## *Section 2.2.6 Saito-450 EGT Experiment*

Internal combustion engines operate on the principle of harnessing the chemical power of fuel to produce useful work. A method of harnessing work is to introduce a quantity of fuel

mixed with an oxygen-containing gas into a closed cylinder then igniting this gaseous mixture. The resulting pressure increase acts on a piston, which is connected to a rotating shaft and produces the desired speed/torque/power. After the gas has burned in the cylinder it is exhausted through an orifice into a pipe that directs the gas away from the engine to a convenient point in space.

The purpose of the exhaust gas experiment was to measure the temperature of the exhaust gasses produced by the Saito-450 engine at various operating conditions so that the combustion pressure can be found providing a complete temperature and pressure picture of the Otto cycle.

A k-type thermocouple was constructed and fixed to the exterior of the muffler as close to the cylinder #1 as possible without touching any other structure. The engine was then run at a constant measured RPM long enough for the thermocouple temperature reading to stabilize and this value was then recorded in Table 2.2 with the ambient temperature measured at the time of the test being 23 °C.

**Table 2.2: RPM vs EGT results.**

| RPM | $T_4$ [°C] or EGT [°C] |
|---|---|
| 3000 | 63 |
| 3500 | 70 |
| 4000 | 100 |

Since each process takes a finite amount of time to complete, the mass flow and temperature fluctuation within the exhaust pipe are continuously changing as a function of time or crankshaft angular position. If a thermocouple is used to measure the exhaust temperature by placing it in direct contact with the outer muffler surface, it is not reading the exhaust gas temperature (corrected for heat transfer effects to obtain the actual gas temperature) because thermocouples typically have time constants that are much longer than the time taken to complete one engine cycle. The time taken to exhaust the hot combusted cylinder gasses is in the order of milliseconds and this is not enough time for the muffler to reach thermodynamic equilibrium with the surroundings.

If the thermocouple is used with a time constant much longer than the time taken for the engine to complete one cycle, then the thermocouple reading will give a pseudo-steady-state temperature of the flow. In this case, the thermocouple temperature will actually be an approximate enthalpy average temperature, shown in Eq. (2.8), and not necessarily a true time average [Pulkrabek, 2004].

$$T_{thermocouple} = \frac{\int \dot{m} c_p T_e dt}{\int \dot{m} c_p dt} \tag{2.8}$$

where, $\dot{m}$ is the mass flow rate of exhaust, $t$ is time, $c_p$ is the specific heat of the working fluid, and $T_e$ is temperature.

The data in Table 2.2 shows that with higher operating speeds (RPM), a higher exhaust gas temperature is produced. This would indicate an elevation of internal combustion pressure indicating more work is being produced by the engine and absorbed by the propeller.

Further testing was not completed due to a faulty engine exhaust system.

## *Section 2.2.7 Throttling*

Throttling is a means to control the speed of an engine through regulation of the air ingested into the engine. The Saito-450 is equipped with a carburetor to control the mass flow of air and fuel drawn into the each cylinder during the intake strokes. By rotating the carburetor barrel the mass flow of air is directly controlled and by controlling the air flow, the fuel drawn into the engine is controlled as well.

As the piston travels downward in the cylinder with the intake valve opened, there is a direct path for air to be drawn into the cylinder caused by a pressure gradient formed through the motion of the piston. The physical shape of the carburetor being similar to that of a converging nozzle and as the air is being drawn sub sonically through the carburetor, the velocity of the air increases with decreasing cross sectional carburetor (nozzle) area.

The fuel system of the Saito-450 is a suction-feed design where a suction pressure draws the fuel from the fuel tank into the carburetor where the mixing of the air and fuel takes place. The fuel tank is mounted such that the fuel output is at the same vertical elevation as the carburetor so no hydraulic pressure head develops.

Fuel is drawn out of the bottom of the tank so the pressure at the fuel pick-up point is a function of fuel depth, the chamber pressure inside the tank and the specific gravity of the fuel itself. Since the specific gravity of the fuel does not change as a function of time, the pressure at the clunker is a function of the fuel depth and the fuel tank chamber pressure.

The fuel tank is pressurized by the exhaust gas for the purpose of preventing the air-fuel mixture from becoming lean and engine power output becoming erratic as the fuel tank nears the empty.

The fuel flow to the engine remains constant throughout the time required to consume the contents of the fuel tank. The amount of fuel entering the cylinder is controlled by the air speed entering the carburetor due to the pressure gradient caused by the downward motion of the piston. Since the carburetor is shaped as a converging nozzle and the incoming air is subsonic, as the air enters the converging nozzle it speeds up according to the Bernoulli Principle. The fuel is introduced into the air flow through a combination of the positive pressure within the fuel tank and the negative pressure caused by the accelerating air flow. Since the fuel is fed into the engine through suction, the air-fuel ratio remains essentially constant for any throttle setting.

All throttle settings are of interest; therefore, a method must be developed to theoretically change the steady state engine operating speed in a predictable manner.

In Section 2.2.4, the slope magnification factor was introduced into the cylinder pressure calculation to control the amount of cylinder pressure and ultimately the power output of the engine. What is to be determined is how to change the slope magnification factor to achieve a desired power output or operating speed.

The method employed involved changing the slope magnification factor in increments of 5 from 5 until the maximum operating speed of the engine is reached and Table 2.3 shows the results of the operating speed survey for each of the three considered blade pitch values.

**Table 2.3: Slope magnification factor, resulting steady state operating speed and the corresponding throttle setting [%].**

| Slope Magnification Factor | Steady State Operating Speed for 4″ Pitch [RPM] | Steady State Operating Speed for 6″ Pitch [RPM] | Steady State Operating Speed for 8″ Pitch [RPM] | Throttle Setting [%] |
|---|---|---|---|---|
| 5 | 3491 | 3013 | 2645 | 33 |
| 10 | 4290 | 3759 | 3179 | 40 |
| 15 | 4964 | 4375 | 3650 | 46 |
| 20 | 5557 | 4911 | 4103 | 51 |
| 25 | 6093 | 5393 | 4531 | 57 |
| 30 | 6586 | 5833 | 4938 | 62 |
| 35 | 7045 | 6242 | 5326 | 67 |
| 40 | 7476 | 6625 | 5698 | 71 |
| 45 | 7884 | 6986 | 6056 | 76 |
| 50 | 8271 | 7330 | 6401 | 80 |
| 55 | 8642 | 7657 | 6735 | 84 |
| 60 | 8997 | 7971 | 7058 | 89 |
| 65 | 9339 | 8272 | 7372 | 92 |
| 70 | 9669 | 8563 | 7677 | 96 |
| 75 | 9988 | 8844 | 7974 | 100 |

Before proceeding with the throttling method, truncation of the data in Table 2.3 is required to take into account the actual maximum operating speed of the engine as found in the engine operating manual. The maximum rated operating speed is 8000 RPM; therefore, a reference point of 100% throttle is set at a slope magnification factor of 75. Examining the operating speed columns corresponding to blade pitch values of 4″ and 6″ it can be seen that the operating speeds exceed the maximum value of 8000 RPM for slope magnification factors of 50 and 65, respectively.

The fifth column of Table 2.3 was calculated by comparing the steady state RPM with a blade pitch of 8″ and dividing the local speed value by the maximum value to determine what percentage of the maximum operating speed corresponds to which slope magnification factor. It was found that the throttle setting percentage was nearly the same for all three blade pitch values so one approximation is required for any load condition.

Figure 2.7 shows the valid slope magnification factors for a blade pitch value of 4″ and corresponding engine throttle settings fit with a second order polynomial generating minimal error.

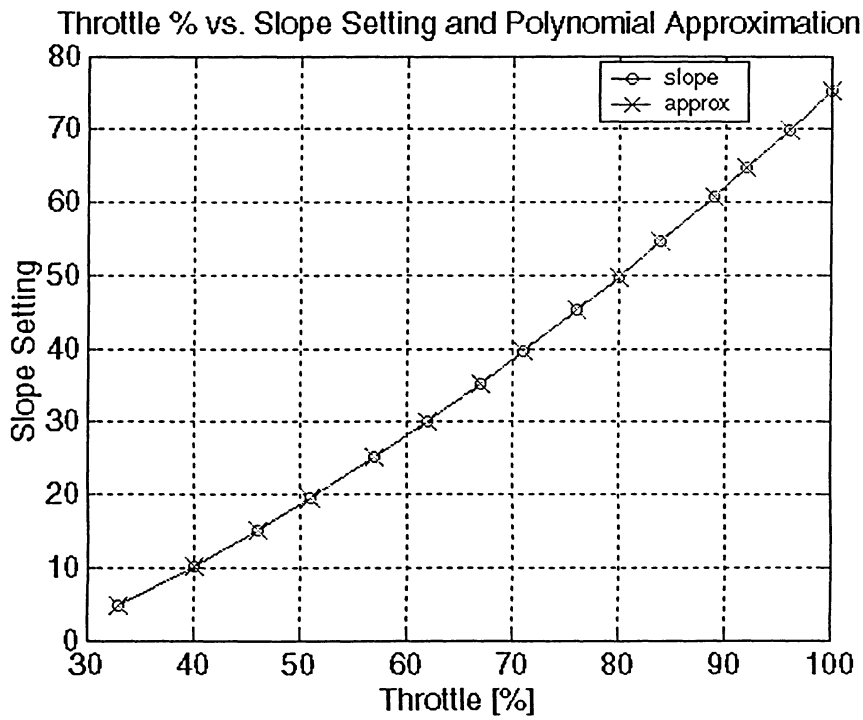


**Figure 2.6: Slope magnification vs. throttle setting.**

Figure 2.7 shows the second order polynomial correlation between throttle setting and steady-state engine operating speed.

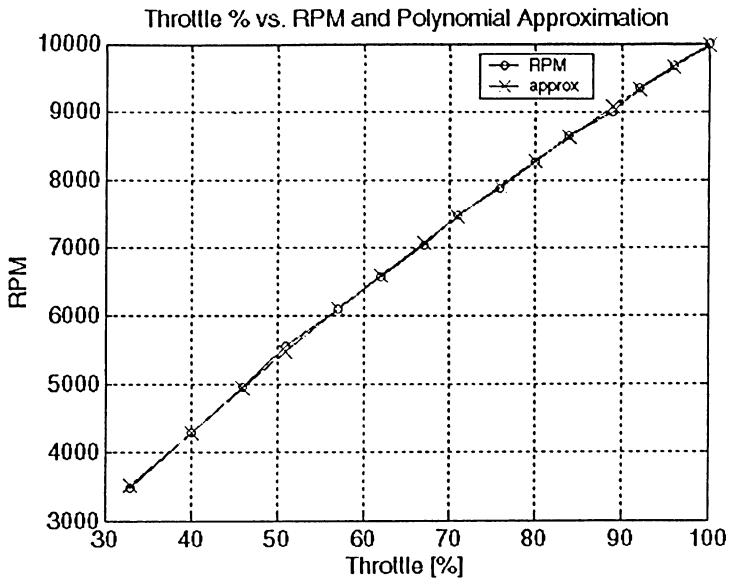


**Figure 2.7: Throttle setting vs. engine operating speed in RPM at 4″ pitch.**

For the case of the propeller set to a 4″ blade pitch, the first 11 rows of Table 2.3 contain valid operating speed data and a second order polynomial can be fit to these 11 data pairs with a minimal error. Figure 2.8 shows the original RPM data for a 6″ blade pitch setting plotted against the throttle setting with the second order approximation.

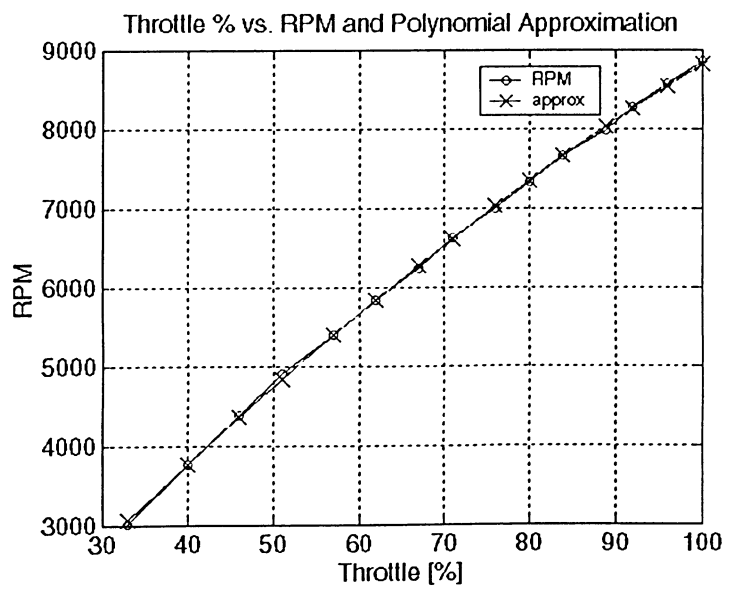


**Figure 2.8: Throttle setting vs. engine operating speed in RPM at 6″ pitch.**

For the case of the propeller set to 8″ pitch, all 14 rows of Table 2.3 contain valid operating speed data and a second order polynomial can be fit to these 14 data pairs with minimal error. Figure 2.9 shows the original RPM data plotted against the throttle setting with the second order approximation.

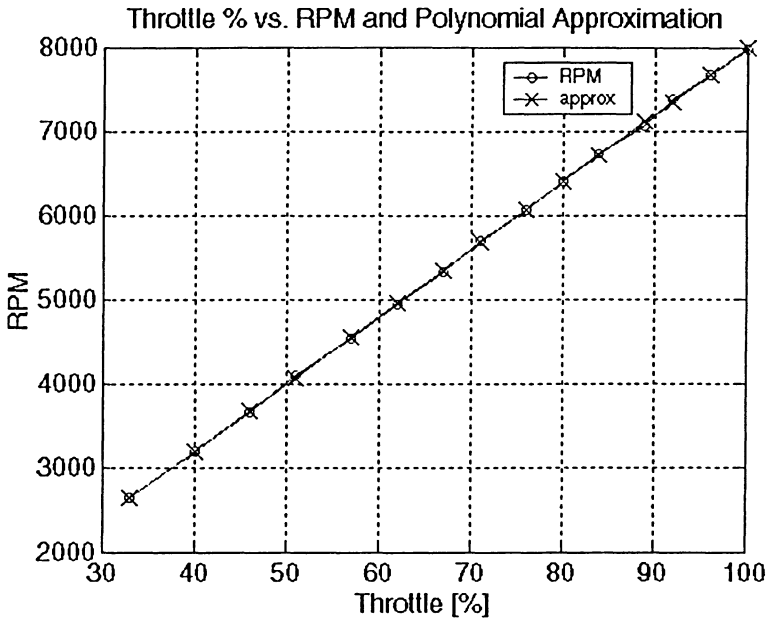


**Figure 2.9: Throttle setting vs. engine operating speed in RPM at 8″ pitch.**

The propeller-engine simulation can now be controlled by setting a throttle percentage, which is a realistic method of controlling the system. High accuracy was achieved when using the slope magnification factor to control the cylinder pressure, which ultimately dictates the power output of the engine.

# *Chapter 3 PROPELLER*

The focus of the research is the simulation of an engine with a propeller attached as the load. Since the original problem posed by Orenda involved a variable pitch propeller, a variable pitch propeller was purchased that is matched to the Saito-450.

## *Section 3.1 Moment of Inertia Calculation for the SOLO Propeller*

To conduct dynamic analysis of the Saito-450 engine, all moving components must be catalogued to determine their mass, volume, density, mass center and moment of inertia. The moment of inertia is required for the SOLO propeller to determine the rotational inertia of the body, which is one component the propeller contributes to the overall dynamical behavior of the system.

The propeller was the only item requiring the use of the experimental physical pendulum method to determine the moment of inertia. It was suspended from a location within the perimeter of the body and made to oscillate with small amplitude such that the small angle approximation ($\sin(\theta_s) \approx \theta_s$) was valid. The second order differential equation describing this physical pendulum system is described by Eq. (3.1).

$$I\frac{\partial^2\theta_s}{dt^2} = -m_p g d_p \sin(\theta_s) \tag{3.1}$$

where $-m_p g d_p \sin(\theta_s)$ is the magnitude of the driving torque causing the pendulum to oscillate.

Making use of the small angle approximation, the second order differential Eq. (3.1) becomes Eq. (3.2).

$$\frac{d^2\theta_s}{dt^2} + \left(\frac{m_p g d_p}{I}\right)\theta_s = 0 \tag{3.2}$$

Eq. (3.2) can also be written as Eq. (3.3).

$$\frac{d^2\theta_s}{dt^2} + \omega_n^2\theta_s = 0 \tag{3.3}$$

Comparing Eqn's (3.2) and (3.3), the natural frequency $\omega_n$ is given by Eq. (3.4).

$$\omega_n = \sqrt{\frac{m_p g d}{I}} \tag{3.4}$$

And the period of oscillation is related to the frequency through Eq (3.5).

$$T_p = \frac{2\pi}{\omega_n} \tag{3.5}$$

Substituting Eq. (3.4) into Eq. (3.5) gives Eq. (3.6).

$$T_p = 2\pi\sqrt{\frac{I}{m_p g d_p}} \tag{3.6}$$

Therefore, by measuring the period of oscillation and averaging this time over several trials and solving for $I$ from Eq. (3.6), the polar moment of inertia was determined through Eq. (3.7) [Serway, 1996].

$$I = m_p g d_p \left(\frac{T_p}{2\pi}\right)^2 \tag{3.7}$$

The parallel axis theorem shown in Eq. (3.8) can be used to determine the moment of inertia about the mass centre.

$$I_{CM} = I - m_p d_p^2 \tag{3.8}$$

Substituting Eq. (3.7) into Eq. (3.8) results in Eq. (3.9).

$$I_{CM} = m_p g d_p \left(\frac{T_p}{2\pi}\right)^2 - m_p d_p^2 \tag{3.9}$$

Simplifying Eq. (3.9) produces the final equation for the moment of inertia about the mass centre as a function of the period of oscillation, Eq. (3.10).

$$I_{CM} = m_p d_p \left[ g\left(\frac{T_p}{2\pi}\right)^2 - d_p \right] \tag{3.10}$$

where $m_p$ is the mass of the propeller, $g$ is the gravitational constant, $d_p$ is the distance between fulcrum and the body center of gravity, and $T_p$ is the measured period.

To increase the accuracy of this method, a data acquisition system running the software Visual Designer was used in conjunction with an accelerometer that was fixed to the propeller at the mass centre. The acceleration was sampled and recorded by the data acquisition system. The Visual Designer software integrated the acceleration readings twice to produce a position history

of the physical pendulum as well as performing a Fast Fourier Transform (FFT) to produce the constituent frequencies of the pendulum oscillation. The fundamental frequency produced by the FFT corresponds to the natural frequency of the pendulum since the accelerometer was placed at the centre of gravity, which is also the axis of rotation of the propeller.

It is this fundamental frequency that is used in Eq. (3.4) to calculate the corresponding period of oscillation, which is used in Eq. (3.10) to generate the moment of inertia of the propeller about the propeller axis of rotation.

The moment of inertia of the propeller as calculated through the use of the data acquisition system is $I = 3.39 \times 10^{-3}$ kgm$^2$.

## *Section 3.2 Propeller*

A propeller is a device that imparts a small velocity increment to a large mass of fluid and is a means of converting the rotational motion of the engine output shaft into useful thrust, which in turn propels the aircraft through the air. A by-product of the production of thrust is the simultaneous production of drag, or torque resisting the rotation of the propeller blade.

The analysis of a propeller can be performed in a manner similar to that employed in wing theory. An assumption is that the local flow over any blade section at a distance $r$ from the axis of rotation, shown in Figure 3.1, is two-dimensional, or alternatively, the local flow lies entirely in the plane normal to the local radius of the blade section. Thus, for a given local inflow velocity vector, the aerodynamic reaction at each propeller element is solely determined by the local section geometry acting independently of any other section. The blade element theory assumes isolated airfoil behavior.

This two-dimensional or isolated airfoil assumption is found to be substantially correct for two and three bladed propellers, except near the hub [Ribner and Foster, 1990], where the aerodynamic loads fall to zero.

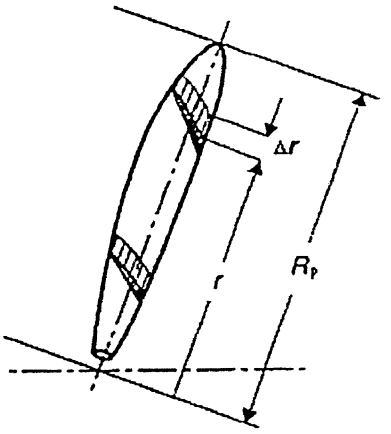


**Figure 3.1: Illustration of a blade element at radius *r* from the axis of rotation.**

Several steps are required should an investigator wish to perform a detailed analysis of a propeller that has been manufactured with no manufacturing data available to assist in the analysis. The detail design of a propeller blade will entail selections, originally made by the designer, of local blade section shape, chord length, and twist at each radial station. Therefore an overall cataloging of propeller design features must be performed.

The investigator will need the two-dimensional aerodynamic characteristics of the airfoil used at each radial blade station, such as section lift and drag variation with local angle of attack. Such characteristics may then be used to assess local forces on a typical blade element, located between radius $r$ and $r + \Delta r$ shown in Figure 3.1. Then by summing all of the like local forces across the blade radius from hub to tip, the total thrust and torque developed by the propeller can be found.

The propeller used in this simulation was a wooden variable pitch two-bladed propeller made by the Solo Propeller Company. The blade pitch can only be changed while the engine is not operating and the aircraft is on the ground.

A variable pitch propeller is shown in Figure 3.2 at four different blade pitch settings. The SOLO propeller is adjustable from the fine to coarse settings shown in Figure 3.2, the feathered and reverse adjustment points are beyond the range of adjustability of this propeller.

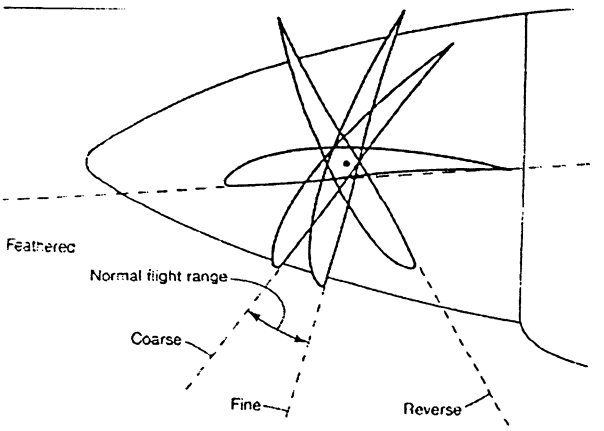


**Figure 3.2: Variable pitch propeller shown at various pitch settings.**

If the propeller were to be sliced at various radial positions along the blade and the blade cross section examined one would notice the cross sectional blade profile would change as the radial blade position is changed. This is called aerodynamic twist.

A second property that can be observed when inspecting the cross sectional shape of the propeller blade at various radial positions is that local angle of attack of each blade section is different from each other blade section for one blade pitch setting. This is called geometric twist. For the SOLO propeller, the local angle of attack decreases as the radial position is increased away from the axis of rotation and this decrease in local angle of attack is called washout.

The definition of blade pitch is: "the pitch of a body rotating about an axis and simultaneously traveling along that axis is the distance traveled forward during the time taken for one revolution. According to this definition, the pitch of a propeller would be the distance traveled by the aircraft during the time taken for one revolution of the propeller [Watts, 1920]."

In an effort to maximize accuracy, a request was made of the manufacturer of the SOLO propeller to provide geometric and aerodynamic data; however, no geometric or aerodynamic information was made available. As a result, the blade was manually divided into 20 sections at ½" increments from the hub to the blade tip and several geometric blade properties were measured at each blade station.

The distribution of local angle of attack for each blade section of the SOLO propeller was determined by adjusting the blade pitch dial to the 0″ pitch position and placing the propeller on a flat, rigid surface. The heights of the leading edge and trailing edges were measured to an

accuracy of $^{1}/_{64}''$ and the height was recorded for this baseline setting. The pitch was then increased to a 12″ pitch setting and a second set of measurements was taken and recorded.

From these two data sets, it was possible to determine the geometric pitch at each local blade station for any user defined pitch setting shown in Figure 3.3.

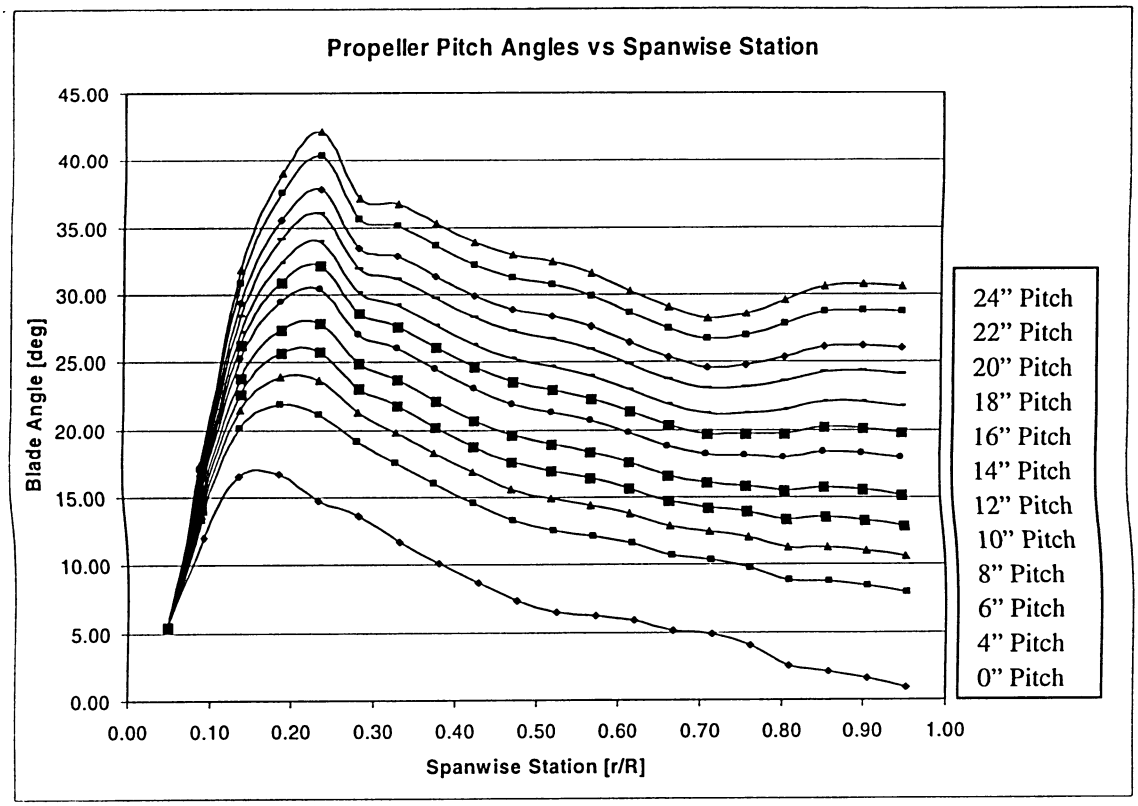


**Figure 3.3: Blade pitch vs. span-wise station.**

Other measured properties were the local blade chord, local blade thickness and chord wise location of maximum blade thickness. In addition to the measured quantities, a straight edge was placed against the lower local airfoil surface to visually observe the profile of the lower surface. The straight edge was also placed on the upper surface overhanging the trailing edge so any reflex could be visually identified.

The geometric properties of the SOLO propeller have been defined at each blade station and this information allowed the author to proceed with the determination of the drag of the inboard blade element sections and then downwash blade element analysis.

## *Section 3.3 Inboard Station Drag Coefficient Analysis*

The modified blade element theory was selected to model the propeller because it allows a very good balance between simplicity and accuracy while taking into account the downwash produced by the propeller. The local blade section properties have been measured and the foundation has been set to determine the airfoil sections that will be used to simulate the actual blade cross sections of the SOLO propeller.

Four assumptions were made to simplify the analysis and they were:

- No rotational inflow;
- No rotational slipstream;
- No blockage effects; and
- No tip vortex losses.

Challenges in identifying cross sectional airfoil profile of the SOLO propeller at each blade station were overcome without the need for destructive testing by using the NACA 4-digit airfoil sections. This method of airfoil classification was selected because it incorporates all of the experimentally measured physical airfoil section data and reliable lift and drag data is readily available.

The four-digit airfoil geometry is defined, as the name implies, by four digits; the first gives the maximum camber in percent chord; the second the location of the maximum camber in tenths of chord; and the last two the maximum thickness in percent chord [McCormick, 1995].

To determine the first digit of the NACA 4-digit airfoil, the other three digits were measured first and the first digit was visually selected.

To determine the second digit of the NACA 4-digit airfoil, the chord-wise location of the maximum camber was estimated by using digital calipers to determine the numerical value of the maximum camber, and then the location the maximum camber measurement was obtained by measuring from the leading edge of the blade section.

The last two digits of the NACA 4-digit airfoil were measured by dividing the local blade section thickness by the local chord length.

The procedure for determining the NACA 4-digit airfoil was repeated for every blade station along the length of the propeller.

Figure 3.4 is a photograph of the SOLO propeller with black stripe markings on one blade indicating the blade stations used in the modified blade element analysis. Blade stations

closer to the root were not approximated with this method since the thickness of the blade profiles was such that the NACA 4-digit airfoil sections were unsuccessful in adequately approximating the actual blade profile. This combined with the relatively low Reynolds numbers experienced at these airfoil sections indicated that very little thrust would be produced by the inner section of the propeller blade and the torque would be approximated through other methods.

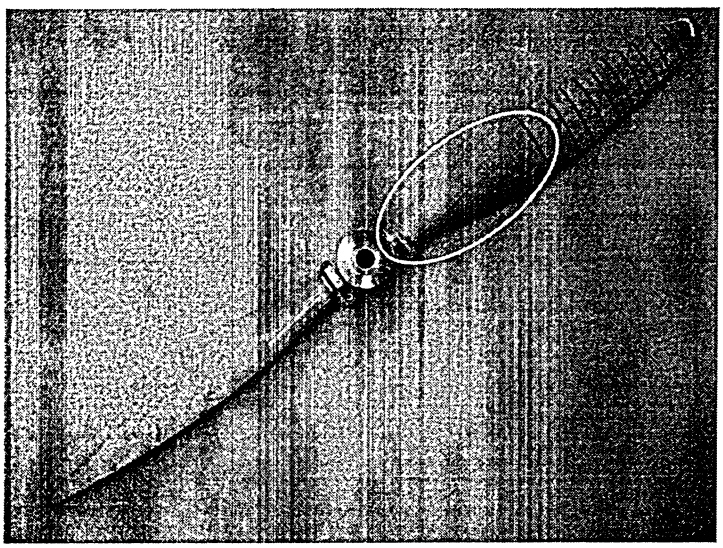

**Figure 3.4: The SOLO propeller.**

The drag coefficients for the inboard stations were obtained from Streeter (1998), using circular and elliptical cylinders to approximate the local blade profile. The drag coefficients are shown in Table 3.1 for the blade stations contained within the ellipse shown in Figure 3.4.

**Table 3.1: Drag Coefficient per Inboard Blade Station.**

| Inboard Station: | 1 | 2 | 3 | 4 | 5 | 6 | 7 | 8 |
|---|---|---|---|---|---|---|---|---|
| Actual t/c | 0.928 | 0.631 | 0.503 | 0.384 | 0.309 | 0.260 | 0.234 | 0.214 |
| $c_d$ | 1.20 | 0.6 | 0.6 | 0.32 | 0.32 | 0.32 | 0.32 | 0.32 |

The drag coefficient for station 1 corresponds to that of a circular cylinder, which is 1.20 for a Reynolds number range of $10^4$ to $1.5 \times 10^5$ since the t/c ratio is close to 1. The actual range of Reynolds numbers at station 1 ranges from $6.7 \times 10^3$ to $1.8 \times 10^4$. Even though the actual range of Reynolds numbers is slightly lower than the range quoted by Streeter (1998), the approximation is still considered to be valid since the contribution to the overall torque and thrust of the propeller blade is small.

The drag coefficient of 0.6 at station 2 corresponds to an elliptical cylinder with a theoretical t/c ratio of 0.5 at zero angle of attack. This theoretical $c_d$ value is valid for a Reynolds number of $4x10^4$ and the actual range of Reynolds numbers at station 2 ranges from $1.6x10^4$ to $4.4x10^4$ making the theoretical approximation valid for the range of Reynolds numbers experienced. The actual t/c ratio was 0.631, which is higher than 0.5; however, the use of the elliptical cylinder more closely approximates the actual propeller than the circular cylinder approximations.

The drag coefficient of 0.6 at station 3 corresponds to an elliptical cylinder with a theoretical t/c ratio of 0.5, at zero angle of attack and a theoretical Reynolds number of $10^5$. The actual range of Reynolds numbers at station 3 was $2.7x10^4$ to $7.2x10^4$, which makes the drag coefficient approximation valid for the Reynolds numbers experienced at station 3.

The drag coefficient of 0.32 at station 4 corresponds to an elliptical cylinder at zero angle of attack, a theoretical t/c ratio of 0.25 and a theoretical Reynolds number range of $2.5x10^4$ to $10^5$. The actual t/c ratio was 0.384, which is closer to the t/c = 0.25 elliptical cylinder than it is to the t/c = 0.5 elliptical cylinder. The actual Reynolds numbers at station 4 ranges from $4.2x10^4$ to $1.1x10^5$, which falls within the range of the theoretical elliptical cylinder with t/c = 0.25.

The drag coefficient of 0.32 at stations 5, 6, 7, and 8 correspond to an elliptical cylinder at zero angle of attack, a theoretical t/c ratio of 0.25 and a theoretical Reynolds number range of $2.5x10^4$ to $10^5$. The actual t/c ratios were 0.309, 0.26, 0.234, and 0.214 for stations 5, 6, 7, and 8, respectively, which is close to the theoretical t/c ratio of 0.25 than it is to the theoretical t/c ratio of 0.5, which is why the elliptical cylinder of t/c = 0.25 was used to approximate this station. The actual range of Reynolds numbers at stations 5, 6, 7, and 8 can be found in Table 3.2.

**Table 3.2: Reynolds' number range for inboard blade stations 5, 6, 7, and 8.**

| Inboard Station: | 5 | 6 | 7 | 8 |
|---|---|---|---|---|
| Reynolds Number Range: | $5.8x10^4$ to $1.6x10^5$ | $7.6x10^4$ to $2.0x10^5$ | $9.2x10^4$ to $2.5x10^5$ | $1.1x10^5$ to $2.9x10^5$ |

The actual range of Reynolds' numbers experienced at blade stations 5, 6, 7, and 8 fall into the range of theoretical Reynolds numbers valid for the t/c = 0.25 elliptical cylinder.

## *Section 3.4 NACA Blade Profiles*

Propellers are cantilever structures with a distributed load across the span of each blade. The highest stresses occur at the root of a cantilever beam so in the case of a propeller, the blade must be thick at the root to ensure failure will not occur. The stresses in the blade will decrease with increasing radial distance from the hub hence; the blade thickness can be reduced without changing the primary mode of failure.

The outer portion of the propeller blade was divided into 12 stations, shown numbered in Figure 3.5.

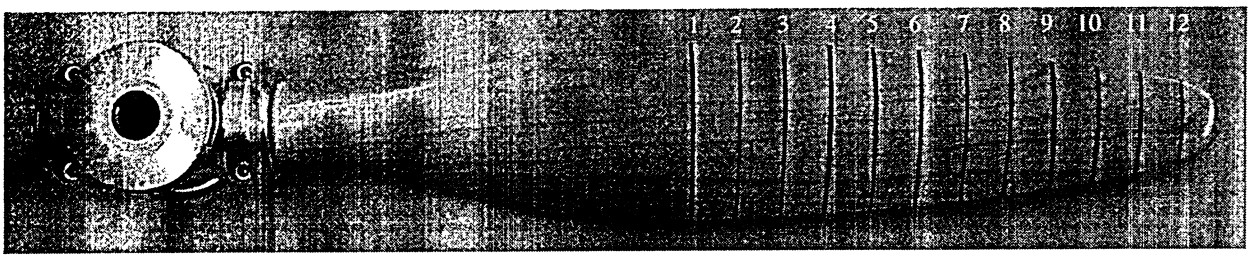


**Figure 3.5: Propeller geometry.**

Table 3.3 contains the 4-digit NACA designation of the airfoils used to approximate the actual propeller blade cross sectional shape.

**Table 3.3: NACA airfoil designation for outboard blade stations.**

| Station | 1 | 2 | 3 | 4 | 5 | 6 | 7 | 8 | 9 | 10 | 11 | 12 |
|---|---|---|---|---|---|---|---|---|---|---|---|---|
| NACA | 6319 | 5318 | 5317 | 5316 | 5316 | 5315 | 5314 | 5314 | 4313 | 4313 | 4313 | 4312 |

Table 3.3 shows the thickness of the 4-digit NACA airfoil cross section decreases with increasing radial distance form the propeller hub and identifies which NACA 4-digit airfoil was selected for each blade station.

## *Section 3.5 Advance Ratio*

The advance ratio ($J$) is a non-dimensional number relating the forward flight speed to the rotational speed of the propeller. At an advance ratio of zero the propeller is said to be operating in the static condition and an advance ratio of 1 is the maximum speed the aircraft can fly in a straight and level flight path since at this $J$ the propeller does not generate any thrust.

The advance ratio is defined by Eq. (3.11).

$$J = \frac{V_\infty}{nD_p} \tag{3.11}$$

where $V_\infty$ is the forward flight speed, $n$ is the rotational speed of the propeller and $D_p$ is the diameter of the propeller.

The SOLO propeller is operating at $J \approx 0$ since there is no forward flight speed but there is a small inflow velocity component of the incoming air, as will be discussed in Section 3.6.

## *Section 3.6 Downwash Blade Element Theory*

The vector diagram of an arbitrary blade element can be seen in Figure 3.6 [McCormick, 1995], where $dL$ is the differential lift force, $dD$ is the differential drag force, $dT$ is the differential thrust force, and $dF_Q$ is the differential torque vector. The quantity $\Gamma$ is the circulation about the blade element, $\beta$ is the user defined blade pitch angle, $\alpha$ is the resultant angle of attack, and $\alpha_i$ is the induced angle of attack. The quantity $\omega_r$ is the angular velocity of the propeller, V is the inflow air velocity, $V_E$ is the resultant velocity (along which lie the trailing edge vortices) or relative velocity, and $V_R$ is the geometric velocity. The quantity $w$ is the velocity induced by the trailing edge vortex system, $w_a$ and $w_t$ are the axial and tangential components, respectively, of the downwash velocity $w$. The downwash angle is $\alpha_i$.

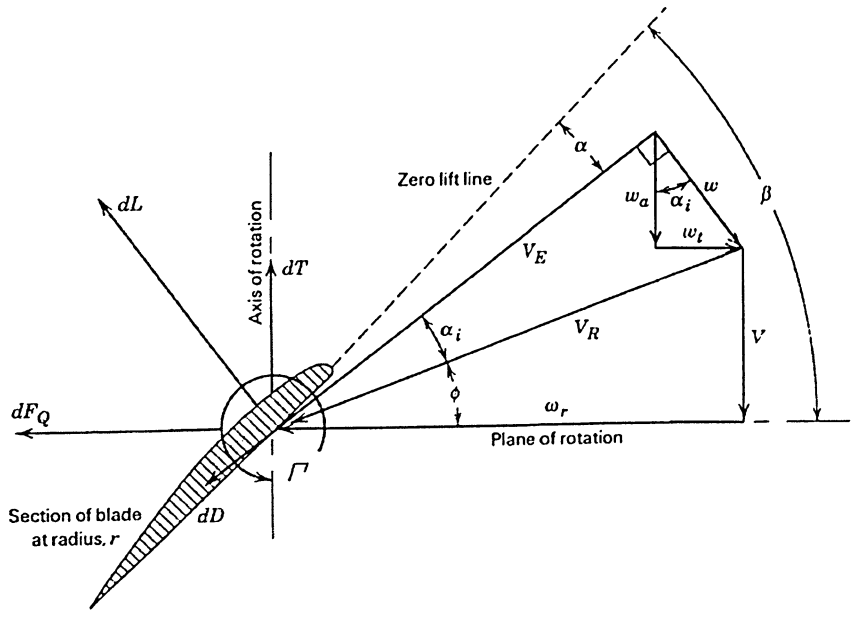


**Figure 3.6: Velocities and forces acting on a propeller blade.**

To determine the lift and drag coefficients of the SOLO propeller through X-Foil in conjunction with the SIMPEL program, there are several quantities that must be determined before the solution can be obtained. The angle of attack at each blade station is a function of geometric pitch angle, the rotational speed of the propeller and the inflow air velocity. For the purposes of this thesis, all testing is to be done under static conditions; therefore, the inflow velocity will be only that which is induced by the propeller itself. This induced inflow was assumed to be 0.1 m/s and constant for all test cases. In reality this is not the case, the induced inflow velocity will change with changing rotational speed and blade pitch.

To determine the angle of attack ($\alpha = \beta - \alpha_i - \phi$) of the blade station, the $\beta$ value is known and set by the operator, $\alpha_i$ and $\phi$ are found by using Eqn's (3.12) and (3.13). Eqn's (3.14) through (3.18) are used to supplement Eq. (3.12).

$$\alpha_i = \frac{1}{2}\sqrt{-\left(\frac{\lambda}{x}+\frac{a\sigma V_R}{8x^2V_T}\right)+\left[\left(\frac{\lambda}{x}+\frac{a\sigma V_R}{8x^2V_T}\right)^2+\frac{c_{l\alpha}\sigma V_R}{2x^2V_T}(\beta-\phi)\right]} \tag{3.12}$$

where $\alpha_i$ is the local induced angle of attack, $c_{l\alpha}$ is the local lift curve slope and $\beta$ is the local blade pitch. The other variables are defined below.

$$\phi = \tan^{-1}\left(\frac{\lambda}{x}\right) \tag{3.13}$$

where $\phi$ is an induced angle of attack resulting from the forward speed of the propeller, $\lambda$ is the non-dimensional ratio of forward flight speed to the local speed of the blade station and $x$ is the local blade radius normalized with respect to the total blade radius.

$$\lambda = \frac{V_\infty}{\omega R_p} \tag{3.14}$$

where, $V$ is the freestream (or flight) velocity, $\omega$ is the rotational speed of the propeller, $R_p$ is the radius of the propeller blade, and

$$\sigma = \frac{Bc_{loc}}{\pi R_p} \tag{3.15}$$

where $B$ is the number of propeller blades, $c_{loc}$ is the local chord (length of blade section), and $\sigma$ is local propeller solidity.

$$V_T = \omega R \tag{3.16}$$

where $V_T$ is the propeller tip speed.

$$V_R = V_T\sqrt{x^2+\lambda^2} \tag{3.17}$$

where $V_R$ is the resulting air speed impinging on the propeller section taking into account the forward speed of the aircraft

$$x = \frac{r}{R_p} \tag{3.18}$$

where $r$ is the local blade radius measured from the hub.

After making the appropriate substitutions, $V_E$ from Figure 3.6 was derived as Eq. (3.19).

$$V_E = \sqrt{V^2 + [\omega x R_p]^2 \cos(\alpha_i)} \tag{3.19}$$

where $V_E$ is the resulting air speed impinging on the propeller section taking into account the blade section downwash.

The Reynolds number is defined as Eq. (3.20).

$$\mathrm{Re} = \frac{\rho V_E d}{\mu} \tag{3.20}$$

where $\rho$ is the ambient density, $d$ is the characteristic length of the body and $\mu$ is the viscosity of the fluid.

Making appropriate substitutions, the Reynolds number ($Re$) was re-written as Eq. (3.21).

$$\mathrm{Re} = \frac{\rho c_{loc} \sqrt{V_E^2 + \left[\omega\left(\frac{r}{R}\right)R_p\right]^2 \cos(\alpha_i)}}{\mu} \tag{3.21}$$

The propeller, by definition and design, rotates about the propeller hub at an angular velocity ($\omega$). This produces a local tangential velocity profile as shown in Figure 3.7 (a) [Hurt, 1965].

The typical blade loading can be seen in Figure 3.7 (b) [Hurt, 1965], where the maximum thrust is developed at approximately 75% of the blade radius measured from the hub, shown in Figure 3.7 (c) [Archer, 1996].

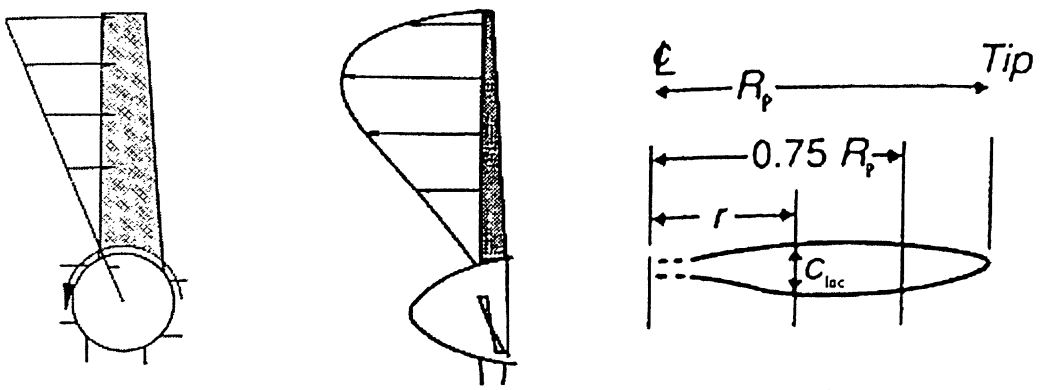


(a) (b) (c)

**Figure 3.7: Tangential velocity profile (a), approximate blade thrust/torque distribution (b), and approximate location of maximum thrust/torque (c).**

The 'rule of thumb' results, shown in Figure 3.7 (b), and (c), will be used to compare with the SIMPEL and X-Foil results to determine if the computationally generated results match with historical trends.

## *Section 3.7 Airfoil Stall*

When the lift coefficient is plotted against the angle of attack ($\alpha$) the following general trends shown in Figure 3.8 (a) [Lennon, 1999] can be observed. If an observer were to look at the top view of a wing during an increase in angle of attack, as shown in Figure 3.8 (a), the stall patterns shown in Figure 3.8 (b) [Lennon, 1999] could be observed.

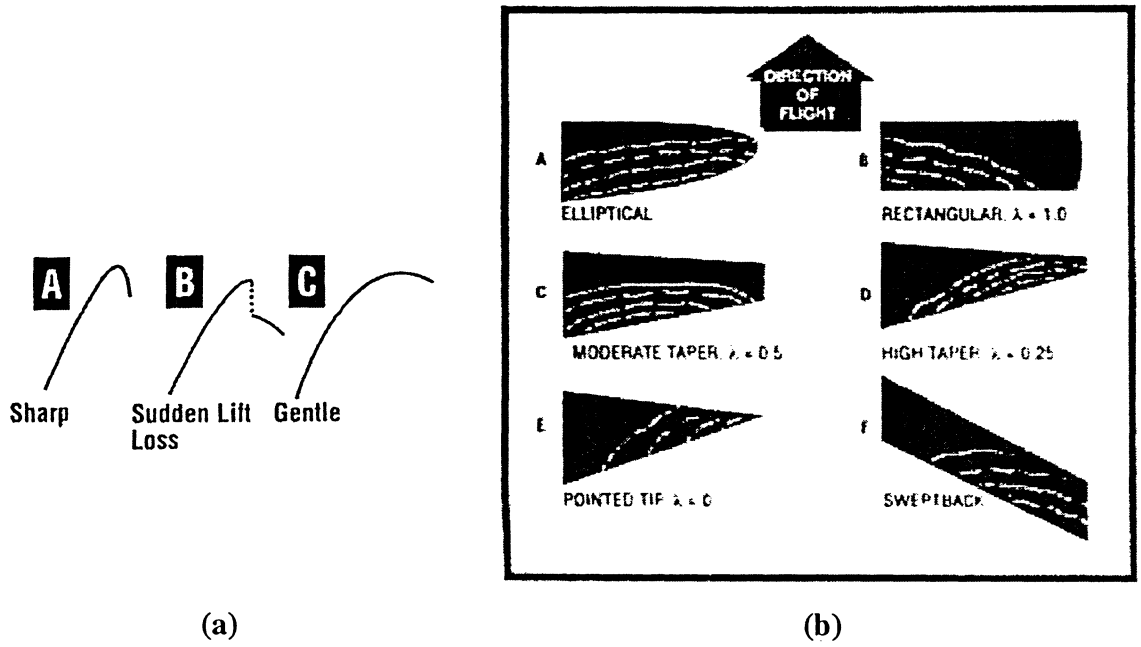


**Figure 3.8: Generic $c_l$ vs $\alpha$ curves representing various types of airfoil stall (a), and trailing edge stall patterns for various wing planforms (b).**

Airfoil stall is a term meaning the separation of the air flow from the surface of the airfoil. There is typically a range of angles through which an airfoil can be inclined to the incoming flow before the air flow separates from the airfoil surface. During the range where the air remains attached to the surface of the airfoil, the slope of the $c_l$ vs $\alpha$ curve remains essentially constant and positive. This trend of increasing $c_l$ with increasing $\alpha$ cannot continue indefinitely; therefore, at some angle of attack the air flow will separate from the airfoil surface.

When examining Figure 3.8 (a), stalling is indicated by the departure of each curve from a constant and positive slope. For a small range of $\alpha$ after the departure from linearly increasing slope the lift coefficient is still increasing but at a decreased rate. The slope will continue to

decrease until becoming zero and with a further increase of angle of attack, the lift coefficient will begin to decrease.

Of particular relevance to this thesis is the leading edge stall, when the airflow suddenly separates from the leading edge of the airfoil. This results in a $c_l$ vs $\alpha$ curve so labeled in Figure 3.8 (a). The lift coefficient steadily increases with an increase in angle of attack until the critical $\alpha$ is reached when the air flow separates and a sudden, discontinuous, drop in $c_l$ is observed.

Figure 3.8 (b) is useful in visualizing how the propeller blade experiences air flow separation and how that separation would propagate across the blade. The Elliptical and Moderate Taper planforms (A and C in Figure 3.8 (b), respectively) most closely approximate the planform of the propeller blade being analyzed.

## *Section 3.8 Outboard Blade Sections Results*

The drag coefficient has been approximated for the inboard blade sections where the NACA 4-digit airfoil profiles failed to adequately approximate the actual blade profile. The lift and drag coefficients for the 12 outboard blade sections needed to be generated in order to calculate the overall torque and thrust generated by the propeller for use as a load in the overall propeller-engine simulation.

## *Section 3.9 Lift and Drag Coefficients*

Two very important aerodynamic quantities are used in the propeller analysis and they are the coefficient of lift and coefficient of drag. These two coefficients arise when an airfoil is inclined at an angle to the incoming flow creating a lift and drag force that is located at the aerodynamic centre of the airfoil. When these lift and drag forces are non-dimensionalized with respect to the dynamic pressure of the incoming flow and to the surface area of the airfoil section, a coefficient of lift and coefficient of drag can be calculated. Eq. (3.22) describes the coefficient of lift and Eq. (3.23) describes the drag coefficient.

$$c_L = \frac{L}{qV_{air}^2 S} \tag{3.22}$$

$$c_d = \frac{D}{qV_{air}^2 S} \tag{3.23}$$

Another essential quantity to include in the propeller simulation is the Mach number. This is a non-dimensional quantity that is used to determine if compressibility effects are present and is also used to correct the lift coefficient should it be required.

## *Section 3.9.1 Mach Number*

When analyzing the propeller, a range of blade rotational speeds was considered and any compressibility corrections must be taken into account, should they be required. The Mach number by definition is the ratio of the freestream velocity to the local speed of sound and is described by Eq. (3.24). Compressibility becomes a concern at Mach numbers greater than 0.4 [Anderson, 1991].

$$M_{\infty} = \frac{V_E}{\sqrt{\gamma R T_{amb}}} \tag{3.24}$$

where the denominator is the local speed of sound and is a function of the ambient temperature, $T_{amb}$, the universal gas constant R = 287 J/kgK, and the specific heat for air $\gamma = 1.4$.

The maximum operating speed of 8000 RPM corresponds to a Mach number of 0.75 at the propeller tip and this indicates that at or near the maximum operating speed, air can no longer be treated as incompressible.

## *Section 3.10 Propeller Simulation Program (SIMPEL)*

The SOLO propeller is variable pitch so an investigation was conducted to determine which propeller pitch settings would generate the maximum thrust and torque.

The aerodynamic performance of the propeller was obtained through a combination of the SIMPEL and X-Foil programs. The local atmospheric and operating conditions were input to the SIMPEL program and it would generate a batch file for X-Foil to process. The results from X-Foil were then read back into SIMPEL to complete the analysis.

During the simulation of the propeller in X-Foil, there were certain blade stations, pitch angles and operating speeds that prevented the vortex panel method used by X-Foil from converging, resulting in X-Foil returning an empty result file.

This empty result file indicated either a stalled condition or a compressibility problem requiring alternative methods for the determination of lift and drag coefficients. To approximate

the lift coefficient post stall, McCormick (1995) shows the lift coefficient dropping to approximately the same value as found at zero angle of attack.

To approximate the drag coefficient during stalled conditions, the stalled airfoil was treated as an inclined flat plate. The drag coefficient of a rectangular flat plate was found as a function of the base/height (b/h) ratio at Reynolds numbers greater than $10^4$ [Streeter, 1998]. For specific application to the SOLO propeller, the base is the distance between blade stations ($\Delta r_i$ = $^1/_2$″) and the height was the projected area normal to the flow. Eq. (3.25) relates the approximated stalled drag coefficient to the section b/h ratio.

$$c_{d_i} = 0.02\left(\frac{\Delta r_i}{c_i \sin(\beta_i - \alpha_i - \phi_i)}\right) + 1.1 \tag{3.25}$$

When a blade station was found to stall at low angles of attack, the denominator of Eq. (3.25) became small and the resulting $c_d$ value was impractically large; therefore, the drag coefficient was limited to 2.0.

## *Section 3.10.1 Drag Coefficient Results*

Since the aerodynamic response of the propeller is being analyzed within X-Foil, it was initially unclear as to how it compensates for the effects of compressibility or even if the it compensates for compressibility at all. Examination of the X-Foil source code revealed a compressibility correction is in fact performed automatically when required according to the Pradtl-Glauert rule [NACA Report no. 646], shown in eq. (3.26).

$$c_l = \frac{c_{l_o}}{\sqrt{1 - M_\infty^2}} \tag{3.26}$$

The SOLO propeller was intended to be tested and operated under static conditions and it was essential to know which blade stations stall under which operating conditions to determine any operating limitations. Some blade stations could stall due to Reynolds numbers being too low combined with an angle of attack that was too high, or the blade stations near the tip of the propeller could experience compressibility effects when operated at high rotational speeds.

To determine the drag coefficient at each blade station under all possible operating conditions, SIMPEL and X-Foil were used in combination. The results for three representative blade pitch values of 4″, 10″ and 24″ are shown in Figure 3.9 to Figure 3.17.

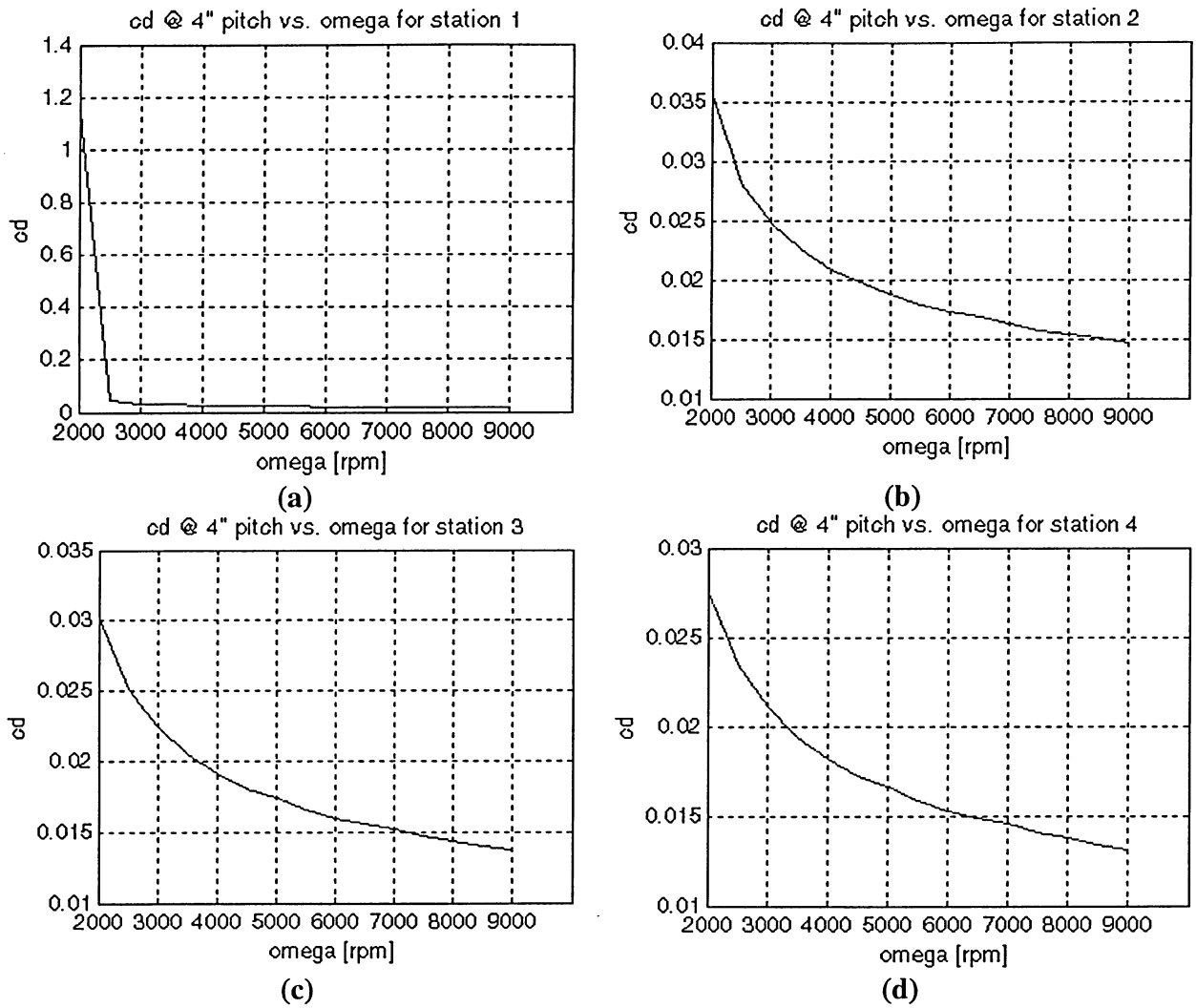


**Figure 3.9: Drag coefficient vs. RPM for stations 1 to 4 at a 4″ blade pitch.**

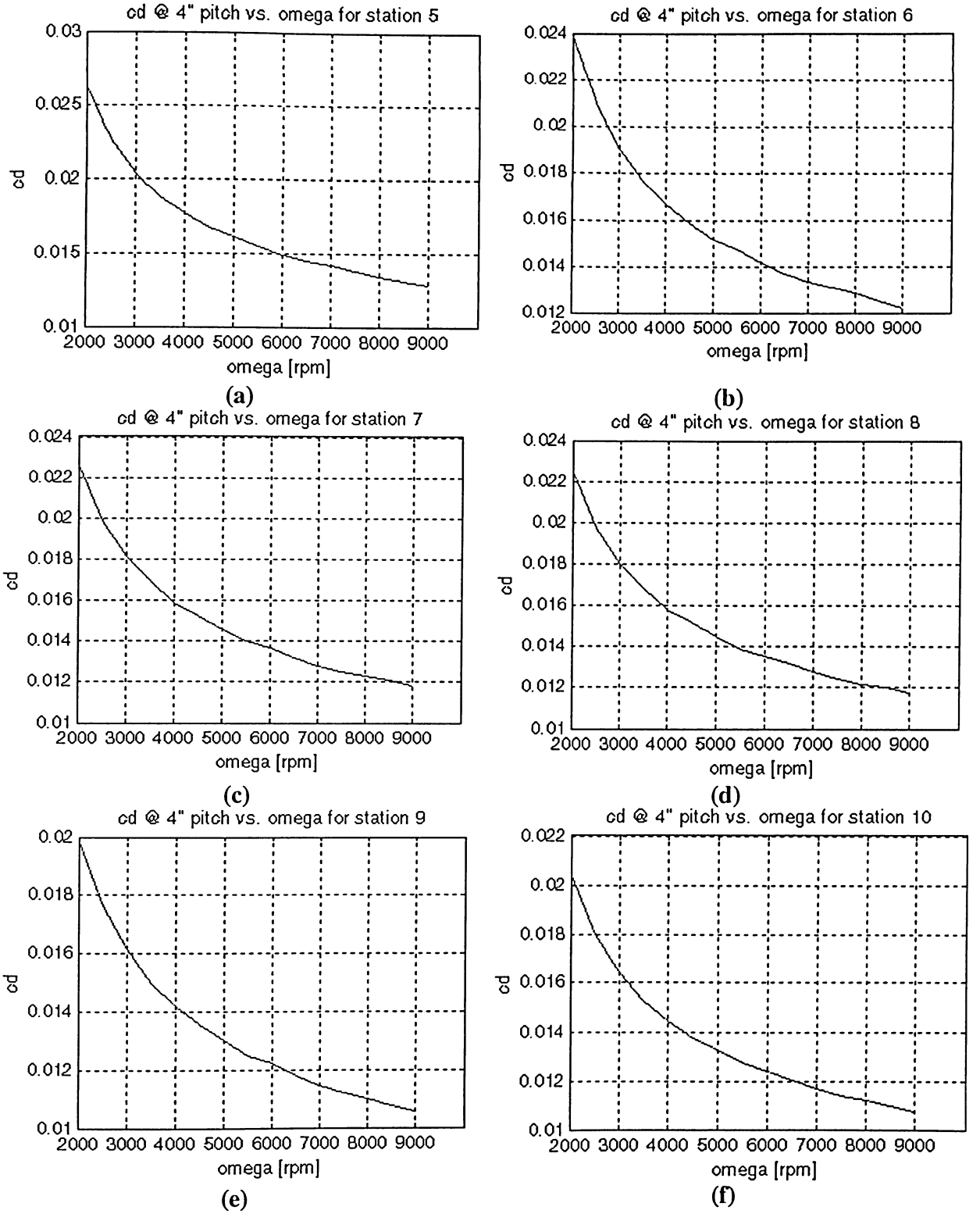


**Figure 3.10: Drag coefficient vs. RPM for stations 5 to 10 at a 4″ blade pitch.**

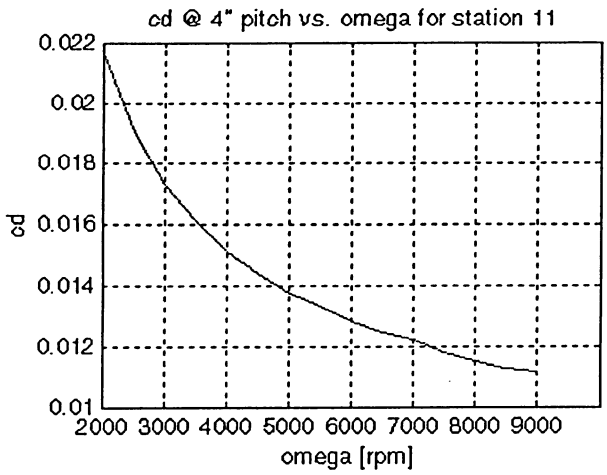


(a)

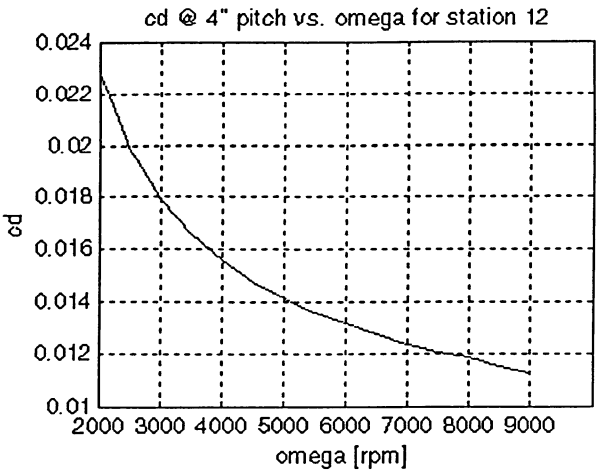


(b)

**Figure 3.11: Drag coefficient vs. RPM for stations 11 to 12 at a 4″ blade pitch.**

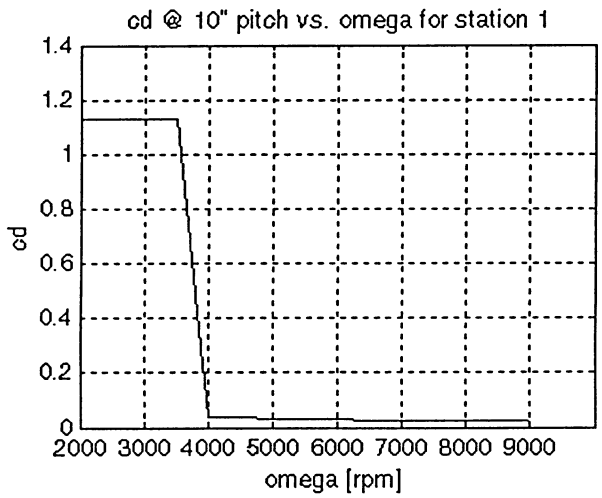


(a)

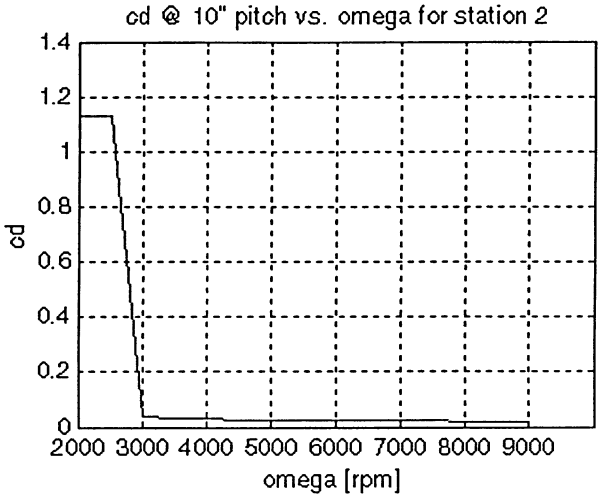


(b)

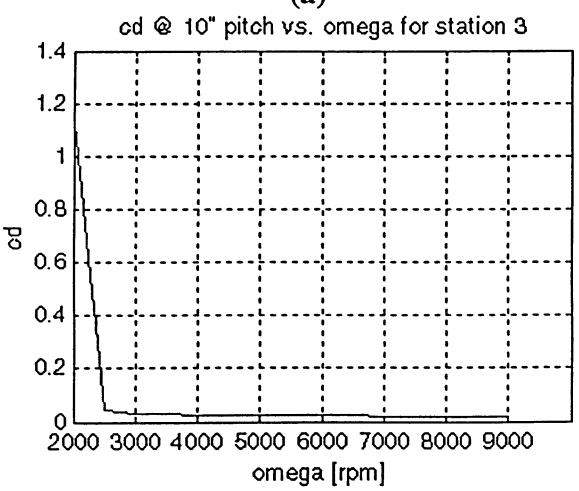


(c)

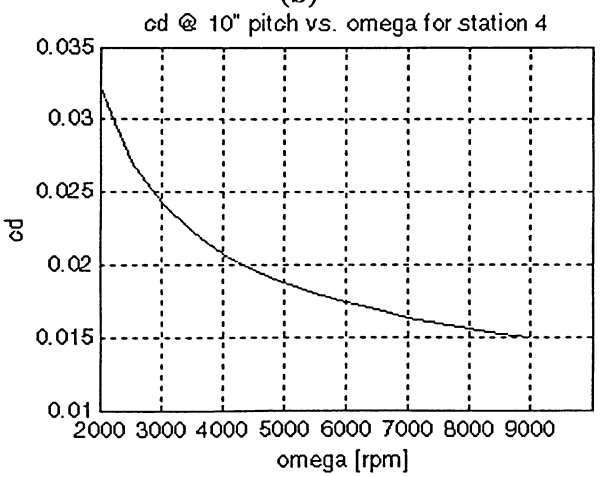


(d)

**Figure 3.12: Drag coefficient vs. RPM for stations 1 to 4 at a 10″ blade pitch.**

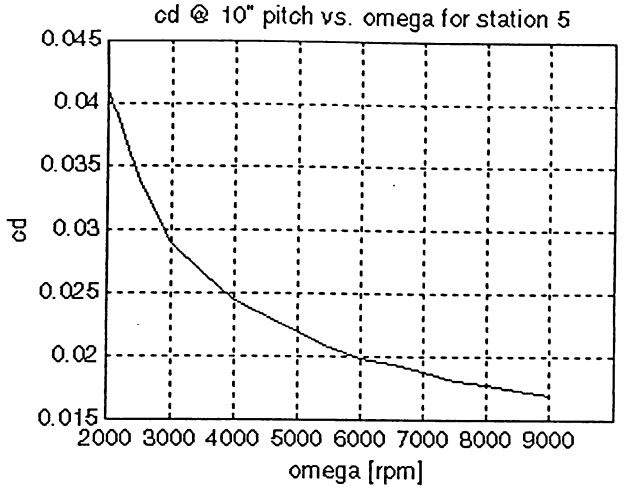


(a)

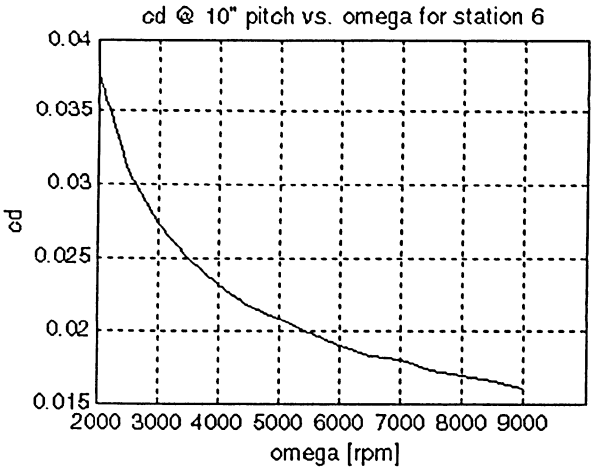


(b)

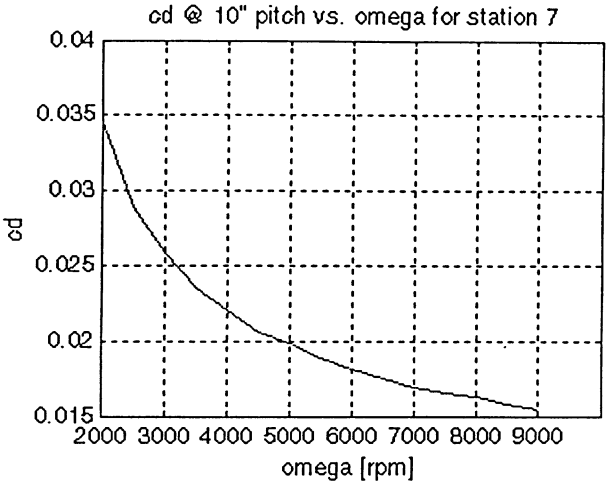


(c)

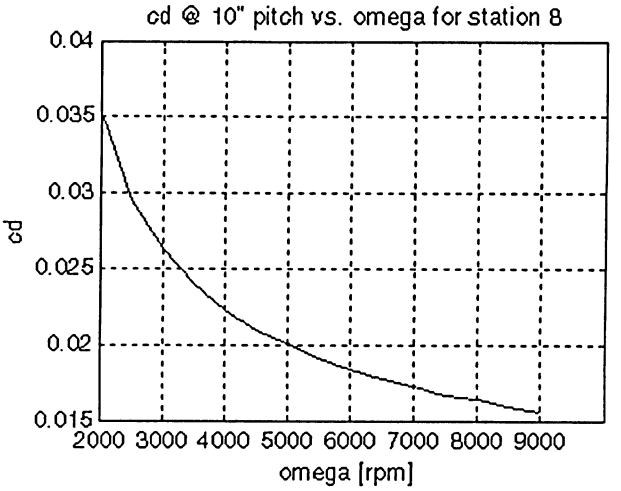


(d)

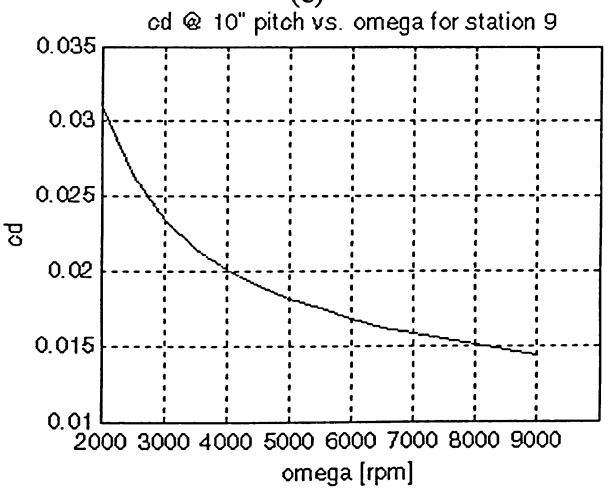


(e)

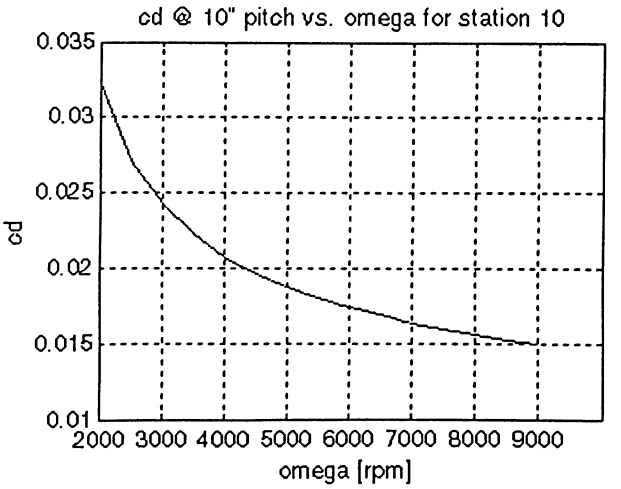


(f)

**Figure 3.13: Drag coefficient vs. RPM for stations 5 to 10 at a 10″ blade pitch.**



PROPERTY OF
RYERSON UNIVERSITY LIBRARY

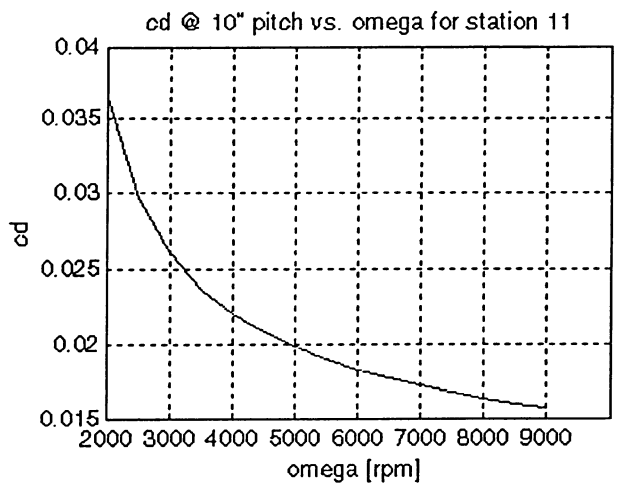


(a)

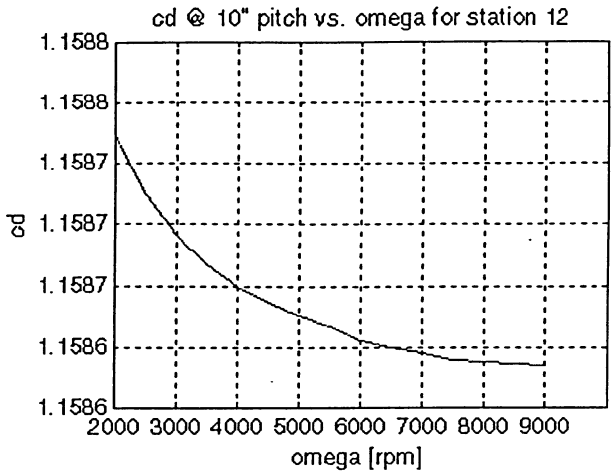


(b)

**Figure 3.14: Drag coefficient vs. RPM for stations 11 to 12 at a 10″ blade pitch.**

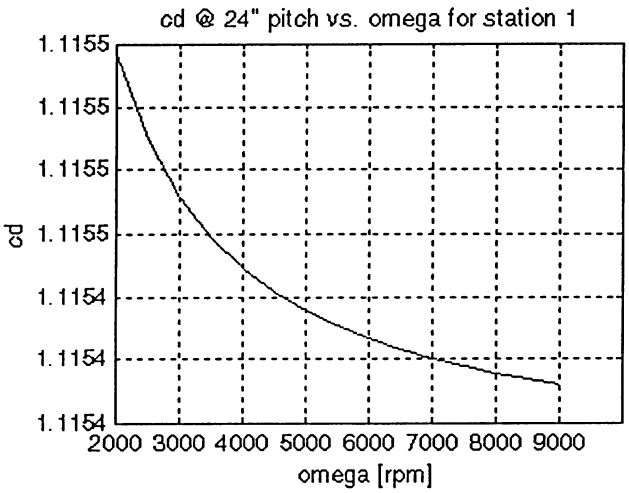


(c)

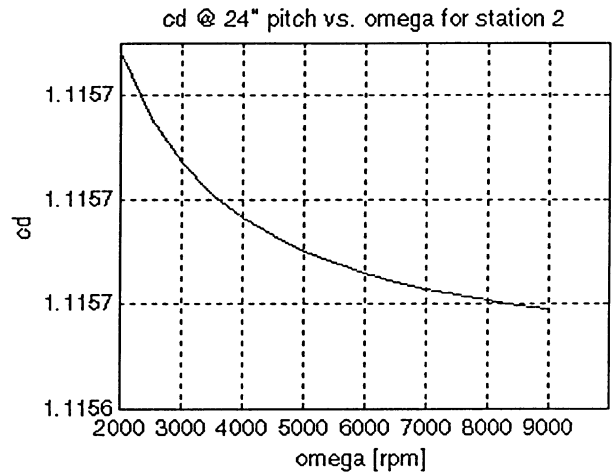


(d)

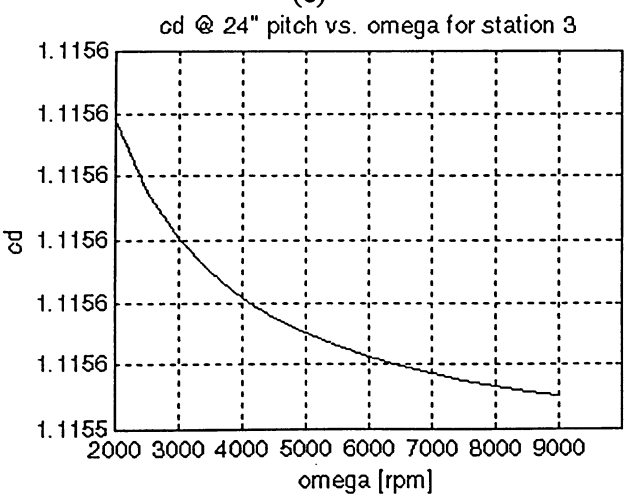


(e)

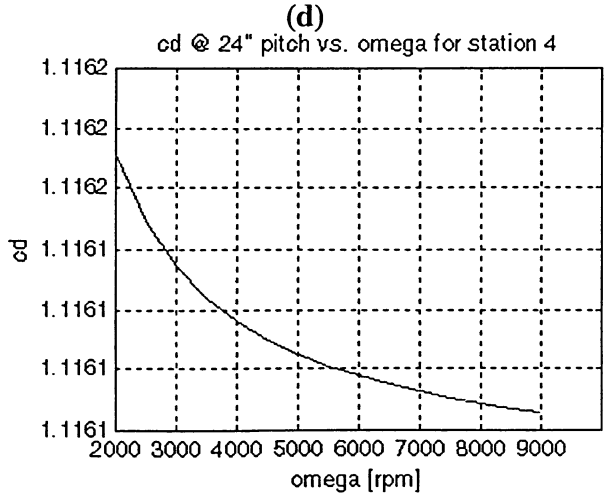


(f)

**Figure 3.15: Drag coefficient vs. RPM for stations 1 to 4 at a 24″ blade pitch.**

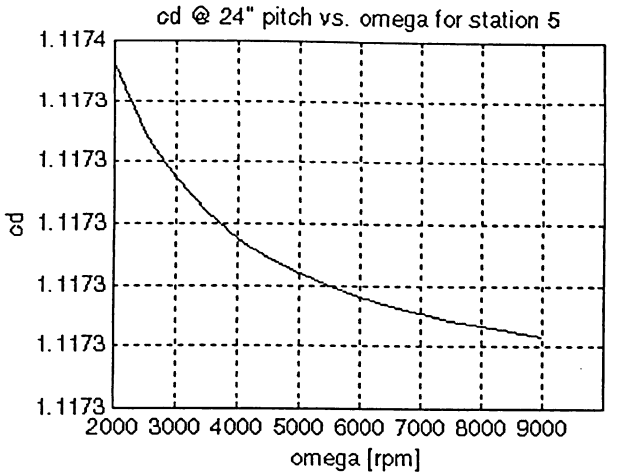


(a)

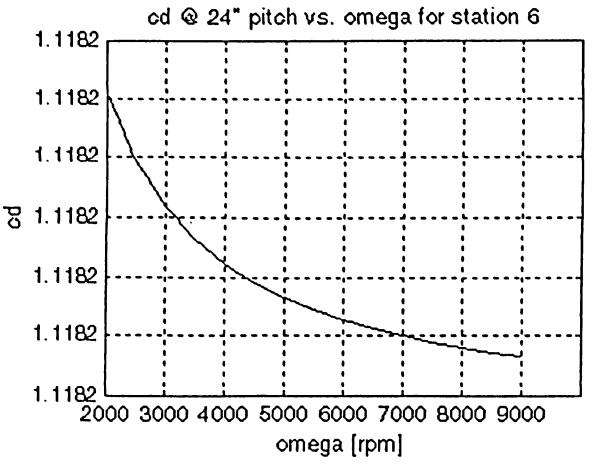


(b)

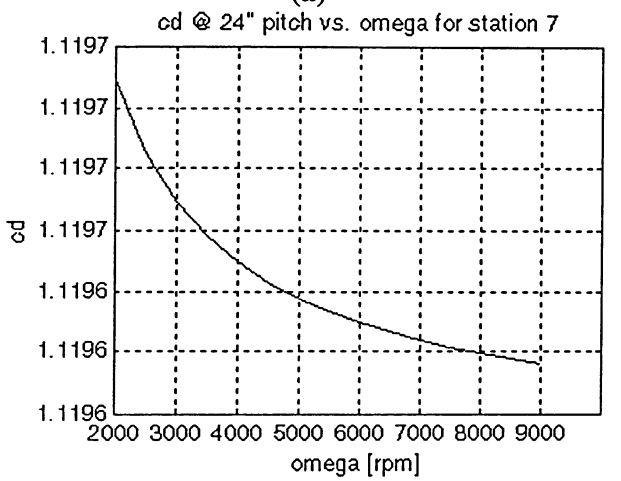


(c)

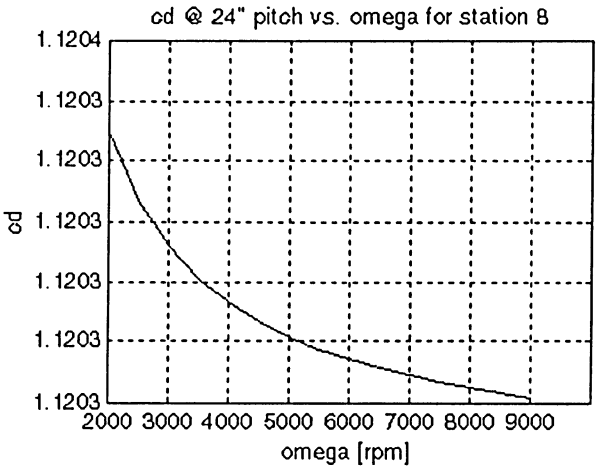


(d)

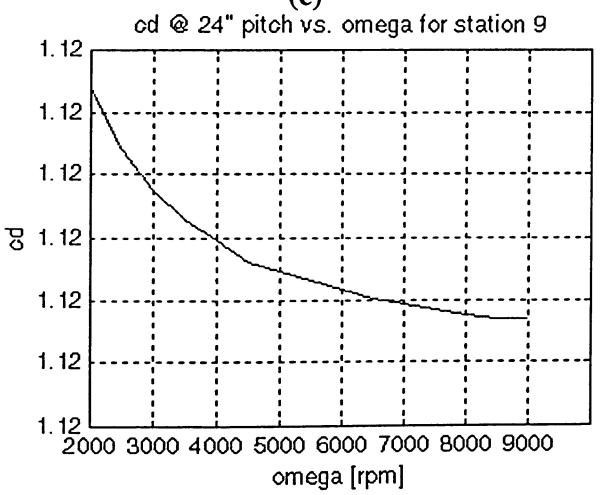


(e)

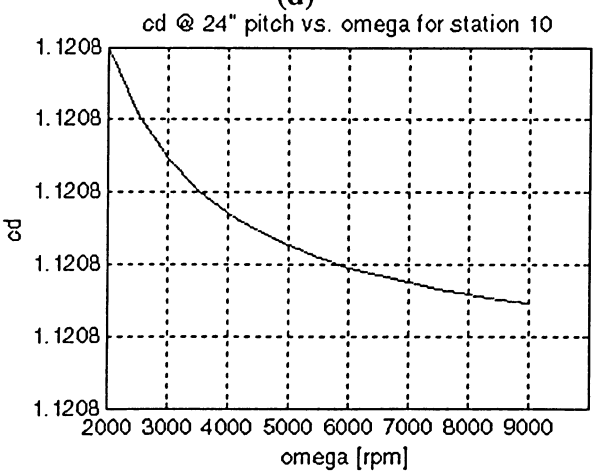


(f)

**Figure 3.16: Drag coefficient vs. RPM for stations 5 to 10 at a 24″ blade pitch.**

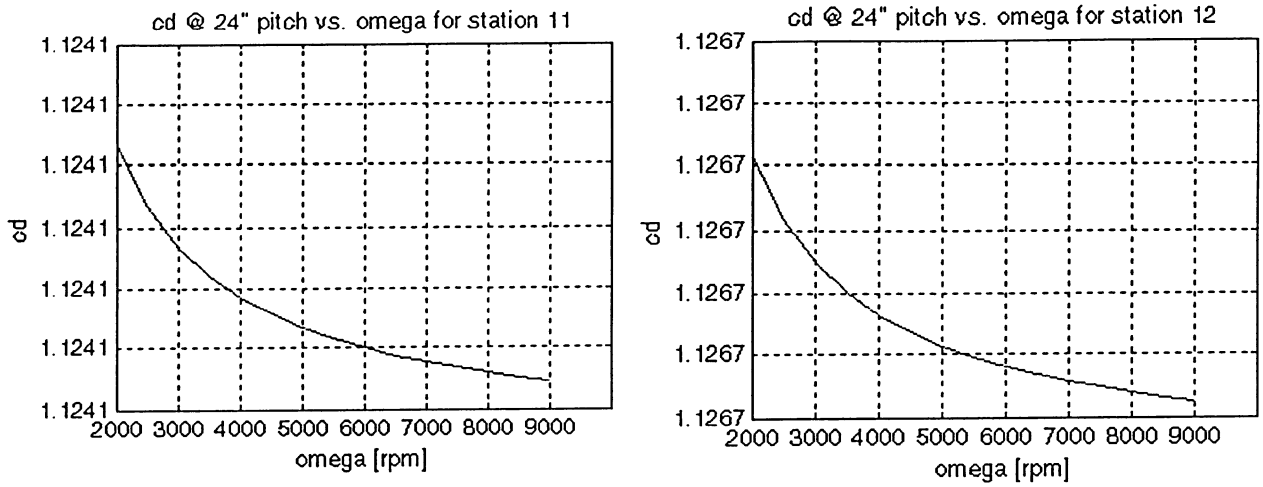


(a) (b)

**Figure 3.17: Drag coefficient vs. RPM for stations 11 to 12 at a 24″ blade pitch.**

The stall pattern observed during the propeller simulations is summarized in Table 3.4 and these results conform to case B from Figure 3.8 (b). The stall pattern of the propeller blade begins at the inboard stations and with an increase in blade pitch the stall line moving outward toward the tip. Many variables influence the propeller analysis and angle of attack alone cannot fully explain the stalling of the blade. Rotational velocity, local angle of attack and in reality, each blade station is coupled with each other adjacent blade station so a disturbance at one station is transmitted to every other blade station at the local sonic velocity.

**Table 3.4: Analysis of stalled blade stations for a given combination of blade pitch and operating speed.**

| RPM/Pitch | 2000 | 2500 | 3000 | 3500 | 4000 | 4500 | 5000 | 5500 | 6000 | 6500 | 7000 | 7500 | 8000 | 8500 | 9000 |
|---|---|---|---|---|---|---|---|---|---|---|---|---|---|---|---|
| 0″ | none | none | none | none | none | none | none | none | none | none | none | none | none | none | none |
| 4″ | 1 | none | none | none | none | none | none | none | none | none | none | none | none | none | none |
| 6″ | 1 | 1 | none | none | none | none | none | none | none | none | none | none | none | none | none |
| 8″ | 1-3 | 1 | 1 | none | none | none | none | none | none | none | none | none | none | none | none |
| 10″ | 1-3<br>12 | 1-3<br>12 | 1<br>12 | 1<br>12 | 12 | 12 | 12 | 12 | 12 | 12 | 12 | 12 | 12 | 12 | 12 |
| 12″ | 1-6<br>9-12 | 1-3<br>9-12 | 1<br>9-12 | 1<br>9-12 | 9-12 | 9-12 | 9-12 | 9-12 | 9-12 | 9-12 | 9-12 | 9-12 | 9-12 | 9-12 | 9-12 |

The results from Table 3.4 indicate that under static operating conditions such as those found in the laboratory, it is inadvisable to increase the blade pitch to a value greater than 10″ for testing purposes. In this case the limit of 10″ at operating speeds greater than 4000 RPM is acceptable; however, a blade pitch setting of 8″ at operating speeds greater than 3000 RPM allows a greater operating range as compared to the 10″ setting.

Since the idle speed of the Saito-450 engine, without glow heating, has a lower limit at 3000 RPM, the pitch setting of 8″ allows for the propeller to remain flying throughout the entire practical operating speed range.

The operational manual supplied by the manufacturer of the propeller strongly recommends avoiding operation of the engine with a propeller setting of 0″ pitch. This warning was heeded resulting in an acceptable range of blade pitch values of 4″, 6″, and 8″.

## *Section 3.11 Overall Torque and Thrust*

Once the SIMPEL airfoil simulation was run in conjunction with X-Foil, the lift coefficient ($c_l$) and drag coefficient ($c_d$) were obtained for a given operating speed and blade pitch. The $c_l$ and $c_d$ values for each blade station were stored in SIMPEL for obtaining the overall propeller thrust and torque values for one operating speed.

The torque ($dQ_p$) and thrust ($dT_h$) for one blade element is represented by Eqn's (3.27) and (3.28) respectively.

$$dQ_p = r[dL\sin(\phi+\alpha_i)+dD\cos(\phi+\alpha_i)] \tag{3.27}$$

$$dT_h = dL\cos(\phi+\alpha_i)-dD\sin(\phi+\alpha_i) \tag{3.28}$$

Making appropriate substitutions to convert the torque and thrust Eqn's (3.27) and (3.28) into a form more convenient for analysis results in Eqn's (3.29) and (3.30).

$$dQ_p = \frac{B}{2}\rho V_E^2 cr[c_l\sin(\phi+\alpha_i)+c_d\cos(\phi+\alpha_i)]dr \tag{3.29}$$

$$dT_h = \left[\frac{1}{2}c\rho V_E^2 c_l\cos(\phi+\alpha_i)+\frac{1}{2}c\rho V_E^2 c_l\sin(\phi+\alpha_i)\right]dr \tag{3.30}$$

Since the propeller was divided into discrete segments, differential Eqn's (3.29) and (3.30) can be discretely solved by conversion to Eqn's (3.31) and (3.32), respectively.

$$Q_p \approx \frac{B}{2}\rho\sum_{i=1}^{12} V_{E_i}^2 c_i r_i \left[c_{l_i}\sin(\phi_i + \alpha_{i_i}) + c_{d_i}\cos(\phi_i + \alpha_{i_i})\right]\Delta r \tag{3.31}$$

$$T_h \approx \frac{B}{2}\rho\sum_{i=1}^{12} \left[V_{E_i}^2 c_i c_{l_i}\cos(\phi_i + \alpha_{i_i}) + V_{E_i}^2 c_i c_{d_i}\sin(\phi_i + \alpha_{i_i})\right]\Delta r \tag{3.32}$$

Eqn's (3.31) and (3.32) provide the overall torque and thrust, respectively, generated by both blades of the SOLO propeller for one operating condition.

The analysis conducted on the SOLO propeller produced overall torque and thrust per blade station shown in Figure 3.18, and Figure 3.19, respectively. The sharp drop in torque and thrust apparent at station 9 is most likely due to the NACA airfoil section chosen to represent that blade station is not optimal.

The maximum torque and thrust were located at 81% and 76% blade span, respectively, measured radially outward from the axis of rotation. The discrepancy between the typical blade loading and the calculated blade loading is due to the fact that this propeller is not ideal and the 75% span rule of thumb is a generalization where the calculation is specific to this propeller.

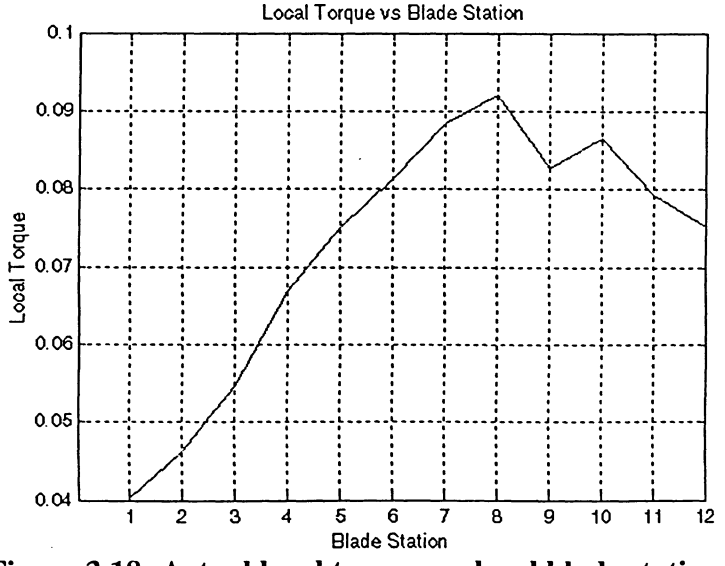


**Figure 3.18: Actual local torque vs. local blade station.**

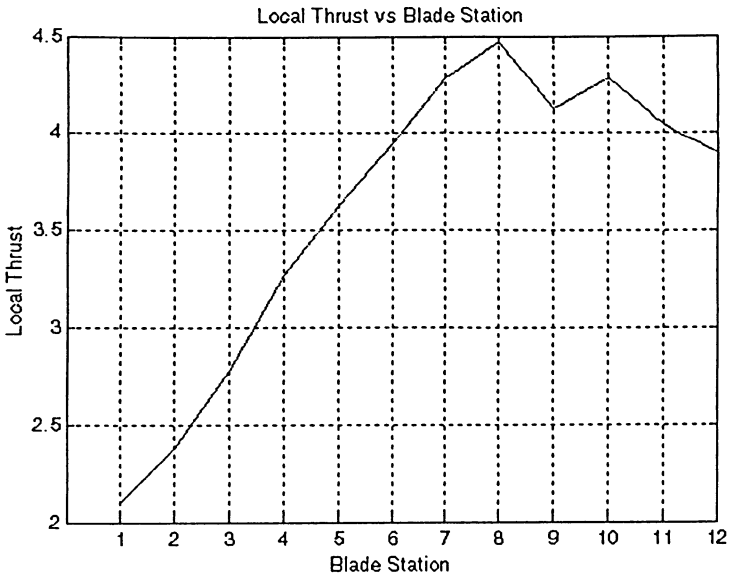


**Figure 3.19: Actual local thrust vs. local blade station.**

Through a regression analysis, the best-fit curve in the form of a second order polynomial provides the torque and thrust data from Figure 3.18, and Figure 3.19, respectively, in functional form, and smoothes the raw data as shown in Figure 3.20, and Figure 3.21.

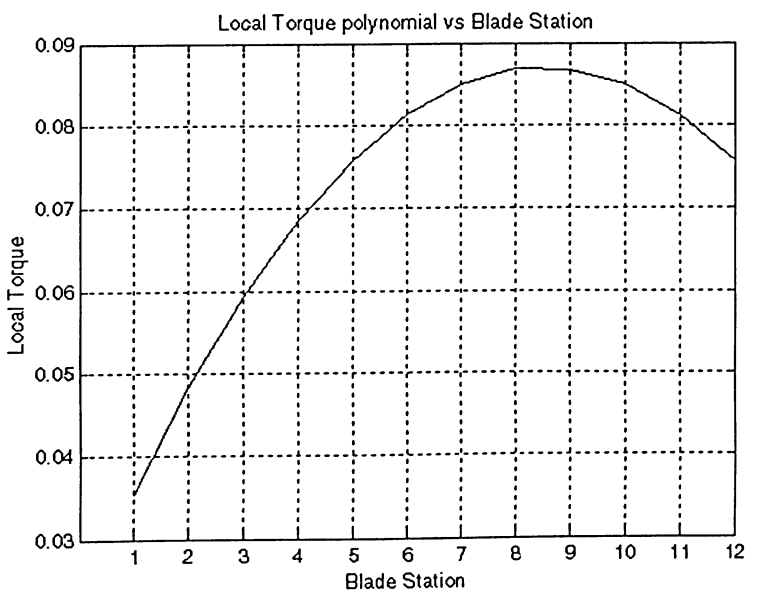


**Figure 3.20: Local torque smoothed by a 2$^{nd}$ order polynomial.**

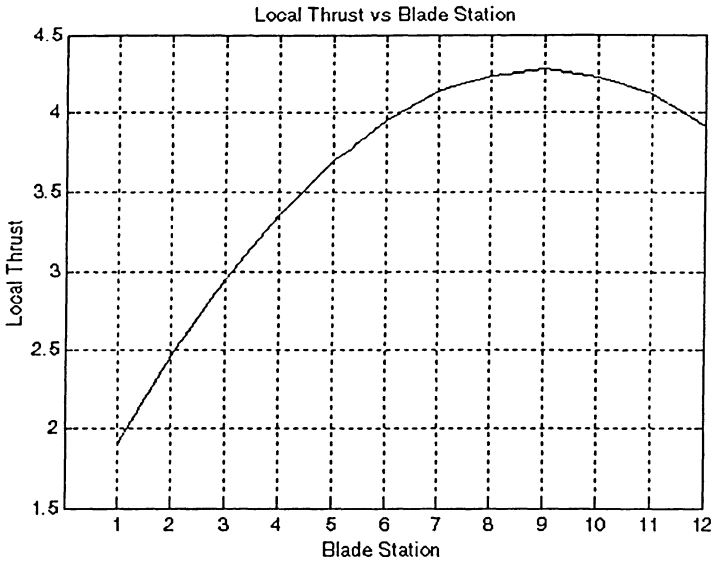


**Figure 3.21: Local thrust smoothed by a 2nd order polynomial.**

The local torque values for each blade station shown in Figure 3.20 were summed over the blade span, doubled and recorded for each pitch setting and operating speed. The raw data were then fit with a second order polynomial shown in Figure 3.22, Figure 3.23, and Figure 3.24 for blade pitch settings of 4″, 6″ and 8″, respectively.

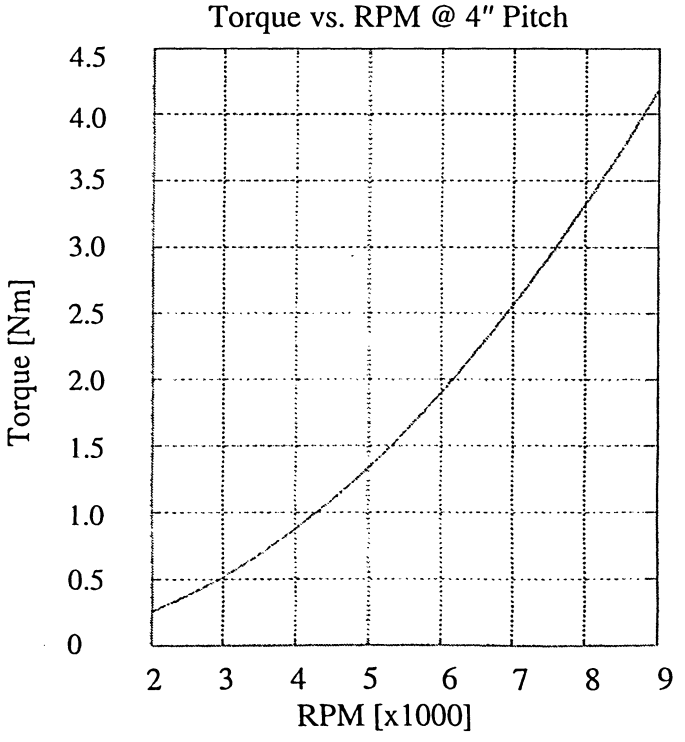


**Figure 3.22: Overall torque at a blade pitch of 4″.**

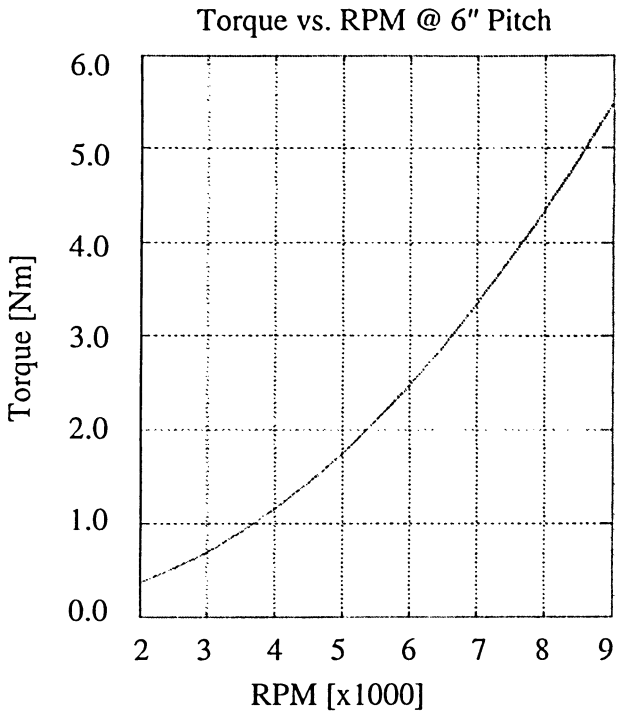


**Figure 3.23: Overall torque at a blade pitch of 6".**

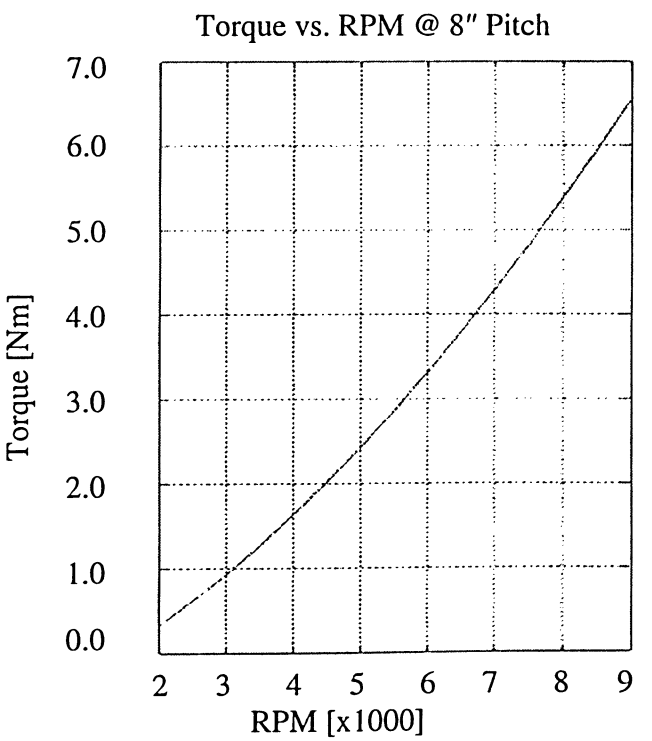


**Figure 3.24: Overall torque at a blade pitch of 8".**

The propeller torque has been found in functional form throughout the entire range of engine operating speeds. To correct the simulation so that it is as realistic as possible, the propeller load must be correlated to the actual maximum engine power output. The operating speed must be determined where this maximum power output is achieved.

If the engine operating speed corresponding to the maximum power output of 7 hp occurs at a speed greater than that recommended by the manufacturer, then an operating speed limit must be included in the simulation.

If the operating speed corresponding to the maximum engine power output occurs at a speed less than the maximum recommended by the manufacturer, then the engine is said to be torque limited and this torque limit must be included in the simulation.

## *Section 3.12 Maximum Operating Speed*

Of interest was the maximum RPM the engine would be expected to achieve for a given propeller torque value with a maximum engine output of 7 hp. Figure 3.25, Figure 3.26, and Figure 3.27, shows the maximum engine power output (Q max) superimposed on the 4″, 6″, and 8″ torque curves, respectively, generated from the X-Foil results taking into account the inner blade section drag approximation.

Figure 3.25 shows the maximum operating speed at a blade pitch of 4″ is an RPM value greater than 9000 RPM. Since the engine is rated at a maximum operating speed of 8000 RPM, at a blade pitch of 4″ the engine is speed limited. Figure 3.26 shows the maximum operating speed at a blade pitch setting of 6″ is 8800 RPM. Since the maximum operating speed recommended by the manufacturer is 8000 RPM, the engine is speed limited when the propeller is set to a 6″ blade pitch. Figure 3.27 shows the maximum operating speed at a blade pitch setting of 8″ is 8200 RPM, which is close to the maximum rated operating speed of the engine and therefore engine was considered to be torque limited at this blade pitch setting.

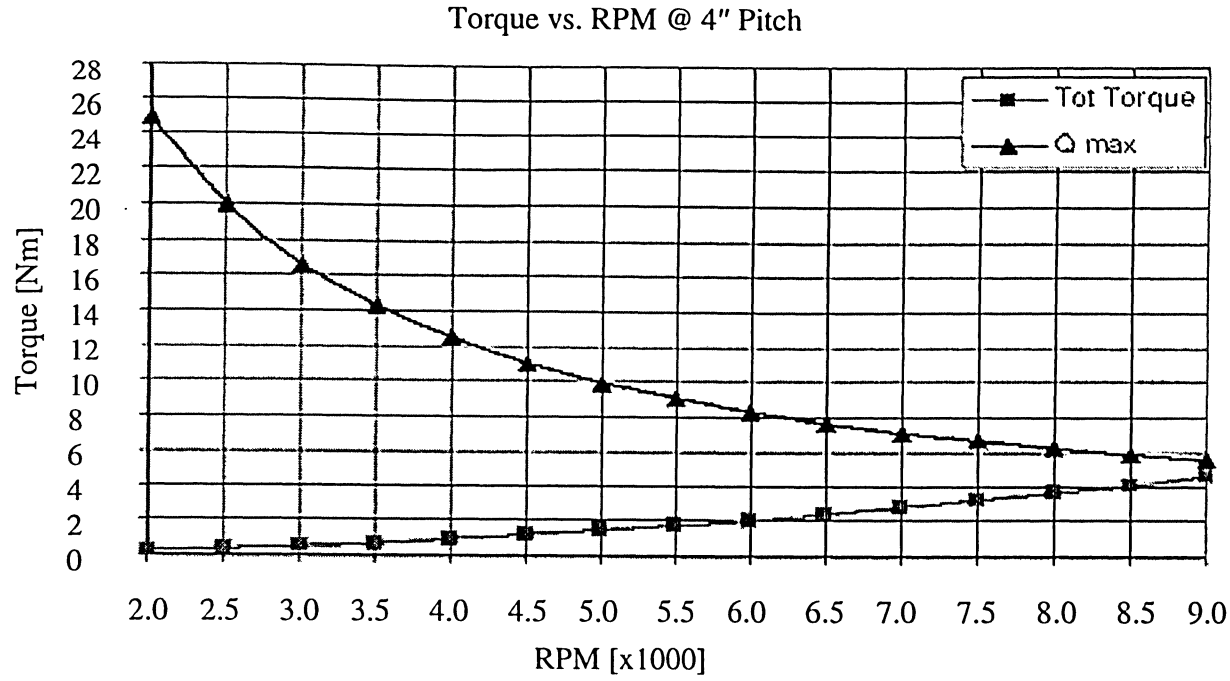


**Figure 3.25: Maximum torque vs. RPM at 4″ pitch.**

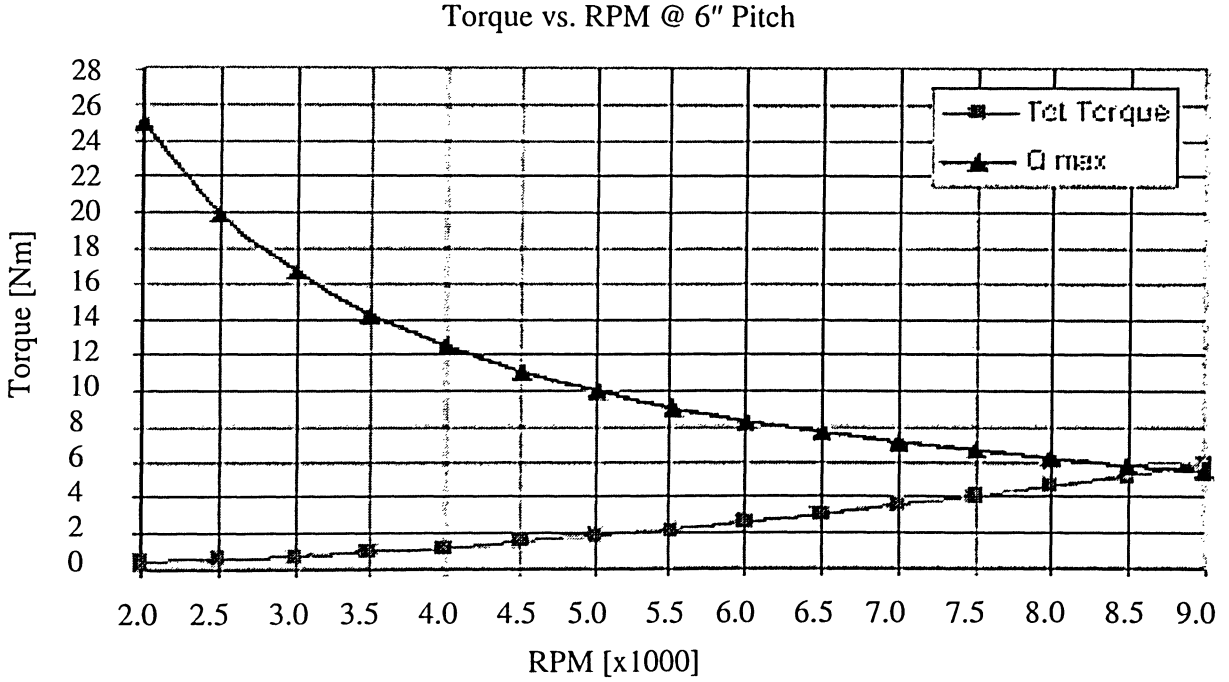


**Figure 3.26: Maximum torque vs. RPM at 6″ pitch.**

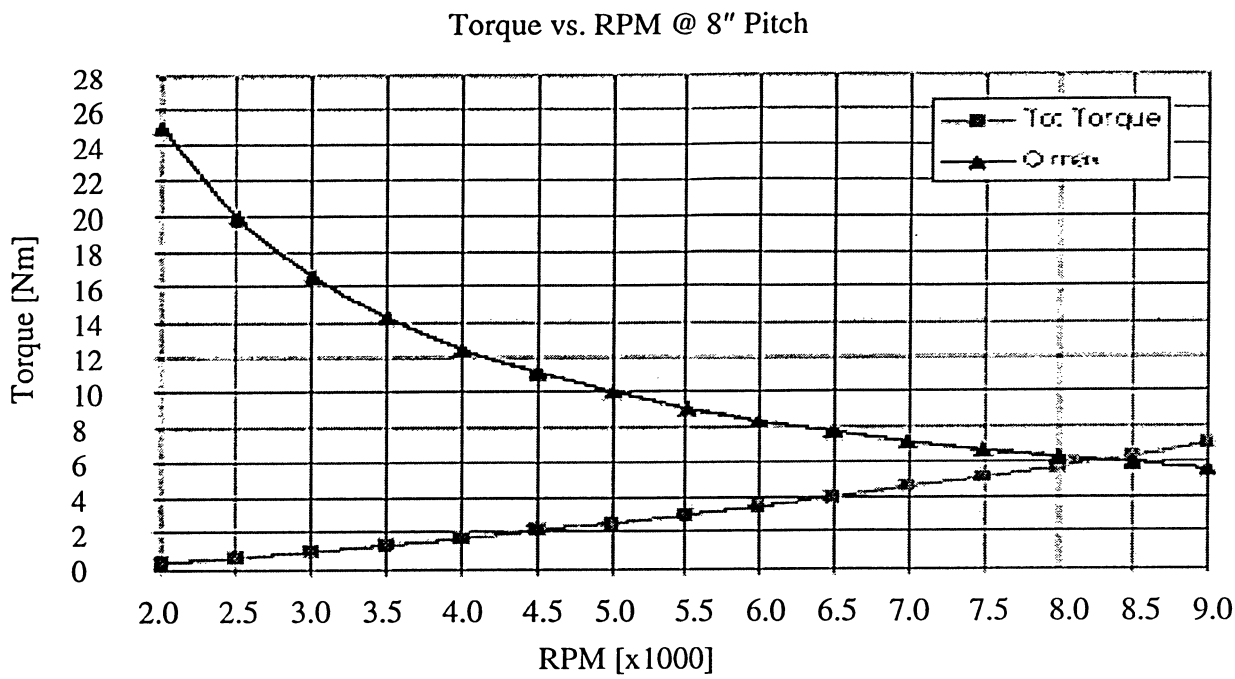


**Figure 3.27: Maximum torque vs. RPM at 8" pitch.**

The aerodynamic properties and characteristics of the SOLO propeller have been determined and the results generally agree with published data regarding general span wise lift and drag profiles as well as span wise torque and thrust profiles.

## *Section 3.13 System Dynamics*

The propeller-engine system is analyzed and simulated by using the Lagrange equation to obtain the equation of motion. In the previous Chapters, the cylinder pressure has been obtained as a function of crankshaft angular position; and the propeller load has been found as a function of operating speed. In this Chapter, the kinematical analysis and the kinetic energy of the engine mechanism are presented.

## *Section 3.14 Rigid Body Kinematics*

The Saito-450 engine was chosen to study for this research. To avoid disassembling the engine and risking forfeiting the warranty, a second engine was purchased for the sole purpose of disassembly to obtain the required physical mechanism properties and the functional relationships between each member of the internal mechanism.

For each component making up the engine mechanism, all linear dimensions were measured using a digital caliper, accurate to 0.001″ and each part was weighed with a digital balance, accurate to 0.1 gram. Through the course of the analysis, 3D computer models were created for the connecting rods and counterweight in order to precisely determine the centroid and moment of inertia values.

### *Section 3.14.1 Position Analysis*

Once all of the internal components were catalogued, an analytical rigid-body model of the engine was created. A scaled skeleton drawing of the internal component (crank shaft, crank pin, connecting rods, wrist pins and piston) positions including motion constraints is shown in Figure 3.28. The axis of rotation of the crankshaft shown in Figure 3.28 is the intersection point of the three cylinder axes. The direction of crankshaft rotation is taken to be positive when it is Counter Clock Wise (CCW) from the positive $x$-axis, which is also the centre line of cylinder #1.

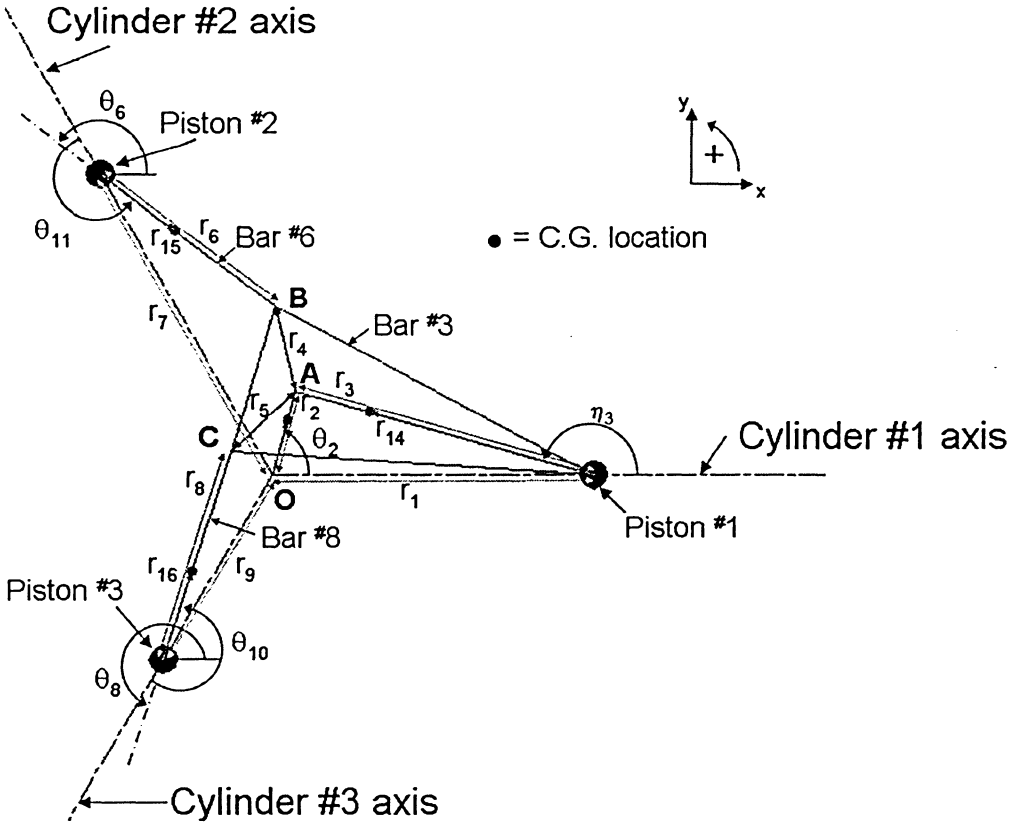


**Figure 3.28: 2-D sketch of the internal engine component positions.**

To begin the position analysis, cylinder #1 was taken to be the primary cylinder; and the other two cylinders were taken to be secondary cylinders. This distinction was helpful in providing a reference to begin the analysis and this particular arrangement of primary and secondary cylinders was chosen mainly because of the physical configuration of the engine mechanism. The crankpin, OA, is constrained to rotate about point O, each piston is constrained to linear motion alone the respective cylinder axes and all joints are full pin joints with the exception of the piston-cylinder joints, which are translating full slider joints [Norton, 2004].

To determine the position of piston #1, the following vector loop equation (3.33) is used.

$$\bar{R}_1 = \bar{R}_2 + \bar{R}_3 \tag{3.33}$$

where $\bar{R}_1$ is the vector from the crankshaft center to the piston pin; $\bar{R}_2$ is the vector from the crankshaft center to the crankpin; $\bar{R}_3$ is the vector from the crankpin to the piston pin.

With the help of complex number notations, Eq. (3.33) may be written as Eq. (3.34).

$$r_1 e^{i\theta_1} = r_2 e^{i\theta_2} + r_3 e^{i\theta_3} \tag{3.34}$$

where $r_k$ and $\theta_k$, k = 1, 2, 3, are lengths and phase angles of the three moving links of the primary cylinder, respectively.

Substituting the Euler equivalents into each term in the vector loop Eq. (3.34), separating into real and imaginary components allows for the solution of $\theta_3$ and $r_1$, one obtains Eq (3.35) and Eq. (3.36).

$$\theta_3 = \pi - \sin^{-1}\left(-\frac{r_2 \sin(\theta_2)}{r_3}\right) \tag{3.35}$$

$$r_1 = r_2 \cos(\theta_2) + r_3 \cos(\pi - \theta_3) \tag{3.36}$$

Eq. (3.35) provides the angle that the primary connecting rod makes with the positive *x*-axis determined as a function of the angular position of the crankshaft, $\theta_2$. Eq. (3.36) provides the linear position of the primary piston as a function of $\theta_2$, measured from the crankshaft axis of rotation.

Figure 3.29 shows one cycle of motion spanning a $2\pi$ rotation of the crankshaft ($\theta_2$) and the motion of the piston #1 is periodic, as predicted by Eq. (3.36). The stroke of piston #1 was found to be 0.0315 m.

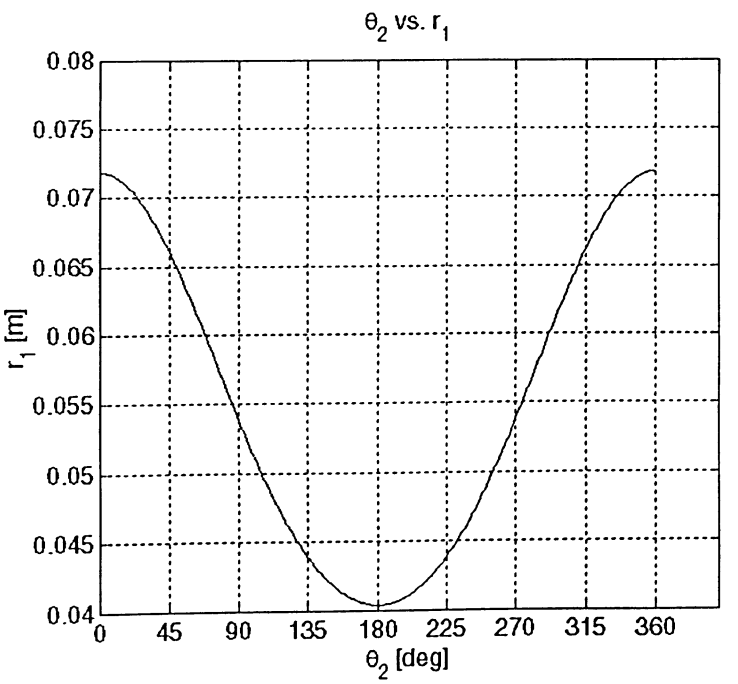


**Figure 3.29: Linear position of piston #1.**

The variation of $\theta_3$ with $\theta_2$ is shows in Figure 3.30 and this motion is also periodic in accordance with Eq. (3.35).

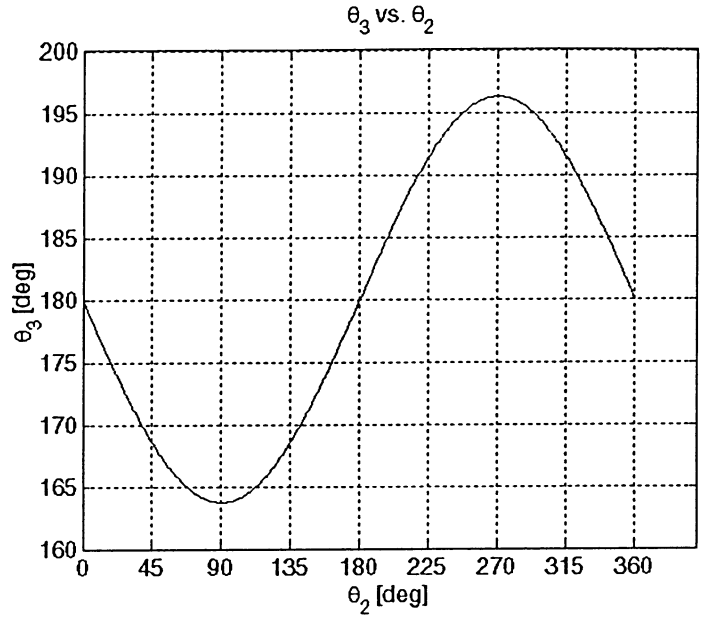


**Figure 3.30: Angular position of link #3.**

Eq. (3.37) shows the position of piston #2 found by the vector loop method.

$$\vec{R}_7 = \vec{R}_2 + \vec{R}_4 + \vec{R}_6 \tag{3.37}$$

Expressing the plane vectors with the complex polar notation, Eq. (3.37) may be written as Eq. (3.38).

$$r_7 = r_2 e^{i\theta_2} + r_4 e^{i\theta_4} + r_6 e^{i\theta_6} \tag{3.38}$$

Substituting the Euler equivalents into each term in the vector loop Eq. (3.38), separating into real and imaginary components allows for the solution of $\theta_6$ (Eq. (3.39)) and $r_7$, the linear position of piston #2 (Eq. (3.40)).

$$\theta_6 = \theta_7 + \sin^{-1}\left(\frac{-r_2\sin(\theta_2-\theta_7)-r_4\sin(\theta_4-\theta_7)}{r_6}\right) \tag{3.39}$$

$$r_7 = \frac{r_2\cos(\theta_2)+r_4\cos(\theta_4)+r_6\cos(\theta_6)}{\cos(\theta_7)} \tag{3.40}$$

where,

$$\theta_4 = \theta_3 - \frac{\pi}{3} \tag{3.41}$$

$$\theta_7 = \frac{2\pi}{3} \tag{3.42}$$

The angle that the connecting rod, link #6, makes with the positive $x$-axis ($\theta_6$) has been found as a function of $\theta_2$; however, this value is not as useful as an angular position referenced to the local right hand coordinate system oriented at the centre of rotation of the crankshaft with the positive local $x$-axis oriented in the direction of the cylinder #2.

The variable $\theta_{11}$ was the quantity used throughout the rest of the simulation rendering $\theta_6$ an intermediate variable used only in the determination of $\theta_{11}$. The relationship between these two angles is given in Eq. (3.43). Eq. (3.43) indicates that $\theta_{11}$ is merely a phase shifted $\theta_6$; however, this phase shifting is crucial in allowing a more intuitive and simpler mechanism model.

$$\theta_{11} = \theta_6 + \frac{\pi}{3} \tag{3.43}$$

Figure 3.31 and Figure 3.32 shows the plot of $r_7$ and $\theta_{11}$, respectively, as a function of $\theta_2$. Since $r_7$ is a function of $\theta_2$, $\theta_4$, $\theta_6$ and $\theta_7$, the resulting plot is expected to be periodic to preserve continuity, constrained by the cyclic nature of the reciprocating engine components.

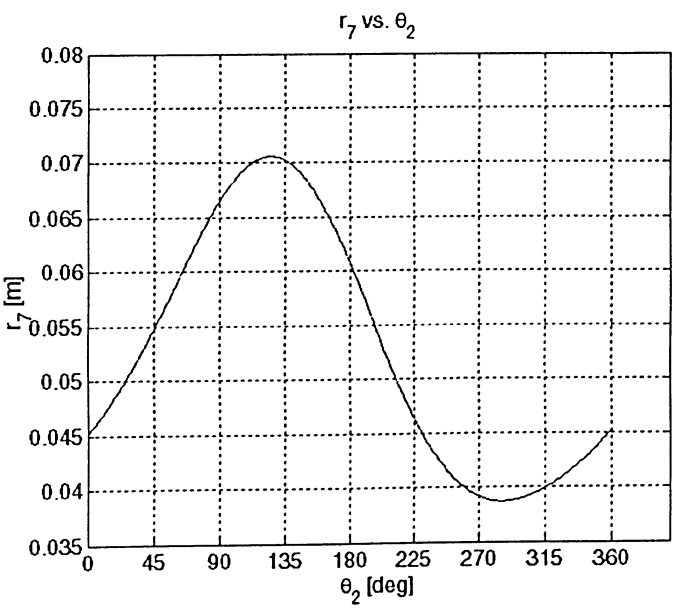


Figure 3.31: Linear position of piston #2.

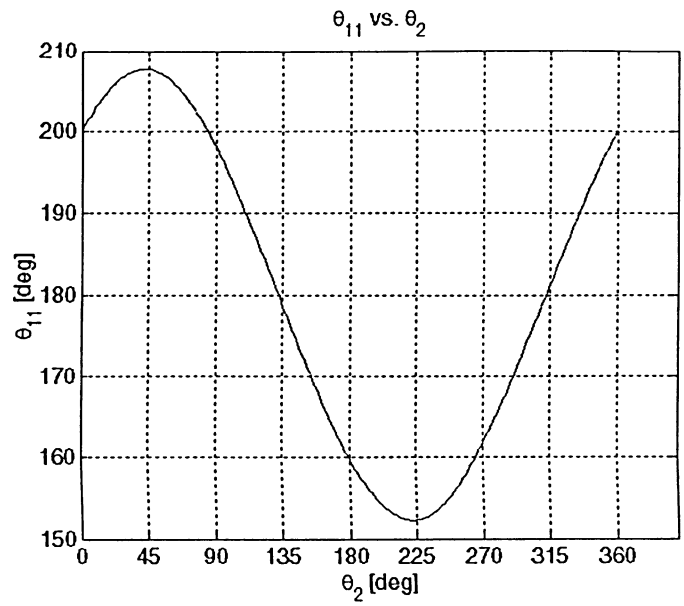


**Figure 3.32: Angular position of link #6**

The value $\theta_4$ is limited to the second quadrant, the $\theta_6$ value spans both the first and second quadrants and $\theta_{11}$ is limited to the second and third quadrants. The stroke of piston #2 was found to be 0.0319m. The 0.004m difference between the stroke of piston #1 and piston #2 can be accounted for by the presence of the fixed link #4.

Eq. (3.44) shows the position of piston #3 found by the vector loop method.

$$\vec{R}_9 = \vec{R}_2 + \vec{R}_5 + \vec{R}_8 \tag{3.44}$$

Eq. (3.45) substitutes the complex polar notation for the position vectors in Eq. (3.44).

$$r_9 e^{i\theta_9} = r_2 e^{i\theta_2} + r_5 e^{i\theta_5} + r_8 e^{i\theta_8} \tag{3.45}$$

Substituting the Euler equivalents into each term in the vector loop Eq. (3.45), separating into real and imaginary components allows for the solution of $\theta_8$ (Eq. (3.46)) and $r_9$, the linear position of piston #3 (Eq. (3.47)).

$$\theta_8 = \theta_9 + \sin^{-1}\left(\frac{-r_2\sin(\theta_2 - \theta_9 - r_5\sin(\theta_5 - \theta_9))}{r_8}\right) \tag{3.46}$$

$$r_9 = \frac{r_2\cos(\theta_2) + r_5\cos(\theta_5) + r_8\cos(\theta_8)}{\cos(\theta_9)} \tag{3.47}$$

where,

$$\theta_5 = \theta_3 + \frac{\pi}{3} \tag{3.48}$$

$$\theta_9 = \frac{4\pi}{3} \tag{3.49}$$

The angle that the connecting rod, link #8, makes with the positive $x$-axis ($\theta_8$) has been found as a function of $\theta_2$; however, this value is not as useful as an angular position reference to the local right hand coordinate system oriented at the centre of rotation of the crankshaft with the positive local $x$-axis oriented in the direction of the cylinder #3.

The variable $\theta_{10}$ was the quantity used throughout the rest of the simulation rendering $\theta_8$ an intermediate variable used only in the determination of $\theta_{10}$. The relationship between these two angles is shown in Eq. (3.50). Eq. (3.50) indicates that $\theta_{10}$ is merely a phase shifted $\theta_8$; however, this phase shifting allows a more intuitive and simpler mechanism model.

$$\theta_{10} = \theta_8 - \frac{\pi}{3} \tag{3.50}$$

When referring to Figure 3.33, the stroke of piston #3 was found to be 0.0319m, which is the same as for the stroke of cylinder #2.

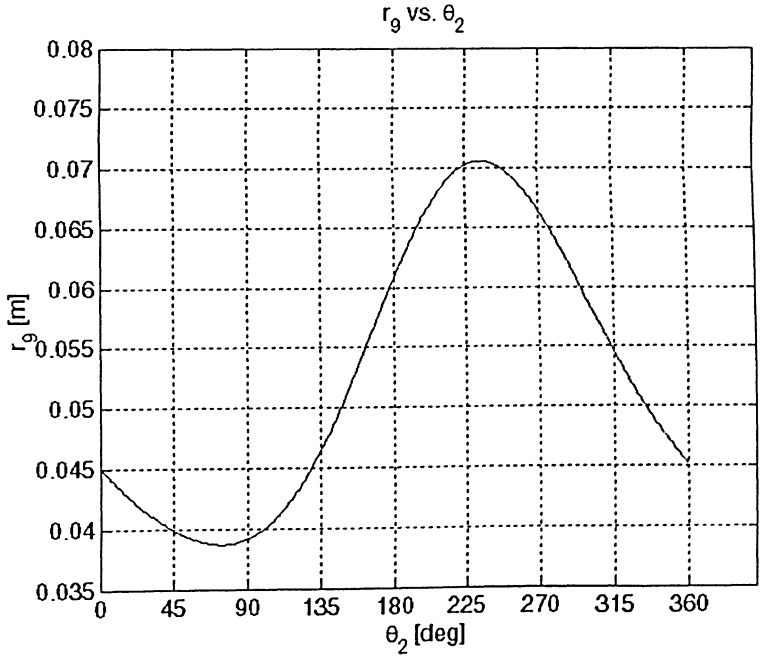


**Figure 3.33: Position of piston #3.**

When referring to Figure 3.34, $\theta_{10}$ is periodic and bound within the second and third quadrants.

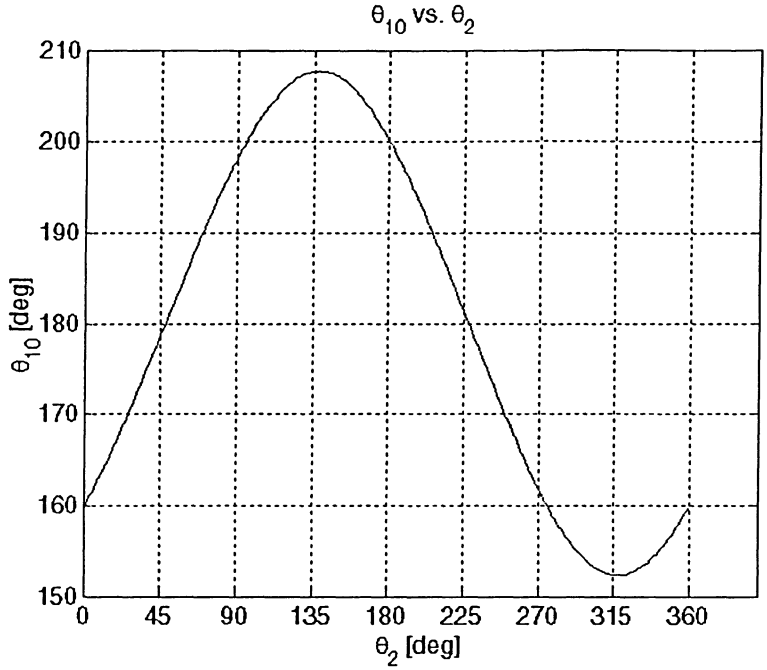


**Figure 3.34: Angular position of link #8.**

It is useful to superimpose similar plots to better visualize the interaction and relative scale of the various components under consideration. Figure 3.35 shows the superimposed piston position plots. Pistons #2 and #3 are approximately $+\pi/3$ and $-\pi/3$ rad out of phase with piston #1.

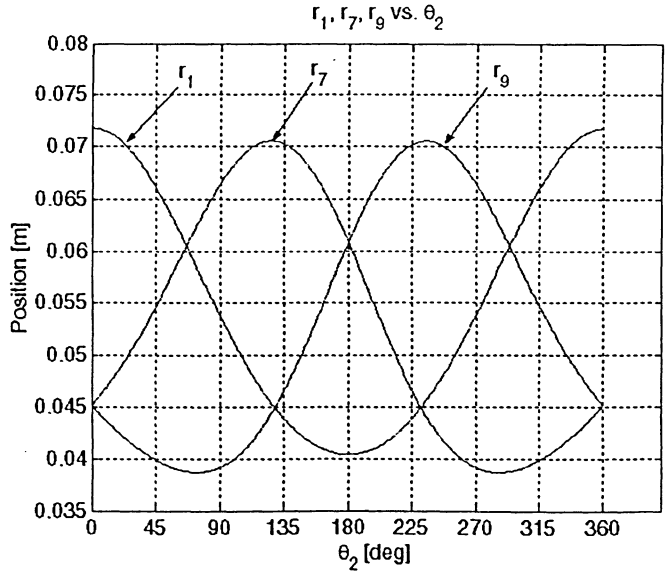

**Figure 3.35: Linear positions of the three pistons.**

Figure 3.36 shows the superimposed angular position plots of the three connecting rods, $\theta_3$, $\theta_{11}$, $\theta_{10}$. The difference in magnitudes of $\theta_3$ to $\theta_{11}$ and $\theta_{10}$ is a result of links #4 and #5 creating a 5-bar linkage to cylinders 3 and 2 respectively as compared with a conventional four-bar crank slider mechanism with zero offset, $\theta_3$.

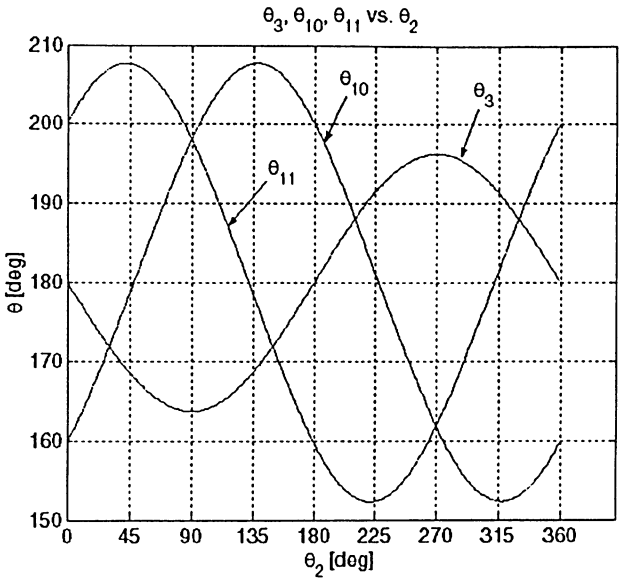


**Figure 3.36: Angular positions of the three connecting rods.**

The position analysis is complete and the next step in developing the kinematic model of the engine mechanism was to find the velocities of all joints and member center of gravities.

## *Section 3.14.2 Velocity Analysis*

To proceed with the velocity analysis a free body diagram was constructed of the engine mechanism with the desired velocity vectors appropriately labeled. Figure 3.37 is the free body diagram constructed for the velocity analysis. The normalized linear velocities of the three pistons, $v_1$, $v_7$, $v_9$ for pistons #1, #2, and #3, respectively, were found by taking a three point central numerical derivative of each position vector.

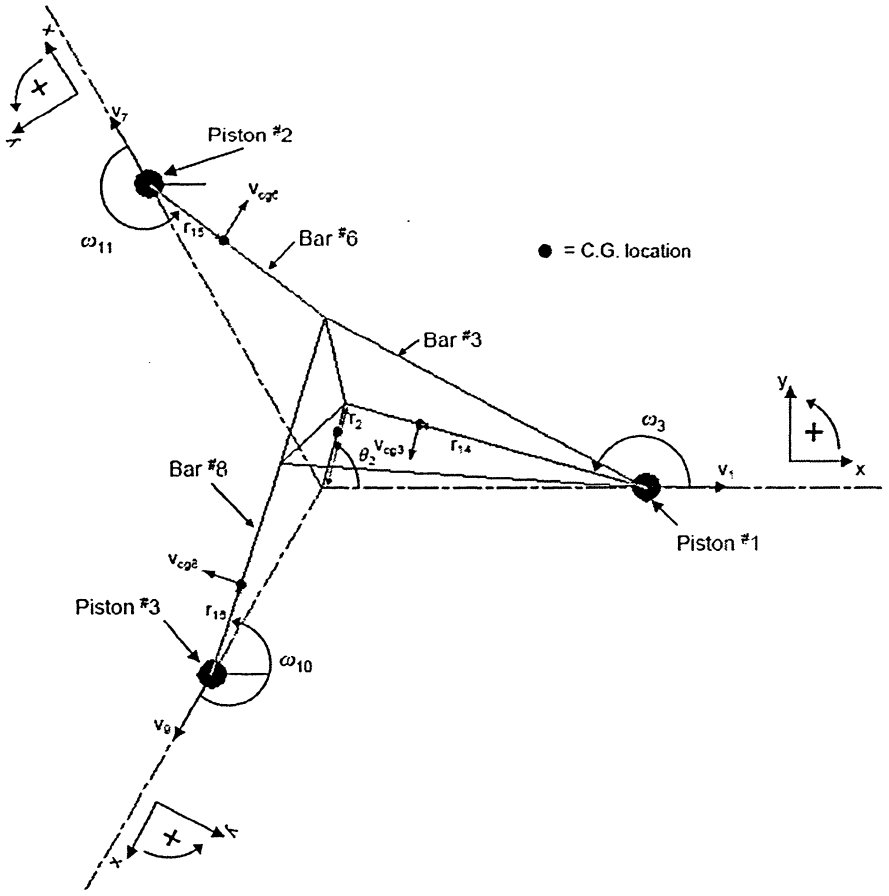


**Figure 3.37: Internal engine component velocity free body diagram.**

Figure 3.38 shows the linear velocities of pistons #1, #2 and #3 vs. the crankshaft angular position. Each of the velocity plots is periodic. Figure 3.38 shows that the velocities of piston #2 and #3 appear to be the same shape, only the mirror image of each other. This is a reasonable conclusion to reach when considering the effect of the firing sequence and the effect of links #4 and #5 included in the mechanism sub-system for those pistons. Figure 3.38 also shows that the velocities of all pistons are relatively closely matched to each other, which is beneficial from an overall engine balance point of view.

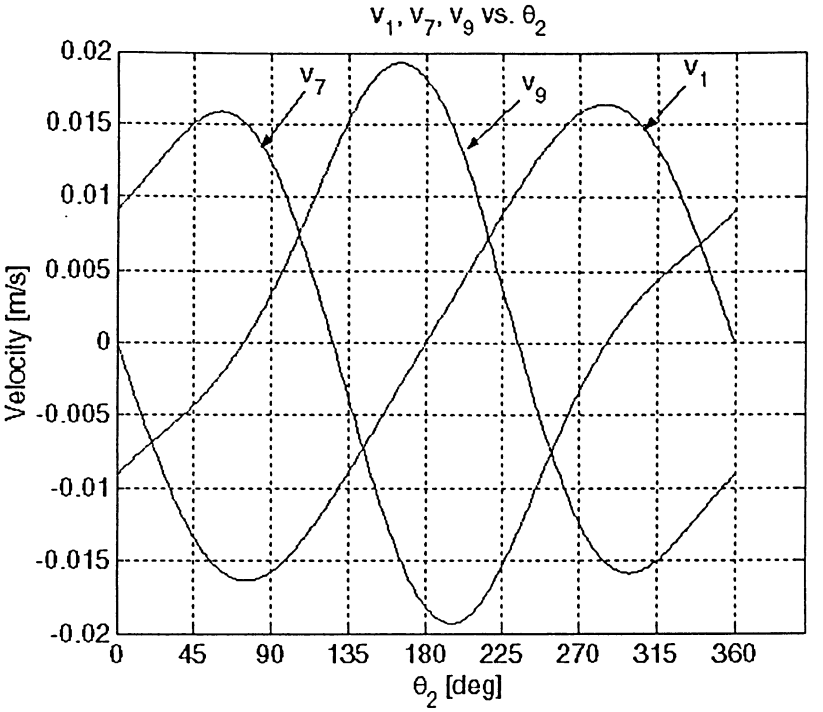


**Figure 3.38: Velocity vs. $\theta_2$ of the three pistons.**

The linear velocity of each piston was found as a function of crankshaft angular position through a period of $2\pi$, the velocity of the mechanism component mass centers was also needed through the same period of $2\pi$. The velocity of the mass center of each connecting rod was found using the relative velocity method with the mass center of each connecting rod is located along the centerline of the part.

The velocity of the master connecting rod (link #3) was found by Eq. (3.51).

$$\vec{v}_{cg_3} = \vec{v}_1 + \vec{v}_{cg_3/Piston_1} \tag{3.51}$$

Expanding the relative velocity term of Eq. (3.51) gives Eq. (3.52).

$$\vec{v}_{cg_3} = v_1 + r_{14}\omega_3 e^{i\left(\theta_3+\frac{\pi}{2}\right)} \tag{3.52}$$

Substituting the Euler equivalents into Eq. (3.52) and separating into real and imaginary components result in Eq. (3.53) and Eq. (3.54).

$$\mathrm{Re}: v_1 + r_{14}\omega_3 \cos\left(\theta_3+\frac{\pi}{2}\right) \tag{3.53}$$

$$\mathrm{Im}: r_{14}\omega_3 \sin\left(\theta_3 + \frac{\pi}{2}\right) \tag{3.54}$$

The magnitude of velocity of the master connecting rod mass center is found by using the results of Eq. (3.53) and Eq. (3.54) in Eq. (3.55).

$$v_{cg_3} = \sqrt{\mathrm{Re}\left(v_{cg_3}\right)^2 + \mathrm{Im}\left(v_{cg_3}\right)^2} \tag{3.55}$$

where,

$$\omega_3 = \omega_2\left(\frac{\partial\theta_3}{\partial\theta_2}\right) = \dot{\theta}_2\left(\frac{\partial\theta_3}{\partial\theta_2}\right) \tag{3.56}$$

$$v_1 = \frac{\partial r_1}{\partial t} = \left(\frac{\partial r_1}{\partial\theta_2}\right)\left(\frac{\partial\theta_2}{\partial t}\right) = \dot{\theta}_2\left(\frac{\partial r_1}{\partial\theta_2}\right) \tag{3.57}$$

$$r_{14} = r_3 - r_{10} \tag{3.58}$$

The velocity of the secondary connecting rod (link #6) connected to piston #2 was found by Eq. (3.59).

$$\vec{v}_{cg_6} = \vec{v}_7 + \vec{v}_{cg_6/Piston_3} \tag{3.59}$$

Expanding the relative velocity term of Eq. (3.59) gives Eq. (3.60).

$$\vec{v}_{cg_6} = v_7 + r_{15}\omega_6 e^{i\left(\theta_6 + \frac{\pi}{3} + \frac{\pi}{2}\right)} \tag{3.60}$$

Substituting the Euler equivalents into Eq. (3.60) and separating into real and imaginary components results in Eq. (3.61) and Eq. (3.62).

$$\mathrm{Re}: v_7 + r_{15}\omega_6 \cos\left(\theta_{11} + \frac{\pi}{2}\right) \tag{3.61}$$

$$\mathrm{Im}: r_{15}\omega_6 \sin\left(\theta_{11} + \frac{\pi}{2}\right) \tag{3.62}$$

The magnitude of velocity of link #6 connecting rod mass center is found by using the results of Eq. (3.61) and Eq. (3.62) in Eq. (3.63).

$$v_{cg_6} = \sqrt{\mathrm{Re}\left(v_{cg_6}\right)^2 + \mathrm{Im}\left(v_{cg_6}\right)^2} \tag{3.63}$$

where,

$$\omega_6 = \dot{\theta}_2\left(\frac{\partial\theta_6}{\partial\theta_2}\right) \tag{3.64}$$

$$\theta_{11} = \theta_6 + \frac{\pi}{3} \tag{3.65}$$

$$v_7 = \dot{\theta}_2\left(\frac{\partial r_7}{\partial\theta_2}\right) \tag{3.66}$$

The velocity of the secondary connecting rod (link #8) connected to piston #3 was found by Eq. (3.67).

$$\vec{v}_{cg_8} = \vec{v}_9 + \vec{v}_{cg_9/Piston_2} \tag{3.67}$$

Expanding the relative velocity term of Eq. (3.67) gives Eq. (3.68).

$$\vec{v}_{cg_8} = v_9 + r_{16}\omega_8 e^{i\left(\theta_8+\frac{\pi}{3}+\frac{\pi}{2}\right)} \tag{3.68}$$

Substituting the Euler equivalents into Eq. (3.68) and separating into real and imaginary components results in Eq. (3.69) and Eq. (3.70).

$$\mathrm{Re}: v_9 + r_{16}\omega_8\cos\left(\theta_{10}+\frac{\pi}{2}\right) \tag{3.69}$$

$$\mathrm{Im}: r_{16}\omega_8\sin\left(\theta_{10}+\frac{\pi}{2}\right) \tag{3.70}$$

The magnitude of velocity of link #8 connecting rod mass center is found by using the results of Eq. (3.69) and Eq. (3.70) in Eq. (3.71).

$$v_{cg_8} = \sqrt{\mathrm{Re}\left(v_{cg_8}\right)^2 + \mathrm{Im}\left(v_{cg_8}\right)^2} \tag{3.71}$$

where,

$$\omega_8 = \dot{\theta}_2\left(\frac{\partial\theta_8}{\partial\theta_2}\right) \tag{3.72}$$

$$\theta_{10} = \theta_8 + \frac{\pi}{3} \tag{3.73}$$

$$v_9 = \dot{\theta}_2 \left( \frac{\partial r_9}{\partial \theta_2} \right) \tag{3.74}$$

The equations describing the velocities of the mass centers of each member of the engine mechanism have been derived; Figure 3.39 shows the velocities of the connecting rod mass center against the crankshaft angular position.

Figure 3.39 shows that for link #3 there are two velocity minima corresponding to crankshaft positions of 0° and 180°. These two crankshaft positions corresponding to the TDC, 0° and the BDC, 180°. With the four-bar sub-mechanism oriented in these two positions a velocity minimum is expected since positions correspond to a change in direction of the piston, with the connecting rod becoming collinear with the global horizontal axis. When the piston changes direction the velocity reduces to zero before moving in the opposite direction.

Figure 3.39 shows the velocity of the mass centers of link #6 and #8, which are connected to pistons #2, and #3, respectively. The local minima of link #6, located at 123° and 284° correspond to the TDC and the BDC of piston #2, respectively. The local minima of link #8, located at 77° and 237° correspond to the BDC the TDC of piston #3, respectively.

The angular velocities of the three connecting rods ($\omega_3$, $\omega_6$, $\omega_8$) were found by taking the central 3-point numerical derivative of the angular positions of the respective connecting rod arrays. Figure 3.40 shows the angular velocities as a function of crankshaft angular position. The magnitudes of the secondary connecting rods angular velocities are greater than that of the master connecting rod. The angular velocity is periodic and twice passes through zero during a period of $2\pi$. At each zero, the crankshaft is at an angular position of 90° or 270°, which corresponds to the maximum linear velocity of the piston #1.

Figure 3.40 shows that link #6 is the mirror image in the y-axis of link #8, due to link #5. Links #6 and #8 have two zeros corresponding to the inflection points in the position plot of piston #3.

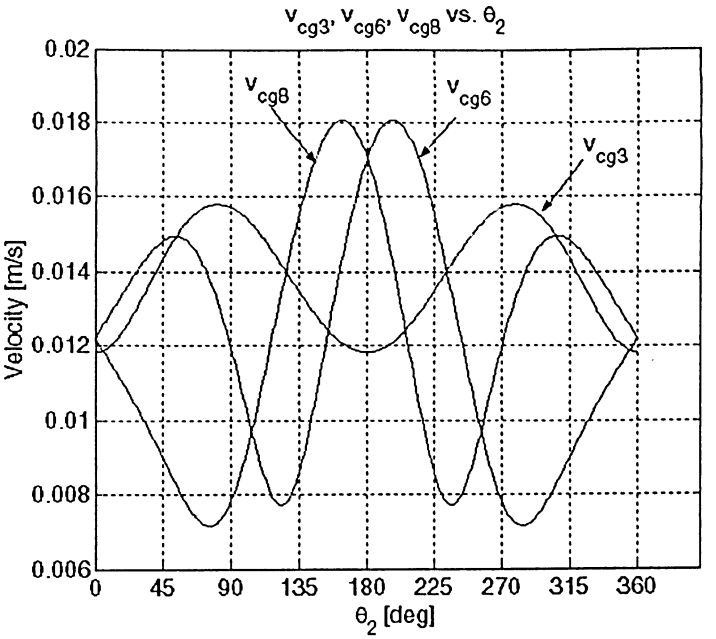


**Figure 3.39: Velocity vs. $\theta_2$ for the primary and secondary connecting rod mass centers.**

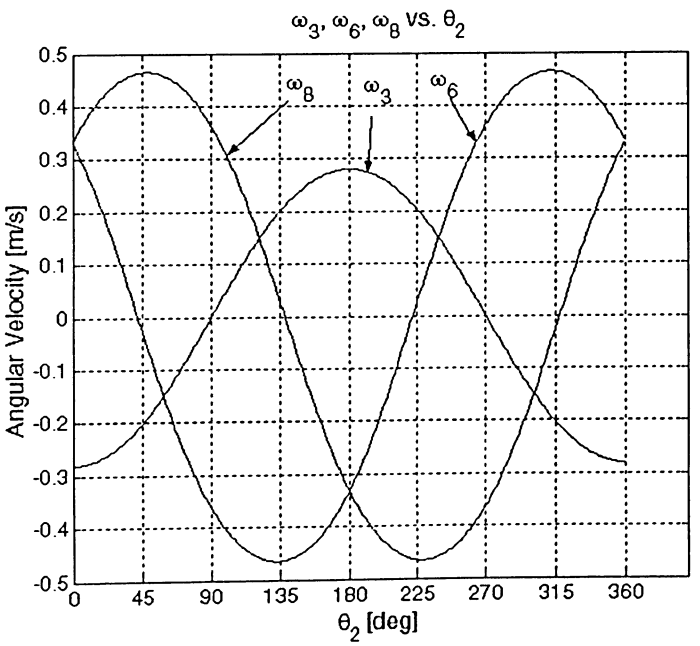


**Figure 3.40: $\omega$ vs. $\theta_2$ for the primary and secondary connecting rod mass centers.**

The rigid body kinematic model of the engine components has been created and both the position and velocity data generated are essential to the subsequent analyses.

## *Section 3.15 Numerical Analysis*

The engine components velocities were found by using a three-point central differentiation scheme shown in Eq. (3.75).

$$f'(x_0)=\frac{1}{2h}[f(x_0+h)-f(x_0-h)]-\frac{h^2}{6}f^{(3)}(\varepsilon_1) \tag{3.75}$$

For an arbitrary array, the central differentiation scheme can be hampered by boundary conditions, that is, how to handle the first point and the last point of the array since the first point would require knowledge of the (-1) point, and the (i + 1) point, which might or might not exist.

To calculate the component velocities, the position array was wrapped such that the (-1) point became the last point of the position array and at the (i+1) point became the first position data point since the motion of the components was known to be periodic in $2\pi$.

The position array was a function of crankshaft angular position ($\theta_2$) so the increment ($h$) in Eq. (3.75) is an angular value, resulting in a normalized velocity, which can be described by Eq. (3.76).

$$v_1(\theta_2)=\frac{\partial r_1}{\partial \theta_2} \tag{3.76}$$

Velocity by definition is the time rate of change of position but for application to the propeller-engine system, this quantity cannot be directly calculated. By expanding the time rate of change of position with respect to the crankshaft angular displacement, Eq. (3.77) can be written.

$$v_1(t)=\frac{\partial r_1}{\partial \theta_2}\frac{d\theta_2}{dt} \tag{3.77}$$

The three point central numerical differentiation scheme was successfully employed in finding the linear and angular velocities of the internal engine components, as well as finding the derivative of the kinetic energy with respect to the angular crank angular position.

## *Section 3.16 Fourier Series Representations*

Discrete values of periodic quantities such as gas pressure, gas torque, kinetic energy and the derivative of kinetic energy with respect to crankshaft position may be determined for a

given crank position in one cycle of motion. However, the Euler solver in Matlab requires analytical functions be provided in order to obtain a solution to the nonlinear ordinary differential equation. Since the kinetic energy and derivative of kinetic energy taken with respect to the position of the crankshaft are $2\pi$-periodic while the gas pressures and torques are $4\pi$-periodic, they can be represented analytically by Fourier series. If $F(t)$ is a periodic function, it can be expressed using a Fourier series as Eq. (3.78).

$$F(t)=\frac{a_o}{2}+\sum_{i=1}^{N} a_i \cos(i\theta_2)+b_i \sin(i\theta_2) \tag{3.78}$$

where $N$ is the highest order of harmonics retained in an analysis.

To obtain the normalized velocity of any periodic function that describes the position of a member of the internal engine mechanism, the first derivative of Eq. (3.78) is performed with respect to $\theta_2$, shown in Eq. (3.79).

$$\frac{\partial F(t)}{\partial \theta_2}=\sum_{i=1}^{N}\left[-\frac{ia_i}{2}\sin\left(\frac{i\theta}{2}\right)+\frac{ib_i}{2}\cos\left(\frac{i\theta}{2}\right)\right] \tag{3.79}$$

The procedure employed within the SIMPEL simulation was to resample the original array of length 720 data points (kinematical analysis performed every one degree of crank position) to a length of 1024 points and then a 1024 point Fast Fourier Transform (FFT) was performed on the array to obtain the spectral coefficients. The use of 1024 sampling points in a FFT produces a credible order of harmonics up to 128, which is considered sufficient in a dynamical analysis of an engine-propeller system.

## *Section 3.17 Kinetic Energy*

This Section deals with the formulation of kinetic energy of each moving body in the engine-propeller system. For each moving member whose mass is deemed significant, the kinetic energy is first determined. The kinetic energy is subsequently normalized with respect to the crank angular velocity squared. In the rigid body dynamics, the crank angular position is chosen as the generalized coordinate of the one DOF system. In the following analysis of the internal combustion engine mechanism, the normalized kinetic energy of each member may be calculated by Eq. (3.80)

$$T=\tilde{T}\dot{\theta}_2^2 \tag{3.80}$$

For the case of rectilinear motion the $\tilde{T}$ variable from Eq. (3.80) can be expended as Eq. (3.81) by knowing the linear and angular velocity of the center of gravity of each member.

$$\tilde{T} = \left[ \frac{1}{2} m \left( \frac{\partial r}{\partial \theta_2} \right)^2 \right] \tag{3.81}$$

where $m$ is the mass; $r$ is the position coordinate.

Should the motion of the member be purely rotational as is the case of the counterweight, cam and propeller, $\tilde{T}$ takes the following form

$$\tilde{T}_i = \frac{1}{2} J_i \tag{3.82}$$

where $J_i$ is the moment of inertia of the $i^{th}$ member exhibiting pure rotational motion.

The motion of each connecting rod is general plane motion; therefore, $\tilde{T}$ takes the form of Eq. (3.83) for the $i^{th}$ member exhibiting this combined motion.

$$\tilde{T}_i = \frac{1}{2} J_i \left( \frac{\partial \theta_i}{\partial \theta_2} \right)^2 + \frac{1}{2} m_i \left( \frac{\partial r_{cg_i}}{\partial \theta_2} \right)^2 \tag{3.83}$$

When conducting the kinematic analysis shown in Section 3.14, the velocity of a mass center was found in complex form; the velocity magnitude may be determined using the real and imaginary parts shown by Eq. (3.84).

$$\tilde{T}_i = \frac{1}{2} J_i \left( \frac{\partial \theta_i}{\partial \theta_2} \right)^2 + \frac{1}{2} m_i \left[ \left( \frac{\partial r_{cg_i}}{\partial \theta_2} \right)^2_{real} + \left( \frac{\partial r_{cg_i}}{\partial \theta_2} \right)^2_{imag} \right] \tag{3.84}$$

The kinetic energy of the mechanical system under consideration is $2\pi$-periodic and the thermodynamic cycle is $4\pi$-periodic; therefore, extending the kinetic energy of the system to a period of $4\pi$ such that all quantities are of the same length, entails simply including two periods of kinetic energy equaling $4\pi$.

To determine the total kinetic energy of the mechanism, the kinetic energy of each component is first found over a period of $2\pi$ and then each kinetic energy term is summed for each discrete crankshaft angle.

## *Section 3.17.1 Kinetic Energy without Accessories*

The engine simulation was conducted in two phases, the first phase excluding the kinetic and potential energies associated with the cam mechanisms and the second phase complimented the first phase by including the effect of the accessory system.

The normalized kinetic energy of the three pistons (Figure 3.41), connecting rods (Figure 3.42), and crank arm, counterweight, torque plate, bearing race, crank pin and prop nut are shown in Figure 3.43, as functions of the crankshaft angular position.

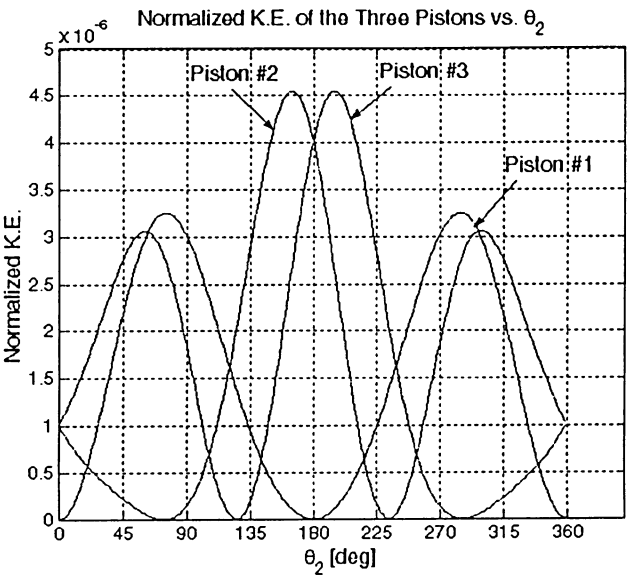


**Figure 3.41: Normalized kinetic energy of the three pistons vs $\theta_2$.**

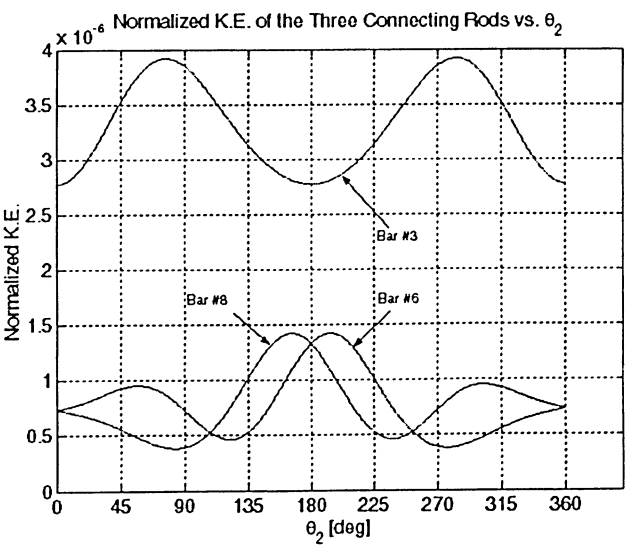


**Figure 3.42: Normalized kinetic energy of the three connecting rods vs. $\theta_2$.**

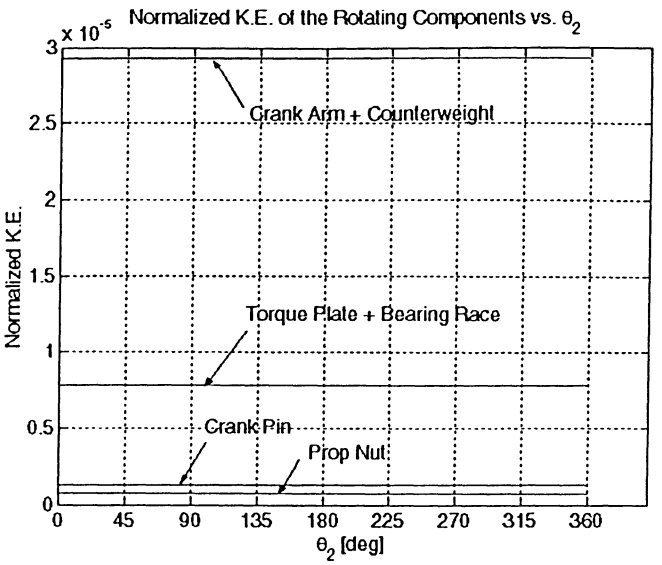


**Figure 3.43: Normalized kinetic energy of the rotating components vs. $\theta_2$.**

The normalized kinetic energy was calculated over a period of $2\pi$ for all the components of the 8-bar internal engine mechanism. The next step was to sum each of the plots shown in Figure 3.41, Figure 3.42, and Figure 3.43 at each value of crankshaft angular position ($\theta_2$) to obtain the total kinetic energy of the components common to both phases of the system analysis. Figure 3.44 shows the total kinetic energy of the common internal engine components over a period of $2\pi$.

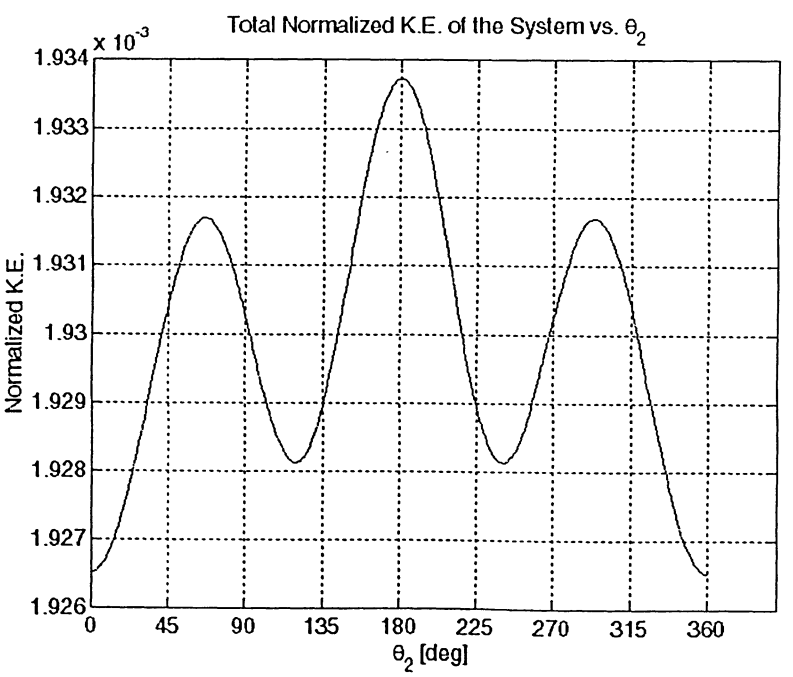


**Figure 3.44: Total normalized kinetic energy vs. $\theta_2$.**

## *Section 3.17.2 Derivative of Kinetic Energy without Accessories*

With the total kinetic energy completely defined over a period of $2\pi$, the first derivative with respect to $\theta_2$ can be found by using a three-point forward numerical method. Figure 3.45 shows the first derivative of the total kinetic energy with respect to $\theta_2$ thereby completely defining the second term on the right hand side of Lagrange's equation, Eq. (3.89). Figure 3.45 shows that there is position and slope continuity at the beginning and the end of the $2\pi$ period. Now the second term on the left hand side of Lagrange's equation (Eq. (3.89)) has been completely defined in discrete form.

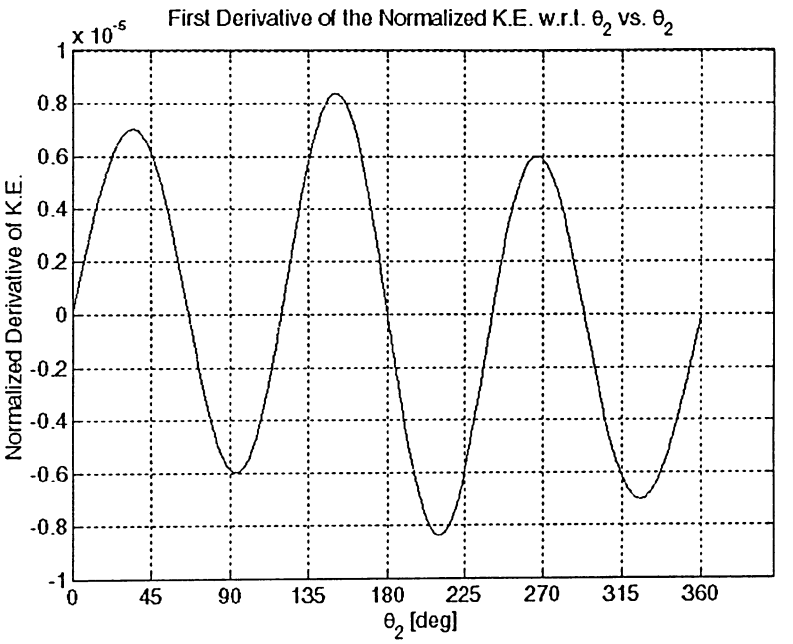


**Figure 3.45: Derivative of the total kinetic energy vs. $\theta_2$.**

To solve Lagrange's equation neglecting the accessory drive system requires $\tilde{T}$ and $\frac{\partial \tilde{T}}{\partial \theta_2}$ in functional form over a period of $4\pi$. Converting the $4\pi$-period array from discrete form into functional form was achieved through the use of a ten-term Fourier series.

## *Section 3.17.3 Kinetic Energy with Accessories*

The second phase of the analysis includes all kinetic energy terms found during the first phase, and takes into account the accessory drive system by finding the normalized kinetic energy of each cam assembly, tappet, push rod, rocker arm and valve.

A summary of the accessory component mass and moment of inertia used to generate the kinetic energy of the accessory components can be found in Table 3.5.

**Table 3.5: Mass and moment of inertia for each member of the accessory drive**

| Part Name | Mass [kg] | Moment of Inertia [kg/m$^2$] |
|---|---|---|
| Intake Tappet | 0.00268 | - |
| Intake Push Rod | 0.00150 | - |
| Exhaust Rocker Arm | - | $7.804 \times 10^{-7}$ |
| Intake Valve | 0.00363 | - |
| Intake Cam | - | $9.171 \times 10^{-9}$ |
| Exhaust Cam | - | $6.9286 \times 10^{-9}$ |
| Cam Gear | - | $1.5084 \times 10^{-6}$ |
| Cam Assembly | - | $1.5245 \times 10^{-6}$ |

The kinetic energy of the spring was neglected since the mass of the spring is extremely small and the kinetic energy of spring elements is typically neglected in dynamic analysis; however, the potential energy contributed by the spring will be considered.

## *Section 3.17.4 Kinetic Energy of the Intake and Exhaust Cam Assemblies*

The geometry of the cam gear and cams is such that each cam gear simultaneously drives one intake cam and one exhaust cam. These three pieces are fixed together into one unit such that they rotate with one speed. When calculating the kinetic energy of the cams, the cam unit was treated as one rotating body described by Eq. (3.85).

$$\tilde{T} = \frac{1}{8}\left(J_{\text{int}\,cam} + J_{exh.cam} + J_{cam.gear}\right) \tag{3.85}$$

The kinetic energy of the cam gear assemblies is a constant value of $1.9056 \times 10^{-7}$ kgm$^3$ since the motion of the cam assembly is purely rotational about a fixed axis.

With the kinetic energy of the intake and exhaust cam assemblies determined the next member of the accessory drive to be considered were the intake and exhaust tappets.

## *Section 3.17.5 Kinetic Energy of the Intake and Exhaust Tappets*

The intake and exhaust tappets are acted upon by the intake and exhaust cams, respectively, with rectilinear motion.

The normalized kinetic energy of the intake and exhaust tappets can be seen in Figure 3.46, and Figure 3.47, respectively. The duplicated labels in Figure 3.46, and Figure 3.47 are for clarity and each label refers to the cylinder on which the cam is acting. The two peaks corresponding to the intake tappet of each cylinder are a result of the tappet velocity increasing as the tappet is displaced from the reference position to the maximum deflection and once at the maximum deflection, the valley between the two peaks of each plot is reached. The second peak corresponds to the velocity of the tappet as it returns to the reference undeflected position. The two peaks are of equal magnitude due to the symmetry between the rise and fall faces of the intake cam.

The two peaks corresponding to the exhaust tappet from Figure 3.47 per cylinder are a result of the tappet velocity increasing as the tappet is being displaced from the reference position to the maximum deflection and once at the maximum deflection, the valley between the two peaks of each plot is reached. The second peak corresponds to the velocity of the tappet as it returns to the reference undeflected position. The two peaks are not of equal magnitude due to the asymmetry between the rise and fall faces of the exhaust cam.

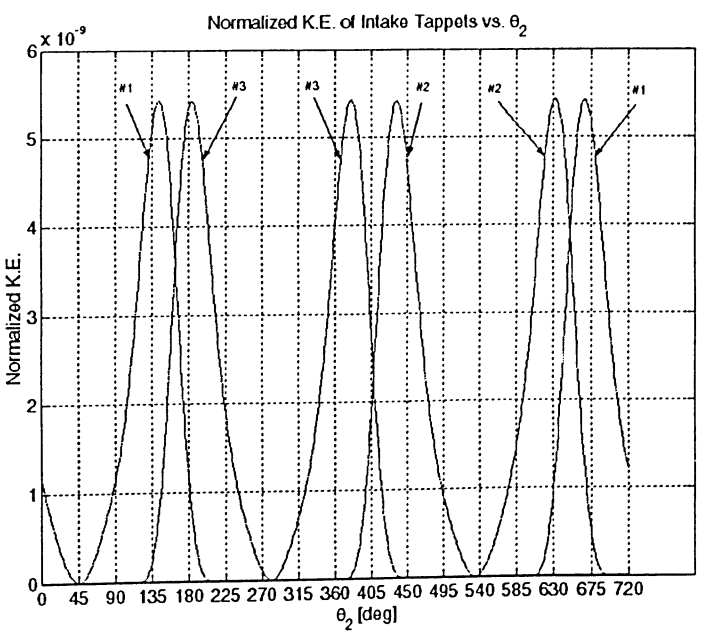


**Figure 3.46: Normalized kinetic energy of the intake tappets vs. $\theta_2$.**

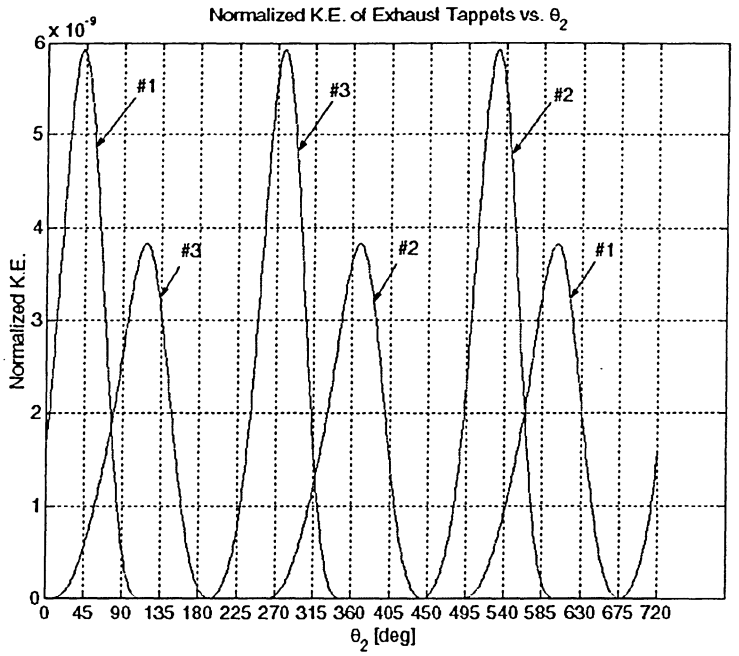


**Figure 3.47: Normalized kinetic energy of the exhaust tappets vs. $\theta_2$.**

The angular velocity of the intake and exhaust tappets was determined in discrete form and converted to functional form through the use of a ten-term Fourier approximation. The next members making up the accessory system to be considered were the intake and exhaust push rods.

## *Section 3.17.6 Kinetic Energy of the Intake and Exhaust Push Rods*

The next members of the accessory drive system to be considered were the intake and exhaust push rods. The kinetic energy of each pushrod can be found by Eq. (3.81).

The normalized kinetic energy of the intake and exhaust pushrods is shown in Figure 3.48, and Figure 3.49, respectively, with the horizontal axis being the angular position of the crankshaft in degrees. The return of the intake kinetic energy pushrod plots to zero at values of 46°, 534°, and 282° to zero for cylinders #1, #2, and #3, respectively, indicate the pushrods are at their most deflected position and has zero velocity due to the reversal in direction experienced at this maximum deflection. There is no variation between peak amplitudes of the rise and fall portions of the intake pushrod motion due to the symmetry between the rise and fall faces of the intake cam.

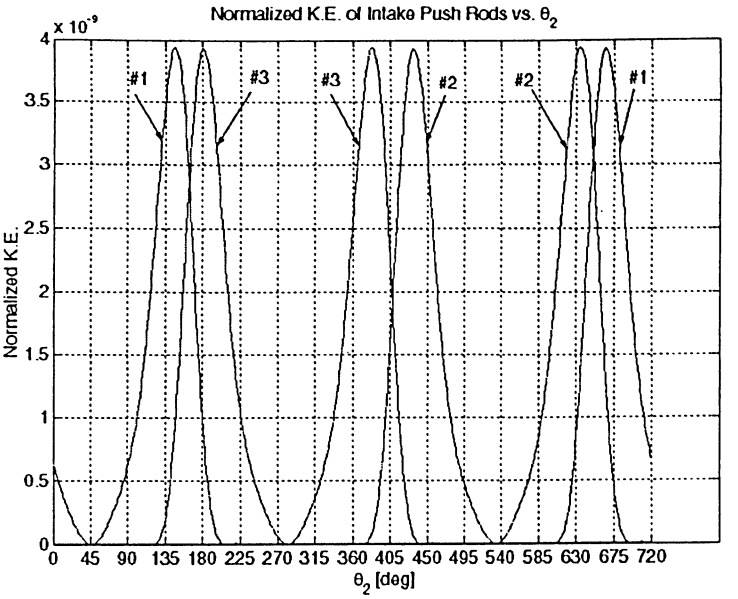


**Figure 3.48: The kinetic energy of the intake pushrods.**

The kinetic energy of the exhaust pushrods is shown in Figure 3.49. The return of the exhaust kinetic energy pushrod plots to zero at values of 677°, 445°, and 193° for cylinders #1, #2, and #3, respectively, indicate the pushrods are at their most deflected position and has zero velocity due to the reversal in direction experienced at maximum deflection. In this case the variation in peak amplitude is a result of the asymmetry of the rise and fall faces exhaust cam.

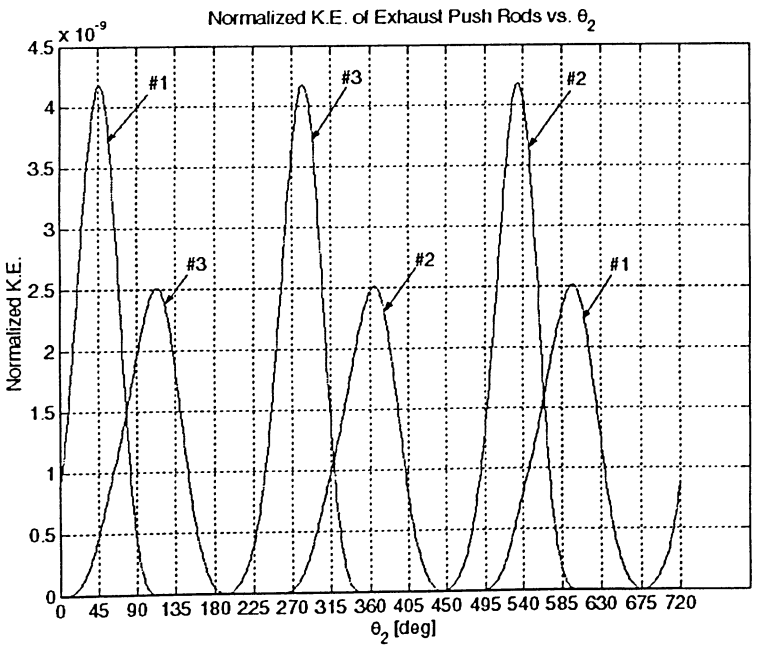


**Figure 3.49: The kinetic energy of the exhaust pushrods.**

The angular velocity of the push rods was determined in discrete form and represented in functional form through the use of a ten-term Fourier approximation. The next members making up the accessory system to be considered were the rocker arms.

## *Section 3.17.7 Kinetic Energy of the Rocker Arms*

The rocker arms are acted upon by the push rods and the rocker arms produce purely rotational motion about a fulcrum fixed in space. The kinetic energy of the rocker arms was found by using Eq. (3.86).

$$\tilde{T}_{rocker.arm} = \frac{1}{2} J_{rocker.arm} \left( \frac{\partial \alpha}{\partial \theta_2} \right)^2 \tag{3.86}$$

where, the moment of inertia of each rocker arm was analytically found to be $7.804 \times 10^{-7}$ kgm$^2$, and $\alpha$ is the angular position of the rocker arm referenced to the horizontal.

The kinetic energy of the intake and exhaust rocker arms is shown in Figure 3.50 and Figure 3.51, respectively. The double peaks of the intake rocker arm kinetic energy plot seen in Figure 3.50 indicate that the angular velocity has two regions, one peak corresponding to the rocker arm being deflected upward by the pushrod and the second peak corresponding to the rocker arm returning to the dwell position. For cylinder #1 the first peak spanning 600° to 50° corresponds to the rocker arm being deflected upward by the pushrod and the second peak spanning 50° to 200° corresponds to the rocker arm returning to the dwell position. The symmetry of the two peaks is due to the symmetry between the rise and fall faces of the intake cam.

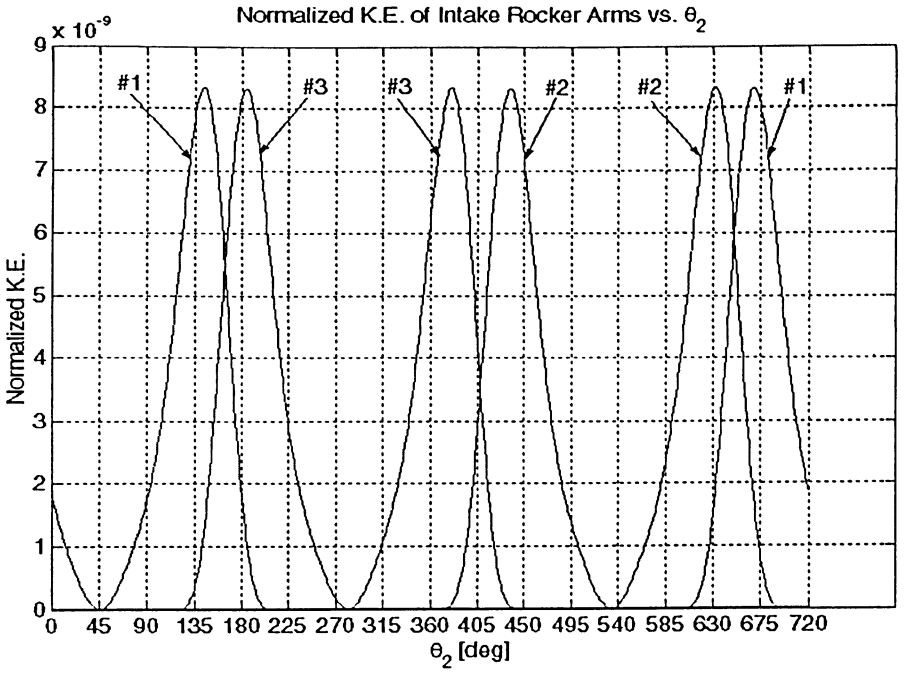


**Figure 3.50: Kinetic energy of the intake rocker arms.**

The kinetic energy of the exhaust rocker arms is shown in Figure 3.51 and the first peak spanning 495° to 675° corresponds to upward motion of the pushrod and the second peak spanning 675° to 110° corresponds to a return to the dwell position. The asymmetry between the rocker arm kinetic energy peaks is due to the exhaust cam asymmetry.

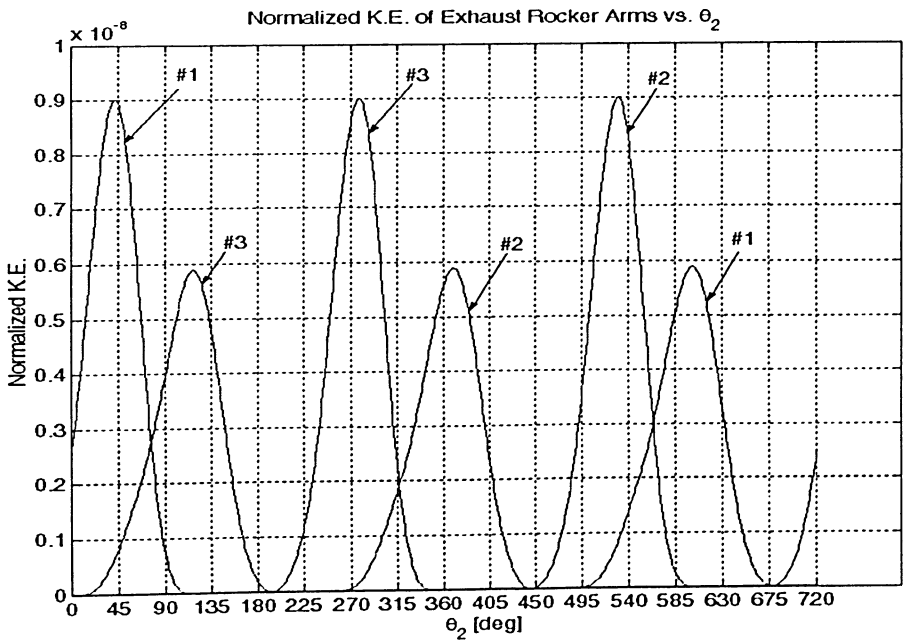


**Figure 3.51: Kinetic energy of the exhaust rocker arms.**

The position of the rocker arms was found in discreet form for each of the intake and exhaust mechanisms and phased according to the firing sequence of the engine. The motion of the rocker arm was found for a period of $2\pi$ and extended to a period of $4\pi$ by adding a $2\pi$ period of dwell. The discrete array describing the position of the rocker arms was converted into functional form through a ten-term Fourier approximation.

## *Section 3.17.8 Kinetic Energy of the Intake and Exhaust Valves*

The fulcrum of the rocker arm was determined through the graphical analysis and the position of the push rod connection end of the rocker arm is known, the motion of the valves can be determined while preserving the phase shift caused by the firing sequence of the engine. The motion of the valves was rectilinear, the kinetic energy was found according to Eq. (3.81).

The kinetic energy of the intake and exhaust valves is shown in Figure 3.52, and Figure 3.53, respectively. The double peaks of the intake valve kinetic energy plots indicate that the velocity of the intake valves has two distinct regions, one peak corresponding to the rocker arm being deflected upward by the pushrod and the second peak corresponding to the rocker arm returning to the dwell position. For cylinder #1 the first peak spanning 600° to 45° corresponds to the rocker arm being deflected upward by the pushrod and the second peak spanning 45° to 200° corresponds to the rocker arm returning to the dwell position. The symmetry of the intake valve kinetic energy peaks is due to the symmetry of the intake cam.

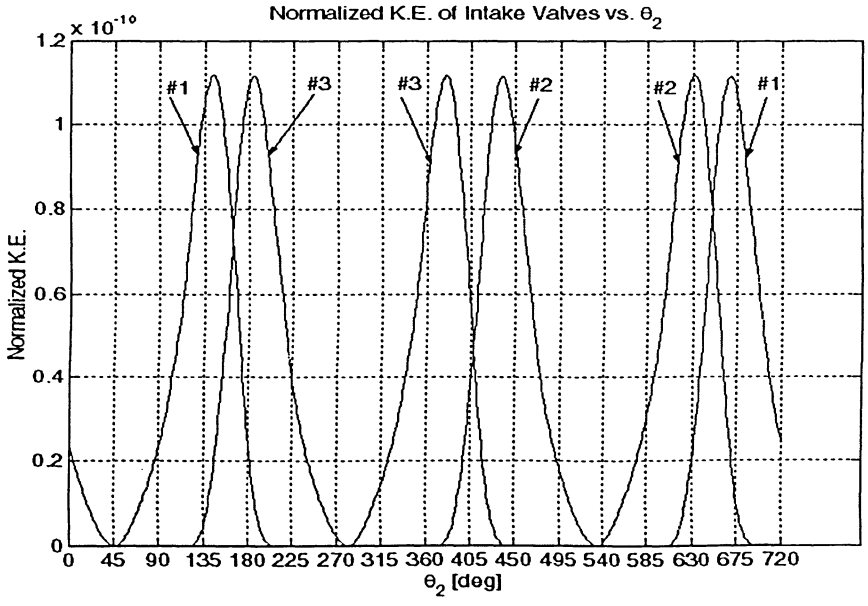


**Figure 3.52: The kinetic energy of the intake valves vs. $\theta_2$.**

The kinetic energy of the exhaust valves is shown in Figure 3.53. The two peaks indicate that the velocity of the exhaust valves has two distinct regions. With the prior knowledge of the angular position of the rocker arms, the kinetic energy plot for cylinder #1 the first peak spanning 495° to 675° corresponds to the exhaust valve being deflected downward by the rocker arm and the second peak beginning at 675° to 115° corresponding to the exhaust valve returning to the dwell position. The asymmetry between the two peaks of the exhaust valve kinetic energy is due to the asymmetry between the rise and fall faces of the exhaust cam.

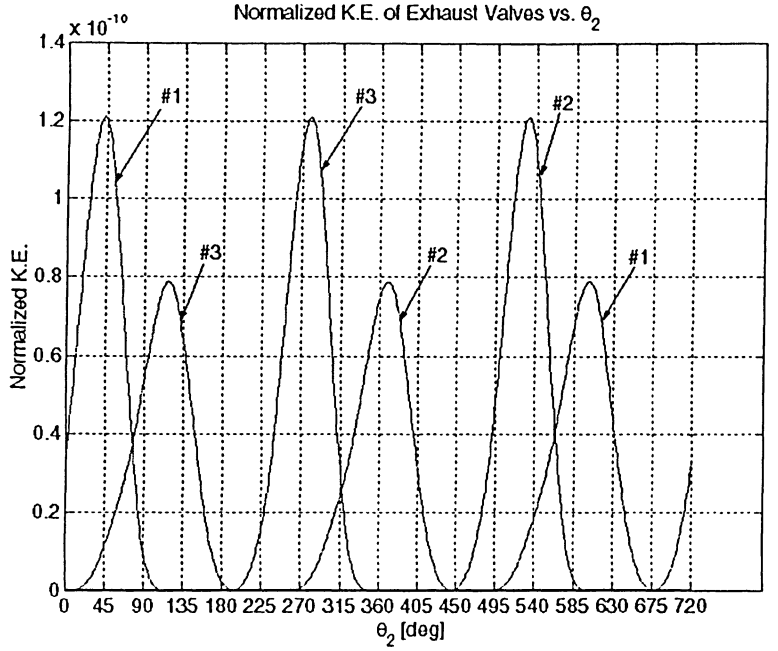


**Figure 3.53: The kinetic energy of the exhaust valves vs. $\theta_2$.**

The velocity of the valves was found by taking the derivative of the ten-term Fourier series approximation of the valve position. Since the valves have been phased during the position analysis, the derivative of the position preserves the phase shift.

## *Section 3.17.9 Total Kinetic Energy with Accessories*

To obtain the total kinetic energy of the system, the individual kinetic energy terms of the internal engine mechanism are summed at each discrete value of $\theta_2$, shown in Figure 3.54. This resulted in a total kinetic energy array in discrete form with a period of $2\pi$. Extending the array from $2\pi$ to $4\pi$ involved wrapping the array once. Converting the discrete $4\pi$-period array into functional form was achieved through the use of a ten-term Fourier series.

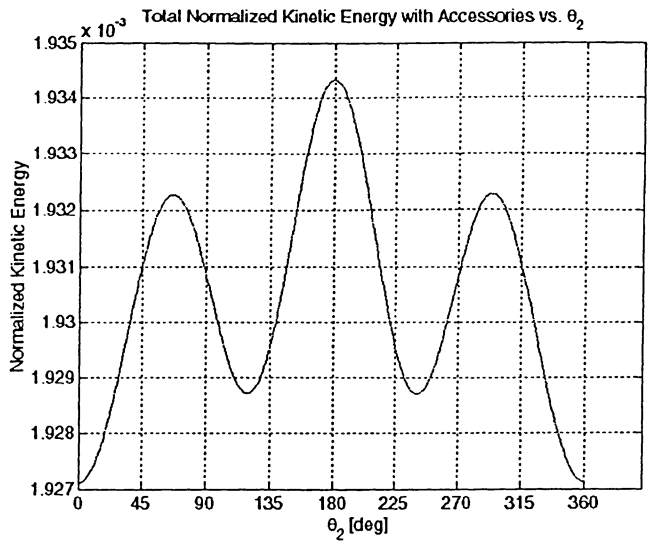


**Figure 3.54: Total kinetic energy with accessories as a function of crank angle.**

## *Section 3.17.10 Derivative of Total Kinetic Energy with Accessories*

The derivative of the total kinetic energy was also required; this was accomplished by using a three-point central numerical method, which produced the derivative of the total kinetic energy with respect to $\omega_2$. A ten-term Fourier approximation was used to generate a functional representation suitable for use in the governing equation of motion. Figure 3.55 shows that position and slope continuity is preserved at the beginning and the end of the $2\pi$-periodic derivative of kinetic energy array.

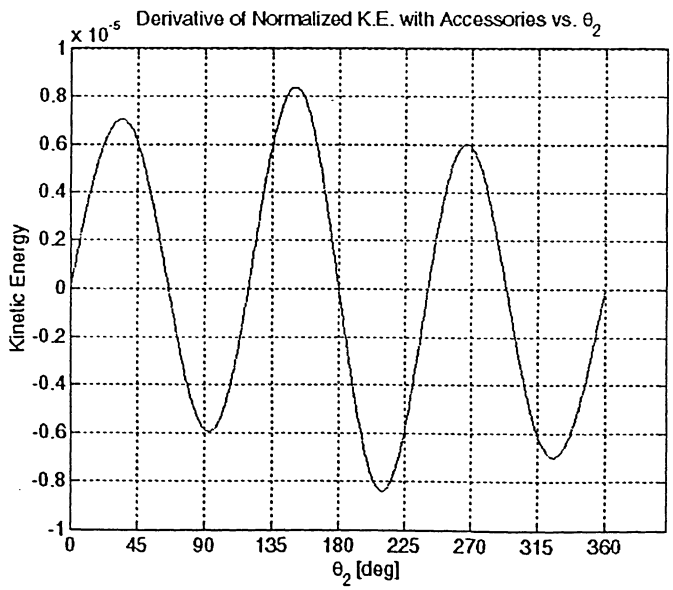


**Figure 3.55: Derivative of total kinetic energy with respect to $\theta_2$.**

To solve the equation of motion including the accessory drive system requires $\tilde{T}$ and $\frac{\partial \tilde{T}}{\partial \theta_2}$ in functional form over a period of $4\pi$. Extending the two arrays from $2\pi$ to $4\pi$ requires wrapping the array once. Converting the $4\pi$-period array from discrete into functional form was achieved through a ten-term Fourier series.

## *Section 3.18 Lagrange Equation*

To generate the equation(s) of motion for a dynamical system, it is essential to first determine the degrees of freedom of the system in question. The internal 8-bar mechanism proprietary to the Saito-450 engine has one degree of freedom when all components are considered rigid. The procedure for applying the Lagrange equation is to select one independent coordinate system that will uniquely define the position of any member of the mechanism at any instant in time. The space-fixed inertial coordinate system selected was centered at the crankshaft axis of rotation with a counter-clockwise direction of shaft rotation taken as positive. The coordinate, $\theta_2$, is the angular position of the crankshaft and is the one coordinate required to uniquely define the position of all other members of the 8-bar mechanism.

For a one DOF dynamical system with $\theta_2$ as the generalized coordinate, the Lagrange equation can be written as [Inmann, 2001].

$$\frac{d}{dt}\left(\frac{\partial T}{\partial \dot{q}_i}\right) - \frac{\partial T}{\partial q_i} + \frac{\partial U}{\partial q_i} = Q_i - W_i \tag{3.87}$$

*where* $T$ is the kinetic energy; $U$ is the potential energy; $Q$ is the generalized force accounting for the gas pressures in all cylinders; $W$ is the generalized force accounting for the aerodynamic load of the propeller. Since the crank angular displacement is chosen as the generalized coordinate, the generalized forces are actually torques.

Eq. (3.87) represents one equation corresponding to one generalized coordinate.

### *Section 3.18.1 ODE Formulation*

In the first phase of research, the potential energy of springs used in the accessory system, is neglected ($U = 0$). With the help of normalized kinetic energy, the Lagrange equation may be written as

$$\frac{d}{dt}\left(\frac{\partial\left(\tilde{T}\dot{\theta}_2^2\right)}{\partial\dot{\theta}_2}\right)-\frac{\partial\left(\tilde{T}\dot{\theta}_2^2\right)}{\partial\theta_2}=Q-W \tag{3.88}$$

It can be shown that Eq. (3.88) can be reduced to

$$2\tilde{T}\ddot{\theta}_2+\frac{\partial\tilde{T}}{\partial\theta_2}\dot{\theta}_2^2=Q-W \tag{3.89}$$

The above equation is the final form of the equation of motion for the engine-propeller drive system. Its solution will be performed numerically using a fixed step Euler solver in Matlab. To implement the numerical solution, the nonlinear second order ordinary differential equation must be converted to a system of two first-order differential equations through the following transformation

$$\begin{aligned} y_1 &= \theta \\ y_2 &= \dot{y}_1 = \dot{\theta} \end{aligned} \tag{3.90}$$

The equivalent first order differential equations to be solved in Matlab are shown in matrix form as Eq. (3.91).

$$\begin{Bmatrix} \dot{y}_1 \\ \dot{y}_2 \end{Bmatrix} = \begin{Bmatrix} y_2 \\ \dfrac{Q-\dfrac{\partial\tilde{T}}{\partial\theta_2}y_2^2-W}{2\tilde{T}} \end{Bmatrix} \tag{3.91}$$

where $y$ is the time response of the system, $Q$ in is an algebraic sum of the gas work done on or by each cylinder for each $\theta_2$ shown in Eq. (3.92) and $W$ is the work done by the propeller.

$$Q=\sum_{i=1}^{3}Q_i \tag{3.92}$$

The initial conditions are the angular position and angular velocity of the crankshaft. The numeric values of these initial conditions were chosen to be $\theta_2 = 0$ rad and $\dot{\theta}_2 = 210$ rad/s.

This concludes the formulation of the equation of motion when neglecting the accessory system. The equation of motion when including the accessory system is derived in Section 3.18.2.

## *Section 3.18.2 Equation of Motion Including Potential Energy*

A schematic representation of the cam system can be seen in Figure 3.56 (a). This figure shows the cam revolving about a fixed axis vertically deflecting the tappet as a function of angular cam position. The tappet and pushrod are connected by a revolute joint, as is the pushrod and rocker arm. The rocker arm rotates about a fixed fulcrum when acted upon by the pushrod, causing the vertically downward constrained motion of the spring and valve.

A cutaway view of a Saito 4-stroke engine and the mechanism can be seen in Figure 3.56 (b).

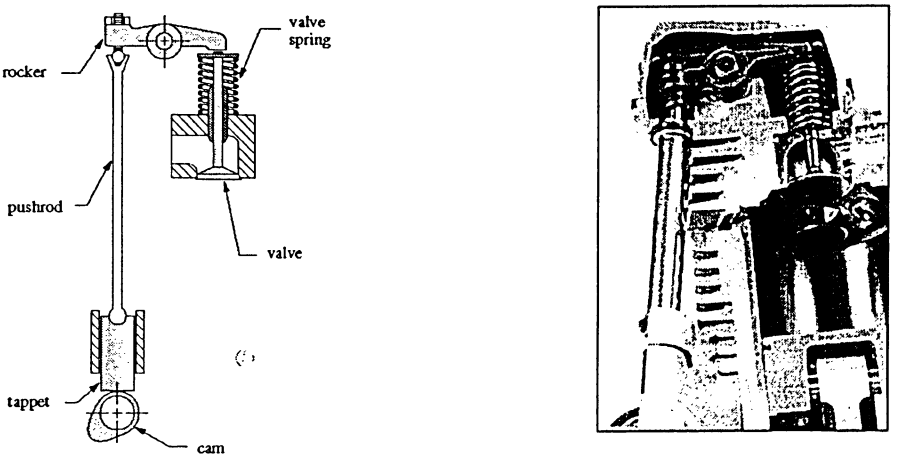


(a) (b)

**Figure 3.56: Schematic of the cam system (a) and cut-away view of a Saito cam system, showing the push rod, rocker arm, spring, valve, cooling fins, inner cylinder wall, piston cross section, wrist pin and connecting rod (b).**

To determine the system dynamics while including the effect of the cam mechanism, the potential energy term must now be accounted for.

Let the potential energy of the springs be described by Eq. (3.93).

$$U = \frac{1}{2}kx^2 \tag{3.93}$$

where $k$ is the spring constant and $x$ is the deflection of the spring as a function of the crank shaft angular position, $\theta_2$.

The equation of motion requires the derivative of the potential energy with respect to the generalized coordinate ($\theta_2$), shown in Eq. (3.94).

$$\frac{\partial U}{\partial \theta_2} = kx\frac{\partial x}{\partial \theta_2} \tag{3.94}$$

The total potential energy is the sum of the potential energies of the six individual springs, for each discreet angular position, $\theta_2$ shown in Eq. (3.95).

$$\left.\frac{\partial U}{\partial \theta_2}\right|_{total} = \sum_{i=1}^{6} kx_i \frac{\partial x_i}{\partial \theta_2} \tag{3.95}$$

where $x_i$ is the deflection of the $i^{th}$ spring as a function of the crank shaft angular position, $\theta_2$.

With the potential energy defined for all six springs, the equation of motion can be modified from Eq.(3.89) to become Eq. (3.89).

$$\left(2\tilde{T}\ddot{\theta}_2\right)+\left(\frac{\partial \tilde{T}}{\partial \theta_2}\dot{\theta}_2^2\right)+\left(\left.\frac{\partial U}{\partial \theta_2}\right|_{total}\right)=Q-W \tag{3.96}$$

The second order differential Eq. (3.96) must be reduced to a system of two first order equations such that Matlab is able to generate a solution for any value of $\theta_2$.

To reduce the order of Eq. (3.96), implement the substitutions shown in Eq. (3.90) resulting in Eq. (3.97).

$$2\tilde{T}\dot{y}_2+\frac{\partial \tilde{T}}{\partial \theta_2}\dot{y}_1^2+\left.\frac{\partial U}{\partial \theta_2}\right|_{total}=Q-W \tag{3.97}$$

The final form of the equation of motion is shown in Eq. (3.98) as a system of two first order differential equations.

$$\begin{Bmatrix}\dot{y}_1\\ \dot{y}_2\end{Bmatrix}=\begin{Bmatrix}\dot{\theta}_2\\ \dfrac{Q-W-\dfrac{\partial \tilde{T}}{\partial \theta_2}\dot{y}_1^2-\left.\dfrac{\partial U}{\partial \theta_2}\right|_{total}}{2\tilde{T}}\end{Bmatrix} \tag{3.98}$$

The addition of the accessory drive system results in additional general plane motion kinetic energy terms that must be included in equation of motion, such as the kinetic energy of all six tappets, six connecting rods, six rocker arms, six valves, the rotational of the six cams and three cam gears. The potential energy term in Eq. (3.98) contains the energy stored and released by each of the six springs.

# *Chapter 4 NUMERICAL RESULTS*

The equation of motion of the propeller-engine system has been derived based on the Lagrange equation by first neglecting the accessory system, then later including the accessory system. The following sections outline the work done by the engine and the time and frequency domain numerical results obtained by the fixed-step Euler solver.

## *Section 4.1 Work Done by Gas Pressure*

To solve the differential equation of motion governing the propeller-engine system, the generalized forces needed to be quantified. One of the two generalized force terms is the work done by the gas pressure on the pistons, $\sum Q_i$, and the second term is the work absorbed by the propeller $\sum W_i$, previously determined in functional form.

The work done by the gas pressure can be determined using the definition of Work, with appropriate substitutions. The definition of gas work is simply a force multiplied by a distance, shown in Eq. (4.1).

$$Q_i = F_i d_i \tag{4.1}$$

The force a fluid imparts on a surface can be calculated by knowing the fluid pressure multiplied by the surface area over which the pressure is acting. Substituting into Eq. (4.1) results in Eq. (4.2).

$$W_i = P_i A_p d_i \tag{4.2}$$

where the distance $d_i$ is the change in piston position with respect to time.

Eq. (4.2) can be re-written to represent the rate of change of the piston with respect to $\theta_2$ resulting in Eq. (4.3).

$$W_i = P_i A_p \delta r_i|_{\delta\theta_2=1} \tag{4.3}$$

Eq. (4.3) can be expanded by using the chain rule to obtain the change in piston position with respect to crankshaft angular position.

$$W_i = P_i A_p \left(\frac{\partial r_i}{\partial \theta_2}\right) \delta r_i|_{\delta\theta_2=1} \tag{4.4}$$

Finally, the work done by the gas pressure on the pistons is shown in Eq. (4.5) normalized with respect to crankshaft angular position, $\theta_2$, resulting in the gas work quantity that is in an appropriate form to be used in the equation of motion.

$$W_i = P_i A_p \left( \frac{\partial r_i}{\partial \theta_2} \right) \tag{4.5}$$

where the subscript $i$ indicates the particular cylinder being considered; $r_i$ is the position of the $i^{th}$ wrist pin measured from the axis of rotation of the crankshaft.

Figure 4.1, and Figure 4.2 shows the gas work done within each cylinder is $4\pi$-periodic and is plotted against the crankshaft angular position. The three plots from Figure 4.1, and Figure 4.2 appear similar in shape; however, the most notable feature is the phase shift between each cylinder accounting for the firing sequence of the engine. Another feature observed in Figure 4.1, and Figure 4.2, is that the plots are not identical; the centre plot corresponds to cylinder #1, and the work done by cylinders #2 and #3 is different due to the presence of links #4 and #5, respectively.

Following the centre reference plot corresponding to cylinder #1, the intake stroke spans an angular position interval from 1° to 194°, and the average work during this interval is zero.

The next phase in the Otto cycle is the compression stroke and this spans an angular interval of 195° to 350°. The average work during this portion of the stroke is negative, indicating that work is input to the system, or the system requires work to move through this angular crankshaft displacement.

After the compression stroke the compressed air-fuel mixture is ignited and the burning of this gas mixture creates a very large pressure differential across the piston. The burning phase takes place through an angular displacement of 48°, from 351° to 399°. The average work during this angular interval is positive indicating that during the burning of the air-fuel mixture, work is being produced by the engine.

The power stroke is assumed to take place through an angular position of 400° to 499° and the average work during this stroke is positive indicating work is being produced by the engine during this angular range.

The last phase of the Otto cycle is the exhaust stroke and this is assumed to take place through an angular position interval of 500° to 720°. The work during this phase is both positive and negative throughout the 220° range. The cylinder pressure during this interval was assumed

to be decreasing linearly from the end of the expansion stroke to the beginning of the intake stroke. This negative pressure gradient and the velocity of the piston through this same angular interval are responsible for the cylinder work becoming negative. During this interval Figure 4.1 is reasonable and matches well with previously published data.

There is position continuity during the transition from the compression to the burning phases; however, slope continuity is not preserved at this juncture. The reason for the lack of slope continuity is a result of the slope magnification factor used in scaling the pressure vs. crank angle plot (Section 2.2.7) to account for the effects of throttling.

When transitioning from the burning phase to the expansion phase there is both position and slope continuity resulting from the initial conditions used when constructing the spline approximating the pressure resulting from the burning of the ingested air-fuel mixture.

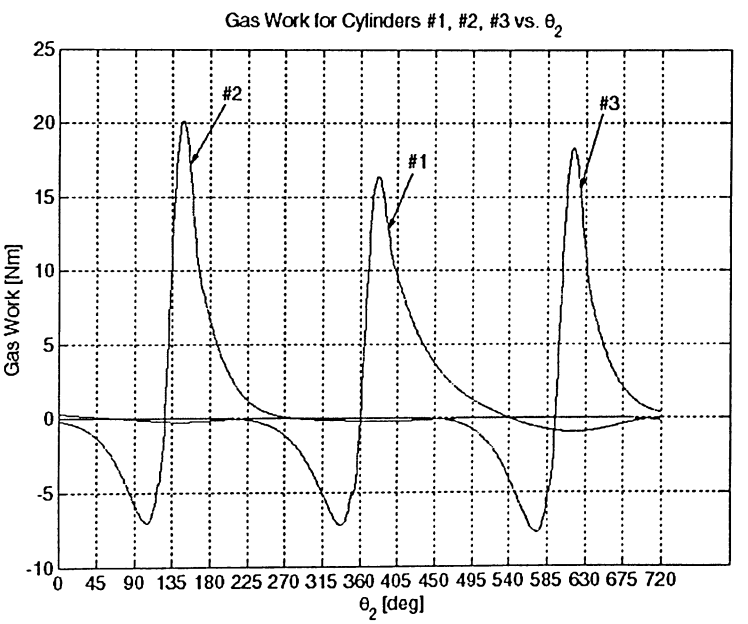


**Figure 4.1: Work done by gas pressure on all three pistons at 35% throttle.**

Figure 4.2 shows the gas work at 100% throttle. At this throttle setting the slope magnification factor used in the construction of the pressure vs. crankshaft angular position curve is 75 and this is to achieve a power output from the engine equal to the manufacturers published value of 7 hp. This sudden change in pressure gradient causes the sudden drop seen on Figure 4.2.

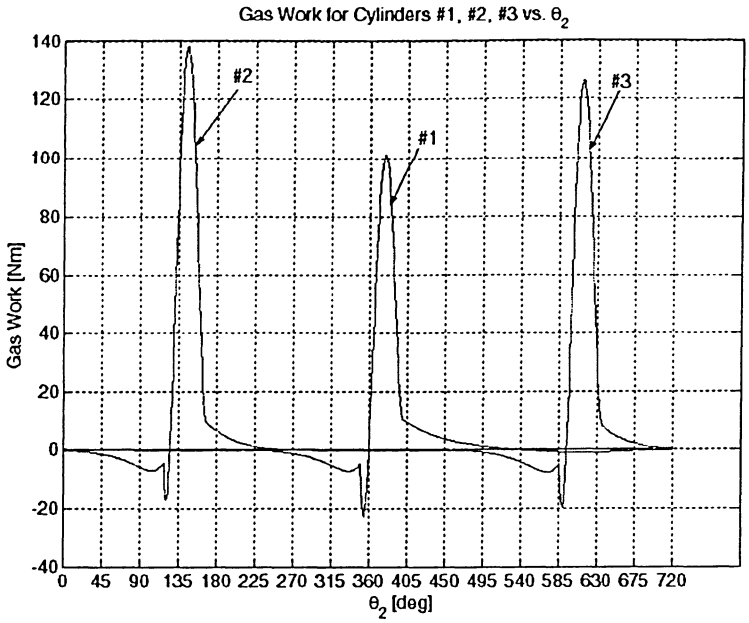


**Figure 4.2: Work done by gas pressure on all three pistons at 100% throttle.**

The work done by the engine for an arbitrary throttle setting has been calculated in discrete form for any crankshaft angular position. This information is required to solve the equation of motion; however, the discrete data was converted into functional form by a Fourier series approximation.

## *Section 4.2 Cam Modeling*

The kinetic energy of each component making up the accessory drive system depends on the mass of that component and its normalized velocity. The velocity of the tappets was obtained by finding the position of the tappets as a function of the crankshaft angular position. Since the cams and tappets experience both edge and face contact, the desired position information was not available from analytical methods, so a graphical method employed using AutoCAD.

Through direct observation the intake and exhaust cams were determined to have different cross-sectional profiles. As a result, the intake and exhaust cams were treated independently when conducting the kinematic analysis.

The intake and exhaust cam profiles were considered to have four distinct regions, each of which could be approximated with a circle of appropriate radius as shown in Figure 4.3 (a), and (b), respectively.

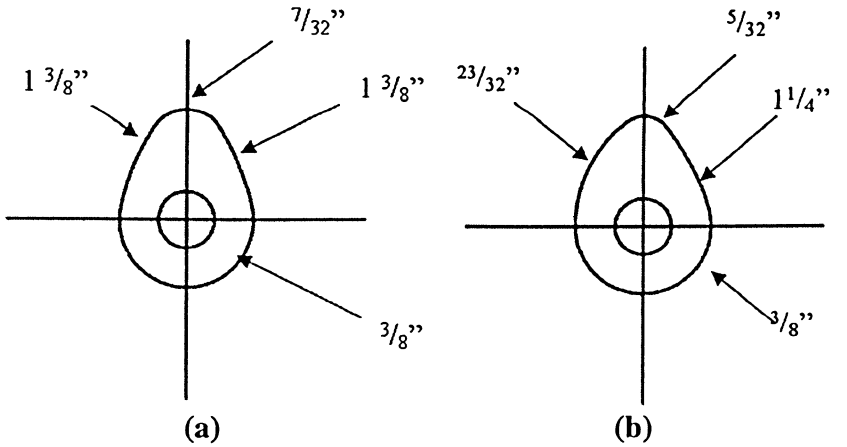


**Figure 4.3: Radius approximation of intake (a) and exhaust (b) cam profile.**

The intake and exhaust cam profiles were drawn in AutoCAD along with the respective tappets in the orientation found in the assembled engine, shown in Figure 4.4, (a) and (b), respectively. The intake and exhaust tappets were angled 40.5° clockwise 36° counter clock wise, respectively, away from the vertical centre line of the respective cylinder. The canting of the tappets away from the global vertical was done to align the tappet with the rocker arm.

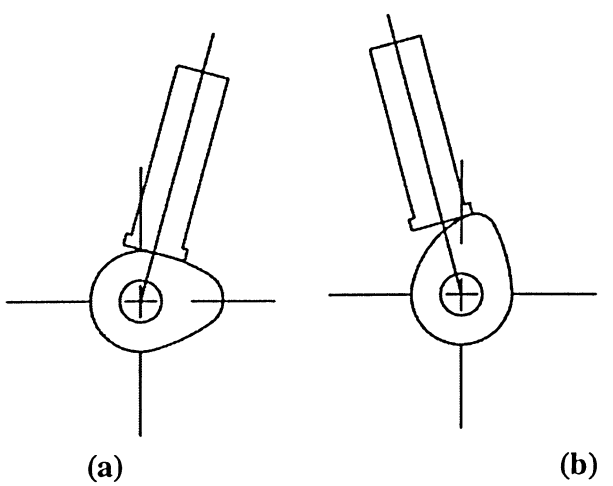


**Figure 4.4: The orientation of the intake cam and tappet (a), and exhaust cam and tappet (b) with respect to the global coordinate system.**

Figure 4.4 (a) shows the initial orientation of the CAD models and it is from this point that the cams were rotated by 0.5° counter clock wise increments. After the 0.5° cam rotation, each tappet was then moved outward or inward along the inclined tappet axis of motion,

depending on the cam phase of motion. The resulting displacements were measured within AutoCAD and recorded for the specified cam angle. This procedure was repeated for 180° of cam rotation with the knowledge that the tappet is not displaced by the cam during the remaining 180° cam rotation. The results of this intake cam displacement analysis can be found in Figure 4.5, and Figure 4.6 with the repeated data removed from the beginning and end of the tappet motion.

The tappet profiles have been determined over a range of $\pi$; however, the cams are rotating elements and therefore are periodic on $2\pi$. To make up the $\pi$ difference, the tappet profiles were extended by $\pi$ at a constant elevation equal to the radius of the cam base circle. The base circle radius was then subtracted from the intake cam profile since the distance the cam moves the tappet is referenced to the base circle.

The three cylinders of the Saito-450 fire at different angular crankshaft positions, and therefore each cam profile must be phase shifted to account for the firing sequence.

Combining the intake and exhaust cam profiles with the appropriate phase shifting can be seen in Figure 4.5, and Figure 4.6, respectively.

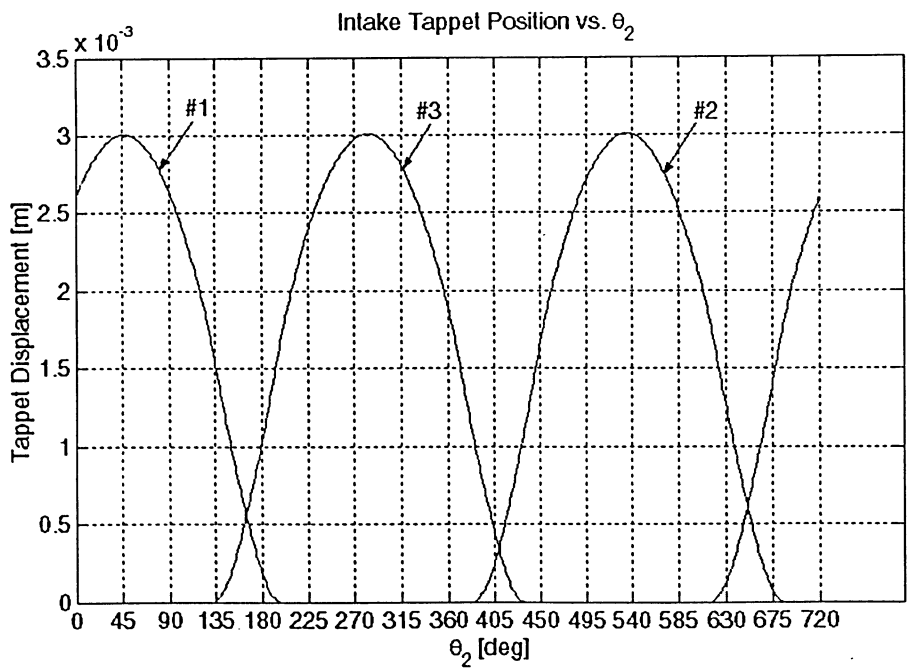


**Figure 4.5: Phased intake tappet positions vs. $\theta_2$.**

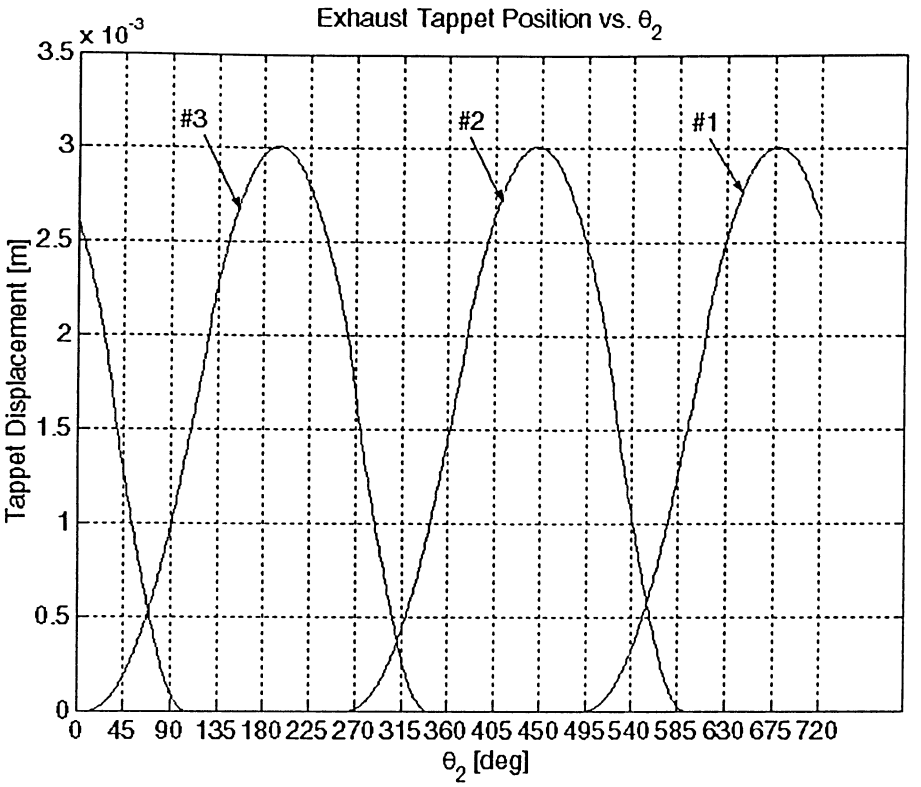


**Figure 4.6: Phased exhaust tappet positions vs. $\theta_2$.**

The intake and exhaust tappet positions have been found for each cylinder and this displacement information will form the basis for the subsequent accessory drive analysis. To make the most use of this position information, a ten-term Fourier approximation was made for each of the six tappet profiles with negligible error.

Figure 4.7, and Figure 4.8 shows the Fourier approximation superimposed on the original data for the intake and exhaust tappets, respectively.

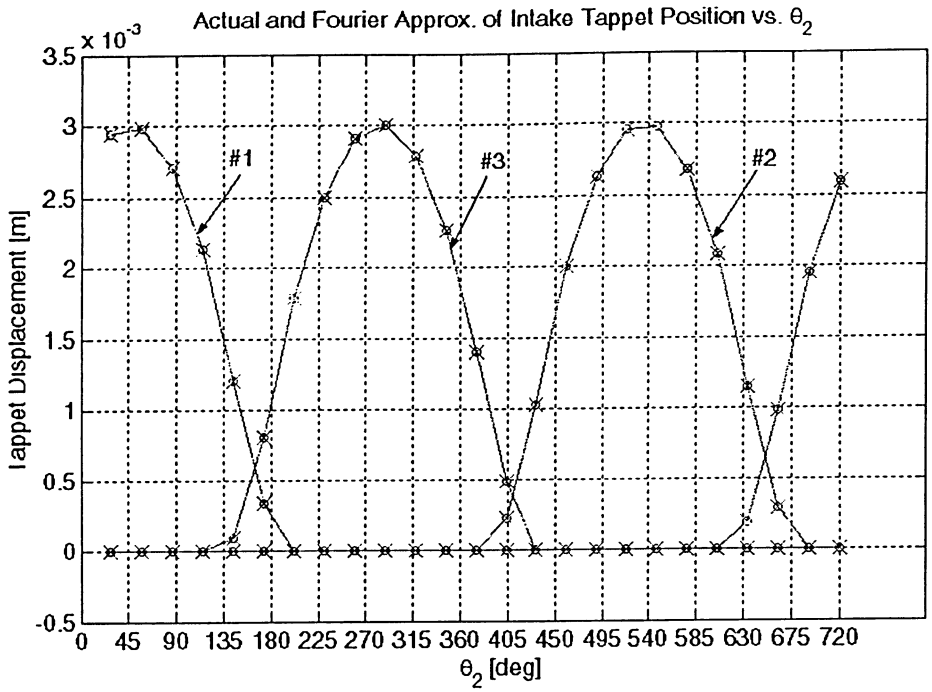


**Figure 4.7: Actual and Fourier approximation of intake tappets vs. $\theta_2$.**

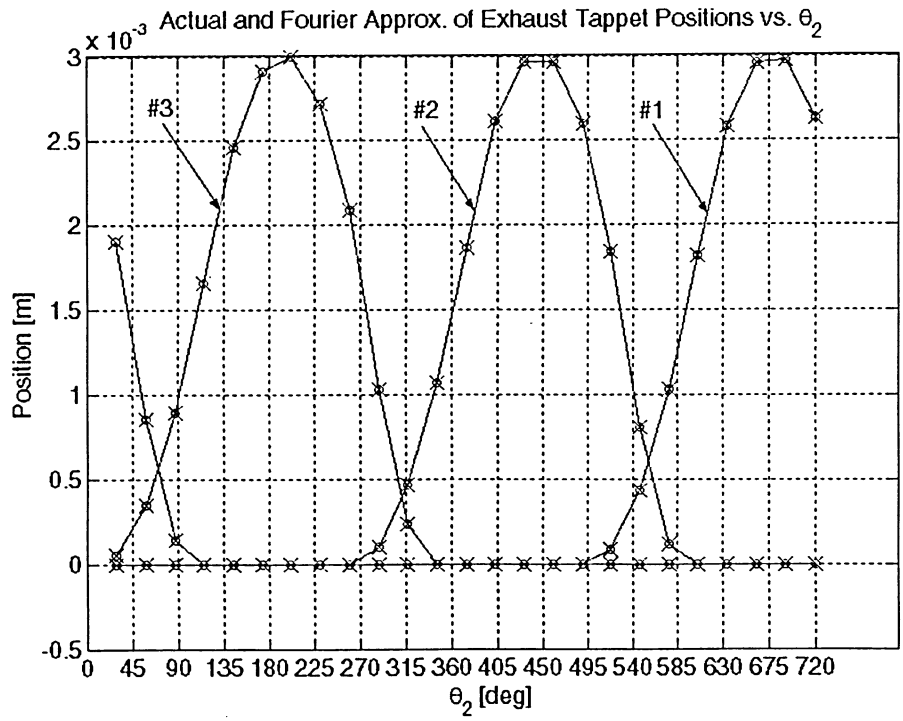


**Figure 4.8: Actual and Fourier approximation of exhaust tappets vs. $\theta_2$.**

The kinetic energy of a component is proportional to the velocity of that part; so, in order to find the kinetic energy of the tappets, the velocity of the tappets must be found.

The velocity of the tappets is the rate of change of the tappet position with respect to time. The velocity can also be represented by the derivative of the Fourier series representing the tappet positions with respect to $\theta_2$. The Fourier representation of the tappet positons was found by using Eq. (4.6) with the appropriate number of terms included in the summation to reduce the error to an acceptable low amount.

$$\vec{s} = a_0 + \sum_{i=1}^{10}\left[a_i \cos\left(\frac{i\theta_2}{2}\right) + b_i \sin\left(\frac{i\theta_2}{2}\right)\right] \tag{4.6}$$

The velocity of the tappets was found by taking the first derivative of Eq. (4.6) with respect to $\theta_2$, shown in Eq. (4.7).

$$\vec{v} = \sum_{i=1}^{10}\left[-\frac{ia_i}{2}\sin\left(\frac{i\theta_2}{2}\right) + \frac{ib_i}{2}\cos\left(\frac{i\theta_2}{2}\right)\right] \tag{4.7}$$

The next members of the accessory drive system considered were the pushrods, which link the tappets to the rocker arms by ball and socket joints. The motion of the push rods was determined by the graphical method generated in AutoCAD.

The mechanism was drawn to scale and the tappets moved from the reference dwell position to maximum deflection in increments of 25% of the maximum deflection. Figure 4.9, (a) and (b), shows the graphical model of the intake and exhaust push rods, respectively.

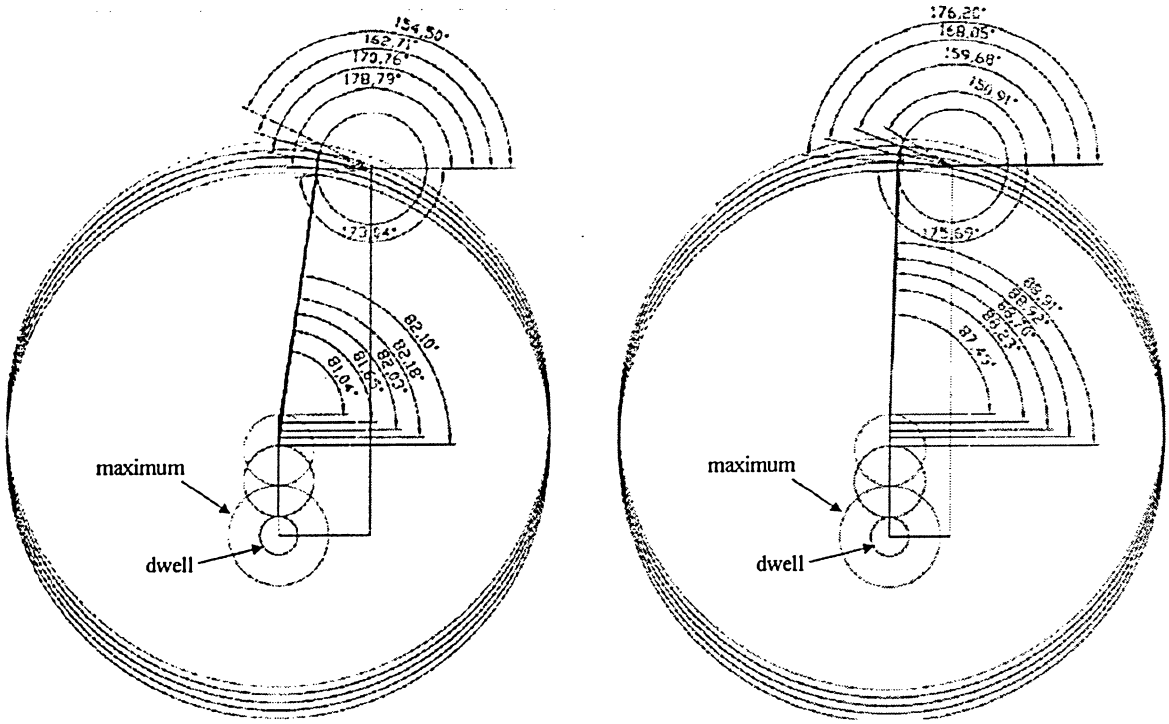


(a) (b)

**Figure 4.9: Graphical representation of the intake (a) and exhaust (b) cam systems.**

The angular measurements seen at the top of Figure 4.9, (a) and (b) are the angular positions of the rocker arms as the tappets are moved throughout their range of motion. The intake and exhaust rocker arms travel from 186.96° at the reference position to 154.50° and from 184.31° at the reference position to 150.91° at the fully deflected position, respectively.

The angular position of the intake and exhaust push rods varies from 82.10° to 81.04° and 88.91° to 87.49°, respectively, in the undeflected position and fully deflected position.

The extreme values for the angular positions are valuable; however, of particular interest is how the push rods travel their respective ranges of motion. To this end, the perpendicular height of the centre of gravity of the pushrods was measured within AutoCAD with respect to the reference tappet height for each of the five deflections considered, shown in Table 4.1.

**Table 4.1: Pushrod positions [m].**

| | Intake | | | Exhaust | | |
|---|---|---|---|---|---|---|
| X [m] | Y [m] | Formula Y | Error [%] | Y [m] | Formula Y | Error [%] |
| 0.00000 | 0.0337 | 0.0340 | 0.950 | 0.0340 | 0.0339 | -0.294 |
| 0.00194 | 0.0356 | 0.0350 | -1.850 | 0.0359 | 0.0361 | 0.574 |
| 0.00389 | 0.0359 | 0.0363 | 1.121 | 0.0379 | 0.0380 | 0.342 |
| 0.00583 | 0.0379 | 0.0381 | 0.625 | 0.0398 | 0.0395 | -0.829 |
| 0.00777 | 0.0404 | 0.0403 | -0.318 | 0.0404 | 0.0406 | 0.415 |

Figure 4.10 shows the data from Table 4.1 plotted against the tappet elevation. Superimposed on the raw data shown in Figure 4.10 is a second order polynomial used to approximate the pushrod elevation data. The percent error resulting from this quadratic polynomial approximation can be found in the right hand column of Table 4.1 for the intake and exhaust pushrods.

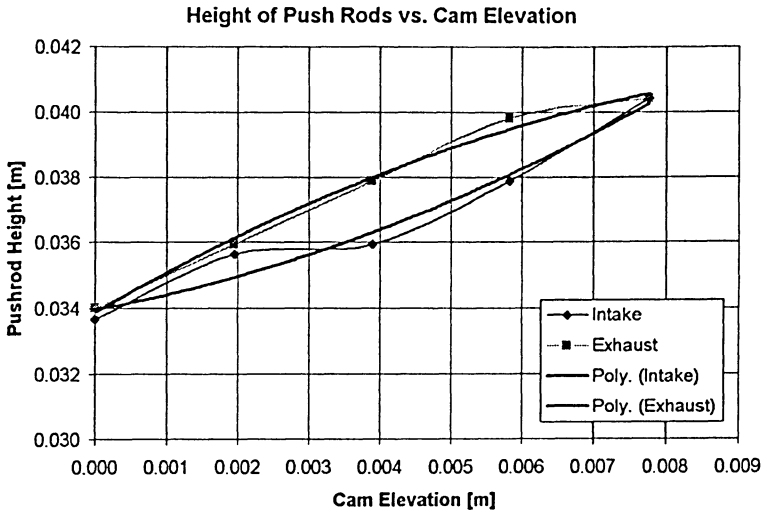


**Figure 4.10: Height of pushrods vs. cam elevation.**

The quadratics approximating the height of the intake and exhaust pushrods are shown in Eqn's (4.8) and (4.9), respectively.

$$y_{\text{int}} = (53.16)h^2_{\text{int.tappet}} + (0.3963)h^2_{\text{int.tappet}} + 0.034 \tag{4.8}$$

$$y_{exh} = (-50.701)h^2_{exh.tappet} + (1.2545)h^2_{exh.tappet} + 0.0339 \tag{4.9}$$

It should be noted that the cam rotates at half the rotational speed of the crankshaft; therefore, the cam profile found for a period of $\pi$ corresponds to a crankshaft angular displacement of $2\pi$. Since the analysis is normalized with respect to the angular displacement of the crankshaft, the tappet height must be found for a period of $4\pi$. During the $4\pi$-period there is a dwell of $2\pi$.

The tappet height was approximated by a second order polynomial valid over a period of $2\pi$; however, it is desirable to have one function that is valid throughout the entire $4\pi$ period and polynomials are poor methods of approximating signals with significant flat regions. For this

reason, a ten-term Fourier series was used to approximate the position of the push rods, in functional form, in terms of $\theta_2$ for the entire $4\pi$ crankshaft period.

Figure 4.11, and Figure 4.12, shows the ten-term Fourier approximation superimposed on the original pushrod deflection for each of the intake and exhaust pushrods, respectively. These figures show that the error generated through the use of the Fourier approximation is negligible.

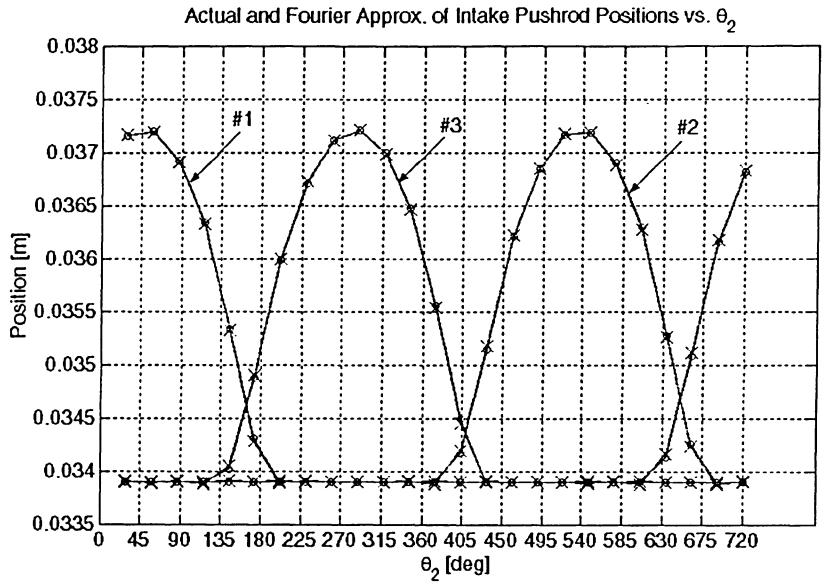


**Figure 4.11: Actual data and Fourier approximation of the intake pushrod positions vs. $\theta_2$.**

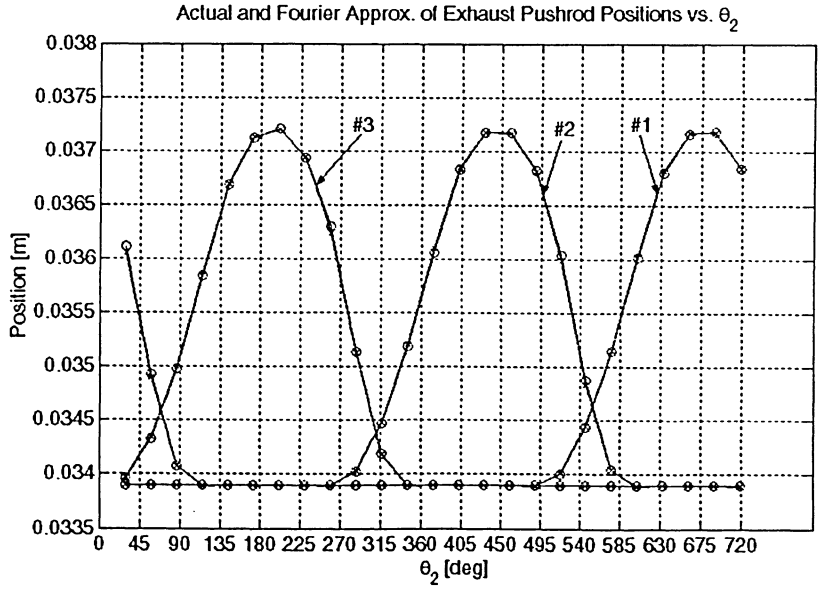


**Figure 4.12: Actual data and Fourier approximation of the exhaust pushrod positions vs. $\theta_2$.**

The position information of the pushrods is essential for a kinematic analysis of the mechanism, and system as a whole; however, the equation of motion was derived on an energy basis through the use of the Lagrange equation. Neglecting the potential energy of the pushrod, the kinetic energy of the push rod must be determined. The velocity of the pushrod mass centers must be determined to evaluate the kinetic energy of each push rod member.

The position of each pushrod has been determined by a ten-term Fourier approximation and it is possible to take the first derivative of the series with respect to the crankshaft angle ($\theta_2$) to obtain the normalized velocity according to Eq. (4.7).

The velocity of the intake and exhaust pushrods can be seen in Figure 4.13, and Figure 4.14, respectively. The magnitude of the oscillations seen in Figure 4.13, and Figure 4.14, are in the order of $10^{-5}$ m/s, which is negligible for this application.

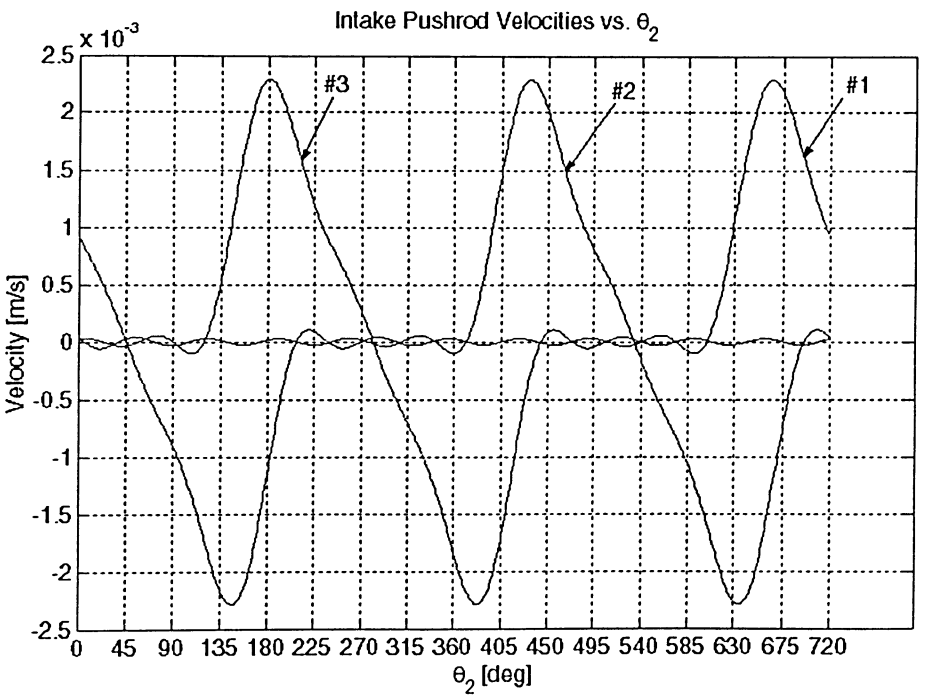


**Figure 4.13: The velocity of the intake pushrod mass centers vs. $\theta_2$.**

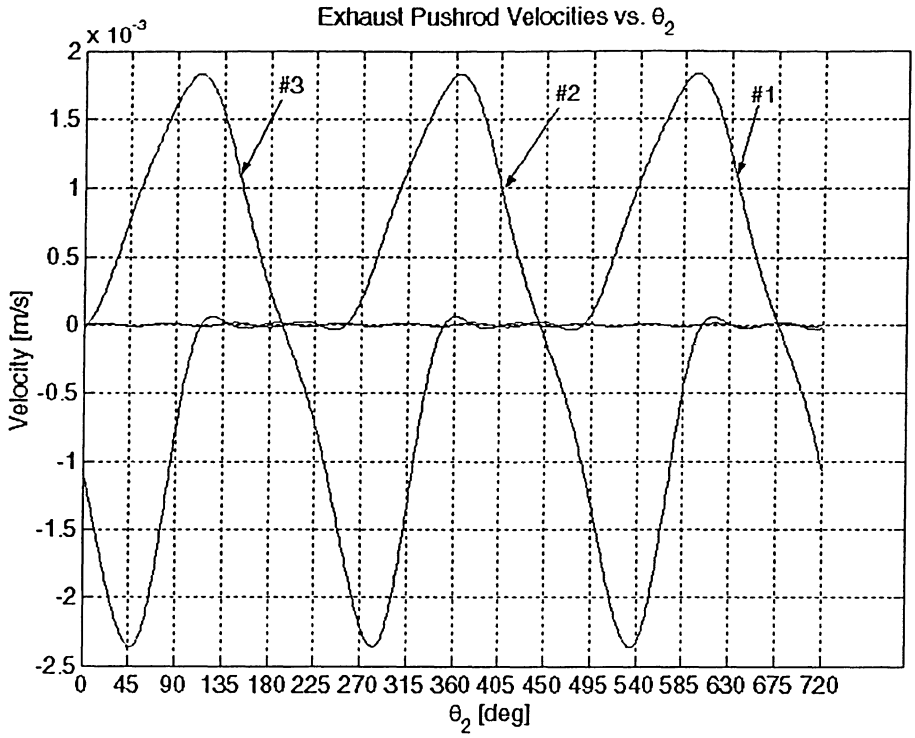


**Figure 4.14: The velocity of the exhaust pushrod mass centers vs. $\theta_2$.**

The velocity of the mass centers of each pushrod have been found in functional form over a period of $4\pi$, taking into account the phase shift caused by the firing sequence.

With the velocity of the intake and exhaust pushrods determined, focus was then turned to determining the angular position of the rocker arms.

A graphical method was implemented in AutoCAD to determine the angular position of each rocker arm as a function of the deflection of the corresponding tappet, sampled at five equally spaced intervals spanning 0%-100% of the maximum tappet deflection. Figure 4.9, (a) and (b), shows the graphical model of the intake and exhaust rocker arm deflections, respectively, and Table 4.2 shows the results of Figure 4.9, (a) and (b), in tabular form.

**Table 4.2: Angular deflection of the exhaust rocker arm with percent error.**

| | Intake | | | Exhaust | | |
|---|---|---|---|---|---|---|
| X [m] | Y [rad] | Formula Y | Error [%] | Y [rad] | Formula Y | Error [%] |
| 0.00000 | 3.2625 | 3.2619 | -0.017 | 3.2162 | 3.2156 | -0.019 |
| 0.00194 | 3.1199 | 3.1209 | 0.033 | 3.0747 | 3.0760 | 0.041 |
| 0.00389 | 2.9798 | 2.9797 | -0.002 | 2.9325 | 2.9325 | 0.001 |
| 0.00583 | 2.8393 | 2.8382 | -0.037 | 2.7864 | 2.7852 | -0.044 |
| 0.00777 | 2.6960 | 2.6965 | 0.018 | 2.6334 | 2.6340 | 0.025 |

Figure 4.15 shows the results of column 1 from Table 4.2 plotted against column 2 for the intake rocker arm. Superimposed on this data is a second order polynomial used to represent the discrete data in functional form. From the fourth column of Table 4.2, and visually from Figure 4.15, the error is negligible for this application.

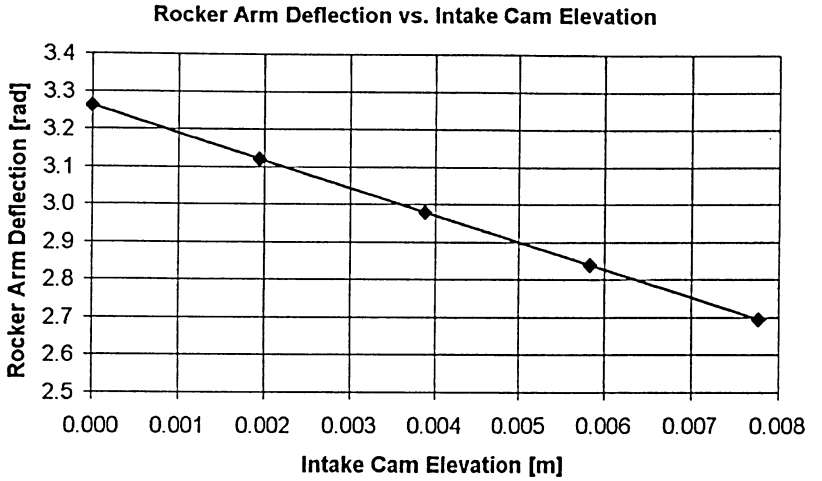


**Figure 4.15: Intake rocker arm angular displacement vs. intake tappet displacement.**

$$y_{RA\,\mathrm{int}} = -33.012x_{\mathrm{int}}^2 - 72.485x_{\mathrm{int}} + 3.2619 \tag{4.10}$$

where, $y_{RAint}$ is the deflection of the rocker arm and $x_{int}$ is the deflection of the intake cam.

The data from the first and fifth column from Table 4.2 are shown in Figure 4.16 superimposed with a second order polynomial approximation. From the seventh column of Table 4.2 and visually from Figure 4.16, the error is negligible for this application.

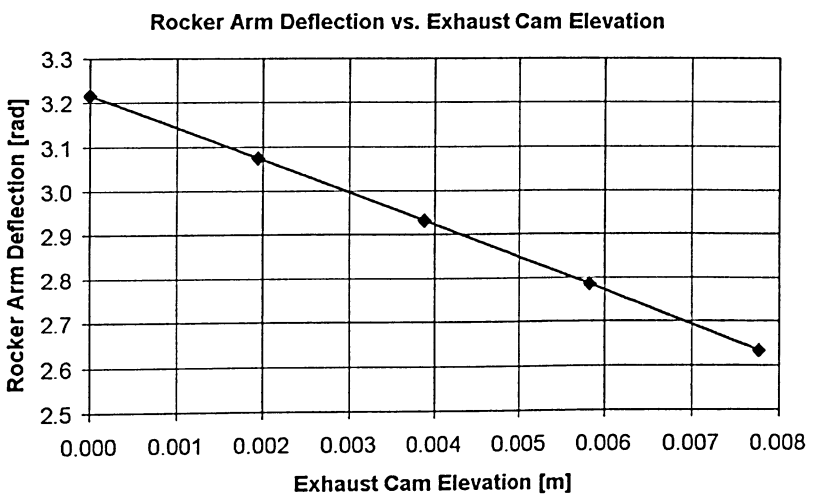


**Figure 4.16: Exhaust rocker arm angular displacement vs. intake tappet displacement.**

$$y_{RAexh} = -508.39x_{exh}^2 - 70.874x_{exh} + 3.2156 \tag{4.11}$$

where $y_{RAexh}$ is the deflection of the exhaust rocker arm and $x_{exh}$ is the deflection of the exhaust tappet.

The angular position of the intake and exhaust rocker arms were found and approximated with second order polynomials. The second order polynomials are very good approximations of the rocker arm deflections during the $2\pi$-period when the rocker arm is moving. During the other period of $2\pi$ when the rocker arm is motionless, the second order polynomial is a very poor method of approximation of the rocker arm deflection; therefore, a Fourier approximation was made of the second order polynomial and dwell portions of the rocker arm deflections.

Figure 4.17, and Figure 4.18, shows the ten-term Fourier approximation fit to the intake and exhaust rocker arm position data, respectively, over a $4\pi$-period and the error generated by this approximation is shown to be negligible.

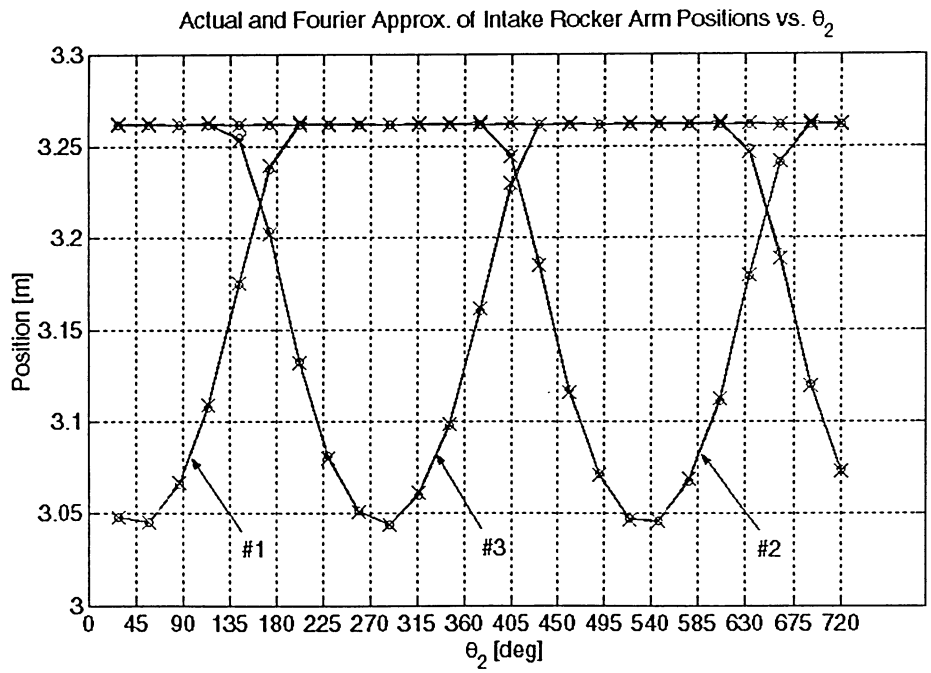


**Figure 4.17: Actual and Fourier approximation of the angular displacement of the intake rocker arms vs. $\theta_2$.**

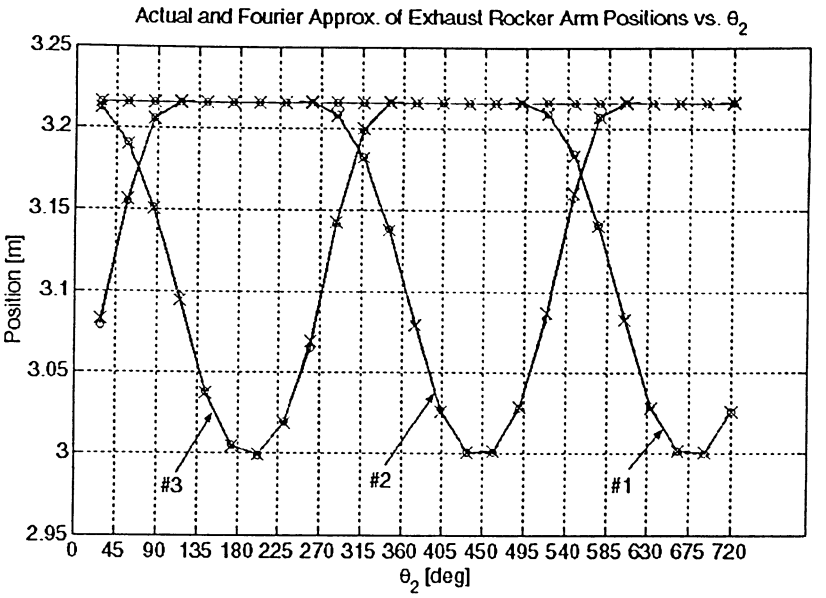


**Figure 4.18: Actual and Fourier approximation of the angular displacement of the exhaust rocker arms vs. $\theta_2$.**

To incorporate the effect of the rocker arms into the equation of motion, the kinetic energy of the rocker arms must be found. The position of the rocker arms was found and approximated with a Fourier series, and the first derivative of the Fourier approximation was taken with respect to the angular position of the crankshaft, which provides the angular velocity of the rocker arms, normalized to the crankshaft angle.

The velocity of the intake and exhaust rocker arms can be seen in Figure 4.19, and Figure 4.20, respectively. The angular velocity of the rocker arms is both positive and negative indicating a reversal of the angular position, which is exactly what happens during the motion of the member. The oscillations seen during the dwell period are in the order of $10^{-3}$ rad/s, which are negligible for this application.

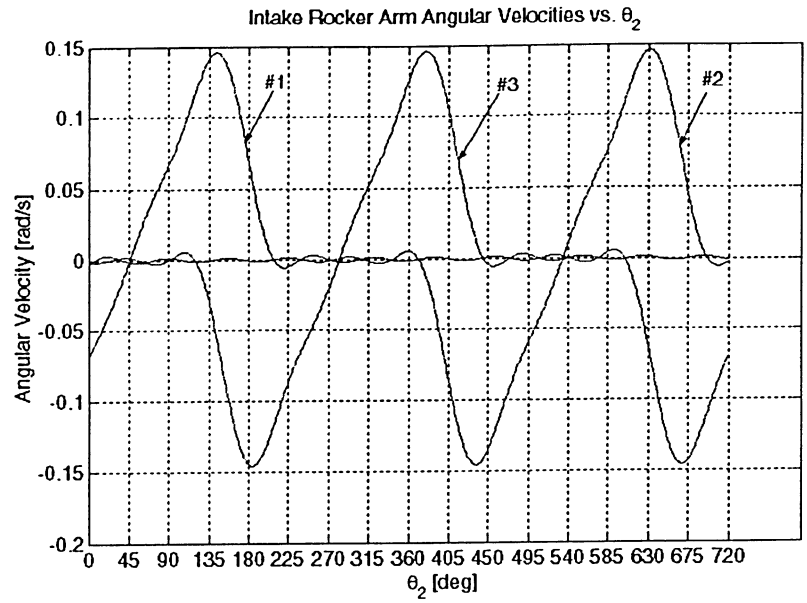


**Figure 4.19: Angular velocity of the intake rocker arms.**

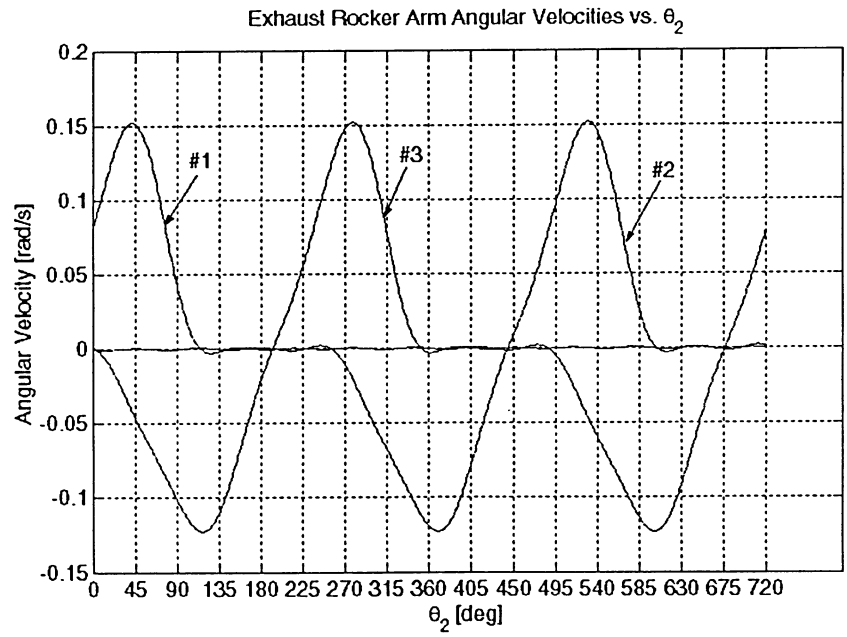


**Figure 4.20: Angular velocity of the exhaust rocker arms.**

The kinetic of the rocker arms can now be completed since the mass of the rocker arms is known as well as the normalized velocity of the rocker arms in functional form.

The next members to be analyzed were the valves, which are constrained to translational motion by bushings. The valves are acted upon by the ends of the rocker arms that are not

attached to the push rods. See Figure 3.56, (a) and (b), for an illustration of the rocker arm-valve contact arrangement.

The linear position of the valves is proportional to the angular position of the rocker arms multiplied by the length of the rocker arm as measured from the fulcrum to the point of contact. Eq. (4.12) elucidates this arrangement.

$$h_{valve} = r_{RA} \sin(-\alpha_r) \tag{4.12}$$

where $r_{RA}$ is the length of the rocker arm from the flcrum to the valve contact point ($r_{RA} = 1.384$), and $\alpha_r$ is the angular position of the rocker arm and the negative sign is to account for the direction of the angular displacement in this context.

The deflection of the intake valves was found using Eq. (4.12) and was approximated with a ten-term Fourier series to accurately approximate the dwell period. The position of the intake and exhaust valves can be seen in Figure 4.21, and Figure 4.22, respectively, superimposed with the ten-term Fourier approximation with negligible error.

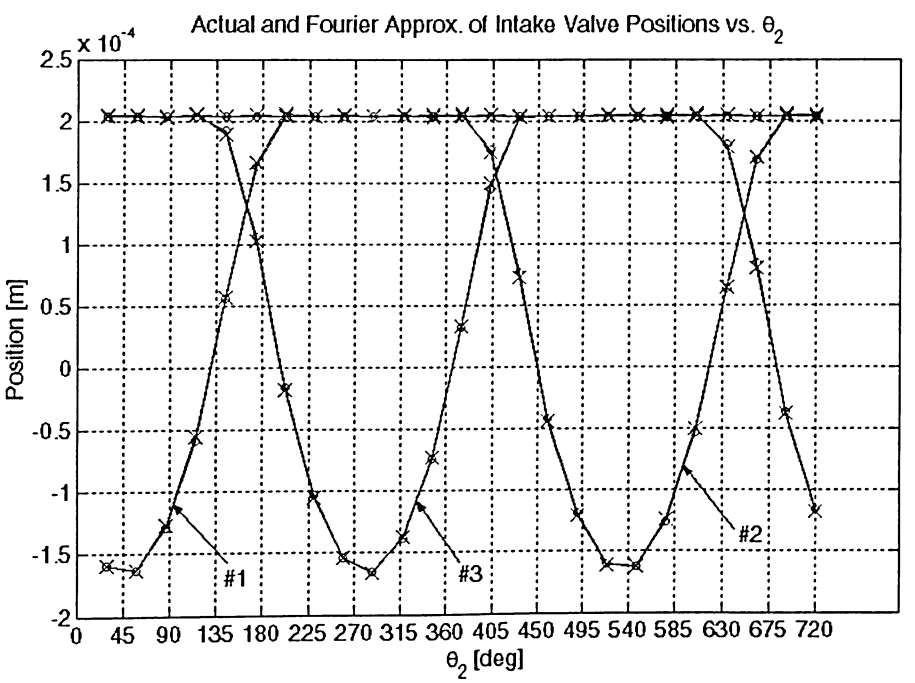


**Figure 4.21: Actual and Fourier representation of the intake valve positions vs. $\theta_2$.**

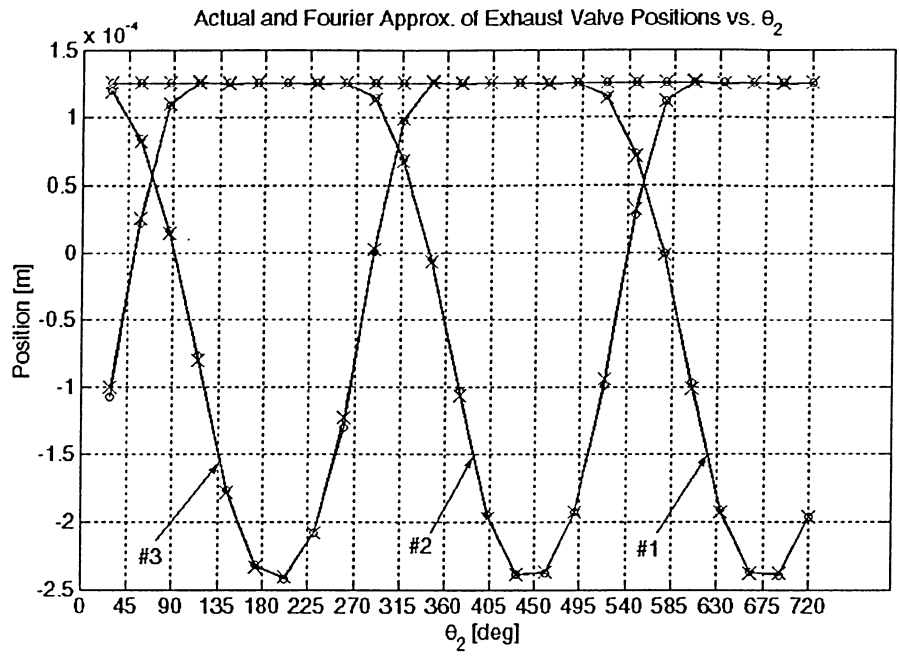


**Figure 4.22: Actual and Fourier representation of the exhaust valve positions vs. $\theta_2$.**

The position of each valve was found in functional form for the entire $4\pi$-period, the first derivative of the Fourier approximation of each valve can be taken to obtain the velocity of that valve while preserving the phase shift created by the firing sequence of the engine. The velocity information will be used to obtain the kinetic energy of each valve as a function of the crankshaft position.

Figure 4.23, and Figure 4.24, each show that the velocity of the intake and exhaust valves, respectively, have regions of essentially zero velocity, the dwell, followed by negative velocities indicating the valves are moving toward the axis of rotation of the crankshaft. During this period the valves are being opened by the cam. The velocity of the valves then changes sign, indicating the valves are slowing down as they approach the fully opened position. The velocities then reach zero and it is at this point that the valves are fully opened. The velocities then continue with positive slopes as the valve is closing and moving radially outward, away from the axis of rotation of the crankshaft. The velocities of the valves then slow down as they approach a zero value and during this portion of the valve motion; they are also slowing down as the valves reach the fully closed position. When the velocities are zero during the dwell phase, they are fully closed and remain in this position until the cycle repeats.

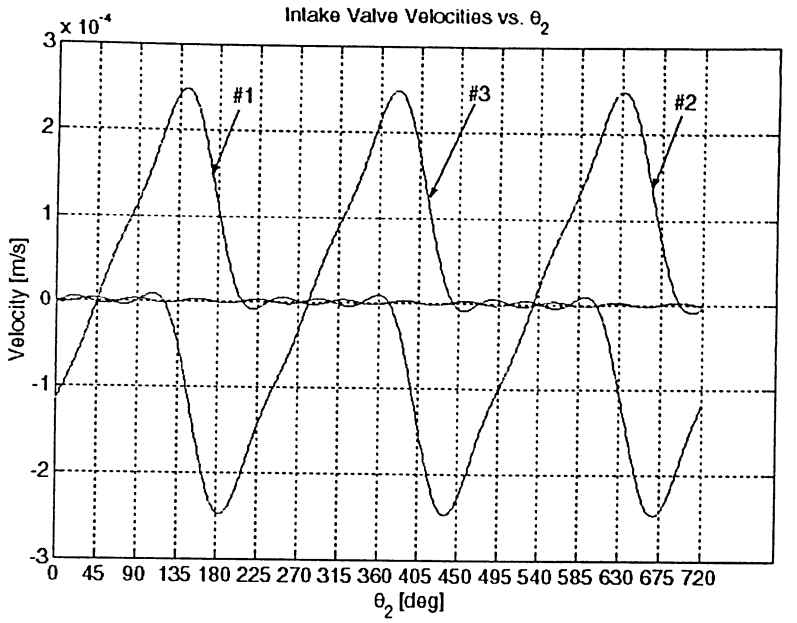


**Figure 4.23: Intake valve velocities vs. $\theta_2$.**

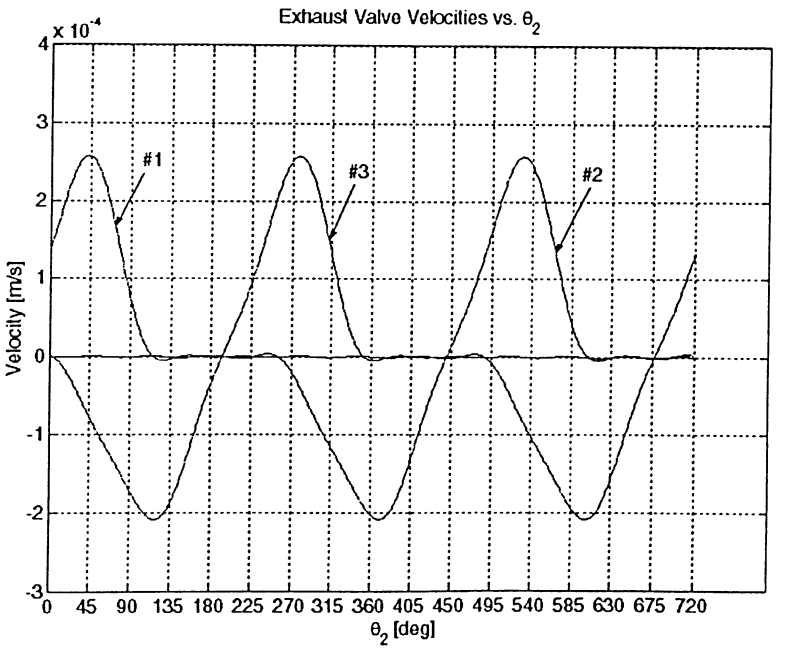


**Figure 4.24: Exhaust valve velocities vs. $\theta_2$.**

The velocity of each valve has been found in functional form preserving the phase shift caused by the firing sequence of the engine.

The last component of the accessory mechanism is the spring that provides the restoring force to return the mechanism to the undeflected position once the cam has passed through the point of maximum deflection.

The kinetic energy of the spring was be neglected since it has a minimal effect on the equation of motion. The potential energy contained within a deflected spring is described by Eq. (4.13)

$$U_{spring} = \frac{1}{2}k(\Delta + x_{sp})^2 \tag{4.13}$$

In Eq. (4.13), $k$ is the spring constant, $\Delta$ is the position of static equilibrium and $x_{sp}$ is the displacement from the static equilibrium position. To make use of Eq. (4.13), each of these three variables must be quantified.

The spring constant, $k$, was experimentally determined as being 833.3 N/m. The procedure for finding this value was to measure the length of the undeflected spring, and then place a known mass on the spring to compress it and measure the resulting deflection. During this test, four masses were placed on the spring and the resulting deflections were recorded in Table 4.3.

**Table 4.3: Spring deflection data.**

| Mass [kg] | Position [m] | Approx. [m] | Error [%] |
|---|---|---|---|
| 0.411 | 0.01787 | 0.01783 | -0.22 |
| 0.821 | 0.01736 | 0.01731 | -0.30 |
| 1.230 | 0.01685 | 0.01679 | -0.37 |
| 1.634 | 0.01641 | 0.01628 | -0.80 |

There are two major types of springs available for use and they are characterized by their response to deflection. These two categories are linear and non-linear. To determine which type of spring is being used in this engine, the first two columns of Table 4.3 were plotted and shown in Figure 4.25. If the resulting curve is linear then the spring is of the linear category; if the response is non-linear then the spring falls into that category, and the analysis becomes more complicated.

Figure 4.25 shows the raw data superimposed with a linear approximation. Equation (4.14) is the equation for the linear approximation.

$$y_{spr} = -0.0012x_{sp} + 0.0184 \tag{4.14}$$

The deflection generated by the approximating function can be seen in the third column of Table 4.3, and the percent error between the original deflection and the approximate deflection can be seen in the fourth column of Table 4.3.

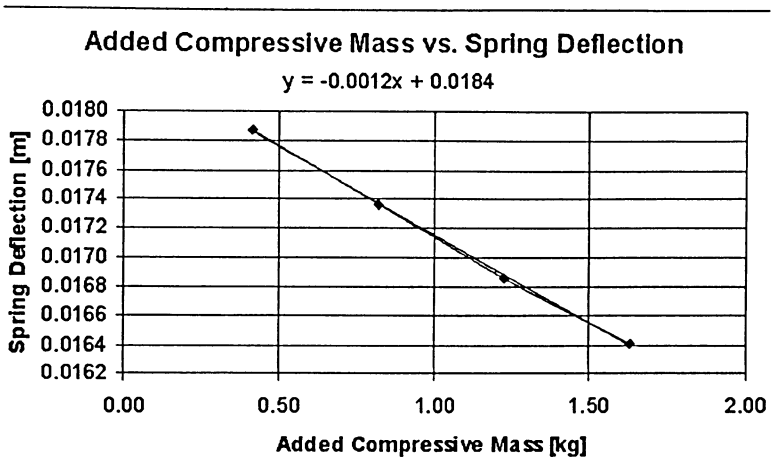


**Figure 4.25: Compressive mass vs. spring deflection.**

The maximum absolute percent error generated by the linear approximation is 0.8%, which corresponds to a maximum error in position of $1.313 \times 10^{-4}$m, or 0.131mm. This very small error in position can be considered negligible for this application.

The spring constant can be obtained from the linear approximation of the deflection data found in Figure 4.25. Since the spring was shown to be linear, the spring constant is the reciprocal of the slope of the mass vs. deflection line. In this case, the spring is a compression spring so the slope of the line is negative, but in order to obtain the spring constant, the positive slope value is required. From Figure 4.25, the slope of the line is -0.0012, the negative reciprocal being 833.3, so the spring constant used was 833.3 N/m.

From Eq. (4.12), the position of the valves is known as a function of the crankshaft angular position, and from direct observation of the spring-valve portion of the mechanism, it is known that the motion of the springs follow the motion of the valves in a 1:1 ratio. Therefore, the motion of the springs has already been described by the motion of the valves.

Since the kinetic energy of the springs was neglected, the potential energy of the springs is described by Eq. (4.13). The potential energy term in the Lagrange equation is $\frac{\partial U}{\partial \theta_2}$, so the potential energy of the spring is described by Eq. (4.15).

$$\frac{\partial U_i}{\partial \theta_2} = -\frac{1}{2} k \frac{\partial}{\partial \theta_2} \left[ x_i(\theta_2)^2 \right] \tag{4.15}$$

where $k$ is the spring constant, and $x_i(\theta_2)$ is the deflection of the $i^{th}$ valve being considered.

The last detail of the spring to take into account before proceeding is the fact that the spring is preloaded when installed in the engine. The preload has the effect of offsetting the reference position of the spring deflection from zero to, in this case a positive value. Figure 4.26, (a) and (b), shows the spring force vs. deflection response without and with preload, respectively.

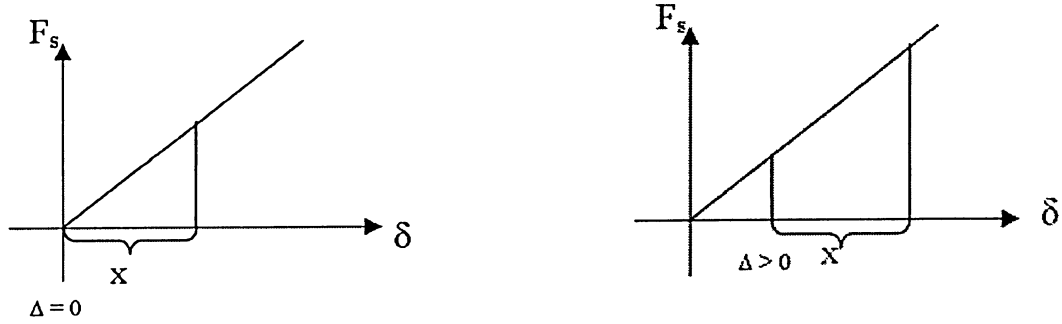


**Figure 4.26: Spring force ($F_s$) vs. deflection response ($\delta$) without (a) and with preload (b).**

The preload of the spring was determined through direct measurement to be $3.683 \times 10^{-4}$m. This preload value was subtracted from the position of the respective valve to obtain the proper spring response, which includes the preload, for a given angular position of the crankshaft.

The position of the springs was found through the use of the respective valve position, minus the preload value; then this position information was squared and approximated with a ten-term Fourier approximation to represent the discrete data in functional form with a period of $4\pi$. The first derivative with respect to the crankshaft angular position $\theta_2$ was taken of the squared spring position function to obtain the $\frac{\partial}{\partial \theta_2}\left[x_{i,1}(\theta_2)^2\right]$ portion of the spring potential energy found in Eq. (4.15).

The potential energy of each spring was calculated by multiplying the $\frac{\partial}{\partial \theta_2}\left[x_{i,1}(\theta_2)^2\right]$ portion of the potential energy equation previously found with the remaining $-\frac{1}{2}k$.

The potential energy of the intake and exhaust springs can be seen in Figure 4.27, and Figure 4.28, respectively. The potential energy shown in Figure 4.27, and Figure 4.28, indicates that there is a dwell period of $2\pi$ when the spring is not moving, and a period of $2\pi$ when the spring is in motion. These two distinct regions of motion correspond to the same regions of valve motion for each respective spring-valve combination.

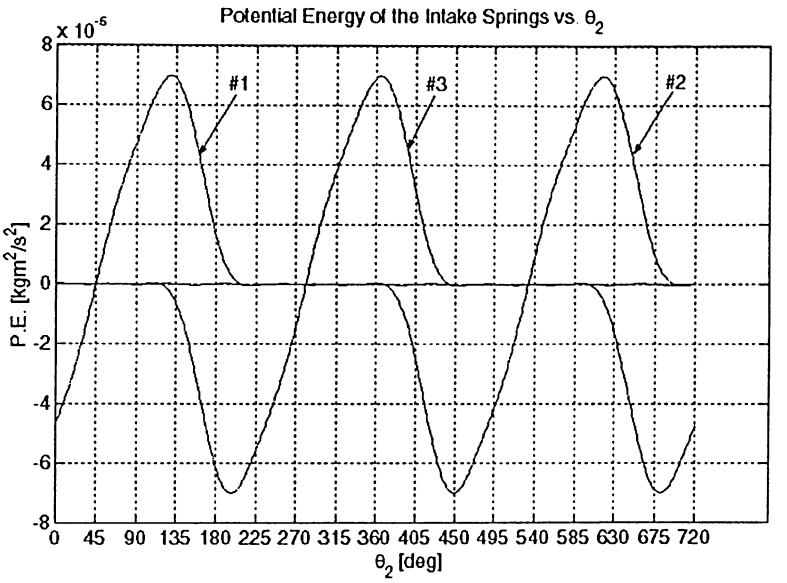


**Figure 4.27: Potential energy of the intake springs vs. $\theta_2$.**

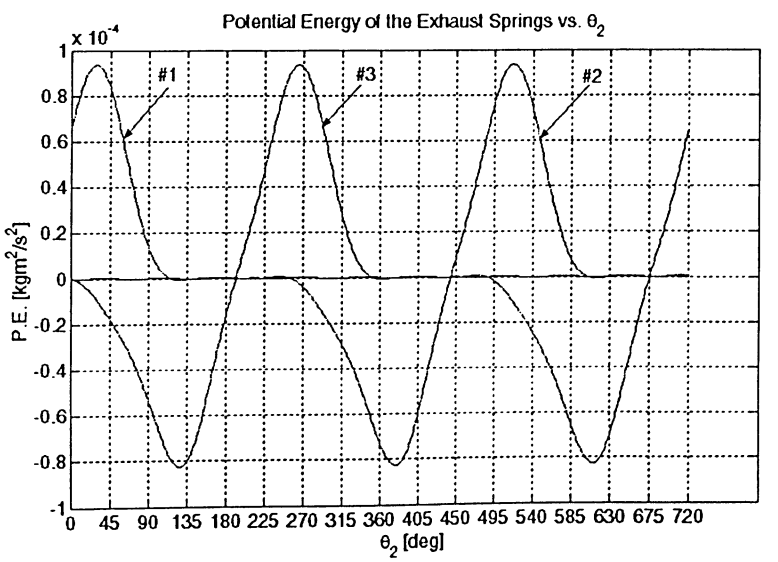


**Figure 4.28: Potential energy of the exhaust springs vs. $\theta_2$.**

Figure 4.29 is the potential energy from all contributing members of the accessory drive system summed at each angular crankshaft position.

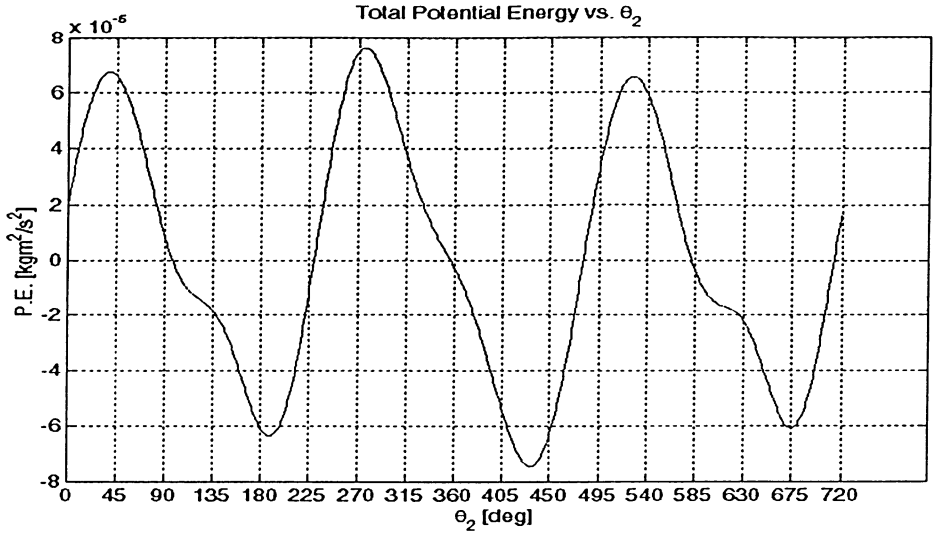


**Figure 4.29: Total potential energy vs. $\theta_2$.**

The equation of motion has been derived for the Saito-450 internal combustion engine, first neglecting the accessory system, then including the effects of the accessory system. The engine kinematics has been derived and all quantities have been found, which allows all required variables to be calculated and converted into functional form.

## *Section 4.3 Fourier Series Representations*

Any general periodic function can be represented as an infinite series of sines and cosines [Inmann, 2001]. Since the sine and cosine functions are continuous, a Fourier series is a method to represent a discrete signal in functional form. An infinite number of terms is impractical to implement, the number of Fourier coefficients required to represent the various discrete quantities varied depending on the complexity of the array; however, in all cases negligible error was observed.

### *Section 4.3.1 Kinetic Energy*

The kinetic energy for the engine system without and with the accessory drive is shown in Figure 4.30, and Figure 4.31, respectively. Superimposed on Figure 4.30 is the Fourier representation (without accessories) generated with ten harmonic terms, and superimposed on Figure 4.31 is the Fourier representation (with accessories) generated with fifteen harmonic terms. The error resulting from the Fourier series representations is negligible.

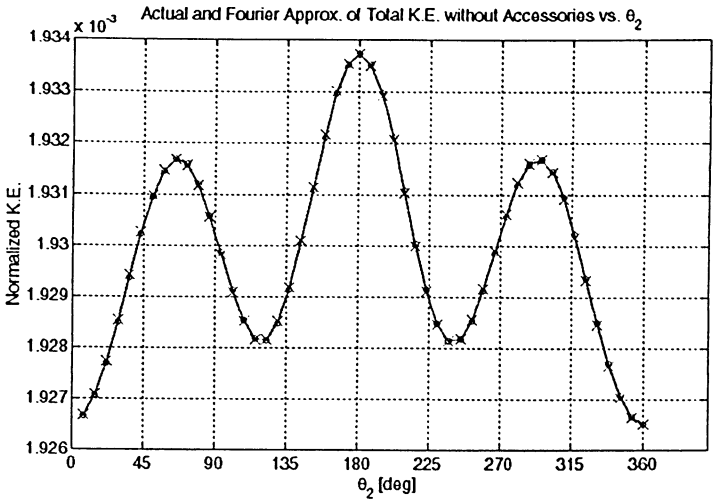


**Figure 4.30: Actual and Fourier representation of the total kinetic energy neglecting accessories vs. $\theta_2$.**

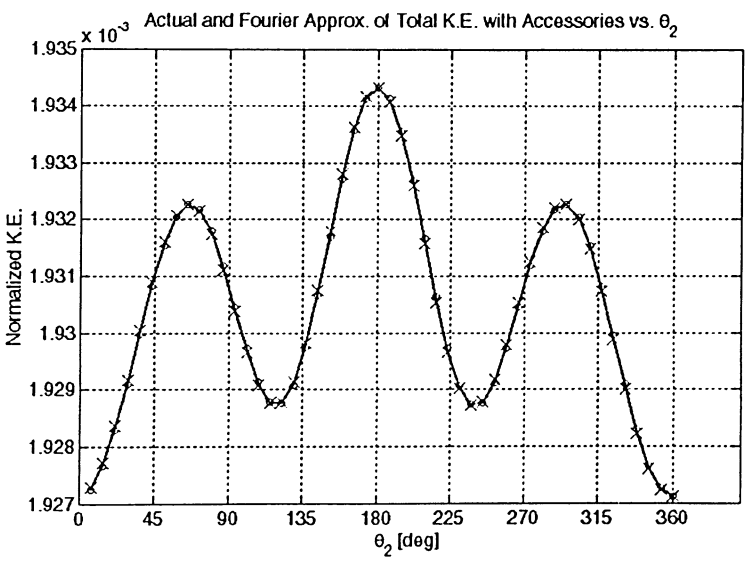


**Figure 4.31: Actual and Fourier representation of the total kinetic energy with including vs. $\theta_2$.**

The difference between Figure 4.30 and Figure 4.31 is that Figure 4.31 has been shifted vertically upward due to addition of the camshaft subsystem.

The kinetic energy has been found in functional form through the use of ten- and fifteen-term Fourier series. The derivative of the kinetic energies taken with respect to $\theta_2$ is also required to complete the equation of motion.

The plot of the derivative of the kinetic energy is the same for both test cases, and can be seen in Figure 4.32. Superimposed on the original data is the ten-term Fourier approximation with minimal error.

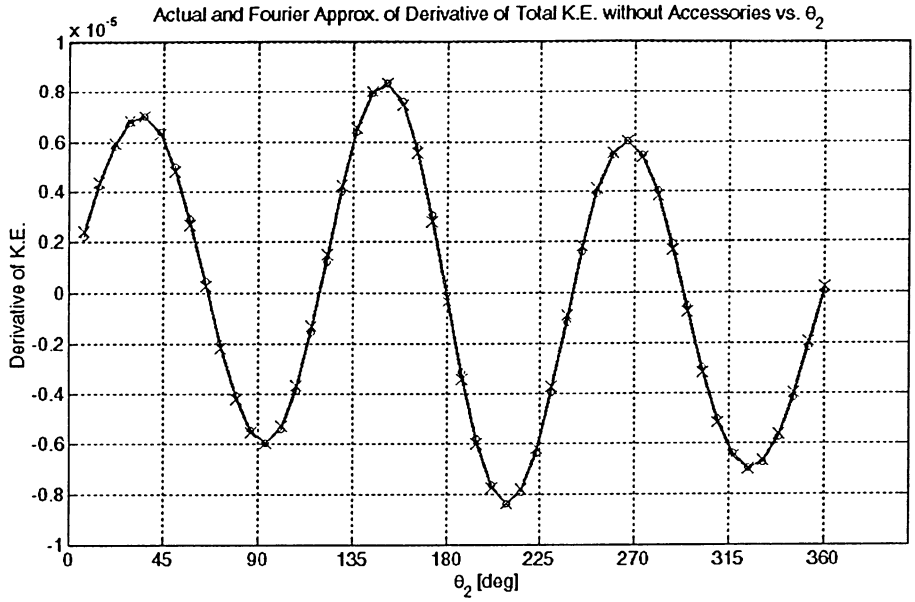


**Figure 4.32: Actual and Fourier representation of the derivative of the kinetic energy w.r.t $\theta_2$ vs. $\theta_2$.**

The derivative of the kinetic energy has been successfully represented in functional form, thereby fully defining the left hand side of the equation of motion. The one remaining quantity to approximate with a Fourier series representation is the gas work done on the pistons.

## *Section 4.3.2 Gas Work*

A plot of the gas work per cylinder at 100% throttle is superimposed with a ten-term Fourier series representation can be seen in Figure 4.33. The gas work is independent of the accessory system; therefore, only one set of curves is shown. Qualitatively the approximation is a good fit to the original data and the error is considered to be negligible.

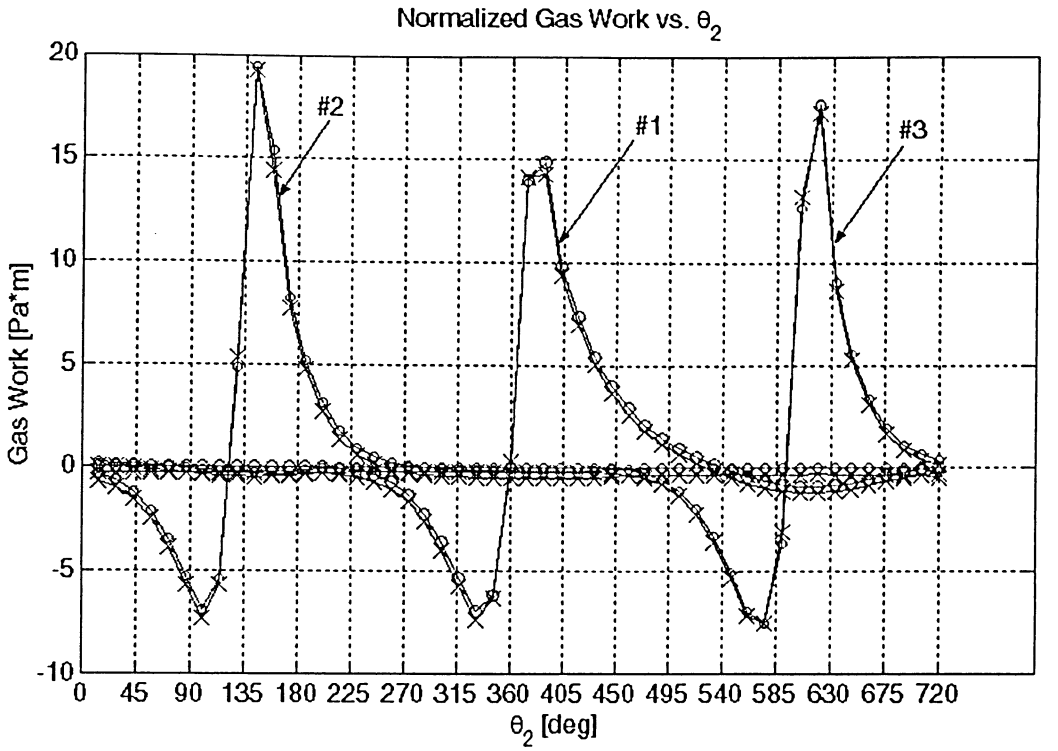


**Figure 4.33 : Actual and Fourier approximation of the gas work as a function of the crankshaft angular position.**

All of the engine related terms appearing in the equation of motion have now been represented in functional form, suitable for calculation by the Euler differential equation solver.

## *Section 4.4 Results – No Accessories*

The engine simulation including the propeller was first performed without the accessory drive system included to ensure that the baseline methodology and implementation was sound. The cylinder firing sequence and the P-$\theta_2$ curve are unchanged with respect to the cam system but the energy associated with the accessory system was not included.

Through the use of a fixed step Euler ODE solver over a time span of seven seconds (to ensure that the engine has reached a steady state condition while minimizing the required solution time), the resulting steady state RPM was in good agreement with what was expected from power balance hand calculations.

The solution strategy was to start the engine at 0 degrees for the crankshaft corresponding to cylinder #1 being at top dead centre and to provide an initial angular velocity of 210 rad/s.

This was arbitrarily chosen to correspond to the very low end of the propeller load curves and to approximate actual starting conditions with reasonable accuracy.

The FFT of the angular velocity data revealed that the strongest harmonic was the 1.5 harmonic, followed by the 3.0, and 1.0. This is consistent with the expected result, which was that the strongest harmonic would be the 1.5 due to the combination of $2\pi$ and $4\pi$-periodic functions that exist simultaneously within the engine system.

## *Section 4.5 Results at 4", 6", and 8"Blade Pitch Values – No Accessories*

The results of the simulation performed without the accessory system are found in Figure 4.35 to Figure 4.40 for throttle settings ranging from 35% to 100%. The analysis for the 4" and 6" blade pitch ends at 75% and 85% throttle, respectively, because the system becomes speed limited. Only four throttle settings were selected to show since all results figures are very similar.

Plot (a) of Figure 4.34 shows the angular position of the crankshaft as a function of time, which is nearly linear and monotonically increasing.

Plot (b) of Figure 4.34 is the plot of the crankshaft angular velocity as a function of time. The plot of omega vs. time shows that after starting with initial conditions of angular position and velocity, the operating speed of the engine increases to reach a steady state value after a short period of time. There is some oscillation in this plot throughout the operating range and this is due to the rotational (periodic) nature of the kinetic energy, potential energy, the firing sequence and the $4\pi$-periodic pressure vs. crank angle characteristic. Superimposed on the angular velocity plot is a flat line, which is the expected steady state operating speed as calculated by a power balance between engine and propeller.

Plot (c) of Figure 4.34 is the FFT representation of the angular velocity vs. time, taken at steady state conditions. Plot (c) shows a dominating harmonic of 1.5, followed by 3.0, and 1.0. The dominating harmonic of 1.5 is a result of the system components having both $2\pi$ and $4\pi$-periodic components. The 3.0 harmonic is the first integer multiple of the 1.5 harmonic and the 1.0 harmonic is the operating speed of the engine.

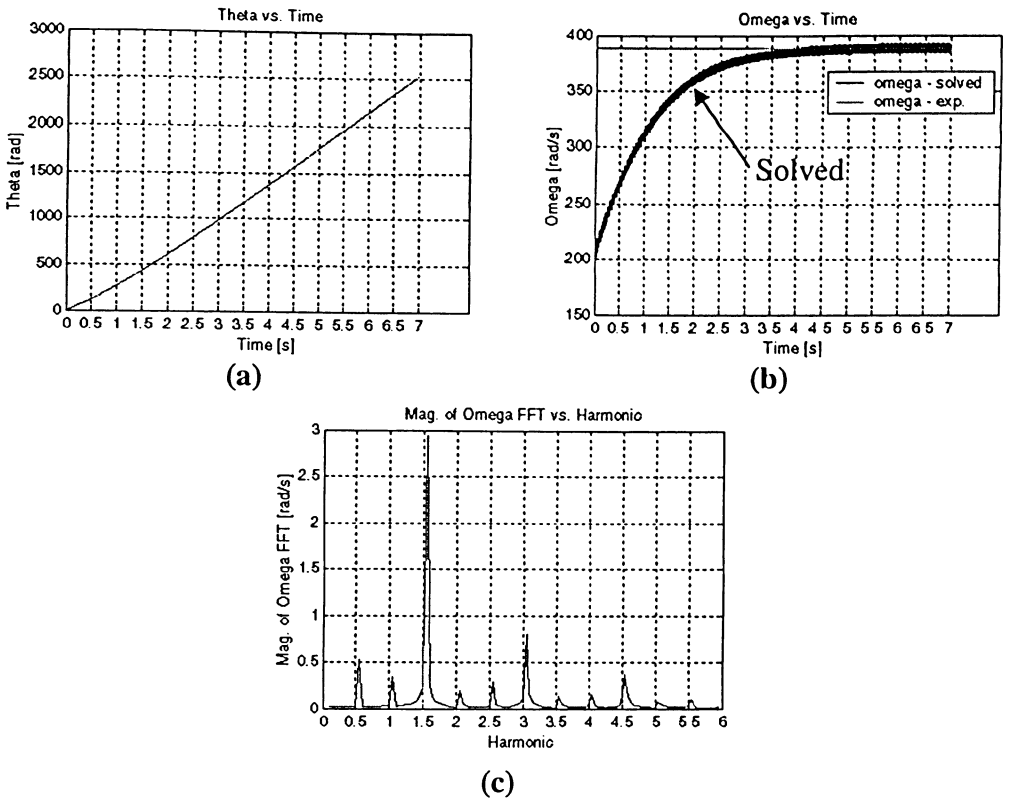


**Figure 4.34: Complete results obtained at a 4″ blade pitch and 35% throttle setting.**

For all test cases, Figure 4.34 (a) was monotonically increasing. As such, the author focused on the omega vs. time and FFT of omega vs. time results, which provided the most useful information. Figure 4.35 to Figure 4.37 shows the omega vs. time results for four selected throttle settings at each of the three blade pitch values considered. In each test case, the engine operating speed increased from the initial speed condition to reach a predicted steady-state value after a short period of time.

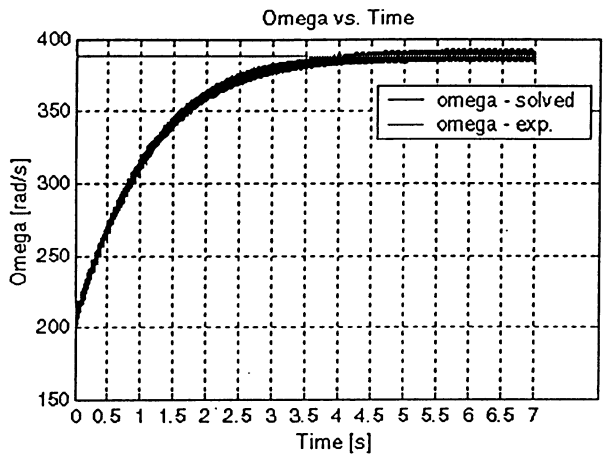


35%

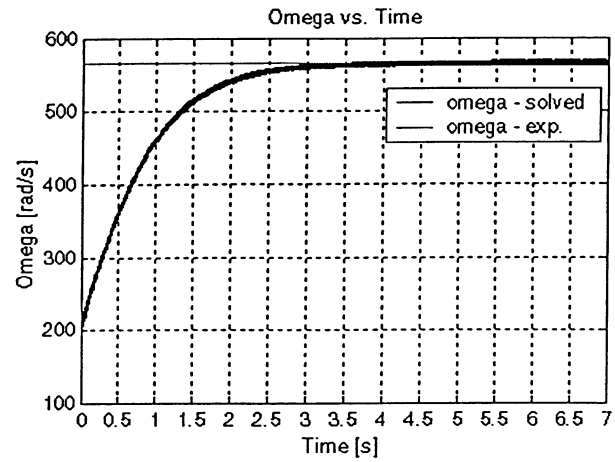


50%

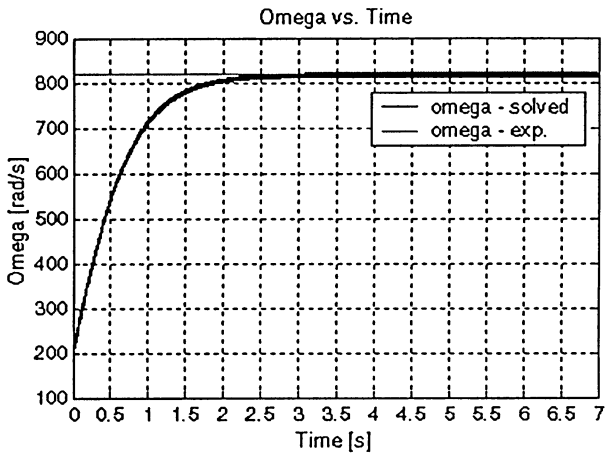


75%

Not Available

85% or 100%

**Figure 4.35: ω vs. time for 4″ blade pitch at 35%, 50%, and 75% throttle settings - without accessories.**

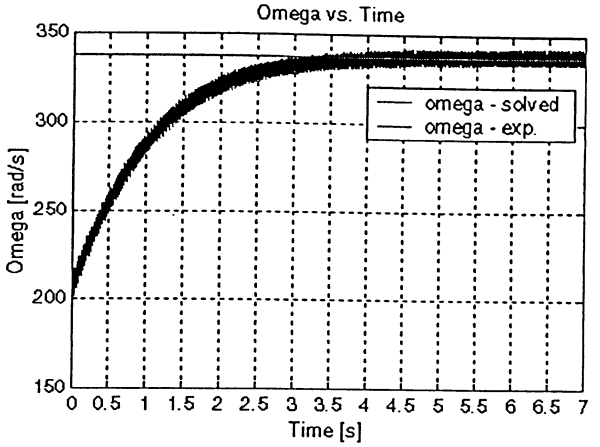


35%

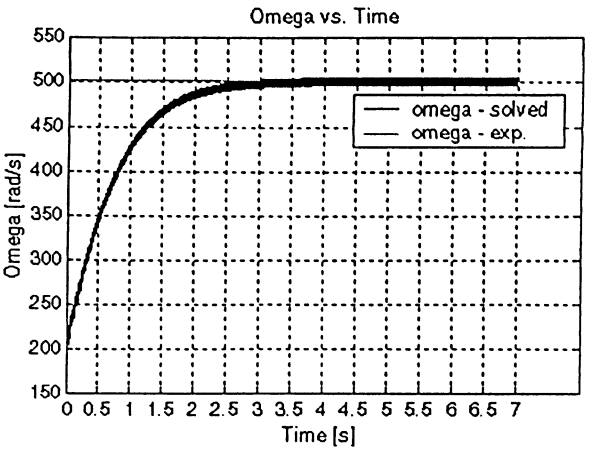


50%

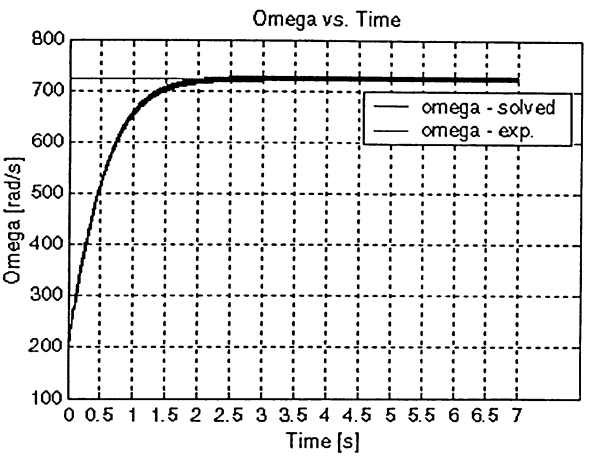


75%

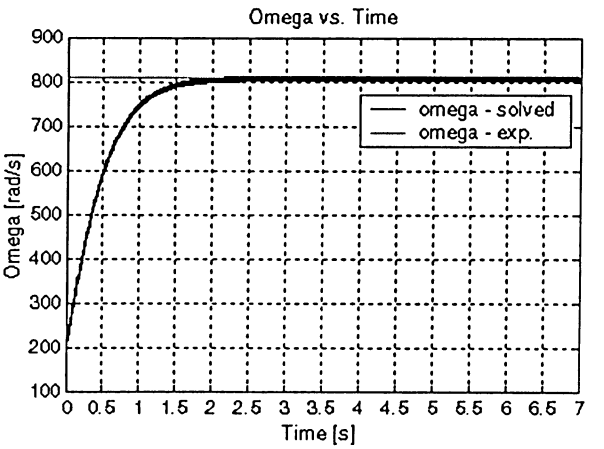


85%

**Figure 4.36: ω vs. time for 6″ blade pitch at 35%, 50%, 75%, and 100% throttle settings - without accessories.**

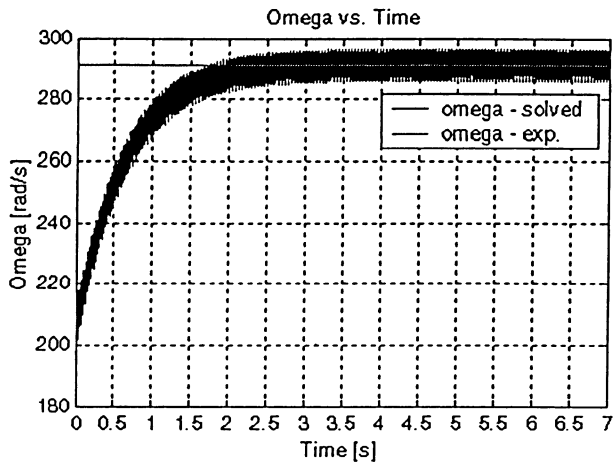


35%

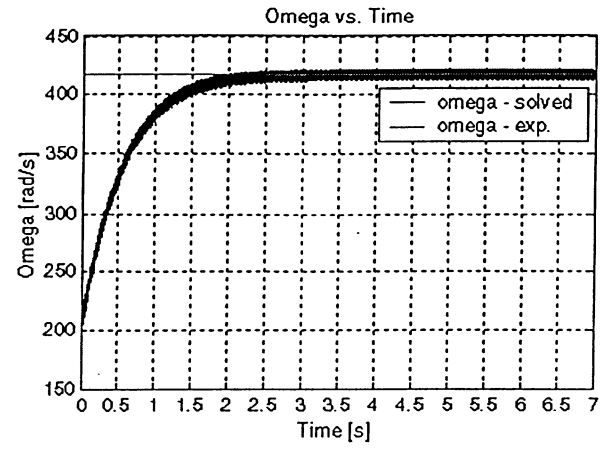


50%

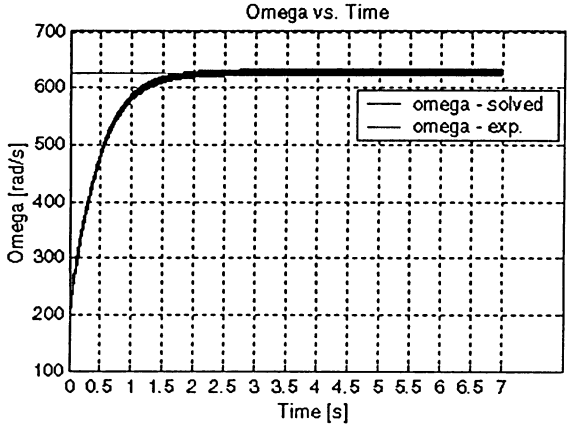


75%

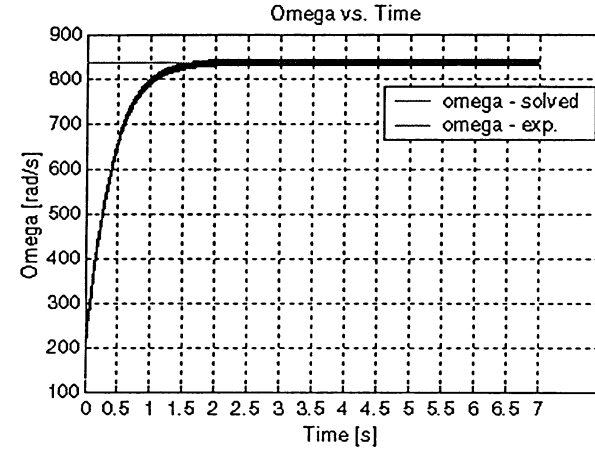


100%

**Figure 4.37: ω vs. time for 8″ blade pitch at 35%, 50%, 75%, and 100% throttle settings - without accessories.**

Figure 4.38 to Figure 4.40 shows the FFT results from each corresponding to the results presented in Figure 4.35 to Figure 4.37. In each test case the 1.5 harmonic was found to dominate, followed by the 3.0 and then the 1.0.

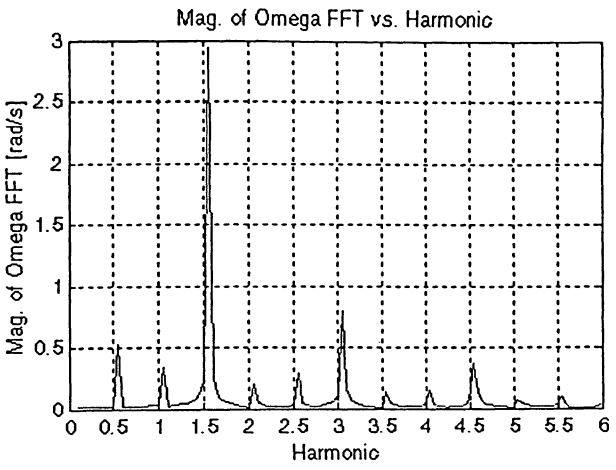


35%

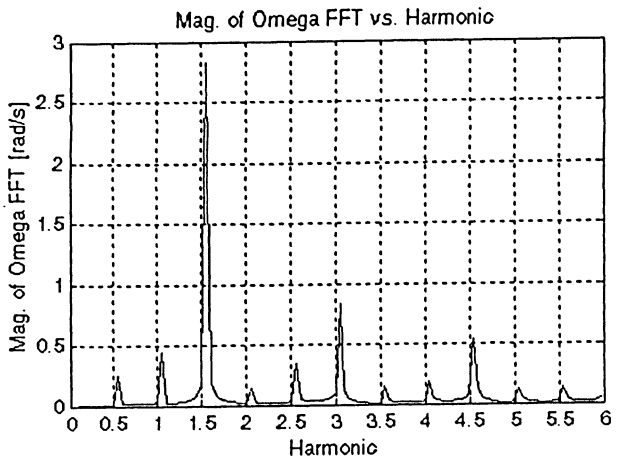


50%

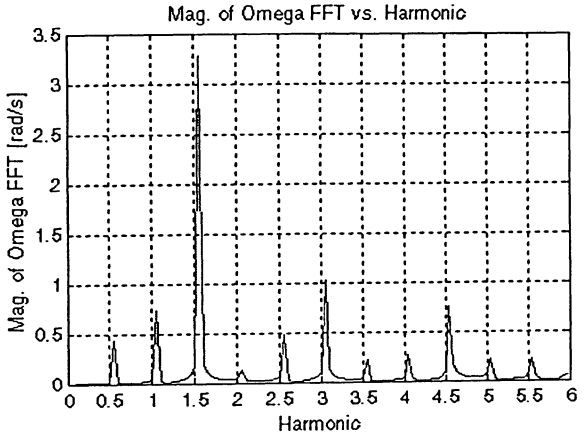


75%

Not Available

85% or 100%

**Figure 4.38: Harmonic spectrum of Figure 4.35 for a 4″ blade pitch setting at 35%, 50%, and 75% throttle settings - without accessories.**

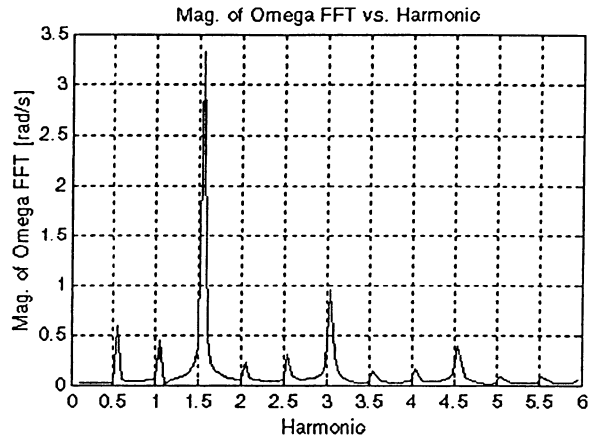


35%

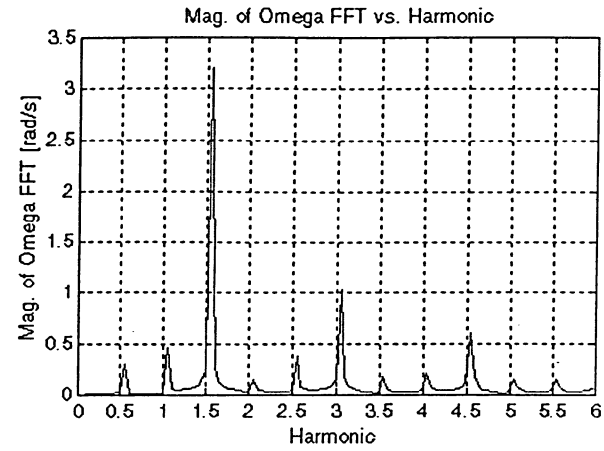


50%

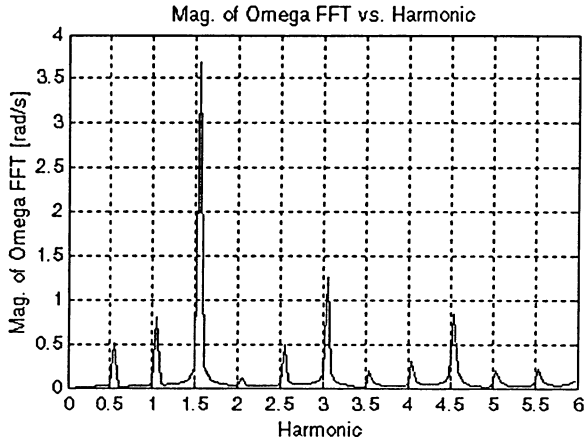


75%

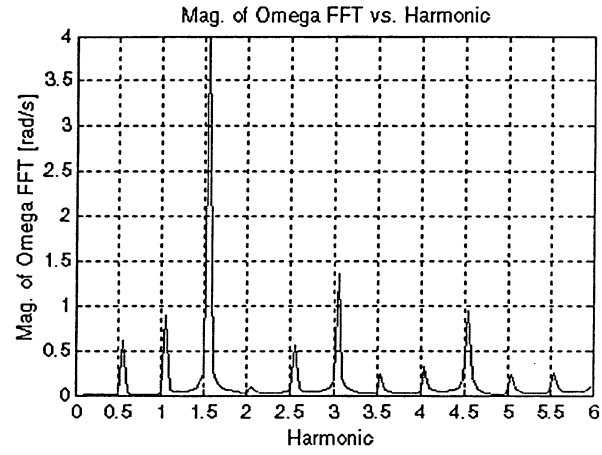


85%

**Figure 4.39: Harmonic spectrum of Figure 4.36 for a 6″ blade pitch setting at 35%, 50%, 75% and 85% throttle settings - without accessories.**

Figure 4.42 shows a comparison of the 0.5 harmonic peaks as a function of throttle setting for each of the three blade pitch values. Each of the plots shown follows a similar trend of decreasing from a throttle setting of 35% to a throttle setting of 55% and then increasing once again from a throttle setting of 55% to the maximum throttle setting permissible for each blade pitch.

For blade pitch settings of 4″, 6″, and 8″ the harmonic magnitudes at 35% throttle are at a maximum value of 0.526 rad/s, 0.584 rad/s and 0.674 rad/s, respectively. Each plot then decreases in magnitude to 0.240 rad/s, 0.298 rad/s and 0.358 rad/s at 55% throttle, respectively, before increasing to a final value of 0.433 rad/s at 75% throttle, 0.616 rad/s at 85%, and 0.880 rad/s at 100% throttle, respectively.

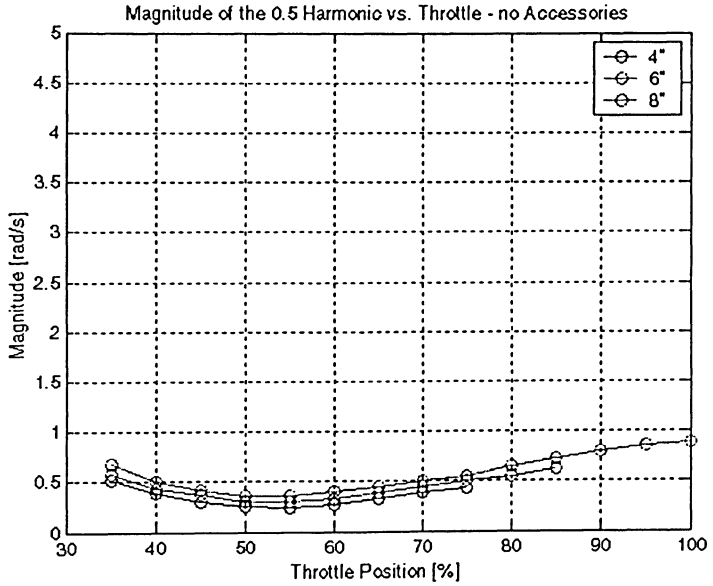


**Figure 4.41: Comparison of FFT results for the 0.5 harmonic for each blade pitch value without accessories.**

Figure 4.42 shows a comparison of the 1.0 harmonic peaks as functions of throttle setting for each of the three blade pitch values considered. The plots corresponding to blade pitch settings of 4″ and 6″ follow a similar trend in that they first decrease to a minimum and then increase in magnitude as the throttle position is increased. The plot of the 1.0 harmonic corresponding to a blade pitch setting of 8″ continually increases as the throttle setting is increased.

With the propeller set to blade pitch values of 4″ and 6″, the magnitude of the 1.0 harmonic at 35% throttle is 0.341 rad/s and 0.443 rad/s, respectively. The magnitude then decreases to a minimum of 0.320 rad/s and 0.431 rad/s at 40% throttle, respectively and then continuously increases to a maximum value of 0.731 rad/s at 75% and 0.900 rad/s at 85% throttle.

When the blade pitch was set to 8″, the amplitude of the 1.0 harmonic was 0.418 rad/s at 35% throttle and continually increased to a maximum of 1.159 rad/s at a maximum throttle setting of 100%.

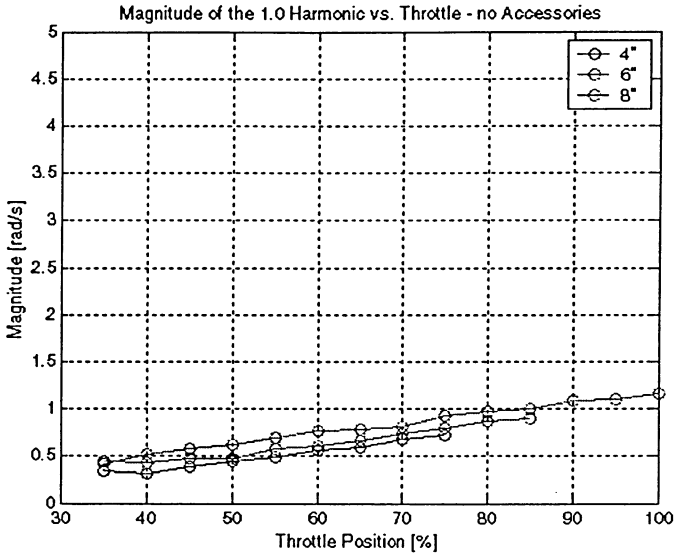


**Figure 4.42: Comparison of FFT results for the 1.0 harmonic for each blade pitch value without accessories.**

Figure 4.43 shows each of the plots for the 1.5 harmonic follow a similar pattern of first decreasing to a minimum amplitude and then increasing harmonic amplitude with increasing throttle position until a respective maximum throttle position is achieved. Examining the 1.5 harmonic with the propeller set to 4″, 6″, and 8″ blade pitch settings, the harmonic amplitude is 2.940 rad/s, 3.333 rad/s, and 3.867 rad/s at a throttle setting of 35%, respectively. The harmonic amplitude then decreases to a minimum value of 2.791 rad/s, 3.169 rad/s, and 3.750 rad/s, respectively, at a throttle setting of 45%. As the throttle is increased beyond 45% the amplitude of the 1.5 harmonic also increases to a maximum value of 3.281 rad/s, 3.982 rad/s and 4.880 rad/s at throttle settings of 75%, 85%, and 100%, respectively.

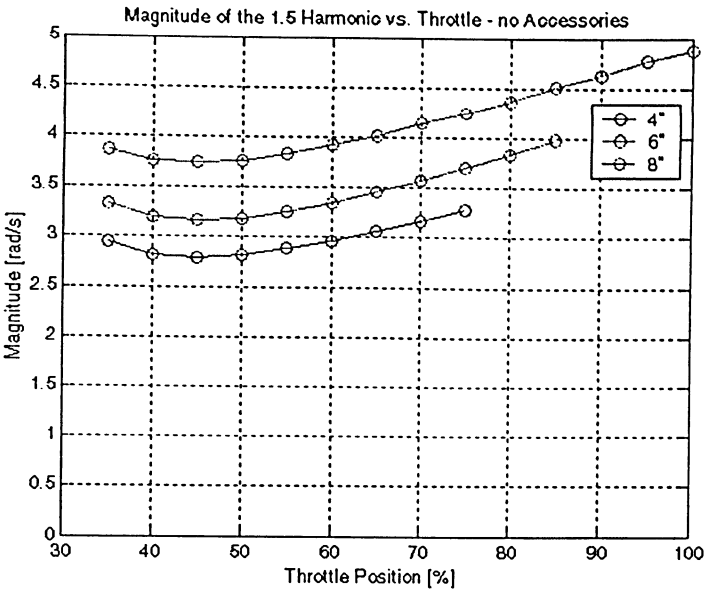


**Figure 4.43: Comparison of FFT results for the 1.5 harmonic for each blade pitch value without accessories.**

Figure 4.44 shows a comparison of the 2.0 harmonic peaks as a function of throttle setting for each of the three blade pitch values. Each of the 2.0 harmonic plots follows a similar trend and that is a decrease in harmonic amplitude with increasing throttle position.

When the blade pitch set to 4″, the maximum harmonic amplitude is found to be 0.197 rad/s at a throttle setting of 35%. The amplitude corresponding to the 4″ blade pitch then decreases to a minimum value of 0.110 rad/s at 65% throttle and increases to 0.135 rad/s as the throttle is increased to 75%.

For the case of the blade pitch set to 6″ and 8″, the maximum harmonic amplitude was found to be 0.233 rad/s and 0.302 rad/s, respectively, at a throttle setting of 35% and decreases to a minimum value of 0.097 rad/s and 0.106 rad/s, respectively, at a maximum throttle position of 85% and 100%, respectively.

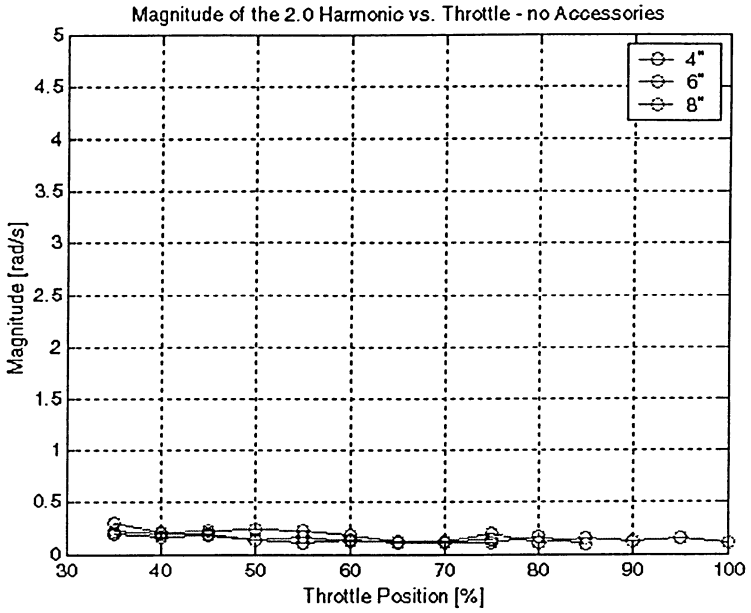


**Figure 4.44: Comparison of FFT results for the 2.0 harmonic for each blade pitch value without accessories.**

When considering Figure 4.45, the 2.5 harmonic is constantly increasing as the throttle position is increased at blade pitch settings of 4″, 6″, and 8″. The minimum harmonic amplitude is found to be 0.290 rad/s, 0.317 rad/s, and 0.369 rad/s, respectively, at 35% throttle and increases to a maximum value of 0.473 rad/s, 0.561 rad/s, and 0.691 rad/s at maximum throttle settings of 75%, 85%, and 100%, respectively.

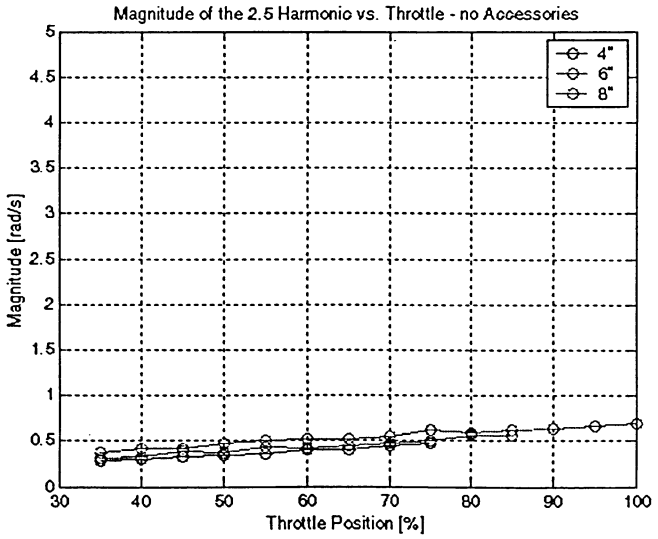


**Figure 4.45: Comparison of FFT results for the 2.5 harmonic for each blade pitch value without accessories.**

Figure 4.46 shows a comparison of the 3.0 harmonic peaks as a function of throttle setting for each of the three blade pitch values. Each of the plots in Figure 4.46 follows the same general trend and that is constantly increasing as the throttle position is increased.

For the cases when the propeller was set to blade pitch values of 4″, 6″, and 8″, the harmonic amplitude is 0.801 rad/s, 0.944 rad/s and 1.095 rad/s, respectively, at 35% throttle and increases to maximum values of 1.019 rad/s, 1.353 rad/s, and 1.740 rad/s at 75% throttle, respectively.

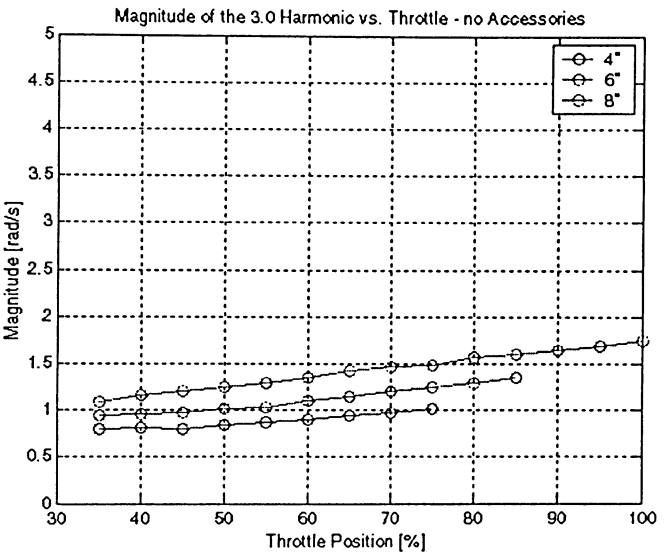


**Figure 4.46: Comparison of FFT results for the 3.0 harmonic for each blade pitch value without accessories.**

Figure 4.47 shows a comparison of the 3.5 harmonic peaks as a function of throttle setting for each of the three blade pitch values. The plot shows very little change in harmonic amplitude with an increase in throttle setting; however, the magnitude of the 3.5 harmonic does increase with increasing throttle setting.

When examining the 3.5 harmonic with the propeller set to blade pitch values of 4″, 6″, and 8″, the harmonic amplitude are 0.135 rad/s, 0.146 rad/s, and 0.197 rad/s at 35% throttle and increases to a value of 0.212 rad/s, 0.226 rad/s, and 0.268 rad/s at 75%, 85% and 100% throttle, respectively.

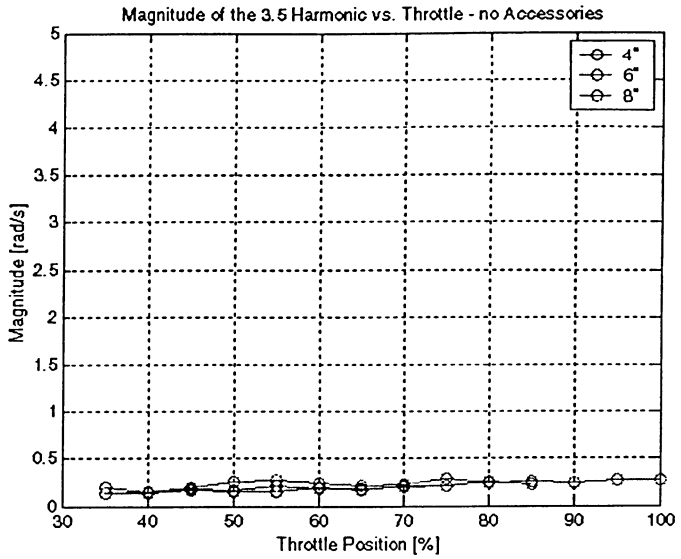


**Figure 4.47: Comparison of FFT results for the 3.5 harmonic for each blade pitch value without accessories.**

Figure 4.48 shows a comparison of the 4.0 harmonic peaks as a function of throttle setting for each of the three blade pitch values and the plot shows very little change in harmonic amplitude with an increase in throttle setting. When the blade pitch was set to 4″, 6″, and 8″, the harmonic amplitude increased from a minimum value of 0.147 rad/s, 0.154 rad/s, and 0.165 rad/s, respectively, at 35% throttle to a value of 0.270 rad/s, 0.324 rad/s, and 0.400 rad/s, respectively, at 75%, 85%, and 100% throttle, respectively.

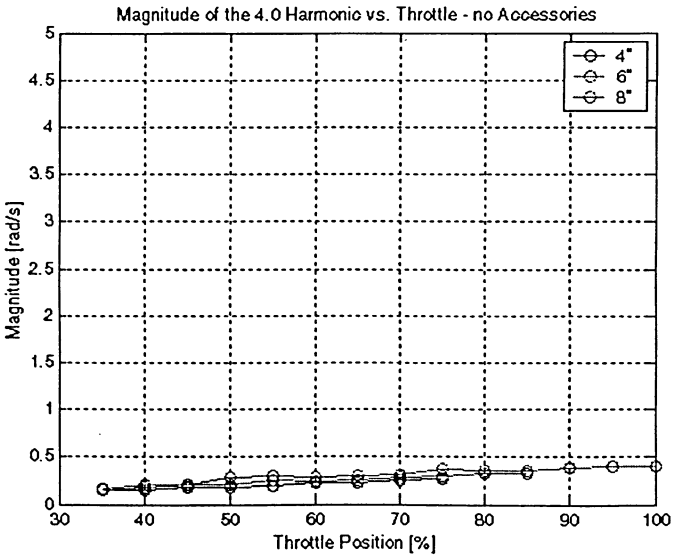


**Figure 4.48: Comparison of FFT results for the 4.0 harmonic for each blade pitch value without accessories.**

Figure 4.49 shows the 4.5 harmonic follows a trend of increasing harmonic amplitude with increasing throttle position at 4″, 6″, and 8″ blade pitch settings. The minimum amplitude of 0.375 rad/s, 0.386 rad/s, and 0.395 rad/s, respectively, corresponds to 35% throttle. The harmonic amplitude increases to the maximum value of 0.745 rad/s, 0.939 rad/s and 1.139 rad/s, respectively at a maximum throttle position of 75%, 85%, and 100%, respectively.

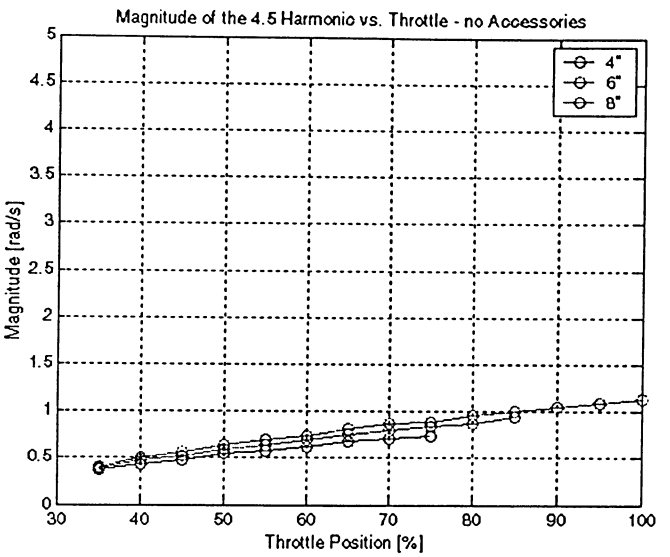


**Figure 4.49: Comparison of FFT results for the 4.5 harmonic for each blade pitch value without accessories.**

Figure 4.50 shows the 5.0 harmonic peaks as a function of throttle setting for each of the three blade pitch values follows a trend of increasing harmonic amplitude with increasing throttle position. Figure 4.50 also shows that the minimum value of 0.077 rad/s, 0.081 rad/s and 0.107 rad/s, respectively, occurs at a throttle setting of 35%, and increases to a value of 0.216 rad/s, 0.226 rad/s, and 0.264 rad/s at throttle settings of 75%, 85%, and 100%, respectively.

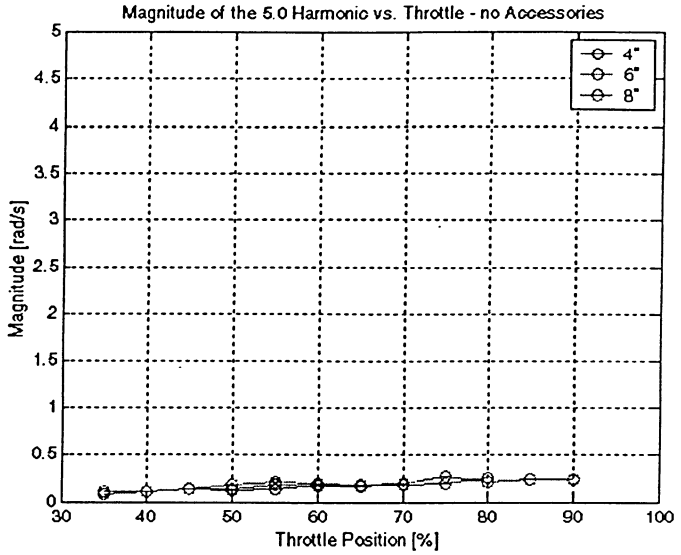


**Figure 4.50: Comparison of FFT results for the 5.0 harmonic for each blade pitch value without accessories.**

The system dynamic results obtained for the case of the propeller-engine combination without the cam system included show a dominant 1.5 harmonic, which reflects historical findings. This corroboration of previously published results provides reassurance to the investigator that the solution thus far is promising but not complete. To complete the rigid body simulation the effect of the cam accessory mechanism must be taken into account.

## *Section 4.6 Results at 4", 6", 8" Blade Pitch Values – With Accessories*

The analysis of this propeller-engine combination was first performed without the accessory system taken into consideration, and then conducted again with the accessory system taken into consideration. The evolution of the analysis was performed in this manner to first validate the method with as few terms as possible, and then to add in the accessory system to complete the simulation. The results shown in Figure 4.52 though Figure 4.54 are representative of the entire system with the accessory system taken into consideration. Table 4.4 shows the variation of steady state operating speed for each throttle setting analyzed for the three blade pitch values taken into consideration, 4", 6", and 8", respectively.

Plot (a) of Figure 4.51 shows the angular position of the crankshaft as a function of time, which is nearly linear and monotonically increasing.

Plot (b) of Figure 4.51 is the plot of the crankshaft angular velocity as a function of time. This is generated by solving the equation of motion with a fixed step Euler solver. The plot of omega vs. time shows that after starting with initial conditions of angular position and velocity, the operating speed of the engine increases to reach a steady state value after a short period of time. There is some oscillation in this plot throughout the operating range and this is due to the periodic nature of the kinetic energy, potential energy, the firing sequence and the $4\pi$-periodic pressure vs. crank angle characteristic. Superimposed on the angular velocity plot is a flat line, which is the expected steady state operating speed as calculated by a power balance between engine and propeller.

Plot (c) of Figure 4.51 is the FFT representation of the angular velocity vs. time, taken at steady state conditions. Plot (c) shows a dominating harmonic of 1.5, followed by 3.0, and 1.0. The dominating harmonic of 1.5 is a result of the system components having both $2\pi$ and $4\pi$-periodic components. The 3.0 harmonic is the first integer multiple of the 1.5 harmonic and the 1.0 harmonic is the operating speed of the engine.

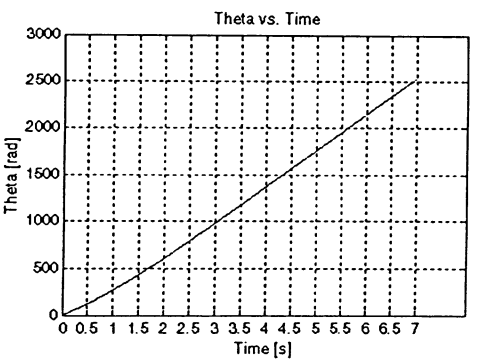


(a)

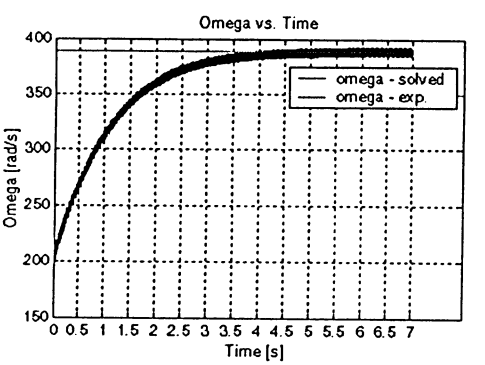


(b)

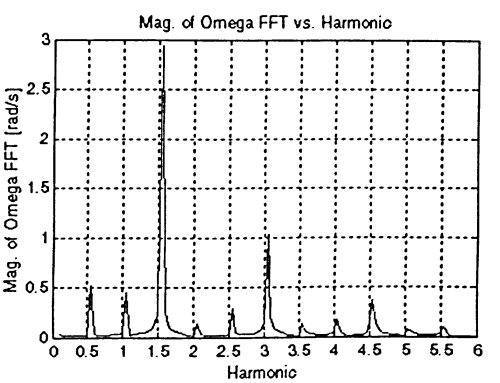


(c)

**Figure 4.51: Operating history at 35% throttle and 4″ blade pitch**

A selection of the simulation results performed with the accessory system for a 4″ blade pitch setting is found in Figure 4.52 for throttle settings of 35%, 50%, and 75%. The analysis for the 4″ and 6″ blade pitch settings ends at 75% and 85% throttle, respectively, because the system becomes speed limited.

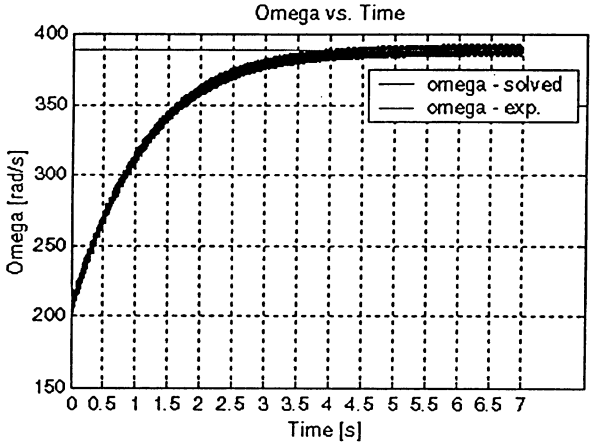


35%

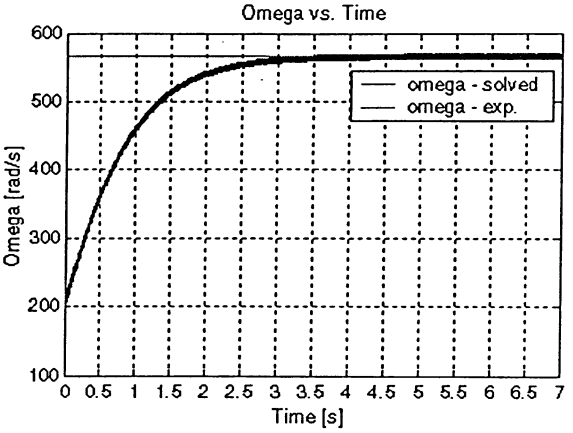


50%

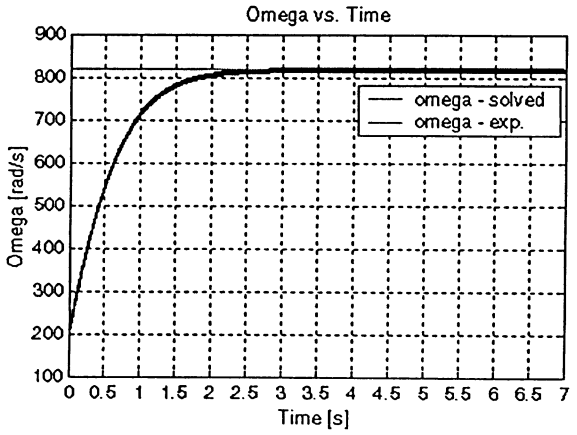


75%

Not Available

85% or 100%

**Figure 4.52: Omega vs. time for a 4″ blade pitch setting - with accessories.**

A selection of the simulation results performed with the accessory system for a 6″ blade pitch setting is found in Figure 4.53 for throttle settings of 35%, 50%, and 85%.

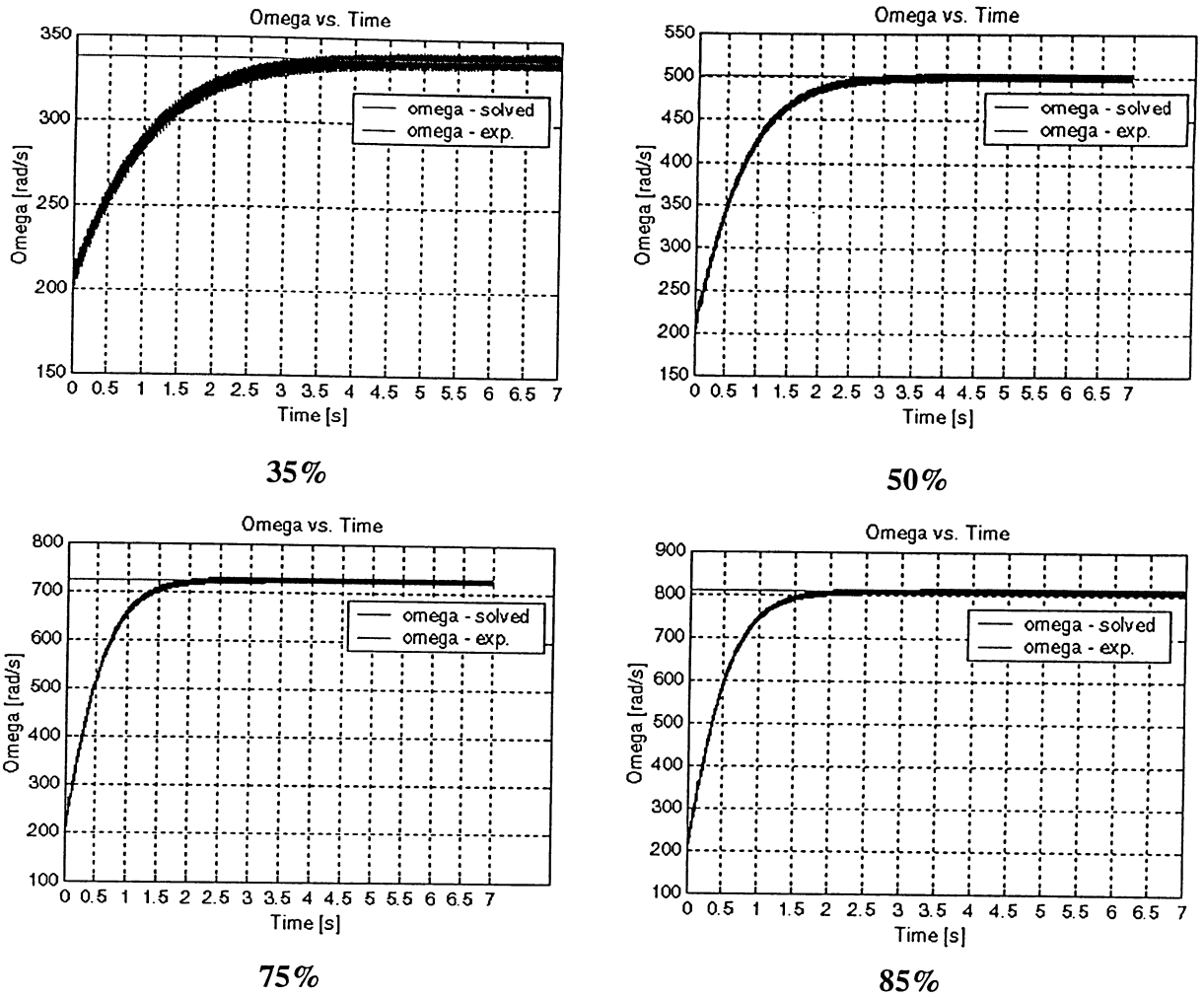


**Figure 4.53: Omega vs. time for a 6″ blade pitch setting - with accessories.**

A selection of the simulation results performed with the accessory system for a 4″ blade pitch setting is found in Figure 4.54 for throttle settings of 35%, 50%, and 100%.

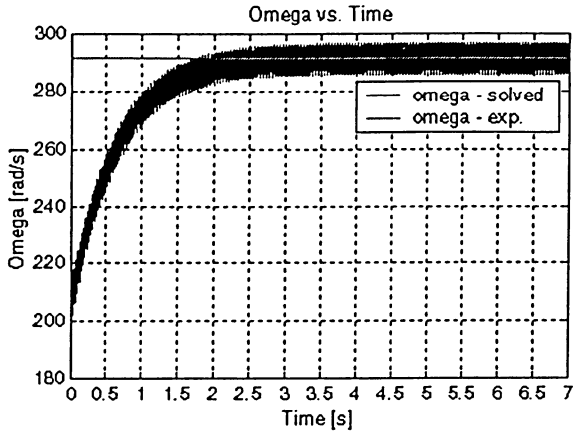


35%

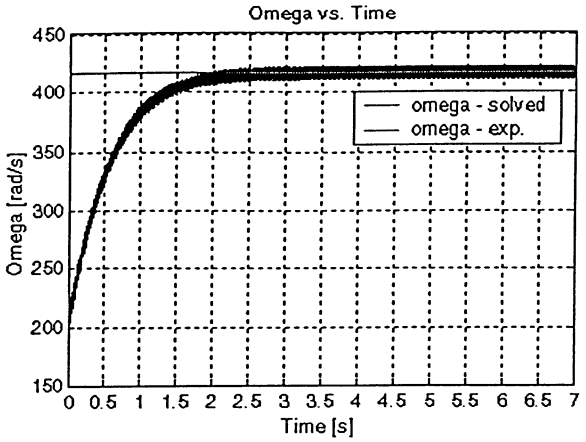


50%

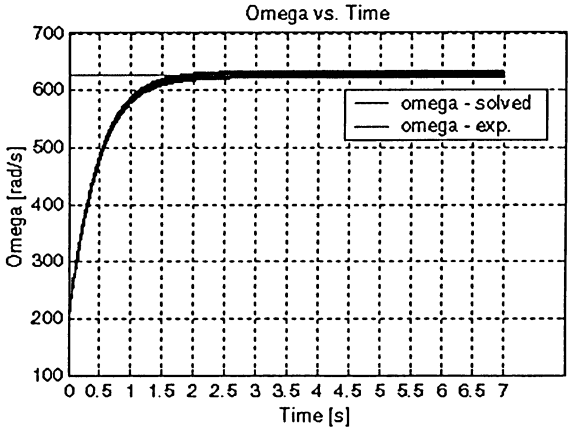


75%

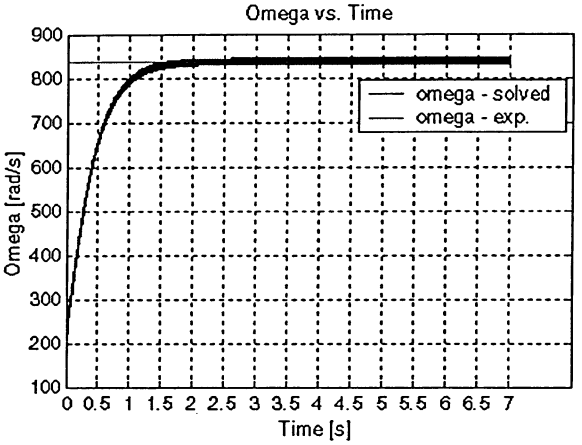


100%

**Figure 4.54: Omega vs. time for an 8″ blade pitch setting - with accessories.**

The FFT results corresponding to the plots shown in Figure 4.52 to Figure 4.54 can be found in Figure 4.55 to Figure 4.57. In each test case, the 1.5 harmonic was shown to dominate followed by the 3.0, then 1.0.

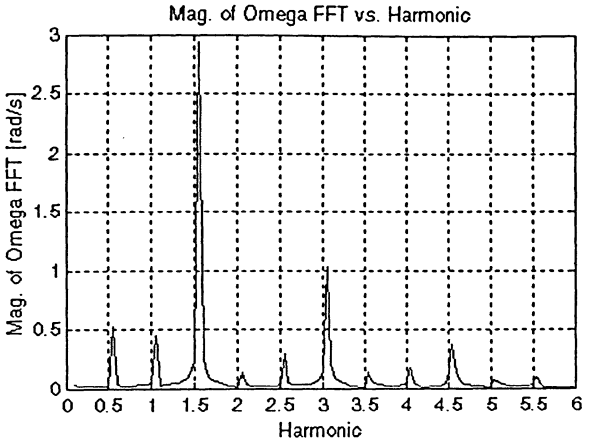


35%

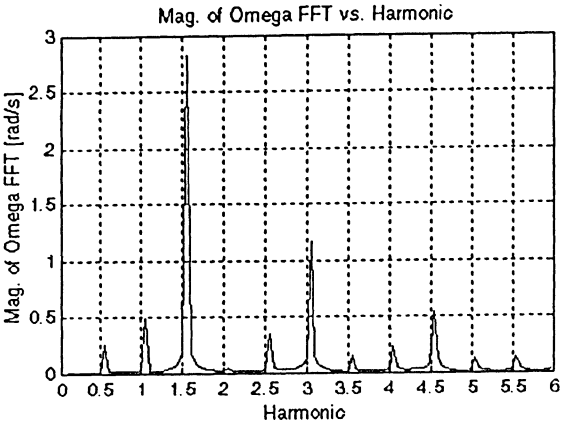


50%

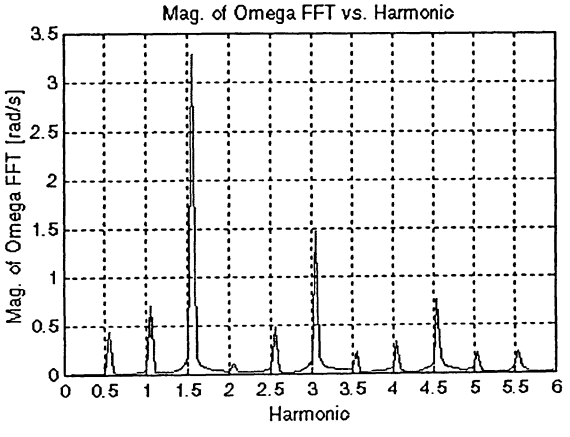


75%

Not Available

85% or 100%

**Figure 4.55: Harmonic spectrum of Figure 4.52 for a 4″ blade pitch setting - with accessories.**

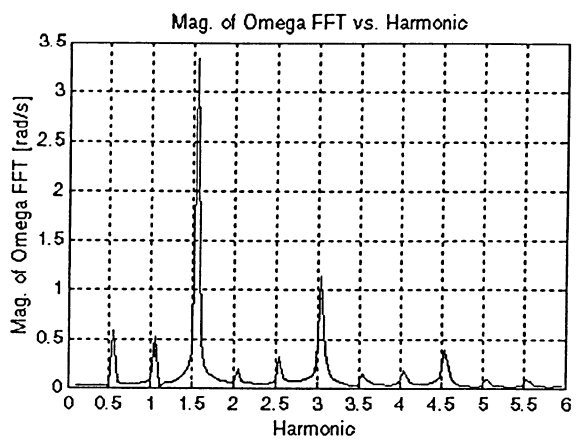


35%

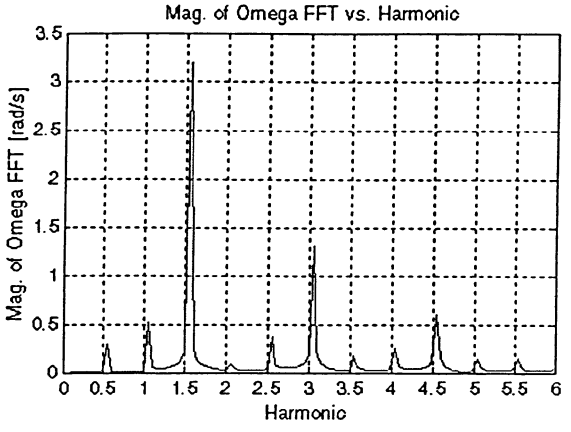


50%

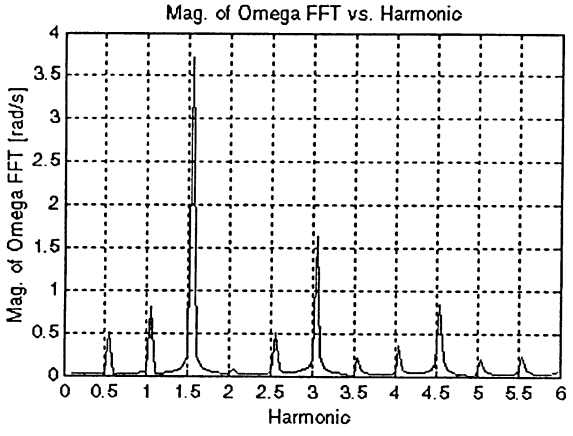


75%

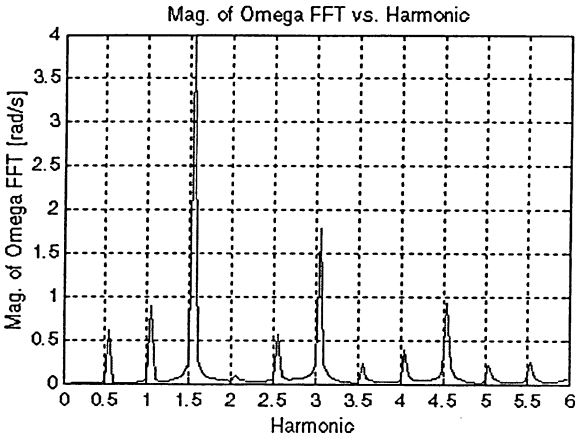


85%

**Figure 4.56: Harmonic spectrum of Figure 4.53 for a 6″ blade pitch setting - with accessories.**

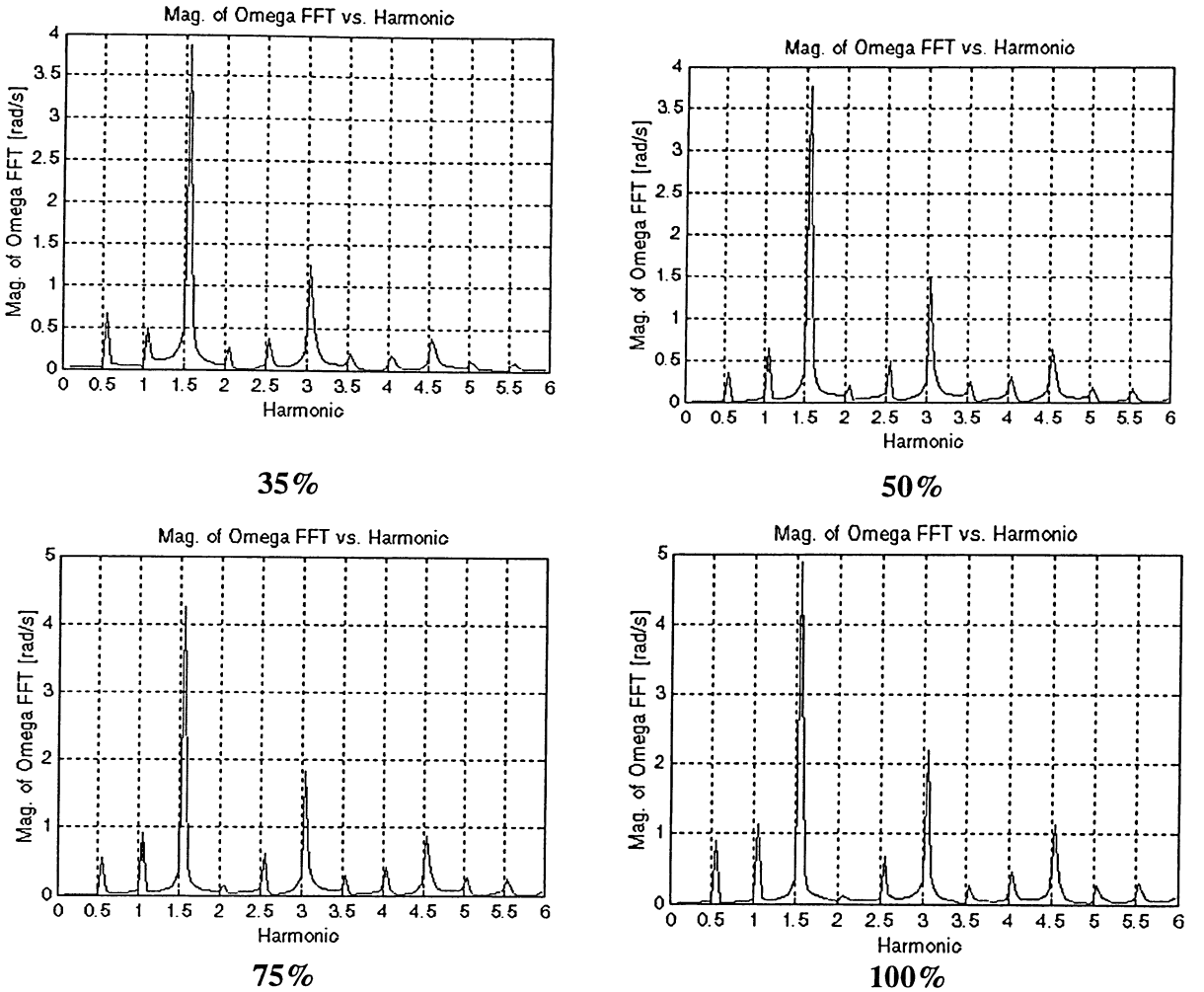


**Figure 4.57: Harmonic spectrum of Figure 4.54 for an 8″ blade pitch setting - with accessories.**

Of interest to the author was to perform a comparison of each harmonic as a function of throttle setting for each blade pitch. The results of this study are found in Section 4.6.1.

## *Section 4.6.1 Individual Harmonic Peak Comparison with Accessories*

Figure 4.58 shows a comparison of the 0.5 harmonic peaks as a function of throttle setting for each of the three blade pitch values. The three curves of the 0.5 harmonic all follow a similar trend in that they all decrease from a throttle setting of 35% to a minimum amplitude at a throttle setting of 55%, then increase in amplitude as the throttle in increased from 55% to 100%, or the RPM limited maximum for the corresponding blade pitch.

Considering the 0.5 harmonic with the propeller set to 4″, 6”, and 8” blade pitch values, the harmonic amplitude is 0.446 rad/s, 0.528 rad/s and 0.495 rad/s, respectively at 35% throttle. The amplitude then decreases to a value of 0.245 rad/s, 0.293 rad/s, and 0.351 rad/s, respectively, at a throttle setting of 55%. The amplitude of the 0.5 harmonic increases to a value of 0.701 rad/s, 0.885 rad/s and 1.147 rad/s at throttle settings of 75%, 85%, and 100%, respectively.

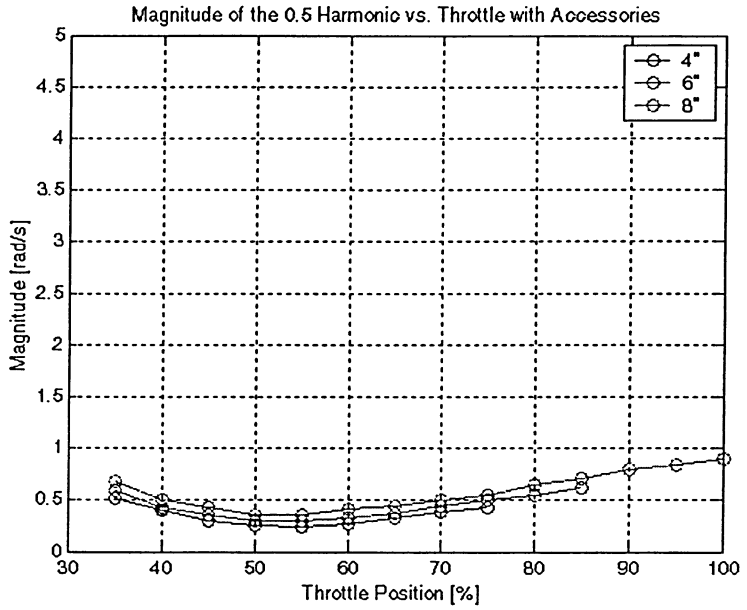


**Figure 4.58: Comparison of FFT results for the 0.5 harmonic for each blade pitch value with accessories.**

Figure 4.59 shows the three curves corresponding to the 1.0 harmonic are all increasing with increasing throttle setting. The magnitude of the 1.0 harmonic peak is expected to increase with increasing throttle setting since the 1.0 harmonic corresponds to the operating speed of the engine. The amplitude of the 1.0 harmonic is 0.446 rad/s, 0.528 rad/s, and 0.495 rad/s, respectively, at a throttle setting of 35% and increase to a value of 0.701 rad/s, 0.885 rad/s, and 1.147 rad/s, respectively at throttle settings of 75%, 85%, and 100%.

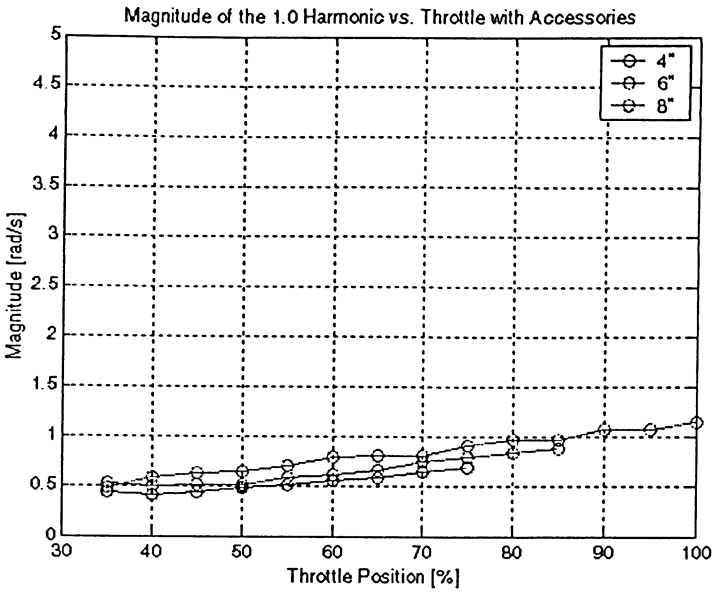


**Figure 4.59: Comparison of FFT results for the 1.0 harmonic for each blade pitch value with accessories.**

Figure 4.60 shows a comparison of the 1.5 harmonic peaks as a function of throttle setting for each of the three blade pitch values, respectively. This is the dominant harmonic of the propeller-engine system due to the interaction of the $2\pi$ and $4\pi$-periodic functions modeled in the simulation. Each curve corresponding to the three blade pitch values investigated follows a similar trend to that found in Figure 4.43.

All blade pitch settings experience a harmonic amplitude of 2.941 rad/s, 3.331 rad/s, and 3.870 rad/s, respectively, at 35% throttle. The amplitude decreases to a minimum value of 2.791 rad/s, 3.169 rad/s, and 3.761 rad/s at 45% throttle. When the throttle was increased beyond 45%, the amplitude of the 1.5 harmonic increased to the respective absolute maximum values of 3.286 rad/s, 3.979 rad/s, and 4.879 rad/s at throttle settings of 75%, 85%, and 100%, respectively.

It is desirable to operate the engine at such a speed as to minimize the amount of oscillation of the system in order to prolong the operating life of the system, maximize the time required before servicing and overhaul, and in the case of a full-size aircraft engine, it is desirable to operate the system at such a speed as to minimize the degree of oscillation for passenger and operator comfort. If the operator wished to operate the Saito-450 engine at a speed such that the 1.5 harmonic is a minimum for any blade pitch setting, Figure 4.43 indicates that this throttle setting would be 45%.

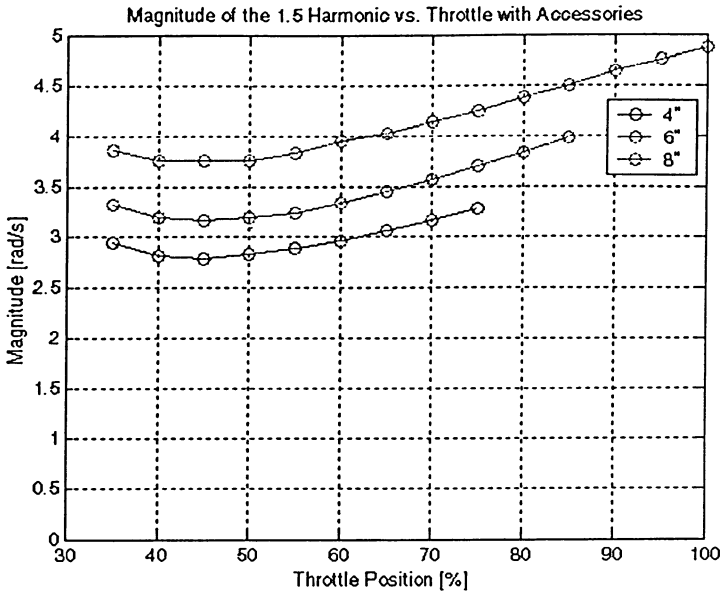


**Figure 4.60: Comparison of FFT results for the 1.5 harmonic for each blade pitch value with accessories.**

Figure 4.61 shows a comparison of the 2.0 harmonic peaks as a function of throttle setting for each of the three blade pitch values. The three curves all follow a similar trend and are of such small magnitude as to render the effect of the 2.0 harmonic on the system to an almost negligible level.

The magnitude of the 2.0 harmonic for blade pitch settings of 4″, 6″, and 8″ are at a maximum value of 0.142 rad/s, 0.187 rad/s, and 0.261 rad/s, respectively, at a throttle setting of 35%. The magnitude of the 2.0 harmonic is at a minimum value of 0.036 rad/s, 0.073 rad/s, and 0.057 rad/s, respectively, at 75%, 85%, and 100% throttle, respectively.

In this case the 2.0 harmonic has such a minimal amplitude for all throttle settings, the operator and designer can ignore the 2.0 harmonic on the system.

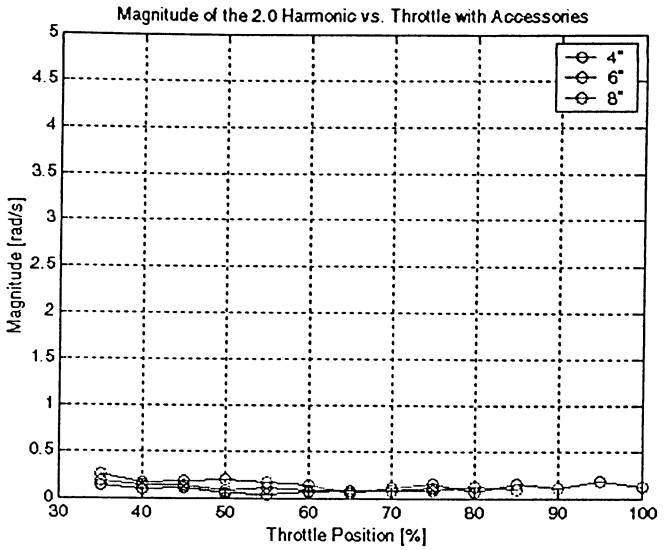


**Figure 4.61: Comparison of FFT results for the 1.5 harmonic for each blade pitch value with accessories.**

Figure 4.62 shows a comparison of the 2.5 harmonic peaks as a function of throttle setting for each of the three blade pitch values. Each curve follows a similar trend of increasing harmonic magnitude with increasing throttle setting.

Considering the 2.5 harmonic at each blade pitch setting of 4″, 6″, and 8″, the minimum harmonic amplitude is 0.288 rad/s, 0.318 rad/s, and 0.374 rad/s at 35% throttle. The magnitude increases to a maximum value of 0.476 rad/s, 0.564 rad/s, and 0.679 rad/s, respectively, at a 75%, 85%, and 100% throttle, respectively.

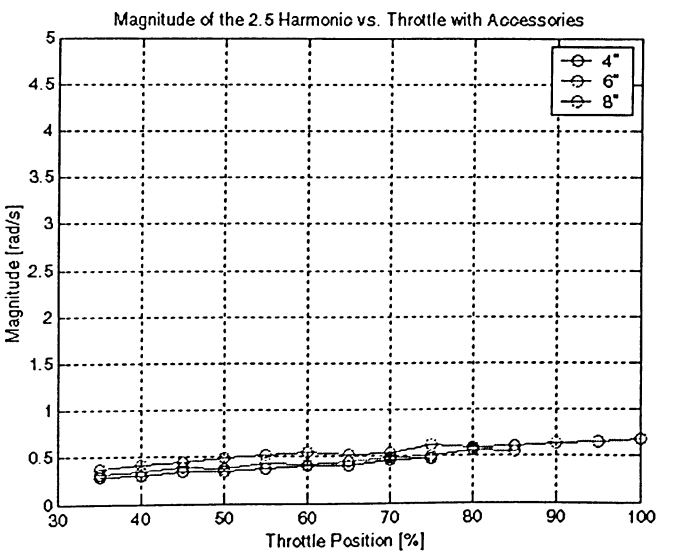


**Figure 4.62: Comparison of FFT results for the 2.5 harmonic for each blade pitch value with accessories.**

Figure 4.63 shows a comparison of the 3.0 harmonic peaks as a function of throttle setting for each of the three blade pitch values. Each curve follows a similar trend of increasing harmonic magnitude with increasing throttle setting.

Considering the 3.0 harmonic at each blade pitch setting of 4″, 6″, and 8″, the minimum value of harmonic amplitude is 1.028 rad/s, 1.129 rad/s, and 1.25 rad/s corresponds to a throttle setting of 35%. When the throttle is increased beyond 35%, the harmonic amplitude increases to a value of 1.457 rad/s, 1.791 rad/s, and 2.187 rad/s, respectively, corresponding to throttle settings of 75%, 85%, and 100%, respectively.

The 3.0 harmonic is the first integer multiple of the dominant 1.5 harmonic; therefore, it is expected that the 3.0 harmonic has the second greatest influence on the system. This expectation has been confirmed by Figure 4.63. It is also expected that the amplitude of the 3.0 harmonic would increase with increasing throttle setting because the 3.0 harmonic is the first integer multiple of the 1.5 harmonic and the second integer multiple of the 1.0 harmonic.

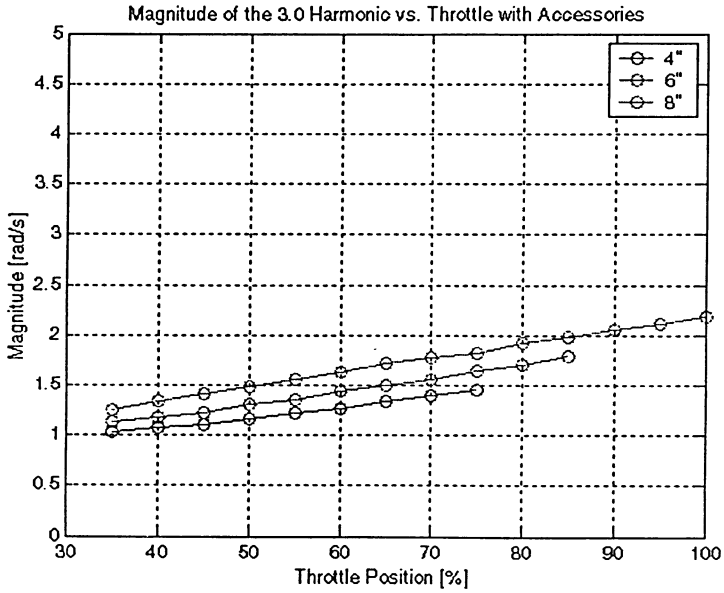


**Figure 4.63: Comparison of FFT results for the 3.0 harmonic for each blade pitch value with accessories.**

Figure 4.64 shows a comparison of the 3.5 harmonic peaks as a function of throttle setting for each of the three blade pitch values. Each of the three plots in Figure 4.64 follows a similarly flat trend.

When considering the 3.5 harmonic at blade pitch settings of 4″, 6″, and 8″, the minimum harmonic amplitude is 0.133 rad/s, 0.145 rad/s, and 0.160 rad/s, respectively, at 35% throttle. The maximum harmonic amplitude is 0.223 rad/s, 0.228 rad/s, and 0.301 rad/s at 75%, 85%, and 100% throttle.

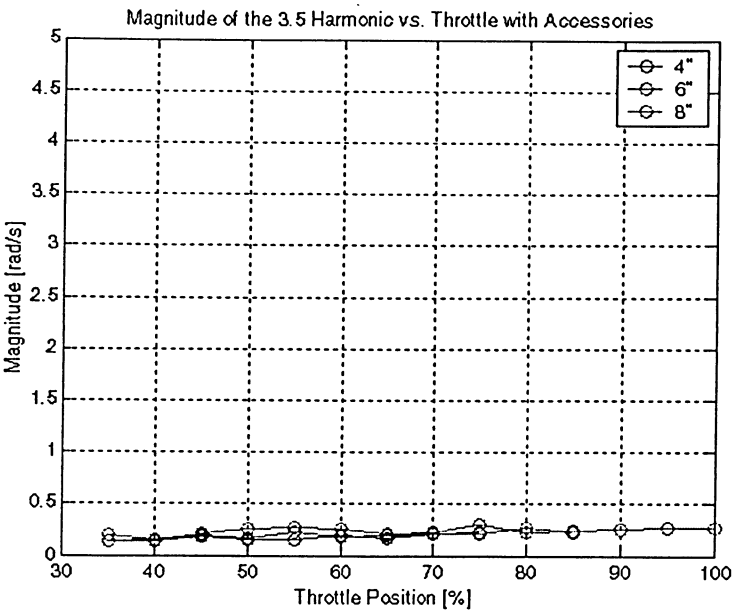


**Figure 4.64: Comparison of FFT results for the 3.5 harmonic for each blade pitch value with accessories.**

Figure 4.65 shows the magnitude of the 4.0 harmonic continuously increases with increasing throttle setting. When the blade pitch is set to 4″, 6″, and 8″, the minimum harmonic amplitude is 0.176 rad/s, 0.174 rad/s, and 0.182 rad/s at 35% throttle. The maximum harmonic amplitude of 0.333 rad/s, 0.393 rad/s, and 0.469 rad/s corresponds to throttle settings of 75%, 85%, and 100%, respectively.

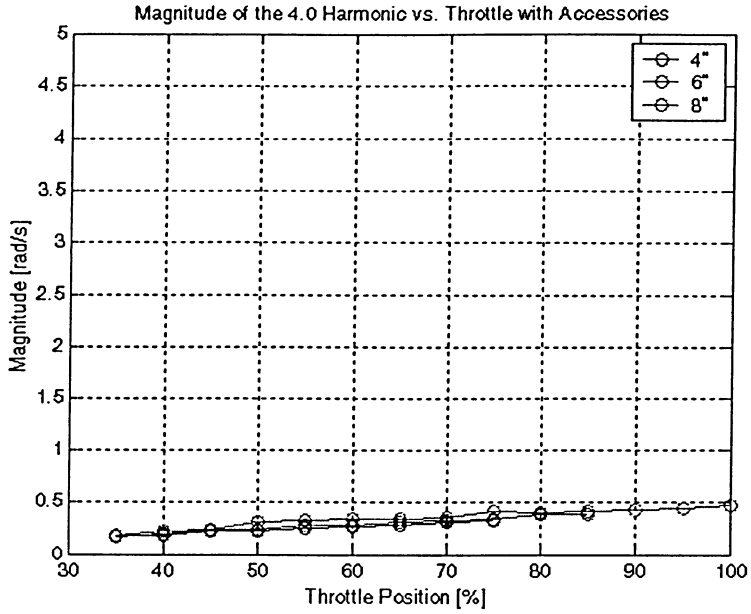


**Figure 4.65: Comparison of FFT results for the 4.0 harmonic for each blade pitch value with accessories.**

Figure 4.66 shows a comparison of the 4.5 harmonic peaks as a function of throttle setting for each of the three blade pitch values, respectively. Each of the plots in this figure follow the same general trend in that they increase with increasing throttle setting.

When considering the 4.5 harmonic for 4″, 6″, and 8″ blade pitch settings, the minimum harmonic amplitude is 0.370 rad/s, 0.385%, and 0.388% corresponding to a throttle setting of 35%. The maximum harmonic amplitude of 0.750 rad/s, 0.935 rad/s, and 1.138 rad/s occur at throttle settings of 75%, 85%, and 100%, respectively.

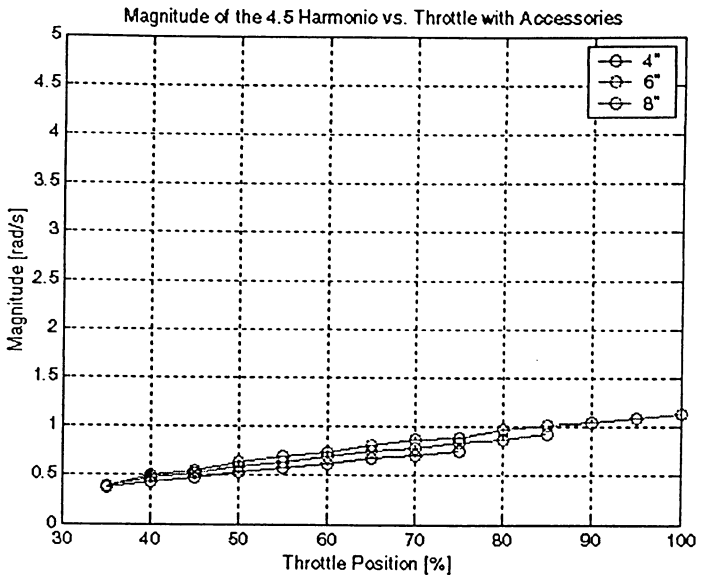


**Figure 4.66: Comparison of FFT results for the 4.5 harmonic for each blade pitch value with accessories.**

Figure 4.67 shows the 5.0 harmonic peaks as a function of throttle setting for each of the three blade pitch values. Considering the 4″, 6″, and 8″ blade pitch settings, the minimum harmonic amplitude value is 0.074 rad/s, 0.081 rad/s, and 0.108 rad/s, respectively, occur at a throttle setting of 35%. The maximum harmonic amplitude of 0.206 rad/s, 0.221 rad/s, and 0.265 rad/s, respectively, occur at throttle settings of 75%, 85%, and 100%, respectively.

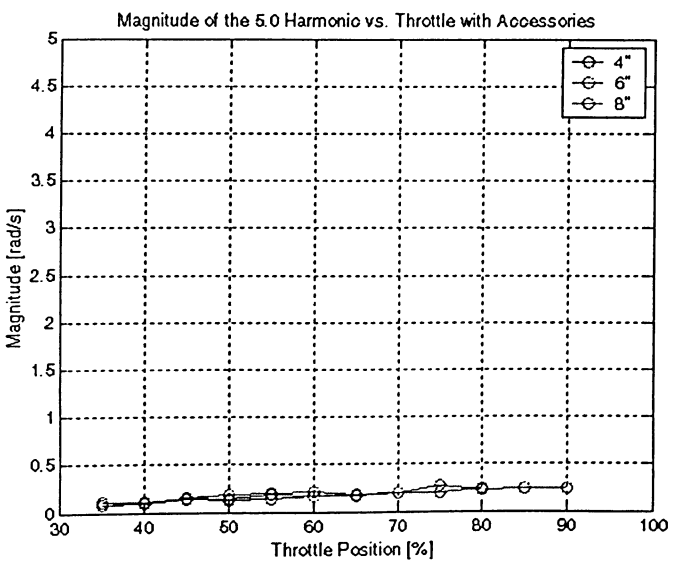


**Figure 4.67: Comparison of FFT results for the 5.0 harmonic for each blade pitch value with accessories.**

The strength of the individual harmonics for each of the three blade pitch values analyzed has been compared and plotted against the throttle setting.

Thus far, the oscillation in steady state omega value has been observed but not quantified. Table 4.4 shows that, with the exception of the 4″ and 6″ blade pitch values and the throttle setting of 35%, when the accessory drive is included in the analysis, the steady state oscillation of the crankshaft angular velocity is greater than when the accessory drive system is not included in the simulation.

**Table 4.4: Omega variation [rad/s] at 4″, 6″ and 8″ pitch settings.**

| | 4″ Pitch | | 6″ Pitch | | 8″ Pitch | |
|---|---|---|---|---|---|---|
| **Throttle** | **No Accessories** | **With Accessories** | **No Accessories** | **With Accessories** | **No Accessories** | **With Accessories** |
| 35% | 7.53 | 7.50 | 8.68 | 8.66 | 10.19 | 10.26 |
| 40% | 6.92 | 7.01 | 8.19 | 8.59 | 10.21 | 10.27 |
| 45% | 6.54 | 6.52 | 7.98 | 8.05 | 9.67 | 9.99 |
| 50% | 7.72 | 8.20 | 8.09 | 9.25 | 8.90 | 9.12 |
| 55% | 7.80 | 8.59 | 7.52 | 7.99 | 9.16 | 9.53 |
| 60% | 6.95 | 7.26 | 7.86 | 8.74 | 10.52 | 10.91 |
| 65% | 6.99 | 8.06 | 8.05 | 9.11 | 11.57 | 12.42 |
| 70% | 7.83 | 8.21 | 9.99 | 9.91 | 11.93 | 12.90 |
| 75% | 8.26 | 8.56 | 10.49 | 11.66 | 11.05 | 11.24 |
| 80% | - | - | 9.96 | 10.13 | 12.82 | 13.86 |
| 85% | - | - | 11.54 | 12.71 | 10.58 | 11.33 |
| 90% | - | - | - | - | 13.82 | 14.80 |
| 95% | - | - | - | - | 11.77 | 10.95 |
| 100% | - | - | - | - | 14.72 | 15.80 |

The effect of the accessory drive system has now been determined for all three blade pitch settings considered during this simulation. The effect of the accessory drive system on the dynamical behavior of the entire rigid-body propeller-engine system is small but not negligible. The accessory drive system does not change the steady state operating speed of the engine because friction and other non conservative forces were neglected; however, the amount of oscillation the propeller experiences under steady state operating conditions is a useful quantity to experimentally validate during future work.

## *Section 4.7 Starting*

To start the Saito-450 engine, the operator has to provide enough power to overcome the compression stroke with enough velocity to initiate combustion. Since this engine operates with

an Otto cycle, the compression ratio is not high enough to support compression ignition, hence a glow plug required. The glow plug is operated during starting by having an electric current is passed through a thin metallic filament that heats to a high temperature, thereby providing an ignition source for the air-fuel mixture that is drawn into the cylinder by the downward motion of the piston.

Typically, the glow plus is heated by the burning of the air-fuel mixture within the cylinder; however, when starting the engine the glow plug has not yet been heated by the gas mixture. To overcome this problem, the glow plug is heated by an external source until the internal gas mixture reaches a sufficient temperature to ensure the glow plug remains heated until the subsequent combustion cycle.

The propeller must be manually rotated through an angular distance with sufficient angular velocity for the ingested air-fuel mixture to ignite. This rotation is imparted to the propeller by the operator through one of three methods, the first being the operator using his/her hand (bare or gloved) to rotate the propeller, the second is the operator using a stick to displace the propeller and the third method is through the use of an electric starter that the operator presses to the spinner to rotate the propeller. Of the three methods to start the engine, in the interest of safety, the second method of using a stick to rotate the propeller was employed. The operator is also responsible for selecting the throttle setting when starting the engine and it is customary to set the throttle at idle conditions or approximately 33%.

To start the engine, the power supplied by the operator must be greater than the power required by the engine to overcome the compression stroke and initiate combustion. The power required from the operator to overcome the compression stroke for all three cylinders can be found in Table 4.5.

**Table 4.5: Work required to overcome the compression stroke [Nm].**

| Cylinder #1 | Cylinder #2 | Cylinder #3 |
|---|---|---|
| 2.7458 | 2.9417 | 2.7553 |

It was found that the power produced by one cylinder is more than adequate to overcome the power required for the compression stroke for the following cylinder. So as long as the operator can initiate combustion in one cylinder, the engine is considered started.

The compression stroke occupies an angular range of 156°, and the operator can be assumed capable of manually rotating the propeller through an angular range of 135°. It can be assumed that the end of the compression stroke corresponds to the end limit of the operator range of motion. This is a justifiable assumption since the operator must locate the compression stroke by 'feel', thereby moving the propeller into the compression stroke by a certain angular distance. The difference in angular displacement between the length of the compression stroke and the operator angular range of motion is 21°. This angular difference is a reasonable amount of distance for the operator to be sure that the propeller is in the proper angular position to commence rotation with the stick method.

The worst case for starting the engine corresponds to cylinder #2 since that configuration requires the most power input from the operator. Acting through a range of 135°, it was found that the operator must rotate the propeller at 60 rad/s in order to supply 173.56 W or 0.23 hp to overcome the power required the compression stroke.

Through the SIMPEL program, the results for the engine being rotated at 58 rad/s with the propeller set to 8″ pitch and the throttle set to 35% can be seen in Figure 4.68.

Figure 4.68 (a) shows the angular position of the propeller as a function of time. The plot shows the propeller oscillating about the starting position with logarithmically decreasing amplitude indicating an over damped system. At this low speed, the propeller is not producing any significant aerodynamic load. As such, the propeller for this condition is simply an inertial element. Figure 4.68 (b) shows the variation of the angular operating speed as a function of time. The angular velocity is oscillating about zero with decreasing amplitude. This is consistent with observations of the propeller angular velocity decreasing to zero after a period of time.

A phase plane representation of Figure 4.68 (a) and (b) is shown in Figure 4.68 (c). The inward spiral of Figure 4.68 (c) indicates the system has not reached a steady state operating condition and that the system is stable. An unstable system is characterized by a phase plane spiraling outward.

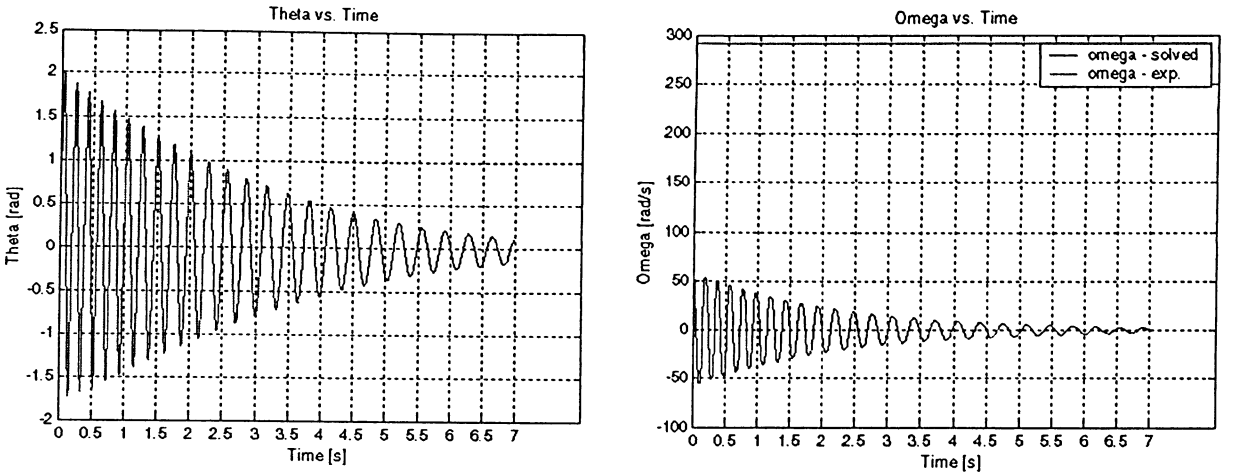


(a) (b)

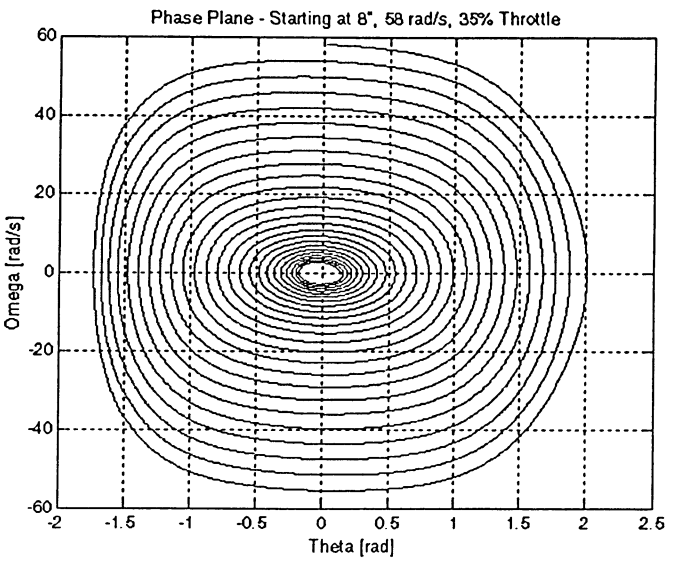


(c)

**Figure 4.68: $\theta_2$ (a) and $\omega$ (b) vs. time during unsuccessful start. Phase plane representation (c) of engine starting at 58 rad/s with the propeller set to 8″ pitch and 35% throttle.**

A successful starting of the engine can be achieved when the throttle is set to 35%, and the engine is rotated at 60 rad/s.

It should be noted that the power required to start the engine varies only slightly with throttle setting, and coupling this slight change with the operator practice of starting the engine at approximately 35% throttle, any variations caused by imprecise operator throttle setting is negligible. The power required to start the engine is also independent of propeller blade pitch setting.

It is extremely difficult to predict the required input angular velocity due to the uncertainty associated with the air-fuel combustion process. The fuel used is a non-standard blend consisting of methyl alcohol mixed with nitromethane and various oils. To achieve combustion, the pressure of the air-fuel mixture needs to be increased and this is accomplished by the motion of the piston within the cylinder. According to the ideal gas law, as the pressure of a gas is increased the temperature of that gas will also increase. The air-fuel mixture within the cylinder is not an ideal gas; however, the principle of a pressure-temperature relationship still holds.

Given that during the starting procedure, the work required to compress the gas is provided by the operator, and during this process the pressure of the air-fuel mixture is increased along with the gas temperature. The glow plug is acting as a source for ignition; however, if the air-fuel mixture is not compressed at a sufficient rate, the glow plug is still not enough of a heat source to initiate combustion. As a result, the operator must compress the air-fuel mixture by rotating the propeller with a sufficient angular velocity in order to raise the cylinder pressure and temperature to a point where ignition will occur.

Identifying this point apriori requires significant advanced knowledge of fuel properties and combustion mechanics, neither of which was available. As such, the analysis of required operator input requirements was performed post simulation analysis.

## *Section 4.8 System Stability*

After determining the steady state response of the mechanical system, it is of interest to determine whether a given operating point is stable or not, and to identify regions of instability.

### *Section 4.8.1 Equilibrium Operating Point of a System*

The torque produced by the rotation of the propeller can be described by a second order polynomial. The power characteristic of the engine has been assumed to be a linearly increasing power output until the maximum 7 hp is reached.

With the power generation (engine output) and power consumption (propeller load) curves described, the two power plots can be superimposed to determine if there is any region of instability.

The intersection of the power generation and load (propeller power consumption) curves can be an equilibrium operating condition, depending on the slopes of each curve at the intersection point. For an operating point, stable or not, to exist there must be a power balance between the power generated and the power consumed, described by Eq. (4.16), where $H_1$ is the power output and $H_2$ is the power consumed.

$$H_1 = -H_2 \tag{4.16}$$

The operating point of the system defined by the intersection of the output and load curves may, or may not, be an optimum one. Typically an engine has a load curve similar to that depicted in Figure 4.69 and is not a linearly increasing quantity; however, for the purpose of modeling the effect of a propeller on the dynamical response of the propeller-engine system, a linear engine power output will suffice. The assumption of linear power output will not alter the engine dynamics but the linear approximation will affect the steady state power output for a given throttle setting.

Typically, the designer has pre-identified a steady state operating condition at which the engine will be operated for most of the operating life. The designer will attempt to pair an engine with a load such that the engine will operate at, or near, the point of highest power output, thereby allowing the system to operate at maximum efficiency. This is called "matching" a converter characteristic (engine) to the load characteristic (propeller) [Thorpe, 1989], or in the case of the system being analyzed, matching the propeller to the engine.

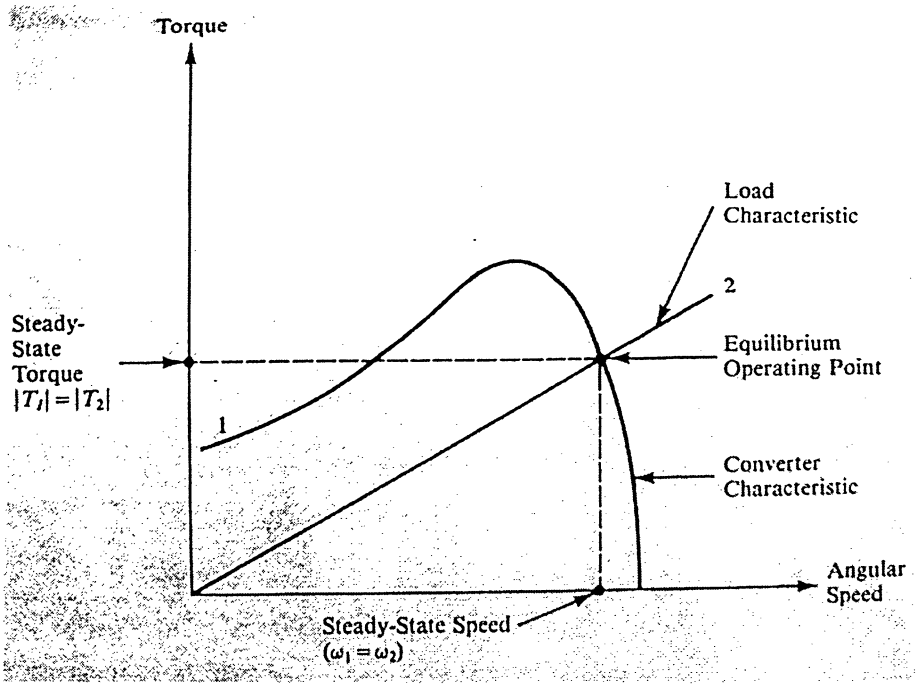


**Figure 4.69: Typical engine power curve superimposed on a linear load curve.**

## *Section 4.8.2 Stability of an Equilibrium Operating Point*

The identification of the steady state operating point does not provide any information regarding the stability of that operating point. If a disturbance were to slightly alter the load or power curves violating Eq. (4.16), the operating condition stability prior to the disturbance will dictate whether the engine will stop or if the engine operating speed will grow until failure, or some other behavior yet to be determined will occur.

The detailed approach requires knowledge of control theory, of transfer functions, and the concept of stability in a feedback control system. The approach used in this analysis was to look at the stability of the operating point in terms of the geometry of the engine power and load characteristics in the vicinity of their intersection.

This approach has a limitation since the curves under consideration are only valid for equilibrium conditions. Equilibrium and stability are not the same; a stable system requires the existence of one or many equilibrium points; however, an unstable system may or may not have any equilibrium points.

Applying the concepts of equilibrium and stability to the propeller-engine combination, consider the engine to be a prime mover and the propeller to be the load in Figure 4.70. Two possible operating points, *A* and *B*, are shown in Figure 4.70.

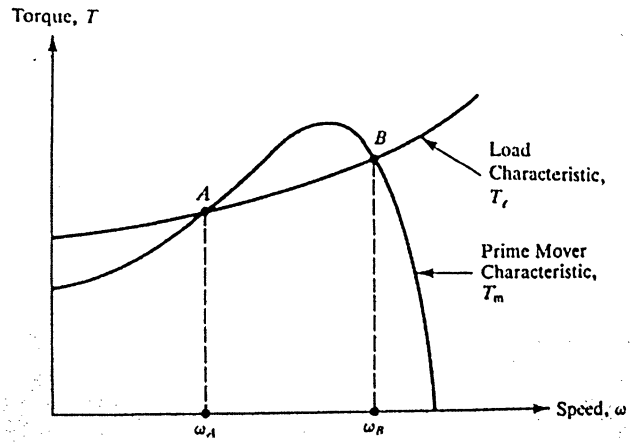


**Figure 4.70: Prime mover (engine) and load characteristic (propeller) curves.**

Let a perturbation be a disturbance in engine operating speed, $\Delta\omega$. In order to determine the stability of the system it is essential to determine if the perturbation decays, or grows, after the disturbance is removed. Associated with the perturbation in engine operating speed are the perturbations $\Delta H_m$ and $\Delta H_l$, the change in engine and load torques, respectively. During this transient period between steady state operating conditions, the perturbations are governed by Eq. (4.17).

$$H_m - H_l = I\frac{\partial \omega}{\partial t} \tag{4.17}$$

where $H_m$ refers to the engine as a whole, $H_l$ refers to the propeller, and $I$ is the moment of inertia of the system.

Assuming the disturbances are applied to the operating point A, the torque equation for the engine is described by Eq. (4.18).

$$H_m = H_{m(A)} + \Delta H_m \tag{4.18}$$

The torque equation for the propeller is Eq. (4.19).

$$H_l = H_{l(A)} + \Delta H_l \tag{4.19}$$

The engine operating speed is described by Eq. (4.20).

$$\omega = \omega_A + \Delta\omega \tag{4.20}$$

Substituting Eqn's (4.18), (4.19), and (4.20) into Eq. (4.17) results in Eq. (4.21).

$$H_{m(A)} + \Delta H_m - H_{l(A)} - \Delta H_l = I\frac{\partial(\omega_A + \Delta\omega)}{\partial t} \tag{4.21}$$

But the equilibrium relationship at point A is shown in Eqn's (4.22) and (4.23).

$$H_{m(A)} = H_{l(A)} \tag{4.22}$$

$$\frac{d\omega_A}{dt} = 0 \tag{4.23}$$

Therefore, substituting Eqn's (4.22) and (4.23) into (4.21) results in Eq. (4.24).

$$\Delta H_m - \Delta H_l = I\frac{d(\Delta\omega)}{dt} \tag{4.24}$$

The propeller and engine torques ($\Delta H_l$ and $\Delta H_m$) resulting from the perturbations can be estimated from the slopes of the characteristic curves in the vicinity of point A. The estimate for the engine characteristic curve about point A is shown in Eq. (4.25).

$$\Delta H_m = \left(\frac{\partial H_m}{\partial\omega}\right)_A \cdot \Delta\omega \tag{4.25}$$

The estimate for the propeller characteristic curve about point A is shown in Eq. (4.26).

$$\Delta H_l = \left(\frac{\partial H_l}{\partial\omega}\right)_A \cdot \Delta\omega \tag{4.26}$$

Substituting Eqn's (4.25) and (4.26) into Eq. (4.24) gives Eq. (4.27).

$$\left[\left(\frac{\partial H_m}{\partial\omega}\right)_A - \left(\frac{\partial H_l}{\partial\omega}\right)_A\right]\Delta\omega = I\frac{d\Delta\omega}{dt} \tag{4.27}$$

The constant coefficient of $\Delta\omega$ on the left side of Eq. (4.27) involves the slopes of the characteristic curves through point A. Define this coefficient as $C_A$ and rearranging Eq. (4.27) gives Eq. (4.28).

$$\frac{d\Delta\omega}{\Delta\omega} = \left(\frac{C_A}{I}\right)dt \tag{4.28}$$

Eq. (4.28) can be integrated to obtain Eq. (4.29).

$$\Delta\omega = Ke^{\left[\frac{C_A}{I}\right]t} \tag{4.29}$$

Eq. (4.29) shows that $\Delta\omega$ will either decay or grow depending on the sign of $C_A$. At point As shown in Figure 4.70, $C_A > 0$ and the local slope of the engine output torque is larger than the local slope of the load curve. This slope inequality is shown in Eq. (4.30).

$$\left(\frac{\partial H_m}{\partial \omega}\right)_A > \left(\frac{\partial H_l}{\partial \omega}\right)_A \tag{4.30}$$

Once point A is disturbed, the system tends to seek a new (more stable) operating point; therefore, point A is an unstable operating point because a small disturbance will produce an exponentially growing perturbation.

Point B shown in Figure 4.71 is a stable operating point because the local slope of the engine power curve is less than the local slope of the load curve. Eq. (4.31) mathematically describes this condition with $C_B < 0$.

$$\left(\frac{\partial H_m}{\partial \omega}\right)_B < \left(\frac{\partial H_l}{\partial \omega}\right)_B \tag{4.31}$$

A small perturbation $\Delta\omega$ will decay once the disturbance is removed, and the operating point tends to be restored to point B.

Consider a positive fluctuation $\Delta\omega$ at operating point A. The fluctuations $\Delta H_m$ and $\Delta H_l$ corresponding to $\Delta\omega$ are such that the prime mover torque $H_m$ exceeds the load torque $H_l$. The excess torque will tend to accelerate the load so $\omega$ tends to move away from $\omega_A$ in the same direction as $\Delta\omega$. With a positive fluctuation $\Delta\omega$ at point B, the associated torques $H_m$ and $H_l$ are such that $H_l$ exceeds $H_m$. Torque deficit tends to decelerate the load so $\omega$ tends to move back toward the equilibrium speed $\omega_B$ (opposite to $\Delta\omega$).

Specifically relating to the propeller-engine combination investigated in this thesis, Figure 4.71 shows a zoomed-in view of the linearly approximated engine output power curves superimposed on the second order propeller torque curve generated for a 6" blade pitch. Figure 4.71 shows a slope magnification factor of 13 intersecting the 6″ load curve, with a magnification factor of 12 shown below the propeller curve and a slope magnification factor of 14 shown above the propeller torque curve.

If a steady state operating point is reached at point A on Figure 4.71, and torque perturbation drops the load to point B, there is a torque imbalance between the engine output and that generated by the propeller. Since the engine is now able to produce more power due to the load reduction, the engine operating speed will increase from point C to point D that is a higher operating speed than the original point A. The cause of the overshoot is the kinetic energy of the system has been increased by the reduction of torque loading allowing the engine operating speed to increase. At the engine operating point D, the propeller is absorbing more torque than the engine is producing, since point E is higher on the y-axis than point D, and this torque imbalance will cause the engine operating speed to slow down and the system to return towards point A. This is a case of a stable system returning to an equilibrium position A after a perturbation.

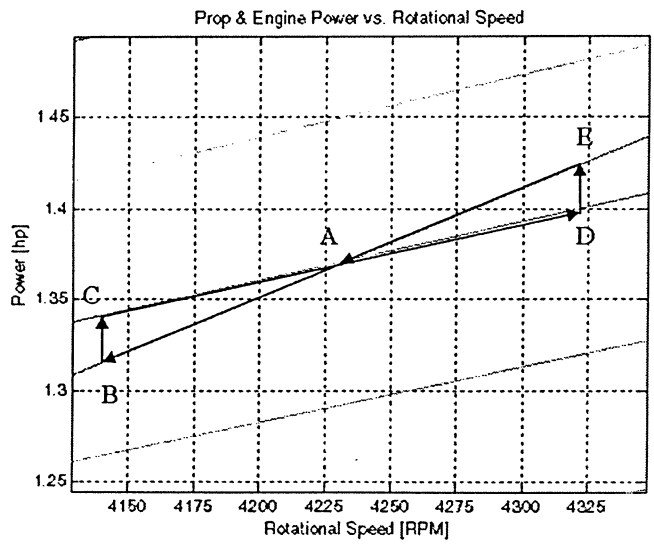


**Figure 4.71: Zoomed-in view of one propeller & engine power vs. $\omega_2$ operating condition.**

Figure 4.72 shows the linearly approximated engine power superimposed on the second order propeller torque curves for the three blade pitch values considered.

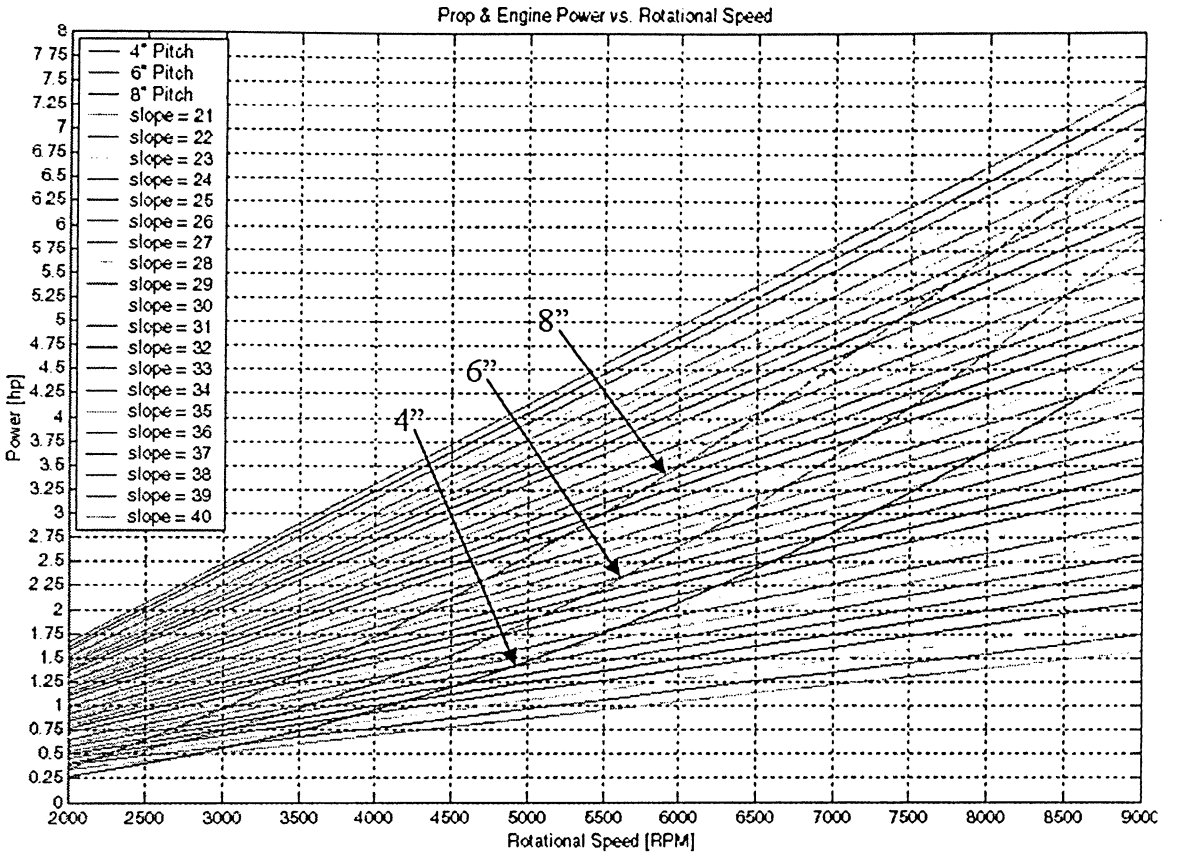


**Figure 4.72: Propeller and engine power vs. engine operating speed.**

Figure 4.72 and Eq. (4.31) show that for any operating condition set by the operator stable throughout the entire operational envelope.

# *Chapter 5 CONCLUSION*

The dynamical response of the propeller-engine combination at arbitrary throttle settings was obtained through energy methods leading to the solution of a second order differential equation of motion by a fixed-step Euler method. Solving Lagrange's equation of motion proved to be a convenient method to obtain the dynamical system response when the energy of all mechanism members was normalized with respect to the generalized coordinate.

Two sets of simulations were conducted - one neglected the effects of the accessory drive system, and the second simulation included the effects of the accessory drive system on the dynamical response of the propeller-engine system. The simulations were successful in generating realistic overall system response results that match well with observational data. The

simulations also provided the harmonic spectrum of the system response that is consistent with published data.

When comparing the results obtained from the two sets of simulations, the following conclusions are drawn:

1. The steady state operating speed is not affected by the accessory drive;
2. The steady state oscillation in the crankshaft rotational speed is slightly higher when the accessory drive system was taken into account;
3. The amplitudes of the harmonic peaks truncated at the $5^{th}$ harmonic are altered as the throttle was increased;
4. The harmonic peaks ordered from highest magnitude to lowest were essentially the same for the two simulations; and
5. The peak amplitude of the individual harmonics increases as a function of throttle position for each of the two simulations considered independently.

At each test condition consisting of a user set throttle position and blade pitch, the steady state operating speed was predicted based on a power balance between the engine output and the propeller power absorption. The simulation accurately converged to this predicted value after approximately 2 to 5 seconds of transient operation, depending on throttle setting.

The variation of the angular velocity of the propeller will create a time varying thrust and torque, which feed back into the engine, thereby altering the engine output characteristics. The time varying torque was taken into account in the Lagrange equation of motion while the time varying thrust was not. For each test condition, the magnitude of the angular velocity of the crankshaft was calculated for both simulations. It was shown that for each corresponding test case with the exception of five test conditions, the amplitude of the angular velocity oscillation was greater when the accessory drive system was included as compared to when the accessory system was neglected. Of the five test conditions where the magnitude of the steady state angular velocity oscillation was greater when the accessory system was neglected, four of the test points has differences less than or equal to 0.08 rad/s and the fifth test condition, at 95% throttle and 8″ blade pitch, the oscillation in steady state angular velocity was greater by 0.82 rad/s when the accessory system was neglected.

When the equation of motion was solved in the time domain and a steady state operating speed had been reached, the FFT was used to find the harmonic spectrum of the oscillating

steady state response for each test condition in both simulations. When comparing the amplitude of the corresponding harmonic peaks, the predicted result was that there would be a variation in harmonic peak amplitudes; however, it was not known which harmonic would increase in magnitude when the accessory drive system was taken into account and which peaks would decrease in magnitude. The results showed that, as the throttle was increased for a given harmonic, there was no pattern to indicate which simulation test case would result in higher harmonic amplitudes. For a given harmonic order and blade pitch, increasing the throttle setting in some cases produced greater harmonic amplitudes when the accessories were neglected, and sometimes increasing the throttle setting produced higher harmonic amplitudes when the accessories were included.

From the outset of this thesis, it was expected that the 1.5 harmonic would dominate all other harmonic orders due to the interaction of the $2\pi$-periodic motion of the internal engine components and $4\pi$-periodic Otto cycle gas force. It was found that for both simulations the 1.5 harmonic did in fact dominate all other harmonic orders. The second most influential harmonic was the 3.0 followed by the 1.0 harmonic for both simulations.

It was expected that the inclusion of the accessory system would alter the harmonic spectrum when compared with the simplified simulation. It was found that the accessory system affected the harmonics of order 6 and above; however, since the harmonics of interest were less than 6, the effect of the accessory system was minimal.

Considering the simulation that neglected the accessory drive system, it was expected that the amplitude of each harmonic would increase as a function of the throttle setting. It was found that the less influential harmonics such as 2.0 was essentially independent of throttle setting, where the highly influential harmonics were non-linear functions of throttle setting, sometimes decreasing in magnitude with increasing throttle setting.

The simulations generated useful data for the propeller-engine system that takes into account the aerodynamic characteristics of the propeller. No longer is the propeller merely an inertial element to be rotated by the engine; now, the feedback from the time varying propeller torque as the crankshaft completes an uneven revolution of $2\pi$ has been taken into account. These data are useful for the propeller designer since they will have the ability to predict the nature of the vibration experienced by the propeller from the engine without having to perform and pay for many expensive lab testing hours.

## *Section 5.1 Future Work*

Experimental validation and verification of the P-$\theta_2$ curve was attempted; however, due to a malfunction of either the A/D converter or the signal conditioner prevented any actual data collection.

The pressure transducer and low-noise connecting wire, purchased for this test, was verified as functional by attaching the pressure transducer and wire to an oscilloscope and verifying that a charge was beign produced by the transducer and transmitted to the oscilloscope by the low-noise wire. The voltage amplifier was working normally within manufacturer's specifications and the PC running the Visual Designer software was also operating normally. By a process of elimination, the malfunction was traced to the A/D converter or the signal conditioner. The malfunction occurred after the data pertaining to the moment of inertia of the propeller was gathered; therefore, the moment of inertia calculation is valid.

To improve the propeller model proposed in the thesis work, more blade stations may be used in the blade element analysis; the shape of airfoil cross section may be measured more accurately using a digitizer or other coordinate measuring devices. More sophisticated propeller models may be developed by taking into account the flexibility of the blades and the cross flow effects of the pressure gradient interacting with the tip vortices. Further refinements to the propeller model can be made by taking into account the rotational inflow, rotational slip slipstream, and blockage due to the engine. The propeller model generated, regardless of sophistication, can be experimentally validated by rotating the propeller with an electric motor. During the experiment, the measurement of the voltage, current and rotational speed will allow the calculation of motor output power, corrected for efficiency, which equals the power absorbed by the propeller.

Simulations obtained using SIMPEL provide the variation in angular velocity of the crankshaft as a function of time. This may be experimentally validated. Although experimental results for the crankshaft torsion may not be easily obtainable for this engine due to the physical size and configuration of the internal members, the total motion of the crankshaft may be obtainable through the use of a gear mounted between the propeller hub and the torque plate of the engine, coupled to a proximity sensor attached to a data acquisition system. Given an adequate number of teeth on the rotating gear and a high enough sample rate, the total motion of the crankshaft as it completes one rotation of $2\pi$ can be captured.

Lastly, the rigid body model may be improved by considering flexibility of some or all "weak" components in the engine-propeller system. These components include crankshaft, connecting rods, propeller blades, etc.

# *Appendix A. Relevant Code of Federal Regulation (CFR)*

The Code of Federal Regulations (CFR) is the codification of the general and permanent rules published in the Federal Register by the executive departments and agencies of the Federal Government [CFR URL]. The purpose of this particular CFR is to ensure the safety and reliability of an aero reciprocating engine.

Reciprocating aircraft engines experience vibration during the normal course of operation and it must be ensured that these vibrations do not cause damage to the engine structure. The emphasis of 14CFR33.43 is on failure in either bending or torsional modes at low or high endurance cycles.

Sec. 33.43 Vibration test.

(a) Each engine must undergo a vibration survey to establish the torsional and bending vibration characteristics of the crankshaft and the propeller shaft or other output shaft, over the range of crankshaft speed and engine power, under steady state and transient conditions, from idling speed to either 110 percent of the desired maximum continuous speed rating or 103 percent of the maximum desired takeoff speed rating, whichever is higher. The survey must be conducted using, for airplane engines, the same configuration of the propeller type which is used for the endurance test, and using, for other engines, the same configuration of the loading device type which is used for the endurance test.

(b) The torsional and bending vibration stresses of the crankshaft and the propeller shaft or other output shaft may not exceed the endurance limit stress of the material from which the shaft is made. If the maximum stress in the shaft cannot be shown to be below the endurance limit by measurement, the vibration frequency and amplitude must be measured. The peak amplitude must be shown to produce a stress below the endurance limit; if not, the engine must be run at the condition producing the peak amplitude until, for steel shafts, 10 million stress reversals have been sustained without fatigue failure and, for other shafts, until it is shown that fatigue will not occur within the endurance limit stress of the material.

(c) Each accessory drive and mounting attachment must be loaded, with the loads imposed by each accessory used only for an aircraft service being the limit load specified by the applicant for the drive or attachment point.

(d) The vibration survey described in paragraph (a) of this section must be repeated with that cylinder not firing which has the most adverse vibration effect, in order to establish the conditions under which the engine can be operated safely in that abnormal state. However, for this vibration survey, the engine speed range need only extend from idle to the maximum desired takeoff speed, and compliance with paragraph (b) of this section need not be shown.

# *Appendix B. Engine, Parts & Material Properties*

All components comprising the reciprocating engine mechanism were measured and weighed to fully catalog their dimensional properties for the purpose of performing an accurate simulation of the actual engine. The location of mass center and moment of inertia of each component was calculated from the measured properties.

Table B.1 summarizes all components in the reciprocating engine. The column entitled "KE Term #" is used to identify which quantity is being calculated when determining the kinetic energy of all engine components. The column entitled "Link Number" corresponds to the positional graphical method diagram. The mass of each component was determined by weighing the component with a digital balance with an accuracy of ±0.1 g. The column entitled "Length from wrist pin" indicated the location of the center of gravity of the connecting rods. The cells for the crank arm + counterweight and the crank pin are filled in; however, the distance found in the respective cells is referenced to the axis of rotation of the crankshaft. The last column entitled "$I_x$ about CG" is the moment of inertia of the part taken about the mass center.

**Table B.1: Mass and moment of inertia for all components in the reciprocating engine.**

| Part | KE Term # | Link Number | Mass [kg] | Length from wrist pin* [m] | $I_z$ about CG [kgm$^2$] |
|---|---|---|---|---|---|
| Piston + wrist pin | 1 | Piston 1 | 0.02436 | 0 | - |
| Piston + wrist pin | 2 | Piston 2 | 0.02436 | 0 | - |
| Piston + wrist pin | 3 | Piston 3 | 0.02436 | 0 | - |
| Crank arm + Counterweight | 4 | 2 | 0.12095 | N/A (CG @ 0.010336 m from axis of rot. towards counterweight) | $5.8679 \times 10^{-5}$ about axis of rotation |
| Crank Pin | 5 | Point A | 0.009809 | N/A (CG @ 0.01574 m from axis of rotation. | $2.7122 \times 10^{-6}$ about axis of rotation |
| Master con rod | 6 | 3 | 0.03109 | 0.046 | $1.5347 \times 10^{-5}$ |
| Secondary con rod (piston #2) | 7 | 6 | 0.00839 | 0.01679 | $2.0104 \times 10^{-6}$ |
| Secondary con rod (piston #3) | 8 | 8 | 0.00839 | 0.01679 | $2.0104 \times 10^{-6}$ |

## *B.1. Counterweight*

The shape of the counterweight was complex and it was determined that the most accurate method of determining the mass properties of the component was to create a solid model in AutoCAD and have the computer generate the required mass properties. The rendering and wireframe representations of the counterweight can be seen in Figure B.1, (a) and (b), respectively.

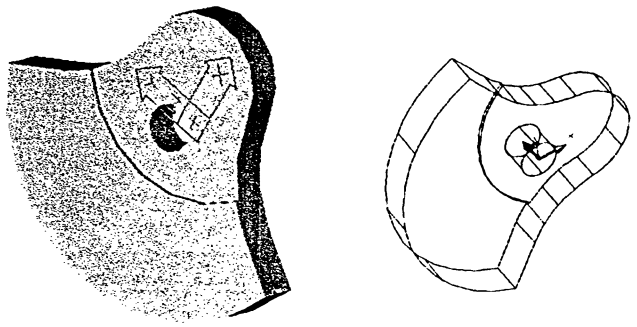

(a) (b)

**Figure B.1: Counterweight Rendering (a) and Wireframe (b).**

The detailed mass properties of the counterweight are shown in Table B.2.

**Table B.2: Mass properties of the counterweight.**

| | |
|---|---|
| Mass (CAD): | 16046.2807 g (16.0463 kg) |
| Mass (ACT): | 120.95 g (0.12095 kg) |
| Volume: | 16046.2807 $mm^3$ ($1.605 \times 10^{-5}$ $m^3$) |
| Density: | $7.56597 \times 10^{-3}$ $g/mm^3$ (7535.97 $kg/m^3$) |
| Centroid: | X: -10.3358 mm ($-1.0336 \times 10^{-2}$ m)<br>Y: 0.0000 mm (0.000 m)<br>Z: 3.8627 mm ($3.863 \times 10^{-3}$ m) |
| Moments of inertia[2]: (about coord. Axis) | X: 25094.533 $gmm^2$ ($2.59045 \times 10^{-5}$ $kgm^2$)<br>Y: 37596.868 $gmm^2$ ($3.7597 \times 10^{-5}$ $kgm^2$)<br>Z: 58679.266 $gmm^2$ ($5.8679 \times 10^{-5}$ $kgm^2$) |
| Products of inertia[2]: | XY: 0.0000 $gmm^2$ (0.0000 $kgm^2$)<br>YZ: 0.0000 $gmm^2$ (0.0000 $kgm^2$)<br>ZX: -5063.637 $gmm^2$ ($-5.063 \times 10^{-6}$ $kgm^2$) |
| Radii of gyration: | X: 14.6347 mm ($1.4635 \times 10^{-2}$ m)<br>Y: 17.6308 mm ($1.763 \times 10^{-2}$ m)<br>Z: 22.0262 mm ($2.2026 \times 10^{-2}$ m) |
| Principal moments[2] and X-Y-Z directions about centroid: | |
| I: 24097.366 $gmm^2$ ($2.4097 \times 10^{-5}$ $kgm^2$) along [1.0000 0.0000 0.0000]<br>J: 22871.429 $gmm^2$ ($2.287 \times 10^{-5}$ $kgm^2$) along [0.0000 1.0000 0.0000]<br>K: 45760.994 $gmm^2$ ($4.576 \times 10^{-5}$ $kgm^2$) along [0.0000 0.0000 1.0000] | |

[1] From AutoCAD 2000.
[2] Moments calculated with actual mass of 120.95 g (density = 7535.97 $kg/m^3$)

## *B.2. Crank Pin*

A solid model of the crank pin was generated since it is a simple shape to analyze and because the position of the mass center of the crank pin is offset in both the *y* and *z* directions. A rendering and wireframe image of the crank pin are shown Figure B.2, (a) and (b), respectively.

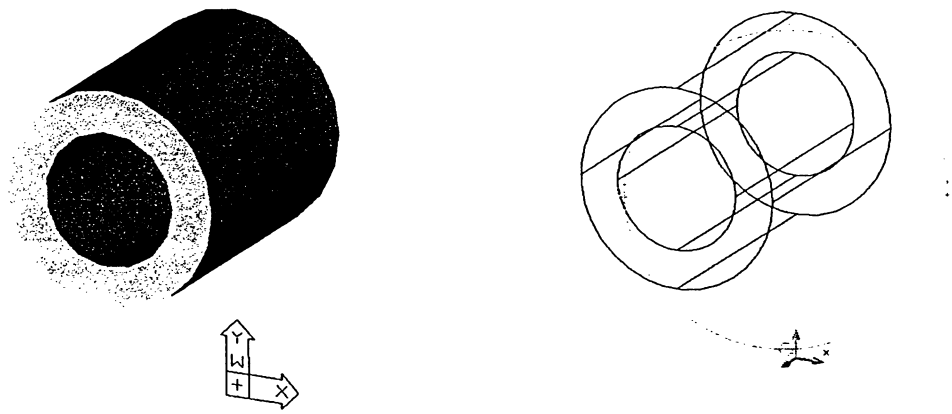


**(a)** **(b)**

**Figure B.2: Rendering (a) and wireframe (b) of the crank pin.**

The detailed mass properties of the crank pin can be found in Table B.3.

**Table B.3: Mass properties of the crank pin.**

| | |
|---|---|
| Mass (CAD): | 1301.6589 g (1.3017 kg) |
| Mass (ACT): | 9.809 g ($9.809 \times 10^{-3}$ kg) |
| Volume: | 1301.6589 $mm^3$ ($1.302 \times 10^{-6}$ $m^3$) |
| Density: | $7.56597 \times 10^{-3}$ g/$mm^3$ (7535.97 kg/$m^3$) |
| Centroid: | X: 0.0000 mm (0.0000 m)<br>Y: 15.7353 mm ($1.574 \times 10^{-2}$ m)<br>Z: 7.9375 mm ($7.9375 \times 10^{-2}$ m) |
| Moments of inertia[2]: | X: 3394.4609 $gmm^2$ ($3.3945 \times 10^{-6}$ $kgm^2$)<br>Y: 965.7557 $gmm^2$ ($9.6576 \times 10^{-7}$ $kgm^2$)<br>Z: 2712.2023 $gmm^2$ ($2.7122 \times 10^{-6}$ $kgm^2$) |
| Products of inertia[2]: | XY: 0.0000 $gmm^2$ (0.0000 $kgm^2$)<br>YZ: 1225.1338 $gmm^2$ ($1.2251 \times 10^{-6}$ $kgm^2$)<br>ZX: 0.0000 $gmm^2$ (0.0000 $kgm^2$) |
| Radii of gyration: | X: 18.6026 mm ($1.860 \times 10^{-2}$ m)<br>Y: 9.9225 mm ($9.923 \times 10^{-2}$ m)<br>Z: 16.6283 mm ($1.663 \times 10^{-2}$ m) |
| Principal moments[2] and X-Y-Z directions about centroid: | |
| I: 347.7504 $gmm^2$ ($3.4775 \times 10^{-7}$ $kgm^2$) along [1.0000 0.0000 0.0000]<br>J: 347.7504 $gmm^2$ ($3.478 \times 10^{-7}$ $kgm^2$) along [0.0000 1.0000 0.0000]<br>K: 283.4971 $gmm^2$ ($2.8349 \times 10^{-7}$ $kgm^2$) along [0.0000 0.0000 1.0000] | |

[1] From AutoCAD 2000.
[2] Moments calculated with actual mass of 9.809 g (density = 7535.97 kg/$m^3$).

## *B.3. Master Connecting Rod*

The geometry of the master connecting rod is complex for an analytical analysis to be performed with the desired accuracy; therefore, a solid model was created in AutoCAD. The rendering and wireframe representation of the master connecting rod can be seen in Figure B.3, (a) and (b), respectively.

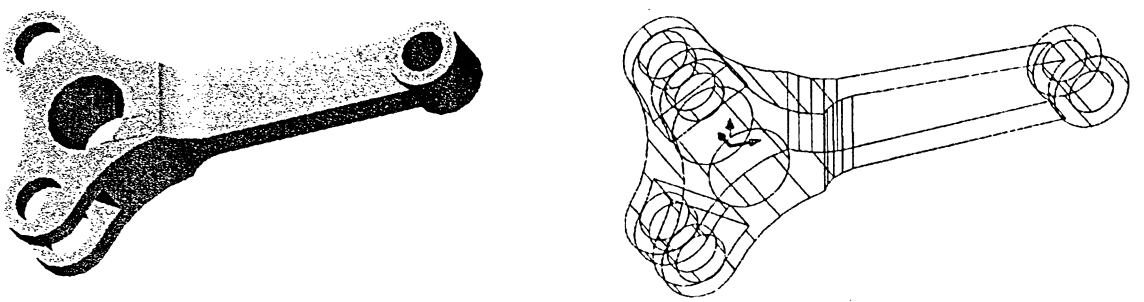

(a) (b)

**Figure B.3: Rendering (a) and wireframe (b) of the master connecting rod.**

The detailed mass properties of the master connecting rod can be found in Table B.4.

**Table B.4: Mass properties of the master connecting rod.**

| | |
|---|---|
| Mass (CAD): | 8851.8754 g (8.8519 kg) |
| Mass (ACT): | 31.09 g (0.03109 kg) |
| Volume: | 8851.8754 $mm^3$ ($8.8519x10^{-6}$ $m^3$) |
| Density: | $3.5122x10^{-3}$ $g/mm^3$ (3512.24 $kg/m^3$) |
| Centroid: | X: 13.9716 mm ($1.3972x10^{-2}$ m)<br>Y: 0.0000 mm (0.0000 m)<br>Z: 0.0000 mm (0.0000 m) |
| Moments of inertia[2]: (about axis of rot.) | X: 1993.652 $gmm^2$ ($1.9937x10^{-6}$ $kgm^2$)<br>Y: 20343.492 $gmm^2$ ($2.0343x10^{-5}$ $kgm^2$)<br>Z: 21416.0565 $gmm^2$ ($2.1416x10^{-5}$ $kgm^2$) |
| Products of inertia[2]: | XY: -0.17329 $gmm^2$ ($-1.7329x10^{-10}$ $kgm^2$)<br>YZ: $-3.744x10^{-3}$ $gmm^2$ ($-3.7437x10^{-12}$ $kgm^2$)<br>ZX: -22.066 $gmm^2$ ($-2.2066x10^{-8}$ $kgm^2$) |
| Radii of gyration: | X: 8.0078 mm ($8.0078x10^{-3}$ m)<br>Y: 25.5801 mm ($2.558x10^{-2}$ m)<br>Z: 26.2457 mm ($2.625x10^{-2}$ m) |
| Principal moments[2] and X-Y-Z directions about centroid: | |
| I: 1993.571 $gmm^2$ ($1.994x10^{-6}$ $kgm^2$) along [1.0000 0.0000 0.0000]<br>J: 14274.49 $gmm^2$ ($1.4274x10^{-5}$ $kgm^2$) along [0.0000 1.0000 0.0000]<br>K: 15347.1358 $gmm^2$ ($1.5347x10^{-5}$ $kgm^2$) along [0.0000 0.0000 1.0000] | |

[1] From AutoCAD 2000.
[2] Moments calculated with actual mass of 31.09 g (density = 3512.24 $kg/m^3$)

## *B.4. Secondary Connecting Rod*

The geometry of the secondary connecting rod is not as complex as the master connecting rod; however, it a solid model was beneficial to the overall analysis of the component. The solid model was able to take into account the generous fillets connecting the two ends to the approximately rectangular center section. Figure B.4 (a) and (b) shows the rendering and wireframe, respectively, of the secondary connecting rod.

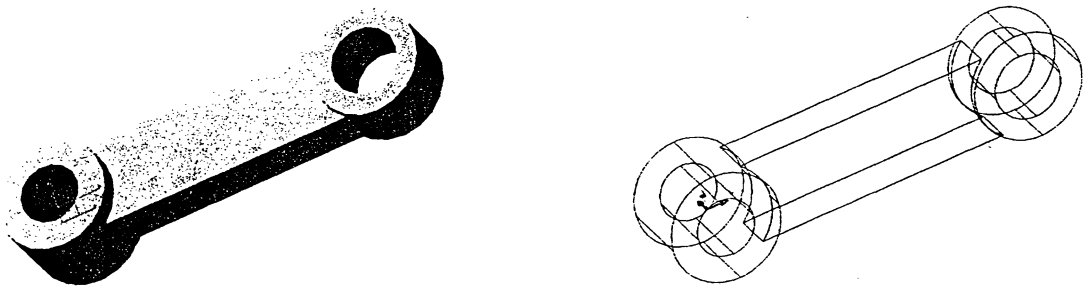

(a) (b)

**Figure B.4: Rendering (a) and wireframe (b) representation of the secondary connecting rods.**

The detailed mass properties of the secondary connecting rod can be found in Table B.5.

**Table B.5: Mass properties of the secondary connecting rod.**

| | |
|---|---|
| Mass (CAD): | 3422.5316 g (3.4225 kg) |
| Mass (ACT): | 8.39 g ($8.39 \times 10^{-3}$ kg) |
| Volume: | 3422.5316 $mm^3$ ($3.4225 \times 10^{-6}$ $m^3$) |
| Density: | $2.45 \times 10^{-3}$ $g/mm^3$ (2451.42 $kg/m^3$) |
| Centroid: | X: 16.7845 mm ($1.6785 \times 10^{-2}$ m)<br>Y: 0.0000 mm (0.0000 m)<br>Z: 0.0000 mm (0.0000 m) |
| Moments of inertia[2]: (about axis shown) | X: 147.792 $gmm^2$ ($1.4779 \times 10^{-7}$ $kgm^2$)<br>Y: 4323.847 $gmm^2$ ($4.3238 \times 10^{-6}$ $kgm^2$)<br>Z: 4374.042 $gmm^2$ ($4.374 \times 10^{-6}$ $kgm^2$) |
| Products of inertia[2]: | XY: 0.0000 $gmm^2$ (0.0000 $kgm^2$)<br>YZ: 0.0000 $gmm^2$ (0.0000 $kgm^2$)<br>ZX: $-4.658 \times 10^{-6}$ $gmm^2$ ($-4.658 \times 10^{-15}$ $kgm^2$) |
| Radii of gyration: | X: 4.1982 mm ($4.1982 \times 10^{-3}$ m)<br>Y: 22.7015 mm ($2.27 \times 10^{-2}$ m)<br>Z: 22.8329 mm ($2.283 \times 10^{-2}$ m) |
| Principal moments[2] and X-Y-Z directions about centroid: | |
| I: 147.876 $gmm^2$ ($1.47876 \times 10^{-7}$ $kgm^2$) along [1.0000 0.0000 0.0000]<br>J: 1960.2126 $gmm^2$ ($1.9602 \times 10^{-6}$ $kgm^2$) along [0.0000 1.0000 0.0000]<br>K: 2010.4077 $gmm^2$ ($2.0104 \times 10^{-6}$ $kgm^2$) along [0.0000 0.0000 1.0000] | |

[1] From AutoCAD 2000.
[2] Moments calculated with actual mass of 8.39 g (density = 2451.42 $kg/m^3$).

## *References*


Orenda Recip. Inc., "OE-600A Crankshaft Vibration Testing", Mississauga, Ontario, 2000.

Archer, Douglas R. & Saarlas, Maido. "An Introduction to Aerospace Propulsion." Prentice Hall, Upper Saddle River, NJ. 1996.

Anderson John, D. "Fundamentals of Aerodynamics, 2nd Ed." McGraw-Hill, Inc. New York, NY. 1991.

Archer, R. D., Saarlas, M. "An Introduction to Aerospace Propulsion" Prentice Hall, Upper Saddle River, New Jersey. 1996.

Gordon P. Blair, "Design and Simulation of Four-Stroke Engines v7" SAE, Warrendale PA, 1999.

Burden, Richard, L. & Faires, Douglas J. "Numerical Analysis, 6th Ed." Brooks/Cole Publishing Company, New York, NY. 1997.

Den Hartog, J. "Mechanical Vibrations 4th Ed." McGraw-Hill, New York, 1956.

Hurt, H. H. Jr. "Aerodynamics for Naval Aviators" Issued by the Office of the Chief of Naval Operations Aviation Training Division. 1965. NAVAIR 00-80T-80.

Kuo, P. (Fall 1996) Cylinder Pressure in a Spark-Ignition Engine: A Computational Model, J. Undergrad. Sci. 3: 141-145.

Lennon, A. "R/C Model Aircraft Design." Air Age, Inc. Ridgefield, CT. 1999.

McCormick, Barnes W. "Aerodynamics Aeronautics and Flight Mechanics 2nd Ed." John Wiley & Sons, Inc. New York, NY. 1995.

Moran, Michael J. & Shapiro, Howard N. "Fundamentals of Engineering Thermodynamics, 3rd Ed." John Wiley & Sons, Inc. New York, NY. 1996.

Norton, Robert, L. "Design of Machinery, 3rd Ed." McGraw-Hill, Inc. New York, NY. 2004.

Pulkrabek, Willard W. "Engineering Fundamentals of the Internal Combustion Engine 2nd Ed." by. Pearson Prentice-Hall, 2004.

Riley, William F. & Sturges, Leroy D. "Engineering Mechanics – Dynamics, 2nd Ed." New York, NY. 1996.

Root, Ralph E. "Dynamics of Engine and Shaft", John Wiley & Sons, New York. 1932.

Streeter, Victor L., Wylie, Benjamin, E., Bedford, Keith, W. "Fluid Mechanics, 9th Ed." McGraw-Hill, New York, NY. 1998.

The Design of Screw Propellers. Watts, Henry. Longmans, Green and Co. New York, NY. 1920.

Thomson, William, T., Dahleh, Marie Dillon. "Theory of Vibration with Applications, 5th Ed." Prentice Hall, Upper Saddle River, NJ. 1998.

Thorpe, James F. "Mechanical System Components". Allyn and Bacon, Needham Heights, Massachusetts, 1989. (p12-19)

Eriksson, L. Andersson, I. "An Analytic Model for Cylinder Pressure in a Four Stroke SI Engine" SAE, 2002-01-0371.

http://www.gpoaccess.gov/cfr/index.html